University of Zagreb
Faculty of Mechanical Engineering and Naval Architecture

Vuko Vukčević

Numerical Modelling of Coupled Potential and Viscous Flow for Marine Applications

DOCTORAL THESIS

Zagreb, 2016.

University of Zagreb
Faculty of Mechanical Engineering and Naval Architecture

Vuko Vukčević

Numerical Modelling of Coupled Potential and Viscous Flow for Marine Applications

DOCTORAL THESIS

Supervisor: prof. Hrvoje Jasak, PhD

Zagreb, 2016.

Sveučilište u Zagrebu
Fakultet strojarstva i brodogradnje

Vuko Vukčević

Numeričko modeliranje spregnutog potencijalnog i viskoznog strujanja za primjenu u pučinskoj i brodskoj hidrodinamici

DOKTORSKI RAD

Mentor: prof. dr. sc. Hrvoje Jasak

Zagreb, 2016.

Acknowledgements

My sincere gratitude and respect goes to my supervisor, Prof. Hrvoje Jasak, who was always ready and eager to help with numerous mathematical, numerical and programming problems I have stumbled upon during my PhD studies. I feel I have learned a lot from him during these three years, yet, it still seems I have only scratched the surface. I am sincerely looking forward to our future collaboration and new challenges it will bring.

I am also very grateful to other members of our CFD group at Faculty of Mechanical Engineering and Naval Architecture. Prof. Željko Tuković was always there to help, especially in the beginning of my PhD studies when I was inexperienced in CFD and OpenFOAM. Special thanks goes to my colleagues and good friends in the group: Inno Gatin, Gregor Cvijetić, Vanja Škurić, Tessa Uroić and Robert Keser, who made sure that there was plenty of laughing in our offices, which I think somehow contributed to an already productive working environment. My gratitude also goes towards Dr. Henrik Rusche, with whom I had numerous wonderful discussions during my studies. I sincerely hope that I will continue to work with all of you in the future.

I am very grateful to Prof. Sanja Singer for sharing the LaTeXtemplate for this thesis and for numerous discussions regarding mathematical problems I had.

My thanks also go to my colleagues at Bureau Veritas: Šime Malenica, Quentin Derbanne, Louis Diebold, Charles Monroy, Sopheak Seng and Guillaume De-Hauteclocque: I fell they have significantly contributed to this work by providing lots of fruitful discussions and made my stays at Bureau Veritas feel like home.

I am also grateful for challenging questions by Dr. Geon-Hong Kim from Hyundai Heavy Industries and the exchange of knowledge they provided.

I would also like to thank Ms. Izidora Herold, Ms. Matea Klanac, Ms. Nevena Grubelić and late Ms. Višnja Doliner for providing administrative support during my PhD studies.

Finally, I would like to express my gratitude towards my family. Without my significant other, Doris Đečević, I definitely would not be here. She kept me on track pursuing the career in naval architecture and marine engineering, although I wanted to "stray" more than once. I am extremely grateful to her for her support, patience and love during my PhD studies. I am thankful to my mother, Vera Vukčević, late father, Mirčeta Vukčević and older brother, Marko Vukčević for giving me the opportunity to pursue higher education and always encouraging it. My thanks go to my aunts and uncles, Mirjana and Đuro Matić, and Vesna and Mišo Radoš for always supporting me. Now the strange part: I am thankful for my restless little dog Gizmo since the long walks I have been taking with him helped solve numerous modelling and programming issues. If the debugger was not able to help, a long walk with Gizmo did the trick.

The financial support for this research provided by Bureau Veritas and Hyundai Heavy Industries is gratefully acknowledged.

Abstract

A numerical framework for coupling arbitrary potential flow with fully nonlinear, two–phase and turbulent Computational Fluid Dynamics model is presented in this work, where the primary focus of this thesis is the development of viscous model.

The model is implemented in arbitrary polyhedral Finite Volume method in `foam-extend`, a community driven fork of the open source Open Field Operation And Manipulation software.

The present model relies on the Ghost Fluid Method for discretisation of jump conditions, yielding infinitesimally sharp density and pressure jumps across the free surface. Interface capturing is achieved with implicitly redistanced Level Set method derived from the Phase Field equation, yielding good conservation properties and rendering additional redistancing steps unnecessary. The potential and viscous flow coupling is achieved via Spectral Wave Explicit Navier–Stokes Equations approach, where the solution is decomposed into incident potential flow solution and perturbation components, facilitating wave transport. Wave reflection is prevented by using relaxation zones with implicit treatment in the far–field. All methodologies are mathematically or numerically reformulated to adhere to strongly conservative, compact stencil, polyhedral Finite Volume method.

The numerical model is validated and verified on four sets of test cases: free surface flow over a ramp, wave propagation, assessment of higher order forces on a vertical cylinder due to wave diffraction and seakeeping of a ship in head and oblique regular waves. The computational results compare well with analytical, other numerical and experimental results. A strong emphasis is given to numerous sensitivity studies addressing numerical uncertainties.

Keywords:
Marine hydrodynamics, Free surface flows, Ghost Fluid Method, Implicitly redistanced Level Set method, Solution and domain decomposition, Polyhedral Finite Volume method, OpenFOAM, Validation and verification

Prošireni sažetak

Ovaj rad predstavlja numerički model za spregu proizvoljnog potencijalnog strujanja s potpuno nelinearnim, dvofaznim i turbulentnim modelom računalne dinamike fluida. Naglasak je stavljen na razvoj viskoznog modela dok se za spregu s potencijalnim strujanjem koriste dobro utemeljene valne teorije.

I Matematički model

Kao osnova za razvoj numeričkog modela korištene su Navier-Stokesove jednadžbe nestlačivog strujanja dvaju fluida, gdje se fluidi međusobno sprežu pomoću skokovitih rubnih uvjeta na slobodnoj površini. Ovaj pristup je poznat kao Ghost Fluid Method (GFM) koji je uspješno korišten za proračune dvofaznih strujanja na strukturiranim proračunskim mrežama.

Za praćenje slobodne površine korištena je Level Set (LS) metoda izvedena iz Phase Field (PF) jednadžbe, što omogućava implicitnu reinicijalizaciju LS funkcije udaljenosti. Rezultirajuća LS metoda također ima dobra svojstva konzervativnosti. Detaljno je predstavljena reformulacija izvornih članova u konvekcijske članove za LS transportnu jednadžbu. Također se pokazao način određivanja difuzijskog parametra u LS jednadžbi te se pokazalo da je konačno rješenje neosjetljivo na njegove promjene.

Sprega matematičkog modela viskoznog strujanja s potencijalnim strujanjem se zasniva na Spectral Wave Explicit Navier–Stokes Equations (SWENSE) dekompoziciji rješenja, gdje se varijable rastavljaju na dio koji predstavlja rješenje iz potencijalnog strujanja i na dio koji predstavlja perturbaciju oko rješenja potencijalnog strujanja. Na taj su način članovi vezani za potencijalno strujanje koje opisuje propagaciju vala u proračunskoj domeni unaprijed poznati, te se mogu tretirati eksplicitno što olakšava numerički prijenos valova. Originalna SWENSE metoda je reformulirana uzevši u obzir razmatranja koja se direktno odnose na metodu kontrolnih volumena. Shodno razmatranjima polje dinamičkog tlaka se nije rastavilo na potencijalnu i perturbacijsku komponentu jer bi to rezultiralo s dvije eliptične jednadžbe tlaka koje predstavljaju proračunski najzahtjevniji dio algoritma. SWENSE metoda predstavlja efikasan način unošenja i prijenosa nailaznih valova u proračun, međutim ona ne spriječava neželjenu refleksiju valova od otvorene granice domene.

U svrhu spriječavanja refleksije valova koriste se implicitne relaksacijske zone postavljene kraj otvorenih granica proračunske domene. U relaksacijskim zonama se postepeno smanjuje perturbacijski dio rješenja da bi se na samoj granici domene dobilo rješenje potencijalnog strujanje, te na taj način spriječila refleksija.

II Numerički model

Numerički model se zasniva na poliedarskoj metodi kontrolnih volumena koja je drugog reda točnosti. Cijeli model je implementiran u `foam-extend` paketu koji predstavlja granu OpenFOAM programskom paketa otvorenog pristupa kodu koja je orijentirana na prihvaćanje doprinosa iz zajednice korisnika.

Važan doprinos ovog rada je diskretizacija diskontinuiteta na slobodnoj površini pomoću GFM pristupa, gdje se uzima u obzir skok u gustoći i dinamičkom tlaku preko slobodne površine. Diskretizacija skokovitih rubnih uvjeta donosi set korigiranih interpolacijskih shema za članove u jednadžbama koji ovise o dinamičkom tlaku i gustoći. Korigirane interpolacijske sheme se koriste samo u neposrednoj blizini slobodne površine koristeći kompaktnu proračunsku molekulu. Kao što je pokazano u radu, sheme rezultiraju simetričnom jednadžbom tlaka, poštujući simetričnost Laplaceovog diferencijalnog operatora. Ove sheme implicitno sprežu dva fluida (zrak i vodu) s inifinitezimalno razlučenim skokom gustoće i dinamičkog tlaka preko slobodne površine, što je pokazano brojnim testnim primjercima.

Detaljno je predstavljen dijagram toka implementiranog algoritma te jaka sprega jednadžbi polja strujanja s jednadžbama gibanja krutog tijela.

III Validacija i verifikacija

U svrhu detaljne verifikacije modela ukratko su predstavljeni načini kvantificiranja raznih numeričkih neizvjesnosti (nesigurnosti u rezultate), s posebnim naglaskom na neizvjesnosti vezane za: rezoluciju proračunske mreže, rezoluciju diskretizacije u vremenu vezane za veličinu vremenskog koraka te neizvjesnost vezana za samu periodičnost strujanja. Validacija je provedena uspoređujući sve rezultate proračuna za sve testne primjerke s analitičkim, referentnim numeričkim ili eksperimentalnim rezultatima.

Prvi testni primjer predstavlja dvodimenzijsko dvofazno strujanje fluida preko rampe, gdje je proračun proveden na skupu blok–strukturiranih i nestrukturiranih mreža. Dobiveno je vrlo dobro slaganje s analitičkim rješenjem. Izvršeno je ispitivanje reda konvergencije gdje je pokazano da je konvergencija bolja na blok–strukturiranim mrežama. Također je proveden jednostavan hidrostatski test na istoj geometriji gdje je pokazano da predloženi model temeljen na GFM pristupu rješava problem parazitskih brzina u lakšem fluidu (zraku).

Drugi skup testnih primjera sadrži studije osjetljivosti vezano za propagaciju progresivnih valova. Izvršene su studije osjetljivosti mreže, vremenske rezolucije, promjene parametara u LS jednadžbi, refleksije mijenjajući duljinu relaksacijskih zona, promjene valne strmine te konačno dvije simulacije s vrlo dugom domenom i vrlo dugim trajanjem simulacije (100 valnih perioda). Rezultati studija osjetljivosti pokazuju da je propagacija valova točna te da je numerički model konzistentno implementiran.

Treći skup testnih primjera predstavlja difrakciju nailaznih pravilnih valova na uronjeni vertikalni cilindar, gdje je poseban naglasak stavljen na sile višeg reda. Sile do sedmog reda za vrlo strme valove su uspoređene s potpuno nelinearnim numeričkim modelom potencijalnog strujanja u vremenskoj domeni te s eksperimentalnim rezultatima, gdje su dobiveni vrlo dobri rezultati. Također je provedena studija rezolucije proračunske mreže i vremenskog koraka u svrhu verifikacije modela.

Konačno, četvrti skup testnih primjera predstavlja simulacije pomorstvenosti kontejnerskog broda pri projektnoj brzini i na pravilnim valovima s različitim valnim duljinama, valnim visinama te kutovima nailaska valova. Svi rezultati su uspoređeni s eksperimentalnim mjerenjima gdje je postignuto dobro poklapanje rezultata. Naglasak je stavljen na brojne studije osjetljivosti, gdje su detaljno kvantificirane numeričke neizvjesnosti vezane za rezoluciju mreže, vremensku rezoluciju, periodičnost konačnog rješenja te razlučivost sprege između strujanja fluida i gibanja krutog tijela. Dobiveni rezultati pokazuju da je implementirani model točan za proračune pomorstvenosti broda te da je konzistentno implementiran, jer se rješenje ne mijenja značajno s rezolucijom mreže. Također se kroz testove paralelnog skaliranja te jedan test brzine simulacije pokazalo da je razvijeni model efikasan u vidu proračunskog vremena te da se dobra procjena dodatnog otpora i gibanja broda može dobiti u par dana s relativno malim računalnim resursima.

IV Zaključak

Sljedeći općeniti zaključci se mogu donijeti na osnovu provedenih studija osjetljivosti:

- Bolja konvergencija se dobije na strukturiranim heksaedarskim mrežama u usporedbi s nestrukturiranim mrežama,
- Numerički model je stabilan na relativno grubim mrežama i pri jako visokim vremenskim koracima, gdje daje razumno dobro rješenje pri samo 25 vremenskih koraka po periodu vala,
- Greške disperzije (promjene faze mjerene veličine) su veće od grešaka disipacije (gubitka amplitude),
- Model točno opisuje i računa utjecaje viših redova.

Studije periodične konvergencije rješenja pomoću brze Fourierove transformacije na pomičnim prozorima ukazuje da je potrebno izvršiti preko deset perioda za simulacije pomorstvenosti da bi se usvojilo periodično kvazi–stacionarno strujanje.

Ključne riječi
Brodska i pučinska hidrodinamika, Strujanja sa slobodnom površinom, Ghost Fluid Method, Implicitno reinicijalizirana Level Set metoda, Dekompozicija rješenja i domene, Poliedarska metoda kontrolnih volumena, OpenFOAM, Validacija i verifikacija

Contents

List of Figures

List of Tables

Nomenclature

Calligraphy letters

$\mathbf{I}$	diagonal inertia tensor of a body in principal coordinates	kg m^2
$\mathcal{A}$	asymptotic range ratio	-
$\mathcal{H}$	explicit dynamic pressure jump	kg m^{-1} s^{-2}
$\mathcal{R}$	relaxation zone operator	-
$\mathcal{T}$	transport operator	-
∇	displacement of the ship	m^3

Greek letters

α	volume fraction	-
β	inverse density	kg^{-1} m^3
χ	arbitrary ranked tensor field, wave encounter angle	-, °
ϵ	width parameter	m
ϵ_n	enstrophy	s^2
ϵ_{fm}	difference in fine/medium resolved solution	-
ϵ_{mc}	difference in medium/coarse resolved solution	-
γ	stabilisation constant for Level Set diffusion parameter	-
γ_χ	diffusion coefficient	m^2 s^{-1}
γ_{H_i}	phase shift of the i^{th} harmonic	rad (or °)
Γ_{ij}	interface between two immiscible fluids	-

$\boldsymbol{\alpha}$	rotational acceleration of a body	rad s^{-2}
$\boldsymbol{\omega}$	rotational velocity of a body	rad s^{-1}
κ	mean interface curvature	m^{-1}
λ	dimensionless distance to the free surface	-
λ_r	relaxation zone length	m
λ_w	wave length	m
μ_e	effective dynamic viscosity	kg m^{-1} s^{-1}
ν_e	effective kinematic viscosity	m^2 s
Ω	fluid domain, excluding the free surface	-
ω	wave frequency	rad s^{-1}
ω_e	encounter frequency	rad s^{-1}
$\overline{\beta_d}$	weighted inverse density for dry cell	kg^{-1} m^3
$\overline{\beta_w}$	weighted inverse density for wet cell	kg^{-1} m^3
ϕ	Phase Field function	-
ψ	signed distance (Level Set) function	m
ψ_w	wave signed distance (Level Set) field	m
ρ	density field	kg m^{-3}
σ	surface tension coefficient	kg s^{-2}
τ	Brard number	-
τ	time scale factor	s
ξ	phase–intensive field	-

Latin letters

Δt	time step	s
$\mathbf{d}_f$	distance vector from cell P to N	m
$\mathbf{I}$	identity tensor	-
e	Euler's number	-
$\mathbf{s}_f$	surface area vector	m^2
$\mathbf{u}$	velocity field	$\mathrm{m\ s^{-1}}$
$\mathbf{u}_b$	body wall velocity	$\mathrm{m\ s^{-1}}$
$\mathbf{u}_i$	boundary cell–centre velocity	$\mathrm{m\ s^{-1}}$
$\mathbf{u}_w$	wave velocity	$\mathrm{m\ s^{-1}}$
$\mathbf{a}$	acceleration of a body	$\mathrm{m\ s^{-2}}$
$\mathbf{b}^*_\mathbf{u}$	combined source term in the momentum equation, excluding the pressure gradient term	$\mathrm{m^4\ s^{-2}}$
$\mathbf{b}_\mathbf{u}$	combined source term in the momentum equation	$\mathrm{m^4\ s^{-2}}$
$\mathbf{c}$	total Level Set convecting term	$\mathrm{m\ s^{-1}}$
$\mathbf{F}$	external force acting on a body	$\mathrm{kg\ m\ s^{-2}}$
$\mathbf{G}$	least squares symmetric tensor	-
$\mathbf{g}$	constant gravitational acceleration	$\mathrm{m^2\ s^{-1}}$
$\mathbf{H}$	off–diagonal and source operator in a discretised equation	-
$\mathbf{l}_f$	least squares vector	m
$\mathbf{n}$	unit normal vector	-
$\mathbf{r}_f$	distance vector from face–centre to Centre–of–Gravity	m
$\mathbf{S}$	twice the symmetric part of the $\nabla\mathbf{u}$ tensor	$\mathrm{s^{-1}}$

$\mathbf{S}_h$	pressure–density imbalance source term	kg m^{-2} s^{-2}
$\mathbf{T}$	external torque acting on a body	kg m^{2} s^{-2}
$\mathbf{t}$	Unit tangential vector	-
$\mathbf{v}$	velocity of a body	m s^{-1}
$\mathbf{w}_1$	hyperbolic tangent Level Set convecting term	m s^{-1}
$\mathbf{w}_2$	curvature Level Set convecting term	m s^{-1}
$\mathbf{x}$	position vector	m
a	wave amplitude	m
a_1	first non–negative Level Set source term constant	m s^{-1}
a_2	second non–negative Level Set source term constant	m^{-1}
a_N	off–diagonal matrix coefficient	-
a_P	diagonal matrix coefficient	-
a_{NP}	lower off–diagonal matrix coefficient for owner P and neighbour N	-
a_{PN}	upper off–diagonal matrix coefficient for owner P and neighbour N	-
B	beam of the ship	m
b	diffusion parameter in the Level Set equation	m^{2} s^{-1}
CFL	fluid velocity field Courant–Friedrichs-Lewy number	-
CFL_c	convective Level Set Courant–Friedrichs-Lewy number	-
CFL_d	diffusive Level Set Courant–Friedrichs-Lewy number	-
CFL_ψ	specified maximum Level Set Courant–Friedrichs-Lewy number	-
d	shortest Euclidian distance to the free surface	m
d_d	domain depth	m

d_N	diagonal matrix coefficient for neighbour N	-
d_P	diagonal matrix coefficient for owner P	-
E_a	absolute error	-
E_r	relative error	-
E_{nr}	normalised relative error	-
F	total volumetric face flux	$\mathrm{m}^3\ \mathrm{s}^{-1}$
f	wave frequency	s^{-1}
F_i	i–th harmonic of the force	$\mathrm{kg\ m\ s}^{-2}$
F_r	Froude number	-
F_s	safety factor in uncertainty estimate	-
G_w	global water/domain volume ratio	-
GCI_{cm}	Grid Convergence Index for medium/coarse grid combination	-
GCI_{mf}	Grid Convergence Index for fine/medium grid combination	-
H	wave height	m
H_i	i^{th} harmonic	-
k	wave steepness	m^{-1}
K_{xx}	roll radius of inertia	m
K_{yy}	pitch radius of inertia	m
K_{zz}	yaw radius of inertia	m
L_{PP}	length between perpendiculars	m
m	mass of a body	kg
p	pressure field, achieved order of accuracy	$\mathrm{kgm}^{-1}\ \mathrm{s}^{-2}$, -

p_d	dynamic pressure field	kg m^{-1} s^{-2}
p_{da}	atmospheric dynamic pressure	kg m^{-1} s^{-2}
q	quaternion representing rotations	-
R	discriminating ratio	-
r	cylinder radius, refinement ratio	m, -
R_e	Reynolds number	-
s	spatial exponent	-
S_L	minimum solution	-
S_N	source term for cell N arising from the discretisation of jump conditions	-
S_P	source term for cell P arising from the discretisation of jump conditions	-
S_R	referent (analytical, other numerical or experimental) solution	-
S_U	maximum solution	-
S_u	source term	s^{-1}
S_w	wetted surface of the ship	m^2
S_{CFD}	CFD solution	-
T	draft of the ship, wave period	m, s
U	forward speed of the ship	m s^{-1}
w_f	least squares weight coefficient	m^{-1}
y^+	dimensionless distance to the wall	-

Superscripts

$\{q\}^e$	explicitly treated term	-
$\{q\}^i$	implicitly treated term	-

q^*	deviatoric part of a tensor	-
q^+	heavier fluid index	-
q^-	lighter fluid index	-
q^n	current time step or iteration	-
q^o	old time step or iteration	-
q_c	coarse–resolved solution	-
q_f	fine–resolved solution	-
q_m	medium–resolved solution	-

Subscripts

q_a	index denoting air	-
q_f	face–centred value	-
q_g	variable in global reference frame	-
q_I	incident component of a field	-
q_i, q_j	fluid index	-
q_m	mooring system part of the force/torque	-
q_n	normal component of a vector field	-
q_P	perturbed component of a field, current cell centred value	-
q_p	pressure part of the force/torque	-
q_t	tangential component of a vector field	-
q_v	viscous part of the force/torque	-
q_w	index denoting water	-
$q_{f\Gamma}$	interface faces	-

q_{f_Γ}	face–interpolated value with interface correction for interface faces	-
$q_{N,P}$	cell centre N perturbed field	-
q_N	neighbouring cell–centred value	-
$q_{P,P}$	cell centre P perturbed field	-

1. Introduction

1.1. Computational Marine Hydrodynamics

Hydrodynamic characteristics of a ship are most often determined in towing tanks by performing various model experiments: steady resistance, self propulsion, seakeeping, zig–zag manoeuvre and rotating circle. Using dimensional analysis with correlation factors unique to each towing tank facility, the resistance of the full scale ship can be extrapolated from the model test. The results are then used to assess the necessary engine power for a determined forward speed of the ship, given by design speed. The steady resistance model tests are relatively straightforward to carry out and the corresponding experimental uncertainties are often below 2%. However, experimental tests concerning waves and wave–induced motions are generally more challenging to carry out, especially for oblique waves since they impose considerable constraints on size, design and equipment of towing tanks.

With the appearance of first computational workstations, various numerical methods naturally started to emerge for naval hydrodynamic problems. Most of the numerical algorithms were first based on the potential flow assumption, allowing the reformulation of a three–dimensional (3–D) problem into a two–dimensional (2–D) problem. Such reformulation made the Boundary Element Method (BEM) extremely popular in CFD due to its low requirement for computational resources: Central Processing Unit (CPU) power and memory. BEM based algorithms are still frequently used for various industrial naval hydrodynamic problems: wave resistance in calm sea, propeller simulations, hull shape optimisation, seakeeping analysis in regular and irregular seas, hydroelasticity, coupling with Reynolds Averaged Navier–Stokes (RANS) based CFD algorithms, *etc.* However, BEM does not have an innate ability to model vorticity, viscosity, turbulence and two–phase effects, making them unsuitable for calculating frictional resistance in calm sea, added resistance of ship in waves, roll decay and large amplitude motions, wave breaking, wind–wave interaction, *etc.*

1. Introduction

The drawbacks of BEM, along with the immense increase in computer resources over the past decades made RANS based CFD methods suitable for many industrial needs. RANS based CFD methods are naturally able to handle coupled, nonlinear equation sets, including two–phase, rotational, viscous and turbulent flows. Such versatility comes with a considerable expense in terms of computer resources compared to BEMs. Nevertheless, high fidelity CFD methods for naval hydrodynamics currently represent an active area of practical application.

Recently, an excellent overview of the modern CFD capabilities for marine hydrodynamics has been presented by Stern *et al.* [1]. Although the presented capabilities include free running ships or highly resolved wave breaking simulations, the validation and verification of numerous CFD algorithms is still under way [2]. Validation and verification process of the CFD algorithms includes a broad spectrum of flows: from basic steady resistance to flows including realistic sea states with ship motion and/or manoeuvring [3]. A large portion of transient flows in marine hydrodynamics is caused by surface gravity waves and their interaction with ships and off–shore structures. The ability of RANS based CFD algorithms to accurately calculate seakeeping response of a ship in head waves has been recently demonstrated at the Tokyo 2015 workshop [4]. The uncertainty estimate via grid refinement studies for all seakeeping tests has not been requested by the organisers, indicating that the CFD methods are still computationally expensive. The Tokyo 2015 workshop included five head wave and five oblique wave test cases for the KRISO (MOERI) Container Ship (KCS) model at design speed. Ten submissions within seven articles have been made for the head wave test cases [5, 6, 7, 8, 9, 10, 11], whereas only two submissions have been made for the oblique wave tests [12, 13], indicating that CFD simulations still have difficulties regarding arbitrary wave heading. Furthermore, out of twelve seakeeping submissions in total, only two participants conducted the verification study via grid refinement and periodic uncertainty assessment [11, 13].

Numerous commercial software packages are currently in use for two–phase CFD simulations: STAR-CCM+, ANSYS Fluent, Fine–Marine to name a few. However, closed access to the source code and large licence fees are often limiting factors for their widespread use in scientific research. Furthermore, publications revealing implementation details and models on which the algorithms are based on often do not exist due to industrial reasons. Other, in house developed CFD packages with strong background in marine hydrodynamics are: ISIS–CFD [14] (commercial provider: Numeca, within Fine–Marine), CFDShip-Iowa [15, 16, 17], ReFRESCO [18, 19], ICARE [20] have accessible publications, but limited access to the software, with almost impossible access to the source code. As an alternative to commercial software packages and in–house CFD algorithms, the use of open source CFD software package Open Field Operation And Manipulation (OpenFOAM) [21, 22] provides a suitable platform for scientific research. Due to its open source philosophy without any licence fees, the use of OpenFOAM is steadily spreading both in research community and in the marine industry. A brief research reveals that 16 out of 39 articles submitted for the Tokyo 2015 workshop [23] included computations in OpenFOAM, which represents approximately 40% of all submissions.

1.2. Previous and Related Studies

Most flows in marine hydrodynamics can often be viewed as incompressible and turbulent, with a presence of a free surface between water and air. Incompressible flow is often modelled with the continuity and the Navier–Stokes equations [24], while a broad spectrum of methods exists for turbulence modelling and free surface treatment.

1.2.1. Numerical Simulation of Free Surface Flows

The free surface treatment in two–phase flows is divided into two parts:

1. Interface capturing or tracking and
2. Treatment of discontinuities at the interface.

Interface capturing or tracking methods investigate the advection of the interface with a given velocity field, while the discontinuities at the interface (*e.g.* density jump in water–air flows) and their treatment needs separate attention.

Interface Capturing and Tracking

The most common free surface flow models [25] can be divided into two categories:

1. Interface capturing via colour functions: Volume–of–Fluid (VOF) [26, 27], LS methods [28] and the Phase Field (PF) method [29].
2. Lagrangian interface tracking.

The conservative and well established VOF method is based on volume fraction. The volume fraction is bounded between 0 and 1: 0 usually representing air and consequently 1 representing water. Isosurface of VOF where the volume fraction is equal to 0.5 enables the reconstruction of the interface. During the advection, special care has to be taken to ensure boundedness and capturing of a sharp interface. Smearing of the interface in the VOF method is often remedied with special compressive schemes [30, 27, 31] or additional compressive terms [32].

Contrary to the VOF method, the smearing of the interface is a user–controlled parameter in the LS method. The method is often based on the signed distance function [33, 34], which does not represent a conserved physical quantity as is the case with the VOF method. In case of the signed distance function, the LS field is unbounded and the zero level set denotes the interface. The LS field often does not preserve its signed distance property due to discretisation errors when it is advected by a velocity field obtained from the incompressible flow. This is often remedied by introducing an additional redistancing equation [35] or directly recalculating the distance to the interface after the advection step. Both approaches usually redistance the LS field only in a narrow band of interest near the interface.

The PF method is based on advecting the hyperbolic tangent profile across the interface and it has been originally used for applications regarding micro flows (Hele–Shaw) [29]. Hyperbolic tangent profile is bounded between -1 and 1 as opposed to 0 and 1 in the VOF method. The attractiveness of the method lies in its ability to preserve the hyperbolic tangent profile during the advection step. Sun and Beckermann [36, 37] presented the LS method derived from PF equation, where the resulting LS equation contains additional terms along with the usual advection. Similar to the preservation of the hyperbolic tangent profile in the PF method, the resulting additional terms serve to maintain the signed distance property of the LS field implicitly during the solution [36], rendering additional explicit redistancing unnecessary.

Another approach often employed in small scale phenomena is sharp interface tracking using moving, interface adhering grids [38, 39]. Dynamic grid interface tracking procedure often introduces additional grid deformation equations, increasing the CPU time. Furthermore, complex geometries (*e.g.* ship hull) and complex flow features (*e.g.* wave breaking) become challenging with this approach.

Treatment of Discontinuities at the Interface

Multiple incompressible fluids are coupled with appropriate boundary (jump) conditions at the moving interface [24]. Kinematic boundary condition ensures the continuity of velocity field across the interface, while tangential and normal stress balance yield jump conditions for pressure and tangential component of the velocity gradient.

Two similar approaches for the treatment of jump conditions at the free surface exist: embedded free surface method [40] and the Ghost Fluid Method (GFM) [15]. Both techniques consider two fluids with an infinitesimally thin interface, the only difference being the treatment (discretisation) of interface jump conditions, as indicated by Wang *et al.* [40].

Johansen and Colella [41] have developed and used the embedded boundary method for solving the Poisson's equation, while Crockett *et al.* [42] embedded the discontinuous jump conditions in both the Poisson and the heat equation, achieving second–order accuracy. Recently, Wang *et al.* [40] extended the method for two phase incompressible flows. It is important to note that the above mentioned publications regarding the embedding technique considered only structured Cartesian grids.

GFM for treatment of jump conditions across a sharp moving interface represents an active area of research during past two decades. Fedkiw *et al.* [43] developed the GFM coupled with LS interface capturing to efficiently capture discontinuities in fields during deflagration and detonation. The method has been extended by Kang *et al.* [44] to simulate multiphase incompressible and laminar flow, while Desjardins *et al.* [45] presented the methodology based on the GFM with the conservative LS method developed by Olsson and Kreiss [46]. They remarked that the GFM provides a good framework for two phase flows with large density variations, which is important for marine hydrodynamics applications. The GFM has also been recently utilised in the lattice Boltzmann framework by Kaneda *et al.* [47] to perform validation and conclude that the method is suitable for curved boundaries in motion. Recently, Lalanne *et al.* [48] provided an extensive overview of the treatment of viscous jump conditions in two phase flow utilising the GFM with LS interface capturing. The GFM has been also recently used alongside the VOF method for compressible multiphase flows [49]. As was the case in the embedded free surface methods, the above mentioned publications on the GFM utilised structured Cartesian grids.

Huang *et al.* [15] implemented a GFM with LS interface capturing in the Finite Difference (FD) framework on curvilinear structured grids. The jump conditions are discretised using second–order accurate schemes, where the LS method is used to calculate one–sided extrapolates of pressure. The authors note that the model is suitable for large length scale free surface water–air flows encountered in marine hydrodynamics. From their publication [15], it is not clear how they treat:

- Density and pressure discontinuity in the pressure gradient term in the momentum equation and
- Density discontinuity in the pressure Laplacian in the pressure equation.

They also report that the resulting linear system for the pressure equation is stiff.

To author's present knowledge, the GFM methodology has not been implemented in polyhedral Finite Volume (FV) method, although Queutey and Visonneau [14] present a similar approach where the free surface is assumed to be aligned with the grid faces.

1.2.2. Wave Modelling

Compared to potential flow based numerical methods, wave modelling in CFD requires special treatment in order to propagate the waves through far–field boundaries and prevent undesirable wave reflection which could in turn disrupt the numerical results. Higuera *et al.* [50, 51] used active wave absorption by dynamically prescribing the velocity field at the outlet boundaries, which may be favourable for simulations in closed domains (*e.g.* experimental setup). For marine applications, the area of interest often lies within a narrow region near an object of interest.

A widely used alternative for preventing wave reflection are various damping regions. Huang *et al.* [15] used a damping source term in the LS interface capturing equation to prevent wave reflection. Jacobsen *et al.* [52] applied explicit relaxation zones to achieve a similar effect. The implicit treatment of relaxation zones has been recently reported by Jasak *et al.* [53]. Inside relaxation zones, the governing CFD transport equations are blended with an arbitrary potential flow solution. The smooth exponential blending function forces the CFD solution to vanish at the far–field boundaries, leaving freely propagating potential flow solution, thus preventing wave reflection. Higuera *et al.* [50] consider this approach inferior due to a larger domain needed to accommodate for relaxation zones. The cells in the relaxation zones are usually very large, which is favourable as this increases numerical dissipation of the CFD solution. In addition, possible use of advanced potential flow methods allows us to model only small area near the object of interest without a detrimental effect on the solution. It is important to mention absorbing boundary conditions [54] which often perform well for regular waves with well–defined frequency, but need significant additional considerations for general irregular sea states.

In order to generate incoming free surface waves, a straightforward approach is to prescribe a time varying boundary conditions [50] at the inlet boundaries. A more advanced approach used by Higuera *et al.* [55] uses moving boundaries, mimicking experimental setting. Instead of generating the waves at a specified boundary, Ferrant *et al.* [20] used a solution decomposition via Spectral Wave Explicit Navier–Stokes Equations (SWENSE) method, introducing the incident wave explicitly present in the whole computational domain at all times. In the SWENSE method, the unknown solution fields are decomposed into incident and diffracted (perturbation, scattered [56]) components. The incident component of a given field is obtained from potential flow models, while the diffracted component is solved for via fully nonlinear, viscous CFD. It is important to note that the method relies on coarse (stretched) grid in far–field region to numerically damp diffracted fields near the boundaries, thus preventing wave reflection. This method has been successfully applied to calm water, regular and irregular waves [57, 58, 59]. In their work, Monroy *et al.* [58] used fully nonlinear potential flow models, such as stream function wave theory solution for regular waves [60] and Higher Order Spectral (HOS) method [61, 62, 63] for irregular waves.

1.2.3. Turbulence Modelling

Due to large length scales in all marine hydrodynamic flows, accurate resolution of the small scale turbulence structures via Direct Numerical Simulation (DNS) is far from feasible. Hence, for practical applications such as steady resistance or seakeeping of a ship in waves, Unsteady Reynolds Averaged Navier–Stokes (URANS) models are most often employed [2]. The turbulence closure is most often achieved via two–equation eddy–viscosity models [64], where $k - \omega$ Shear Stress Transport (SST) model [65, 66] is most widely used [2]. As an alternative to two–equation models, Large Eddy Simulation (LES) models represent an active area of research, especially for flows around propellers [67]. The LES resolves eddies which are large enough relative to the grid size, but still requires modelling of the Sub–Grid Scale (SGS) turbulence. Since the LESs are still computationally expensive, a number of hybrid RANS/LES models have been developed. One of the hybrid models is the Detached Eddy Simulation (DES), *e.g.* used for propeller cavitation simulations [68].

For a more detailed discussion regarding turbulence modelling for marine hydrodynamic flows, reader is referred to 27th International Towing Tank Conference (ITTC) report [69].

1.3. Numerical Frameworks for Marine Hydrodynamics

An excellent overview of a broad spectrum of numerical methods used by participants of the Gothenburg 2010 workshop [70] is given by Larsson *et al.* [2].

Approximately 80% of participants used FV discretisation (26 out of 33), while all others used FD discretisation. There were not participants using *e.g.* Finite Element (FE) method. The widespread use of the FV method can be related to its inherent ability in handling unstructured polyhedral grids. Arbitrary unstructured grids are favourable for complex geometries due to well established automatic grid generation algorithms which require minimal user input. As opposed to FV based algorithms, FD algorithms require structured grids as used by all participants. The apparent limitation of the arbitrary polyhedral FV method is its inherent second–order accuracy, however, it is important to note that the second–order accuracy has been used by most of the participants utilising FD algorithms [70].

1.4. Present Contributions

The objective of this thesis is to introduce a new numerical model for two–phase flow modelling in marine hydrodynamics using arbitrary polyhedral FV method. The thesis makes the following specific contributions to the field of CFD related to two–phase flow modelling for marine applications:

- Interface capturing is achieved with implicitly redistanced LS method derived from PF equation. The transport equation contains additional terms in a form which is not suitable for polyhedral FV discretisation, as opposed to the original implementation by Sun and Beckermann [36, 37] carried out in the FD framework on uniform computational grids. Additional terms responsible for implicit redistancing are mathematically reformulated in order to achieve implicit FV discretisation. The influence of the implicit discretisation of additional terms to the resulting linear system is discussed in detail from numerical point of view.

- Solution decomposition with SWENSE method [20, 56] is originally implemented in the FD framework, discretising governing equations in differential form. The FV method uses integral, conservative form of governing equations, rendering additional numerical considerations necessary for the successful implementation of the SWENSE method. Solution decomposition model is given in detail, with additional considerations regarding CPU time efficiency.

- In order to ensure prevention of the wave reflection, solution decomposition is combined with domain decomposition approach with implicit relaxation zones. In relaxation zones, diffracted fields are smoothly forced to vanish, leaving only incident potential flow solution at the far–field boundaries. The implicit treatment of the relaxation zones is explained in detail and its impact on the resulting linear system is discussed from numerical point of view.

- The GFM method [15]) is extended to arbitrary polyhedral FV method. Original second–order accurate FD discretisation of free surface jump conditions introduced by Huang *et al.* [15] requires additional considerations using compact stencil in arbitrary polyhedral FV framework, which often uses unstructured computational grids. The resulting pressure equation and its properties are investigated in detail, producing a symmetric coupling between water and air.

The combination of methods for two–phase flow treatment, interface capturing, solution and domain decomposition require additional considerations for their implementation in the arbitrary polyhedral FV framework. Moreover, to author's knowledge, their combination has not yet been implemented in any numerical framework.

The numerical model is implemented in the `Naval Hydro` pack [71] based on the open source object–oriented C++ `foam-extend` library (community driven fork of the OpenFOAM software for general computational continuum mechanics). Special attention has been given to object–oriented and generic programming paradigm to ensure easier maintenance and further development of the present model.

An extensive Validation and Verification (V&V) is carried out regarding marine hydrodynamics flows of scientific and industrial importance. Validation is carried out by comparing simulation results with analytical, other numerical and experimental data, while the verification is carried out by performing grid, time step and periodic uncertainty assessments. Additional sensitivity studies are carried out to establish a best practice guidelines for parameters influencing implicit redistancing of the LS field. Following sets of test cases are considered in this study:

1. Free surface flow over a ramp,
2. Progressive wave propagation,
3. Assessment of higher order forces exerted on vertical surface piercing cylinder,
4. Seakeeping of the KCS model in head and oblique waves at the design speed.

1.5. Thesis Outline

The rest of this thesis is organised as follows.

Ch. 2. presents the governing equations for a general incompressible two–phase flow. The jump conditions at the interface between two immiscible phases are summarised and approximated for water–air free surface flows at naval hydrodynamics length scales. A brief overview of interface capturing methodology is also given.

Ch. 3. presents the solution and domain decomposition methodologies for efficient coupling of arbitrary potential flow models with fully nonlinear, two–phase, turbulent flow model. The governing equations are first decomposed using the SWENSE solution decomposition, followed by domain decomposition via implicit relaxation zones.

Ch. 4. presents the numerical modelling framework. A brief overview of the FV discretisation of governing equations is presented first, with the emphasis on the pressure equation. Discretisation of pressure and density terms in the governing equations is explained in detail and the second order accurate discretisation of the pressure jump conditions, used to define one–sided extrapolation across the interface, is the focal point of Ch. 4. The extrapolation formulae and their use for the pressure gradient and Laplacian terms at the free surface are explained in detail, where it is demonstrated that the pressure equation remains symmetric.

Finally, rigid body motion modelling is briefly described, followed by a detailed explanation of the segregated solution algorithm.

Ch. 5. presents Validation and Verification procedures used for all test cases, where the special attention is given to the verification procedures in order to assess numerical uncertainties. Periodic uncertainty assessment for temporally periodic flows is presented first, followed by the grid and temporal uncertainty assessment.

Ch. 6. presents test cases used to validate and verify the developed methodology. The first test case deals with the steady state free surface flow over a ramp. The second set of test cases considers 2–D progressive wave propagation with various sensitivity studies. The third set of test cases deals with the assessment of higher order forces on a surface piercing cylinder in regular waves. Finally, the fourth set of test cases refers to seakeeping simulations of container ships in head and oblique waves, at design speed. Performance in terms of the CPU times for utilised computer resources are reported for more demanding cases.

Ch. 7. presents the summary and conclusion regarding this study. Proposals for future research are briefly discussed.

2. Governing Equations

2.1. Two–Phase Flow Model

This section starts by examining the conditionally averaged momentum equation and provides a theoretical explanation for spurious acceleration of the lighter phase. The remainder of the section presents an alternative modelling approach for incompressible, turbulent flow of two immiscible fluids with a presumably infinitesimally sharp interface, where the coupling of fluids is achieved with appropriate interface conditions. Since the two fluids of interest are water and air, incompressible Newtonian fluid [24] model is used, which is a justified assumption for low speed phenomena. Turbulence is accounted for with Bousinessq eddy viscosity assumption [72], allowing the use of general turbulence models.

2.1.1. A Remark on Conditionally Averaged Momentum Equation

To model two–phase flows concerning water and air in off–shore and marine hydrodynamics, some authors [52, 50, 51, 73, 74, 14, 54] use a two–phase momentum equation, which is derived based on conditional averaging [75].

The two–phase momentum equation includes variable two–phase density and usually has the following form:

$$\frac{\partial(\rho\mathbf{u})}{\partial t} + \nabla\bullet(\rho\mathbf{u}\mathbf{u}) - \nabla\bullet(\mu_{eff}\nabla\mathbf{u}) = -\nabla p_d - \mathbf{g}\bullet\mathbf{x}\nabla\rho + \nabla\mathbf{u}\bullet\nabla\mu_e + \sigma\kappa\nabla\alpha\,, \quad (2.1)$$

where ρ is the density field of the water–air mixture, $\mathbf{u}$ is the continuous velocity field, μ_e is the two–phase effective dynamic viscosity, p_d is the dynamic pressure, $\mathbf{g}$ is the gravitational acceleration, $\mathbf{x}$ is the position vector, σ is the surface tension coefficient, κ is the mean curvature of the interface and α is the volume fraction. In the hydrostatic case, the dynamic pressure gradient ∇p_d and density gradient $\nabla\rho$ term, which do not vanish at the interface, should be balanced: $\nabla p_d + \mathbf{g}\bullet\mathbf{x}\nabla\rho = 0$. Hence, the coupling between dynamic pressure and density is resolved in the momentum equation, which leads to spurious air velocities in the lighter fluid near the free surface when one uses segregated solution algorithms. To elaborate, consider a hydrostatic case of inviscid fluid where the surface tension is neglected. Eqn. (2.1) becomes:

$$\frac{\partial(\rho\mathbf{u})}{\partial t} = -\nabla p_d - \mathbf{g}\bullet\mathbf{x}\nabla\rho = \mathbf{S}_h\,, \tag{2.2}$$

where the source term $\mathbf{S}_h$ represents the imbalance between dynamic pressure gradient and density gradient terms. Such imbalance is naturally present during segregated numerical solution, which is used by most CFD algorithms [15, 14, 16, 17, 52, 50, 73]. The source term causes temporal change in the velocity field, spuriously affecting the lighter phase because of the ρ prefactor in the time derivative term. Furthermore, dynamic pressure gradient and density gradient terms are often discretised using conventional gradient discretisation schemes that do not take the density discontinuity into account, making them ineffective near the interface. It is important to stress that this consideration does not include surface tension effects, thus, this observation is unrelated to parasitic currents due to numerical modelling issues related to the surface tension, often encountered in atomisation calculations using the Continuous Surface Stress (CSS) model [76]. The model implementing the conditionally averaged equations (*i.e.* `interFoam` solver from foam–extend–3.2) shall be compared to the present model for the hydrostatic test case in Ch. 6.

An alternative two–phase flow modelling approach is presented in detail in following text, where the interface between two incompressible fluids is assumed infinitesimally sharp.

2.1.2. Single Phase Flow Equations

The continuity equation for an incompressible flow states that the velocity field $\mathbf{u}_i$ is solenoidal:

$$\nabla\bullet\mathbf{u}_i = 0\,, \tag{2.3}$$

where i is the fluid index.

The momentum equation, or the Navier–Stokes equations, for a single phase denoted by the subscript i, incompressible flow in Earth's gravitational field reads:

$$\frac{\partial \mathbf{u}_i}{\partial t} + \nabla\bullet(\mathbf{u}_i\mathbf{u}_i) - \nabla\bullet\left(\nu_{e,i}\nabla\mathbf{u}_i\right) = -\frac{1}{\rho_i}\nabla p_i + \mathbf{g}\,, \tag{2.4}$$

where $\nu_{e,i}$ is the effective kinematic viscosity, p_i is the pressure and $\mathbf{g}$ is the gravitational acceleration, which is assumed constant. ρ_i denotes constant density of the fluid i since the incompressible flow is considered. The r.h.s. of Eqn. (2.4) can be written in a more convenient way:

$$-\frac{1}{\rho_i}\nabla p_i + \mathbf{g} = -\beta_i\nabla p_i + \mathbf{g}\,, \tag{2.5}$$

introducing the following substitution:

$$\beta_i = \frac{1}{\rho_i}\,. \tag{2.6}$$

Two terms in Eqn. (2.5) denoting the pressure gradient and gravitational acceleration can be written as follows:

$$-\beta_i\nabla p_i + \mathbf{g} = -\beta_i\nabla p_i + \nabla(\mathbf{g}\bullet\mathbf{x}) = -\beta_i\nabla\left(p_i - \frac{\mathbf{g}\bullet\mathbf{x}}{\beta_i}\right) = -\beta_i\nabla p_{d,i}\,, \tag{2.7}$$

where the decomposition of pressure into hydrostatic and dynamic part reads:

$$p_i = p_{d,i} + \frac{\mathbf{g}\bullet\mathbf{x}}{\beta_i}\,. \tag{2.8}$$

Using Eqn. (2.7), the momentum equation for incompressible, turbulent, single–phase flow, Eqn. (2.4) is rewritten as:

$$\frac{\partial \mathbf{u}_i}{\partial t} + \nabla\bullet(\mathbf{u}_i\mathbf{u}_i) - \nabla\bullet\left(\nu_{e,i}\nabla\mathbf{u}_i\right) = -\beta_i\nabla p_{d,i}\,. \tag{2.9}$$

Compared to Eqn. (2.1), note that ρ is not present inside differential operators in Eqn. (2.9) due to assumed constant density of the fluid.

2.1.3. Inter–Phase Boundary Conditions

Since two fluid phases are considered immiscible, fluid flow model given by Eqn. (2.3) and Eqn. (2.9) may be applied to each phase separately [38], taking into account boundary conditions at the moving interface between the fluids.

Kinematic boundary condition [77] gives a relation between fluid velocities on opposite sides of the interface:

$$\mathbf{u}_i = \mathbf{u}_j \,, \quad \mathbf{x} \in \Gamma_{ij} \,, \tag{2.10}$$

where Γ_{ij} is the free surface between two immiscible fluids, i and j. $\mathbf{u}_i$ is the velocity field of the fluid i at the interface and $\mathbf{u}_j$ is the velocity field of the fluid j at the interface. Eqn. (2.10) states that the velocity field must be continuous across the interface, which will later be used to define a single volumetric continuity equation valid for two incompressible phases.

The dynamic boundary condition follows from conservation of momentum, stating that stresses at the interface have to be in local equilibrium [78]. The stress balance at the interface can be divided into the tangential and the normal part. Following Tuković and Jasak [38], the tangential stress balance yields a relation between the normal derivative of the tangential velocity field on opposite sides of the interface:

$$\mu_{e,j} \left(\mathbf{n}{\bullet}\nabla\mathbf{u}_t\right)_j - \mu_{e,i} \left(\mathbf{n}{\bullet}\nabla\mathbf{u}_t\right)_i = -\nabla_s\sigma - \left(\mu_{e,j} - \mu_{e,i}\right)\left(\nabla_s u_n\right) \,, \quad \mathbf{x} \in \Gamma_{ij} \,, \tag{2.11}$$

where $\mu_{e,i} = \rho_i \nu_{e,i}$ is the effective dynamic viscosity of the fluid i and $\mu_{e,j}$ is the effective dynamic viscosity for the fluid j. $\mathbf{n}$ is the unit normal vector on the interface, oriented from the fluid i towards the fluid j. $\mathbf{u}_t = \left(\mathbf{I} - \mathbf{nn}\right){\bullet}\mathbf{u}$ is the tangential velocity component, $\nabla_s = \nabla - \mathbf{nn}{\bullet}\nabla$ is the surface gradient operator, σ is the surface tension coefficient, $u_n = \mathbf{n}{\bullet}\mathbf{u}$ is the normal velocity component at the interface and $\mathbf{I}$ is the identity tensor.

The l.h.s. of Eqn. (2.11) represents the discontinuity in the tangential velocity gradient due to different effective dynamic viscosities of two fluids. The discontinuity is also caused by terms on the r.h.s. of Eqn. (2.11), which represent a possibly non zero gradient of the surface tension coefficient and additional term due to surface gradient of normal velocity component, respectively. A non–zero gradient of the surface tension coefficient may occur in interfacial flows with temperature gradients and due to non–uniform distribution of surfactants at the interface [38].

The pressure jump across the interface is obtained from normal stress balance:

$$p_j - p_i = \sigma\kappa - 2\left(\mu_{e,j} - \mu_{e,i}\right)\nabla_s{\bullet}\mathbf{u} \,, \quad \mathbf{x} \in \Gamma_{ij} \,, \tag{2.12}$$

where $\kappa = -\nabla_s \bullet \mathbf{n}$ is the mean curvature of the interface. The first term on the r.h.s. of Eqn. (2.12) models a pressure jump due to surface tension, while the second term models a jump due to normal viscous force across the interface, expressed through surface divergence of the velocity field at the interface [79].

2.2. Marine Hydrodynamics Two–Phase Flow Model

The focus of the present study is the free surface flow concerning water and air at naval hydrodynamics length and time scales, which may be considered a special case of two–phase flow. At low speed, both water and air may be considered incompressible and the inter–phase (free surface) boundary conditions may be simplified without significant loss of generality.

2.2.1. Approximate Jump Conditions

In order to simplify resulting mathematical expressions, the kinematic boundary condition using a slightly different notation is first introduced. Considerations regarding the tangential dynamic condition are given next, followed by dynamic pressure jump condition at the interface arising from normal stress balance.

Kinematic Boundary Condition

Following the notation used by GFM authors [15, 45], the kinematic boundary condition at the free surface given by Eqn. (2.10) can be written as:

$$[\mathbf{u}] = \mathbf{u}^- - \mathbf{u}^+ = 0\,, \quad \mathbf{x} \in \Gamma_{ij}\,, \tag{2.13}$$

where the linear operator $[\cdot]$ indicates jump across the free surface. Superscript "+" denotes the value infinitesimally close to the free surface from the heavier fluid (water), while superscript "−" denotes the value infinitesimally close to the free surface from the lighter fluid (air):

$$\mathbf{u}^+ = \lim_{\mathbf{x} \to \Gamma_{ij}^+} \mathbf{u}(\mathbf{x})\,, \tag{2.14}$$

$$\mathbf{u}^- = \lim_{\mathbf{x}\to\Gamma_{ij}^-} \mathbf{u}(\mathbf{x})\,, \tag{2.15}$$

where $\lim_{\mathbf{x}\to\Gamma_{ij}^+}$ denotes one sided limit from the heavier fluid, and similarly for the lighter fluid. Eqn. (2.13) states that the velocity field is continuous across the free surface.

Tangential Dynamic Boundary Condition

Eqn. (2.11) denotes the jump in the tangential velocity gradient ($\mathbf{n}\bullet\nabla\mathbf{u}_t$) in the normal direction to the interface, caused by differing dynamic viscosities of two fluids. Although it would be possible to include the tangential jump in the present model, tangential dynamic condition is of minor importance for free surface flows at marine hydrodynamics length scales [15, 14], and is thus simplified. In order to approximately satisfy the tangential dynamic condition, dynamic viscosity is assumed to be a continuous function across the free surface, albeit with a possibly steep gradient:

$$[\mu_e] = 0\,, \quad \mathbf{x} \in \Gamma_{ij}\,. \tag{2.16}$$

Hence, Eqn. (2.16) states that the effective dynamic viscosity does not have a jump across the free surface. Furthermore, by neglecting the gradient of surface tension coefficient, and assuming that the tangential velocity gradient is continuous across the free surface, Eqn. (2.11) takes the following, simplified form:

$$[\nabla\mathbf{u}] = 0\,, \quad \mathbf{x} \in \Gamma_{ij}\,. \tag{2.17}$$

Eqn. (2.17) states that the velocity gradient is continuous across the free surface.

Normal Dynamic Boundary Condition

The normal stress balance at the free surface is given by Eqn. (2.12) in terms of pressure jump. Neglecting surface tension effects and using the assumption of continuous dynamic viscosity across the interface, Eqn. (2.16), a simplified expression for the pressure jump is obtained:

$$[p] = 0\,, \quad \mathbf{x} \in \Gamma_{ij}\,. \tag{2.18}$$

The momentum equation, Eqn. (2.9) is written in terms of dynamic pressure, p_d. Hence, the pressure jump condition given by Eqn. (2.18) is rewritten in terms of dynamic pressure using Eqn. (2.8):

$$[p_d] = -\frac{1}{[\beta]}\mathbf{g}\bullet\mathbf{x} = -[\rho]\mathbf{g}\bullet\mathbf{x}\,, \quad \mathbf{x} \in \Gamma_{ij}\,. \tag{2.19}$$

Eqn. (2.19) states that the dynamic pressure has a jump proportional to the jump in density and the inner product of the gravitational acceleration with the position vector.

Summary of the Approximate Jump Conditions

Approximate jump conditions in two–phase free surface flows at naval hydrodynamics scales are summarized in this section.

- Continuity of the velocity field across the free surface, Eqn. (2.13) is obtained without simplifications [24];
- Surface tension effects are considered negligible for large scale flows [15];
- Tangential stress balance is achieved by assuming continuous effective viscosity, Eqn. (2.16) and velocity gradient, Eqn. (2.17) at the free surface, although viscosity could possibly have steep gradient;
- Dynamic pressure jump due to density discontinuity is taken into account exactly without simplifications.

Above assumptions are justified for large scale flows in naval hydrodynamics [14, 15] and are exact for inviscid flows. Large density variation across the free surface, having the most important effect, is taken into account.

2.2.2. Combined Governing Equations

Before the derivation of combined governing equations for the immiscible two–phase flow, an arbitrary, phase–intensive field ξ_i is defined as:

$$\xi_i(\mathbf{x}) \begin{cases} \neq 0\,, & \text{if } \mathbf{x} \in \Omega_i\,, \\ = 0\,, & \text{if } \mathbf{x} \in \Omega_j \cup \Gamma_{ij}\,, j \neq i\,, \end{cases} \tag{2.20}$$

where ξ_i stands for all fields of interest: velocity, effective viscosity, density and dynamic pressure. Eqn. (2.20) states that the field ξ_i vanishes for other phases,

$j \neq i$, and at the free surface Γ_{ij}. For example, velocity field in water (Ω_w), $\mathbf{u}_w$ is defined to be zero in air (Ω_a) and at the free surface Γ_{wa}. At the free surface, jump conditions hold and shall be later used to define continuous fields defined for $\mathbf{x} \in \Omega_i \cup \Gamma_{ij} \cup \Omega_j$. The definition where Γ_{ij} is not a part of $\Omega_i \cup \Omega_j$ is used to facilitate future developments. Without loss of generality, a two–phase immiscible flow of water and air with a sharp phase interface is assumed in further text.

Combined Continuity Equation

Incompressible flow continuity equations, Eqn. (2.3) for water and air read:

$$\nabla\bullet\mathbf{u}_w = 0\,, \quad \mathbf{x} \in \Omega_w\,. \tag{2.21}$$

$$\nabla\bullet\mathbf{u}_a = 0\,, \quad \mathbf{x} \in \Omega_a\,. \tag{2.22}$$

where index w denotes water and index a denotes air. Having in mind the definition given by Eqn. (2.20), combined velocity field for water and air is defined as:

$$\mathbf{u} = \mathbf{u}_w + \mathbf{u}_a\,, \quad \mathbf{x} \in \Omega_w \cup \Gamma_{wa} \cup \Omega_a\,. \tag{2.23}$$

where the resulting velocity field $\mathbf{u}$ is continuous across the free surface due to kinematic boundary condition Eqn. (2.13).

As the velocity field is continuous across the free surface, a combined two–phase volumetric continuity equation is obtained by summing Eqn. (2.21) and Eqn. (2.22):

$$\nabla\bullet\mathbf{u}_w + \nabla\bullet\mathbf{u}_a = \nabla\bullet(\mathbf{u}_w + \mathbf{u}_a) = \nabla\bullet\mathbf{u} = 0\,, \quad \mathbf{x} \in \Omega_w \cup \Gamma_{wa} \cup \Omega_a\,. \tag{2.24}$$

valid both inside each of the phases and at the interface.

Combined Momentum Equation

Incompressible flow momentum equations, Eqn. (2.9) for water and air read:

$$\frac{\partial \mathbf{u}_w}{\partial t} + \nabla\bullet(\mathbf{u}_w\mathbf{u}_w) - \nabla\bullet\left(\nu_{e,w}\nabla\mathbf{u}_w\right) = -\beta_w\nabla p_{d,w}\,, \quad \mathbf{x} \in \Omega_w\,, \tag{2.25}$$

$$\frac{\partial \mathbf{u}_a}{\partial t} + \nabla\bullet(\mathbf{u}_a\mathbf{u}_a) - \nabla\bullet\left(\nu_{e,a}\nabla\mathbf{u}_a\right) = -\beta_a\nabla p_{d,a}\,, \quad \mathbf{x} \in \Omega_a\,. \tag{2.26}$$

Proposition 2.1. *It is assumed that the combined momentum equation has the following form obtained via summation of Eqn.* (2.25) *and Eqn.* (2.26)*:*

$$\frac{\partial \mathbf{u}}{\partial t} + \nabla\bullet(\mathbf{u}\mathbf{u}) - \nabla\bullet\left(\nu_e \nabla \mathbf{u}\right) = -\beta \nabla p_d\,, \quad \mathbf{x} \in \Omega_w \cup \Omega_a\,, \tag{2.27}$$

Note that the Eqn. (2.27) is not assumed to be valid at the free surface, *i.e.* for $\mathbf{x} \in \Gamma_{wa}$. In Eqn. (2.27), ν_e is the continuous effective kinematic viscosity. Due to phase separation (see Eqn. (2.20)), $p_d = p_{d,w} + p_{d,a}$ represents the single dynamic pressure field and $\beta = \beta_w + \beta_a$ represents the single density field.

Proof. The assumption that the combined momentum equation, Eqn. (2.27) is the sum of two single–phase momentum equations, Eqn. (2.25) and Eqn. (2.26), is proved on a term by term basis using Eqn. (2.23) for continuous velocity field. Expanding the time derivative term on the l.h.s. of Eqn. (2.27) yields:

$$\frac{\partial \mathbf{u}}{\partial t} = \frac{\partial(\mathbf{u}_w + \mathbf{u}_a)}{\partial t} = \frac{\partial \mathbf{u}_w}{\partial t} + \frac{\partial \mathbf{u}_a}{\partial t}\,, \tag{2.28}$$

Expanding the convection term on the l.h.s. of Eqn. (2.27) yields:

$$\begin{aligned} \nabla\bullet(\mathbf{u}\mathbf{u}) &= \nabla\bullet(\mathbf{u}_w\mathbf{u}_w) + \cancelto{0}{\nabla\bullet(\mathbf{u}_w\mathbf{u}_a)} + \cancelto{0}{\nabla\bullet(\mathbf{u}_a\mathbf{u}_w)} + \nabla\bullet(\mathbf{u}_a\mathbf{u}_a) \\ &= \nabla\bullet(\mathbf{u}_w\mathbf{u}_w) + \nabla\bullet(\mathbf{u}_a\mathbf{u}_a)\,, \end{aligned} \tag{2.29}$$

where the second identity results by cross coupling terms being zero by phase separation definition, Eqn. (2.20) and assumption of a sharp interface. Expanding the diffusion term on the l.h.s. of Eqn. (2.27) yields:

$$\begin{aligned} \nabla\bullet(\nu_e\nabla\mathbf{u}) &= \nabla\bullet(\nu_{e,w}\nabla\mathbf{u}_w) + \cancelto{0}{\nabla\bullet(\nu_{e,w}\nabla\mathbf{u}_a)} + \cancelto{0}{\nabla\bullet(\nu_{e,a}\nabla\mathbf{u}_w)} + \nabla\bullet(\nu_{e,a}\nabla\mathbf{u}_a) \\ &= \nabla\bullet(\nu_{e,w}\nabla\mathbf{u}_w) + \nabla\bullet(\nu_{e,a}\nabla\mathbf{u}_a)\,. \end{aligned} \tag{2.30}$$

Expanding the pressure gradient term on the r.h.s. of Eqn. (2.27) yields similar results:

$$\begin{aligned} \beta\nabla p_d &= \beta_w\nabla p_{d,w} + \cancelto{0}{\beta_w\nabla p_{d,a}} + \cancelto{0}{\beta_a\nabla p_{d,w}} + \beta_a\nabla p_{d,a} \\ &= \beta_w\nabla p_{d,w} + \beta_a\nabla p_{d,a}\,. \end{aligned} \tag{2.31}$$

Combining Eqn. (2.28) to Eqn. (2.31), it is clear that the combined momentum equation given by Eqn. (2.26) is valid for either water or air. □

Combined Momentum Equation at the Free Surface

To inspect the combined momentum equation at the free surface, the jump operator is applied to Eqn. (2.27), yielding:

$$\left[\frac{\partial \mathbf{u}}{\partial t} + \nabla\bullet(\mathbf{uu}) - \nabla\bullet\left(\nu_e \nabla \mathbf{u}\right) + \beta \nabla p_d\right] = 0\,. \tag{2.32}$$

By linearity of jump operator $[\cdot]$, Eqn. (2.32) is written and simplified as:

$$\cancelto{0}{\left[\frac{\partial \mathbf{u}}{\partial t}\right]} + \cancelto{0}{[\nabla\bullet(\mathbf{uu})]} - \cancelto{0}{[\nabla\bullet\left(\nu_e \nabla \mathbf{u}\right)]} + [\beta \nabla p_d] = 0\,. \tag{2.33}$$

In Eqn. (2.33), the time derivative and the convection term are identically equal to zero because they do not have a jump across the free surface (continuity of the velocity field Eqn. (2.13)). In the current approach, jump in the diffusion term is not accounted for due to assumed continuity of the effective viscosity, Eqn. (2.16) and the velocity gradient, Eqn. (2.17). Note that the assumption of continuous dynamic effective viscosity given by Eqn. (2.16) is extended for kinematic viscosity as well. Eqn. (2.33) therefore reveals an additional jump condition that needs to be taken into account:

$$[\beta \nabla p_d] = 0\,. \tag{2.34}$$

This represents an additional constraint on the dynamic pressure gradient and density at the free surface together with dynamic pressure jump condition given by Eqn. (2.19). The dynamic pressure gradient jump condition, Eqn. (2.34) has been previously successfully used by Huang *et al.* [15], Queutey and Visonneau [14] and Wang *et al.* [40]. Eqn. (2.34) is crucial for further development of the discretised jump conditions and is the critical point of this derivation. Furthermore, if the dynamic pressure gradient jump condition, Eqn. (2.34) is satisfied, the domain of validity of the combined momentum equation, Eqn. (2.27) includes the free surface along with the water and air domains, *i.e.*:

$$\frac{\partial \mathbf{u}}{\partial t} + \nabla\bullet(\mathbf{uu}) - \nabla\bullet\left(\nu_e \nabla \mathbf{u}\right) = -\beta \nabla p_d\,, \quad \mathbf{x} \in \Omega_w \cup \Gamma_{wa} \cup \Omega_a\,, \tag{2.35}$$

giving a single combined equation for water, air and the free surface.

2.3. Interface Capturing

Governing equations described in Sec. 2.2.2. require the information regarding exact location of the interface in order to successfully apply the jump conditions. The evolution of free surface in time is often modelled via Lagrangian interface tracking methods [80] or interface capturing methods. Most of the former methods use Lagrangian points to advect the sharp interface, with possible difficulties arising from complex flow patterns (*e.g.* wave breaking). The latter methods often use a colour function to denote the location of the interface, which is then advected by a velocity field to model the motion of the interface. Interface capturing methods often diffuse (smear) the interface over several computational points to ensure numerical stability when combined with conventional discretisation schemes for density gradient calculation within the pressure–velocity system. Although it is possible to geometrically reconstruct perfectly sharp interface from the colour function, such need rarely arises if the interface is confined to a small region in space. In this thesis, the interface capturing methods will be further considered due to their ability to handle breaking surface.

Interface capturing methods can be divided into three major groups:

1. Level Set (LS) methods [34, 33];
2. Phase Field (PF) methods [36, 37];
3. Volume–of–Fluid (VOF) methods [26, 27, 30, 32],

as presented in Figure 2.1. Two phases, namely water and air, Ω_w and Ω_a are separated by a free surface Γ_{wa}.

2.3.1. Level Set Method

The Level Set (LS) method based on the signed distance function is used in this thesis, with the signed distance function defined as:

$$\psi(\mathbf{x}) = \begin{cases} d\,, & \text{if } \mathbf{x} \in \Omega_w\,, \\ 0\,, & \text{if } \mathbf{x} \in \Gamma_{wa}\,, \\ -d\,, & \text{if } \mathbf{x} \in \Omega_a\,, \end{cases} \tag{2.36}$$

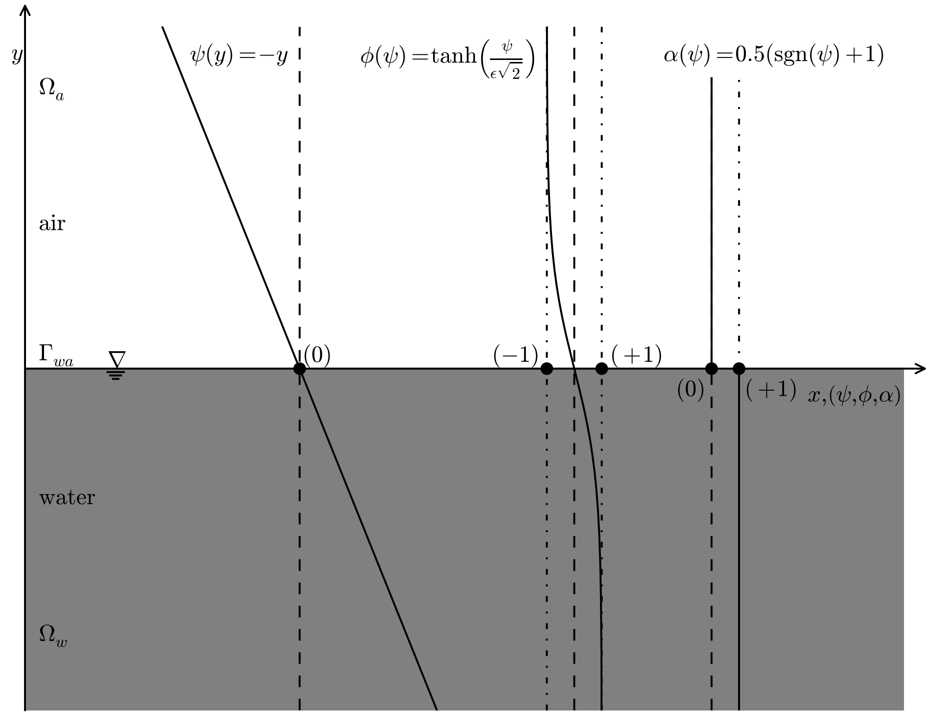

Figure 2.1: Comparison of interface capturing schemes. ψ is the signed distance function for the LS field, ϕ is the PF and α is the volume fraction in the VOF approach.

where d is the shortest Euclidian distance to the free surface. The interface is reconstructed with zero level set $\psi(\mathbf{x}) = 0$. It is important to note that the signed distance function is not bounded, making it easier to advect numerically as there is no need for special boundedness preserving schemes.

2.3.2. Phase Field Method

As opposed to the unbounded LS method, the Phase Field (PF) is bounded between -1 and 1 with a prescribed hyperbolic tangent profile across the interface, which in turn may be written as a function of the signed distance field:

$$\phi(\psi) = \tanh\left(\frac{\psi}{\epsilon\sqrt{2}}\right), \tag{2.37}$$

where the width parameter ϵ is used to control the smearing of the interface. The smearing of the interface in Eqn. (2.37) is by definition a user controlled parameter. For example, Sun and Beckermann [36] show that ϕ varies from -0.9 and 0.9 over $3\sqrt{2}\epsilon$. The interface is reconstructed in the same way as in the LS method, $\phi(\mathbf{x}) = 0$.

2.3.3. Volume–of–Fluid Method

By definition, the Volume–of–Fluid (VOF) method represents a fraction of the volume occupied by water inside an arbitrary closed volume. The volume fraction, α can also be written in terms of the LS field:

$$\alpha(\psi) = 0.5\left(\operatorname{sgn}(\psi) + 1\right) , \tag{2.38}$$

where $\operatorname{sgn}(\psi)$ denotes the sign (signum) function. Looking at the mathematical definition of volume fraction in Eqn. (2.38), which corresponds to the Heaviside step function, the interface may be reconstructed as an iso–surface of $0 < \alpha(\mathbf{x}) < 1$. However, the initially sharp interface often gets smeared due to numerical discretisation error in handling of bounded convection terms. Geometrical reconstruction of the interface in the VOF method is a computationally challenging task, especially for unstructured polyhedral grids, nevertheless, Luppes *et al.* [54] and Kleefsman [81] apply it successfully on Cartesian grids.

In order to define a continuous effective viscosity field as assumed in Eqn. (2.16), a combination of Eqn. (2.37) and Eqn. (2.38) is used:

$$\alpha(\psi) = 0.5\left(\tanh\left(\frac{\psi}{\epsilon\sqrt{2}}\right) + 1\right) . \tag{2.39}$$

Similar to the PF method, Eqn. (2.37), the interface is smeared using the width parameter, ϵ. The combined two–phase, continuous effective kinematic viscosity field is defined as:

$$\nu_e = \alpha\nu_{e,w} + (1-\alpha)\nu_{e,a} . \tag{2.40}$$

Definition given by Eqn. (2.40) satisfies the approximate jump condition regarding effective viscosity, Eqn. (2.16), since α is now a continuous function. Note that this assumption is invalid if one uses Eqn. (2.38), which defines a discontinuous α distribution. The density field is not artificially smeared.

2.3.4. Level Set Transport Equation

As opposed to the PF and VOF methods, the solution variable in the LS method is not bounded. In this study, the LS method is used to advect the interface between two phases because the unboundedness of the signed distance function facilitates the implementation of the solution decomposition via the SWENSE method, which shall be described in Ch. 3.

The solution of the advection equation for the LS field does not guarantee the preservation of the signed distance function due to numerical discretisation error, which is the practical drawback of the LS method. Moreover, the field often gets distorted to a point where it is unusable without effective reinitialisation. This is called redistancing, where numerous redistancing algorithms [82, 83, 35] often redistance the LS field after the advection step, increasing the computational cost and causing potential phase conservation issues.

Recently, Sun and Beckermann [36] have derived a transport equation for the PF that preserves the hyperbolic tangent profile given by Eqn. (2.37). Eqn. (2.37) also presents a relation between the PF and LS function, *i.e.* ϕ and ψ, respectively. This identity is used to derive a transport equation for the LS field from the PF equation presented by Sun and Beckermann [36]. Reader is referred to Appendix A for a detailed derivation of the LS transport equation from the original PF equation [36], while the resulting equation is given here:

$$\begin{aligned}&\frac{\partial \psi}{\partial t} + \mathbf{u}\bullet\nabla\psi = \\ &b\left(\nabla\bullet\left(\nabla\psi\right) + \frac{\sqrt{2}}{\epsilon}\left(1-|\nabla\psi|^2\right)\tanh\left(\frac{\psi}{\epsilon\sqrt{2}}\right) - |\nabla\psi|\nabla\bullet\left(\frac{\nabla\psi}{|\nabla\psi|}\right)\right).\end{aligned} \tag{2.41}$$

The terms in Eqn. (2.41) are briefly discussed here: the reader is referred to Sun and Beckermann [36] for a detailed derivation and analysis. The terms on the l.h.s. represent advection of the signed distance field, ψ. The first term on the r.h.s. is a diffusion term that serves to smooth out possible singularities. The second term on the r.h.s. models the curvature–driven motion of the interface. In water and air two–phase flows at marine hydrodynamics length scale, this term could be neglected because of the fluid properties. The third term on the r.h.s. counteracts the first and the second term. Folch *et al.* [29] show that the inclusion of the r.h.s. terms is numerically beneficial, even though the first two terms may be canceled out by the third term. In the absence of curvature–driven motion, b is no more than a numerical parameter, whose meaning shall be described in Sec. 4.1.3.

2.4. Closure

A general two–phase flow model for incompressible, turbulent flows has been presented. The approximate jump conditions at the free surface are derived for flows at marine hydrodynamics length scales, which are then used to define combined governing equations for both water and air. Different interface capturing methodologies are discussed, where the implicitly redistanced LS transport equation is presented in detail.

The resulting Partial Differential Equations (PDEs) in the present mathematical model for free surface marine hydrodynamics flows used in this thesis is summarized below.

- Combined (mixture) continuity equation:

$$\nabla\bullet\mathbf{u} = 0\,, \tag{2.42}$$

- Combined (mixture) momentum equation:

$$\frac{\partial \mathbf{u}}{\partial t} + \nabla\bullet(\mathbf{u}\mathbf{u}) - \nabla\bullet\left(\nu_e \nabla \mathbf{u}\right) = -\beta \nabla p_d\,, \tag{2.43}$$

- Implicitly redistanced LS interface capturing equation:

$$\begin{aligned}&\frac{\partial \psi}{\partial t} + \mathbf{u}\bullet\nabla\psi = \\ &b\left(\nabla\bullet\left(\nabla\psi\right) + \frac{\sqrt{2}}{\epsilon}\left(1 - |\nabla\psi|^2\right)\tanh\left(\frac{\psi}{\epsilon\sqrt{2}}\right) - |\nabla\psi|\nabla\bullet\left(\frac{\nabla\psi}{|\nabla\psi|}\right)\right)\,.\end{aligned} \tag{2.44}$$

Combined momentum equation, Eqn. (2.43) shall be used to solve for the continuous velocity field, while the combined continuity equation, Eqn. (2.42) shall be used to formulate dynamic pressure equation using a segregated solution algorithm. LS transport equation, Eqn. (2.44) shall be used to capture the location of the free surface and to calculate effective kinematic viscosity of the two–phase mixture, Eqn. (2.40).

Along with governing equations, the following jump conditions at the free surface need to be appropriately modelled:

- Density jump condition:

$$[\rho] = \rho_a - \rho_w \,, \tag{2.45}$$

- Dynamic pressure jump condition:

$$[p_d] = -\frac{1}{[\beta]}\mathbf{g}{\bullet}\mathbf{x} \,, \tag{2.46}$$

- Dynamic pressure gradient jump condition:

$$[\beta \nabla p_d] = 0 \,. \tag{2.47}$$

Jump conditions given by Eqn. (2.45), (2.46) and (2.47) shall be used to discretise the dynamic pressure and density terms near the free surface. Continuity of velocity field, Eqn. (2.13) has been already assumed (*i.e.* explicitly used) in the derivation of the combined continuity and momentum equations, Eqn. (2.42) and Eqn. (2.43), respectively. Continuity of the effective viscosity and the velocity gradient at the free surface, Eqn. (2.16) and Eqn. (2.17), respectively, along with the continuous velocity field allow the use of single–phase turbulence models [64].

It is important to stress that this model is not obtained using conditional averaging; rather it presents GFM [15] where the density distribution in two phases is assumed to define infinitesimally sharp interface.

Using the VOF method, the model can be easily extended for more than two phases. It is straightforward to prove that the combined momentum and continuity equations would have the same form, while additional VOF equations need to be introduced to capture multiple phases, as described by Kissling *et al.* [39].

3. Solution and Domain Decomposition

3.1. Wave Modelling

Ch. 2. presented a general model for fully nonlinear, two–phase, turbulent flow, governed by the combined two–phase continuity equation, Eqn. (2.42), combined two–phase momentum equation, Eqn. (2.43) and the interface capturing equation via implicitly redistanced LS method, Eqn. (2.44). The governing equations are accompanied by the free surface jump conditions for density, Eqn. (2.45) and dynamic pressure, Eqn. (2.46) and Eqn. (2.47). Since the derivation of governing equations assumed that the jump conditions hold, they need to be incorporated in the discretisation procedure via the GFM, which shall be presented in detail in Ch. 4.

Free surface gravity waves represent a large group of solutions for governing equations presented in Ch. 2. Traditionally, analytical solutions were first obtained using a linear potential flow model on an infinite domain, yielding linear Stokes' wave theory [84]. The linear solution has been extended to incorporate weakly nonlinear effects, yielding higher order Stokes' theories [85]. With the popularisation of computers, fully nonlinear numerical solutions of regular waves were obtained [60]. Furthermore, potential flow methods have been successfully used to numerically simulate ship diffraction and radiation problems, allowing linear seakeeping analysis in frequency domain using the BEM [86]. Hence, one can deduce that the potential flow models (both analytical and numerical) have been widely used for marine hydrodynamics. For this reason, the present CFD model needs to be formulated in order to take the advantage of the well established potential flow models. This is achieved by a twofold decomposition:

1. Solution decomposition to efficiently introduce waves in the CFD domain and

2. Domain decomposition to prevent spurious wave reflection off the far–field boundaries.

The two decomposition strategies and their combination are discussed in the following text.

3.2. Solution Decomposition via the SWENSE Method

In order to allow efficient coupling of arbitrary potential flow solution with the fully nonlinear, two–phase, free surface turbulent CFD solution governed by equations presented in Ch. 2., a variant of the original SWENSE method introduced by Ferrant *et al.* [20] is used.

The original SWENSE method [20] has been used to calculate wave diffraction, hence the fields are decomposed into incident and diffracted components. In this thesis, a slightly different notation shall be used where the fields are decomposed into incident and perturbed fields. The change of nomenclature is made since the perturbed fields always contain vorticity, viscosity and two–phase effects, and may contain diffraction and radiation effects, based on a specific problem. Hence, the SWENSE decomposition for an arbitrary field χ reads:

$$\chi = \chi_I + \chi_P \,, \tag{3.1}$$

where index I denotes the incident component and P denotes the perturbed component. The idea of SWENSE decomposition is to capture main features of free surface waves with a potential flow model, providing χ_I, and superimpose nonlinear, two–phase and turbulent effects by extending χ_I to a full Navier–Stokes model via χ_P. Note that χ_I may be an arbitrary field, and χ_P should adjust accordingly to satisfy the governing equations. However, from computational perspective, it is desirable to have χ_I to be as close to χ as possible. Such decomposition is desirable since the incident wave field often accurately models a large portion of the desired solution. Moreover, neglecting rotational motion and viscosity provides potential flow models with significant speed up compared to full CFD simulations.

Governing equations, Eqns. (2.42–2.44) shall be decomposed using Eqn. (3.1), where special considerations regarding strongly conservative FV discretisation need to be taken into account.

3.2.1. Solution Decomposition of the Continuity Equation

Decomposing the combined continuity equation, Eqn. (2.42) into the incident and perturbed components yields:

$$\nabla \bullet \mathbf{u}_P = -\nabla \bullet \mathbf{u}_I \,. \tag{3.2}$$

The velocity field obtained from the potential flow solution is indeed ideally solenoidal, *i.e.* $\nabla \bullet \mathbf{u}_I = 0$. Nevertheless, this is valid on a differential level (for Stokes's wave theories) and arbitrary numerical level (stream function or HOS method) in the discrete form. When the incident flow velocity field is mapped on an arbitrary CFD grid, using an arbitrary numerical framework (FV, FD or FE method), there is no guarantee that $\nabla \bullet \mathbf{u}_I$ vanishes. Hence, the term on the r.h.s. of Eqn. (3.2) is kept when evaluated numerically due to the (arbitrary) numerical discretisation error.

3.2.2. Solution Decomposition of the Momentum Equation

Decomposing the combined momentum equation, Eqn. (2.43) yields:

$$\frac{\partial \mathbf{u}_P}{\partial t} + \nabla \bullet (\mathbf{u}\mathbf{u}_P) - \nabla \bullet (\nu_e \nabla \mathbf{u}_P) = -\frac{\partial \mathbf{u}_I}{\partial t} - \nabla \bullet (\mathbf{u}\mathbf{u}_I) + \nabla \bullet (\nu_e \nabla \mathbf{u}_I) - \beta \nabla p_d \,, \tag{3.3}$$

Eqn. (3.3) is discussed in detail term by term:

- The velocity field in the time derivative term is decomposed, resulting in time derivative terms for both perturbed and incident field;
- The convected velocity field in the nonlinear convection term is decomposed, while the convecting velocity field **u** is not decomposed because the convection term shall be linearised using the total explicit volumetric flux from previous iteration (see Ch. 4.). Such a procedure yields two convective terms for incident and perturbed velocity fields, both convected by the total velocity field;
- The velocity field in the diffusion term is also decomposed, yielding two diffusion terms for the perturbed and incident field;

- The dynamic pressure field p_d is not decomposed because the volumetric flux in the convection term is not decomposed. Their decomposition would yield two pressure equations: one for the incident field and one for the perturbed field, which would separately force $\nabla\bullet\mathbf{u}_P$ and $\nabla\bullet\mathbf{u}_I$ to vanish. Due to the elliptic nature of the pressure equation in incompressible flows, the pressure equation is often the most time–consuming part of a CFD algorithm, hence, the dynamic pressure and the convecting velocity field are not decomposed for efficiency reasons.

The possible decomposition of dynamic pressure and the convecting velocity field would yield a part of the momentum equation which could be identified with the Euler equation for the incident flow. Since there is no guarantee that the Euler part of the equation should vanish when the incident solution is mapped on an arbitrary CFD grid, this part should be kept in the final equation set.

3.2.3. Solution Decomposition of the Level Set Equation

If one would choose the volume fraction α in the VOF approach, it is easy to verify that the solution decomposition given by Eqn. (3.1) would yield two bounded variables. Since α is bounded between 0 and 1 (*i.e.* $0 < \alpha < 1$), α_D would be bounded between $-\alpha_I$ and $1 - \alpha_I$ (*i.e.* $-\alpha_I < \alpha_D < 1 - \alpha_I$). This would require additional considerations for boundedness–preserving convection schemes [87, 88]. The same reasoning applies for the hyperbolic tangent profile ϕ in the PF method, where the only difference is its boundedness between -1 and 1 (*i.e.* $-1 < \phi < 1$). As an alternative, unboundedness of the signed distance field ψ in the LS method makes it suitable for the solution decomposition, which shall yield two unbounded fields.

Prior to the solution decomposition, implicitly redistanced LS transport equation, Eqn. (2.41) shall be written in a form more suitable for strongly conservative FV discretisation. The last two terms on the r.h.s. of Eqn. (2.41) can be expanded as:

$$\begin{aligned}
-b\frac{\sqrt{2}}{\epsilon}\tanh\left(\frac{\psi}{\epsilon\sqrt{2}}\right)|\nabla\psi|^2 &= -b\frac{\sqrt{2}}{\epsilon}\tanh\left(\frac{\psi}{\epsilon\sqrt{2}}\right)\nabla\psi{\bullet}\nabla\psi \\
&= -\mathbf{w}_1{\bullet}\nabla\psi \\
&= -\nabla{\bullet}(\mathbf{w}_1\psi) + \psi\nabla{\bullet}\mathbf{w}_1\,,
\end{aligned} \tag{3.4}$$

where the second identity introduces $\mathbf{w}_1$ as:

$$\mathbf{w}_1 = b\frac{\sqrt{2}}{\epsilon}\tanh\left(\frac{\psi}{\epsilon\sqrt{2}}\right)\nabla\psi\,, \tag{3.5}$$

which is an additional term which transports (convects) the signed distance field ψ. The procedure for the last term on the r.h.s. of Eqn. (2.41) is similar and yields:

$$\begin{aligned}
-b\nabla{\bullet}\left(\frac{\nabla\psi}{|\nabla\psi|}\right)|\nabla\psi| = -b\kappa|\nabla\psi| &= -b\kappa\frac{\nabla\psi}{|\nabla\psi|}{\bullet}\nabla\psi \\
&= -\mathbf{w}_2{\bullet}\nabla\psi \\
&= -\nabla{\bullet}(\mathbf{w}_2\psi) + \psi\nabla{\bullet}\mathbf{w}_2\,,
\end{aligned} \tag{3.6}$$

where κ is already introduced as the mean interface curvature and $\mathbf{w}_2$ is an additional term that transports (convects) the signed distance field ψ:

$$\mathbf{w}_2 = b\kappa\frac{\nabla\psi}{|\nabla\psi|}\,. \tag{3.7}$$

Inserting identities given by Eqn. (3.4) and Eqn. (3.6) into the transport equation, Eqn. (2.41) yields:

$$\begin{aligned}
&\frac{\partial\psi}{\partial t} + \mathbf{u}{\bullet}\nabla\psi + \nabla{\bullet}(\mathbf{w}_1\psi) - \psi\nabla{\bullet}\mathbf{w}_1 + \nabla{\bullet}(\mathbf{w}_2\psi) - \psi\nabla{\bullet}\mathbf{w}_2 - b\nabla{\bullet}\left(\nabla\psi\right) = \\
&b\frac{\sqrt{2}}{\epsilon}\tanh\left(\frac{\psi}{\epsilon\sqrt{2}}\right)\,.
\end{aligned} \tag{3.8}$$

The convective terms can be grouped together and the final form of the transport equation reads:

$$\frac{\partial\psi}{\partial t} + \nabla{\bullet}(\mathbf{c}\psi) - \psi\nabla{\bullet}\mathbf{c} - b\nabla{\bullet}\left(\nabla\psi\right) = b\frac{\sqrt{2}}{\epsilon}\tanh\left(\frac{\psi}{\epsilon\sqrt{2}}\right)\,, \tag{3.9}$$

where $\mathbf{c} = \mathbf{u} + \mathbf{w}_1 + \mathbf{w}_2$ is the modified convecting velocity field that transports and maintains the signed distance function with the help of diffusion and source term. This form of the LS transport equation is favourable from the numerical perspective because the source terms are reformulated into divergence terms.

The solution decomposition of Eqn. (3.9) via Eqn. (3.1) yields:

$$\begin{aligned} &\frac{\partial \psi_P}{\partial t} + \nabla\text{•}(\mathbf{c}\psi_P) - \psi_P \nabla\text{•}\mathbf{c} - b\nabla\text{•}\left(\nabla \psi_P\right) = \\ &-\frac{\partial \psi_I}{\partial t} - \nabla\text{•}(\mathbf{c}\psi_I) + \psi_I \nabla\text{•}\mathbf{c} + b\nabla\text{•}\left(\nabla \psi_I\right) + b\frac{\sqrt{2}}{\epsilon}\tanh\left(\frac{\psi}{\epsilon\sqrt{2}}\right) , \end{aligned} \tag{3.10}$$

In Eqn. (3.10), the time derivative, convection and diffusion terms are decomposed. The total convecting field $\mathbf{c}$ is not decomposed for the same reason as in the momentum equation (see Sec. 3.2.2.). The last, hyperbolic tangent source term is not decomposed since it will not be treated implicitly. Although Picard linearisation is possible [89], the linearisation of the hyperbolic tangent would create a source term, since the diffusion parameter b and the width parameter ϵ are always positive. Since the source term is positive on the r.h.s. of the equation, its implicit treatment would decrease the diagonal dominance of the resulting matrix. Interested reader is referred to Appendix B for a more detailed discussion.

Using the SWENSE solution decomposition, only the perturbation in ψ around ψ_I is calculated, rather than complete signed distance profile. Thus, the linear profile in the hydrostatic case does not have to be calculated. This decomposition allows efficient introduction of incoming waves in the CFD simulation, by prescribing $\mathbf{u}_I$ and ψ_I at each time step, and solving only for the perturbed component. It should be noted that the wave is present in the whole computational domain explicitly, instead of prescribing wave boundary conditions at far–field boundaries.

3.3. Domain Decomposition via Relaxation Zones

Sec. 3.2. presented solution decomposition where the wave field is introduced with explicit incident components. However, if the perturbed component does not vanish near the far–field boundaries, wave reflection will occur, disrupting the CFD results in the area of interest. Monroy *et al.* [58] and Marcer *et al.* [59] used an extremely coarse computational grid do numerically damp perturbed fields and prevent wave reflection. A more general approach based on the implicit treatment [53] of relaxation zones [52] is presented and used in this study. The relaxation zones volumetrically combine governing equations for the nonlinear, two–phase flow model and the prescribed incident wave field solution in order to force the perturbed field to vanish in the far–field. This procedure leaves only the incident flow near computational boundaries and thus prevents undesirable wave reflection. This procedure is described for a general solution decomposed transport equation for a variable $\chi = \chi_I + \chi_P$:

$$\begin{aligned} &\frac{\partial(\rho\chi_P)}{\partial t} + \nabla\bullet(\rho\mathbf{u}\chi_P) - \nabla\bullet(\gamma_\chi\nabla\chi_P) + \\ +&\frac{\partial(\rho\chi_I)}{\partial t} + \nabla\bullet(\rho\mathbf{u}\chi_I) - \nabla\bullet(\gamma_\chi\nabla\chi_I) - S_u = \mathcal{T}(\chi_P) = 0\,, \end{aligned} \tag{3.11}$$

where γ_χ is the corresponding diffusion coefficient and S_u is the source term. $\mathcal{T}(\chi_P)$ is introduced as a general transport operator acting on the perturbed field. In order to prevent wave reflection, the perturbed field should be zero at the boundaries:

$$\frac{1}{\tau}\chi_P = 0 \rightarrow \mathcal{R}(\chi_P) = 0\,, \tag{3.12}$$

where $\mathcal{R}$ is the relaxation zone operator, which is in this case defined as: $\mathcal{R}(\chi_P) = \chi_P/\tau$. τ is an arbitrary time scale parameter introduced to ensure that the transport equation, Eqn. (3.11) and the relaxation zone equation, Eqn. (3.12) have the same physical dimensions. Although arbitrary, τ is equal to the time step size during numerical simulations in order to preserve the matrix condition number since the diagonal of the matrix scales with the inverse of the time step size due to discretisation of the time derivative term.

In order to smoothly blend the two models represented by Eqn. (3.11) and Eqn. (3.12), weight field w is introduced. w is equal to 1 at far–field boundaries (Figure 3.1), forcing the perturbed field to vanish. In the interior of the domain near the area of interest, w reduces to 0. A straightforward linear combination of Eqn. (3.11) and Eqn. (3.12) with the weight field yields:

$$(1-w)\mathcal{T}(\chi_P) + w\mathcal{R}(\chi_P) = 0\,, \tag{3.13}$$

The linear combination given by Eqn. (3.13) forces the perturbed field to vanish where $w = 1$, and gives the fully nonlinear, two–phase CFD solution where $w = 0$.

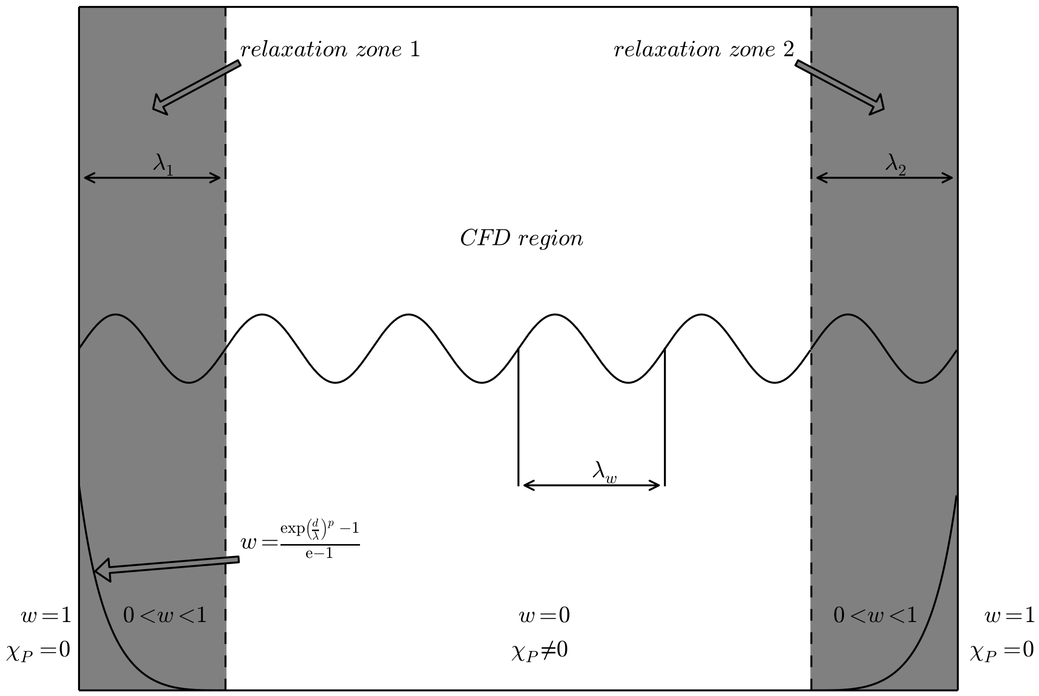

Figure 3.1: Relaxation zones with qualitative weight field function. The white region represents full CFD domain, while the shaded gray region represents relaxation zones. Within relaxation zones, the solution is a linear combination of calculated CFD solution and prescribed incident flow solution.

Following Jacobsen *et al.* [52], w is an exponential function of the following form:

$$w = \frac{\mathrm{e}^{\left(\frac{d}{\lambda_r}\right)^s} - 1}{\mathrm{e} - 1}\,, \tag{3.14}$$

where d is the shortest distance to the boundary and λ_r is the relaxation zone length. s is the spatial exponent, controlling the steepness of the exponential function. Following Jacobsen *et al.* [52], $p = 3.5$ is used in this study. Note that the length of relaxation zones controls the smoothness of the forcing, which indicates that the longer relaxation zones should reduce wave reflection more successfully. A detailed study of wave reflection with varying relaxation zone length is presented in Sec. 6.3.

The domain decomposition strategy given by Eqn. (3.13) shall be applied to the combined momentum equation, Eqn. (3.3) and the LS interface capturing equation, Eqn. (3.10). The combined continuity equation, Eqn. (3.2) is not decomposed because it will later be used to formulate the dynamic pressure equation. An attempt to blend the dynamic pressure in early stages of the development lead to severe stability issues. Such outcome is expected, since the dynamic pressure in the strongly conservative FV method is used to enforce volumetric continuity, while blending the dynamic pressure directly affects the fluxes, making them non–conservative.

3.3.1. Domain Decomposition of the Momentum Equation

Applying the domain decomposition strategy given by Eqn. (3.13) to the solution decomposed combined momentum equation, Eqn. (3.3), yields:

$$\begin{aligned}(1-w)\left(\frac{\partial \mathbf{u}_P}{\partial t} + \nabla \bullet (\mathbf{u}\mathbf{u}_P) - \nabla \bullet \left(\nu_e \nabla \mathbf{u}_P\right)\right) = -\frac{w}{\tau}\mathbf{u}_P - \\ -(1-w)\left(\frac{\partial \mathbf{u}_I}{\partial t} + \nabla \bullet (\mathbf{u}\mathbf{u}_I) - \nabla \bullet \left(\nu_e \nabla \mathbf{u}_I\right) + \beta \nabla p_d\right) .\end{aligned} \tag{3.15}$$

The sink term $-w/\tau\mathbf{u}_P$ gradually forces $\mathbf{u}_P$ to vanish inside relaxation zones where $w \neq 0$, leaving only incident velocity field at the boundaries where $w = 1$.

3.3.2. Domain Decomposition of the Level Set Equation

The domain decomposition performed on the implicitly redistanced LS transport equation, Eqn. (3.10) yields:

$$\begin{aligned}(1-w)\left(\frac{\partial \psi_P}{\partial t} + \nabla \bullet (\mathbf{c}\psi_P) - \psi_P \nabla \bullet \mathbf{c} - b\nabla \bullet \left(\nabla \psi_P\right)\right) = -\frac{w}{\tau}\psi_P - \\ -(1-w)\left(\frac{\partial \psi_I}{\partial t} + \nabla \bullet (\mathbf{c}\psi_I) - \psi_I \nabla \bullet \mathbf{c} - b\nabla \bullet \left(\nabla \psi_I\right) - b\frac{\sqrt{2}}{\epsilon}\tanh\left(\frac{\psi}{\epsilon\sqrt{2}}\right)\right) ,\end{aligned} \tag{3.16}$$

where the sink term $-w/\tau\psi_P$ leaves only the incident wave elevation field at the boundaries where $w = 1$.

3.4. Closure

The solution decomposition strategy via SWENSE approach has been presented. The governing equations are decomposed into incident and perturbed fields, with important considerations regarding consistency concerning arbitrary potential flow models and numerical FV discretisation. Due to incompressibility assumption and the strongly conservative FV method which shall be used for numerical discretisation, dynamic pressure and the convecting velocity field (*i.e.* flux) has not been decomposed. Special attention has been given to the reformulation of the source terms in the implicitly redistanced LS transport equation, where almost all of the source terms are treated as additional convective terms, allowing their implicit treatment. All governing equations are written in terms of the unknown perturbed fields, containing additional explicit forcing terms related to arbitrary potential flow incident wave field.

In order to prevent wave reflection off the far–field boundaries, implicit relaxation zones have been introduced, where the CFD domain is decomposed into the full CFD region and the blending region (relaxation zones). Inside relaxation zones, the governing CFD transport equations are blended with the target potential flow solution. Hence, fully nonlinear, two–phase turbulent model is solved in the CFD region, whereas in the blending region, the solution is a combination of the prescribed potential flow solution and the CFD solution. At far–field boundaries, perturbed component is forced to vanish, leaving only the non–reflecting incident potential flow solution. It has also been shown that the resulting implicit treatment is numerically beneficial as it yields additional sink terms that are favourable for iterative linear system solvers.

Note that the presented method is general:

- The methodology does not depend on a given potential flow theory,
- The framework also allows the possibility of two–way coupling with advanced potential flow models, although this has not been investigated in this study,
- The definition of relaxation zones does not depend on wave direction.

4. Numerical Modelling

4.1. Finite Volume Discretisation of Free Surface Flow Equations

Ch. 3. presented the final form of governing equations for a fully nonlinear, two–phase, turbulent flow combined with an arbitrary potential flow solution for the incident wave via solution decomposition technique. Prevention of wave reflection is achieved with domain decomposition via introduction of implicit relaxation zones, combining the two sets of governing equations into a single set. The governing equations are written in the conservative form suitable for implicit FV discretisation.

This chapter presents numerical discretisation of governing PDEs, Eqn. (3.2), (3.15) and (3.16), using second–order accurate, collocated FV method for arbitrary polyhedral (unstructured) grids [90]. Collocated, polyhedral framework is preferred due to its simplicity regarding grid generation for complex geometries often encountered in marine hydrodynamics (*e.g.* ship hull with appendages). It is important to note that the methodology presented here is general in a sense that block structured grids may be used without additional overhead. In FV based CFD computations, computational domain is divided into Control Volumes (CVs), or cells, presented in Figure 4.1. The cell has a finite number of neighbours connected through common faces, where $\mathbf{s}_f$ represents a surface area vector and $\mathbf{d}_f$ is the distance vector from cell centre P to cell centre N.

The general FV discretisation practice for all equations shall be briefly presented. Without detailed analysis, terms enclosed in curly braces $\{\cdot\}^i$ (as opposed to $[\cdot]$ as used by Rusche [32]) shall represent implicit FV discretisation, while $\{\cdot\}^e$ shall represent explicit FV discretisation, where the integral form of the governing equations obtained by integrating over the CV is implied. For additional details regarding general FV discretisaton on collocated grids, reader is referred to [89, 91, 90, 32, 92]. Special attention shall be given to pressure terms due to

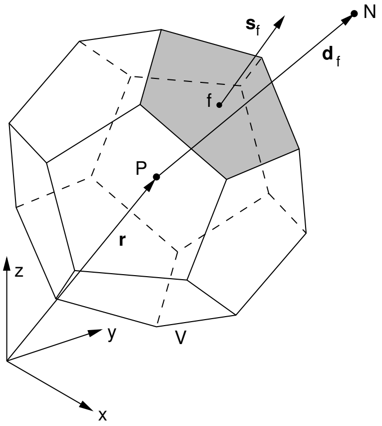

Figure 4.1: Polyhedral control volume P (cell) sharing a common face with its immediate neighbour N [38].

jump conditions across the free surface, Eqn. (2.46) and Eqn. (2.47), using the GFM. Furthermore, second–order accurate discretisation of pressure jump conditions shall be presented in detail, followed by a detailed inspection of the resulting interface–corrected interpolation schemes. Modelling of rigid body motion shall be presented next, with a detailed overview of the segregated solution algorithm for strongly resolved coupling of rigid body motion and fluid flow equations.

4.1.1. Discretised Momentum Equation

The discretisation of the combined and decomposed momentum equation, Eqn. (3.15) yields:

$$\begin{aligned}(1-w)\left(\left\{\frac{\partial \mathbf{u}_P}{\partial t}\right\}^i + \{\nabla\bullet(\mathbf{u}\mathbf{u}_P)\}^i - \{\nabla\bullet(\nu_e\nabla\mathbf{u}_P)\}^i\right) = -\left\{\frac{w}{\tau}\mathbf{u}_P\right\}^i - \\ -(1-w)\left(\left\{\frac{\partial \mathbf{u}_I}{\partial t}\right\}^e + \{\nabla\bullet(\mathbf{u}\mathbf{u}_I)\}^e - \{\nabla\bullet(\nu_e\nabla\mathbf{u}_I)\}^e + \{\beta\nabla p_d\}^e\right)\,.\end{aligned} \tag{4.1}$$

where superscripts $\{\cdot\}^i$ and $\{\cdot\}^e$ imply implicit and explicit FV discretisation, respectively. In Eqn. (4.1), the time derivative, convection and diffusion terms of the perturbed field are discretised implicitly, where the usual linearisation of the convection term is employed to avoid nonlinear algebraic equations [91, 90]. Special considerations are not required for implicit terms in Eqn. (4.1) because they do not have a discontinuity at the interface (see Eqn. (2.13), (2.16) and (2.17)).

The discretisation of the pressure gradient term shall be given in Sec. 4.2.1. (Gauss gradient with linear interpolation) and Sec. 4.2.2. (least squares gradient), while the jump condition corrections shall be presented in Sec. 4.4.

On assembly, Eqn. (4.1) is represented by a linear algebraic equation for each cell:

$$a_P \mathbf{u}_{P,P} + \sum_f a_N \mathbf{u}_{N,P} = \mathbf{b}_{\mathbf{u}} \, , \tag{4.2}$$

where a_P represents the diagonal matrix coefficient and a_N the off–diagonal coefficient for the equation regarding control volume P. In P, P index combinations, first index denotes field value at cell centre P and the second index denotes the perturbed component of the field. Similarly, index N, P denotes the perturbed component of the field evaluated at neighbouring cell centre N. $\sum_f$ denotes sum over all neighbouring faces for cell P, while $\mathbf{b}_{\mathbf{u}}$ represents combined source terms arising from:

- Old time step contribution in the time derivative term for the perturbed field,
- Possible non–orthogonal correction in the diffusion term [90] for the perturbed field,
- Possible deferred correction [91] in the convection term for the perturbed field,
- Explicit dynamic pressure gradient term,
- All terms related to incident flow field (time derivative, convection and diffusion).

Over–relaxed non–orthogonal correction approach following Jasak [90] is exclusively used in present study for non–orthogonal correction in all diffusion terms. Note that boundary cells have additional diagonal and/or source contributions arising from the treatment of boundary conditions [90].

4.1.2. Discretised Pressure Equation

The pressure equation in the FV framework is used to create conservative fluxes for incompressible fluid flow. The pressure–velocity coupling algorithm shall be derived following Patankar and Spalding [93]. Using notation by Jasak [90], the derivation of the pressure equation begins by writing a semi–discretised form of the combined momentum equation, Eqn. (4.2):

$$a_P \mathbf{u}_{P,P} = \mathbf{H}(\mathbf{u}_{N,P}) - \beta \nabla p_d \,. \tag{4.3}$$

In analogy to the Rhie and Chow correction [94], the dynamic pressure gradient terms is left undiscretised to facilitate the derivation of the dynamic pressure equation. $\mathbf{H}(\mathbf{u}_{N,P})$ term comprises two parts: the perturbed velocity field transport part containing matrix coefficients for all neighbours multiplied with corresponding velocities; and the source part $\mathbf{b}^*_{\mathbf{u}}$ as in Eqn. (4.2), but excluding the dynamic pressure gradient term:

$$\mathbf{H}(\mathbf{u}_{N,P}) = -\sum_f a_N \mathbf{u}_{N,P} + \mathbf{b}^*_{\mathbf{u}} \,. \tag{4.4}$$

The integral FV discretisation of the combined continuity equation, Eqn. (3.2) reads:

$$\begin{gathered}\int_{CV} \nabla\bullet (\mathbf{u}_P + \mathbf{u}_I)\, \mathrm{d}V = \int_{\partial CV} \mathrm{d}\mathbf{S}\bullet (\mathbf{u}_P + \mathbf{u}_I) = \sum_f \mathbf{s}_f\bullet (\mathbf{u}_{f,P} + \mathbf{u}_{f,I}) = 0\,, \text{ or} \\ \sum_f \mathbf{s}_f\bullet\mathbf{u}_{f,P} = -\sum_f \mathbf{s}_f\bullet\mathbf{u}_{f,I}\,,\end{gathered} \tag{4.5}$$

where the first identity follows from Gauss' theorem and the second identity follows from second–order accurate polyhedral FV discretisation, implying interpolation from cell–centred values to face–centred values, denoted by index f. The perturbed velocity field at cell centre P can be defined using the semi–discretised combined momentum equation, Eqn. (4.3) as:

$$\mathbf{u}_{P,P} = \frac{\mathbf{H}(\mathbf{u}_{N,P})}{a_P} - \frac{\beta \nabla p_d}{a_P} \,. \tag{4.6}$$

Cell–centred perturbed velocities given by Eqn. (4.6) are linearly interpolated to obtain face–centred values:

$$\mathbf{u}_{f,P} = \frac{\mathbf{H}(\mathbf{u}_{N,P})_f}{(a_P)_f} - \frac{1}{(a_P)_f} (\beta)_{f_\Gamma} \left(\nabla p_d\right)_{f_\Gamma} \,, \tag{4.7}$$

where $(\cdot)_f$ denotes ordinary cell–to–face interpolation, while $(\cdot)_{f_\Gamma}$ denotes cell–to–face interpolation with correction at the interface Γ due to jump conditions given by Eqn. (2.46) and Eqn. (2.47). The interface–corrected interpolation based on the GFM shall be described in detail in Sec. 4.3.

The dynamic pressure equation is obtained by substituting face–centred perturbed velocities given by Eqn. (4.7) into the discretised combined continuity equation, Eqn. (4.5), yielding:

$$\sum_f \mathbf{s}_f \bullet \frac{1}{(a_P)_f} (\beta)_{f_\Gamma} (\nabla p_d)_{f_\Gamma} = \sum_f \mathbf{s}_f \bullet \left(\frac{\mathbf{H}(\mathbf{u}_{N,P})_f}{(a_P)_f} + \mathbf{u}_{f,I} \right) . \tag{4.8}$$

Compared to ordinary pressure equation in incompressible flows [90], an additional term resulting from SWENSE solution decomposition is present in Eqn. (4.8), taking into account the explicit incident velocity field. Furthermore, individual terms of the dynamic pressure equation at the free surface need to be closely examined:

- $(1/a_P)_f$ represents the face–interpolated inverse diagonal coefficient of the combined momentum equation. The diagonal matrix coefficient does not have a discontinuity across the free surface since the combined momentum equation is continuous (see Sec. 2.2.2.). Under such circumstances, ordinary interpolation practices are sufficient;

- $(\beta)_{f_\Gamma}$ represents the face–interpolated inverse density field of the two–fluid mixture. Density field has a discontinuity across the free surface given by Eqn. (2.45), hence, ordinary interpolation practices are not sufficient;

- $(\nabla p_d)_{f_\Gamma}$ represents the surface normal gradient of the dynamic pressure field. Since the dynamic pressure field has a discontinuity across the free surface given by Eqn. (2.46), ordinary interpolation schemes practices are not sufficient;

- $\mathbf{H}(\mathbf{u}_{N,P})_f/(a_P)_f$ represents intermediate perturbed velocity field obtained from the combined momentum equation, which does not have a discontinuity across the free surface because the velocity field is continuous, Eqn. (2.13);

- $\mathbf{u}_{f,I}$ represents explicit incident velocity field. It is important to note that the incident velocity field is often defined only in water (up to free surface) in most of the potential flow models. In present study, the incident velocity

> field obtained from wave theories (such as Stokes') is analytically extended in air to ensure the physical constraint of continuity of the total velocity field given by Eqn. (2.13). However, in order to avoid potentially large incident velocity magnitudes in the air due to the exponential nature of analytical solutions [85], a numerical limit for the incident velocity field is often set as approximately 120% of the incident velocity magnitude at the wave crest. The sensitivity studies regarding the limit parameter are presented in Sec. 6.1., where it is shown that the solution does not significantly vary with the limit parameter.

It is important to note that even though β and ∇p_d are discontinuous at the free surface, their product is continuous according to Eqn. (2.47). The continuity of $\beta \nabla p_d$ has an important implication: interface corrected interpolation schemes (denoted with $(\cdot)_{f_\Gamma}$, which shall be obtained via GFM) for density and dynamic pressure fields have to preserve the symmetry of the pressure Laplacian in Eqn. (4.8), making the resulting matrix symmetric.

After the solution of the pressure equation, Eqn. (4.8), total conservative volumetric face fluxes can be calculated as:

$$F = \mathbf{s}_f \bullet (\mathbf{u}_{f,P} + \mathbf{u}_{f,I}) = \mathbf{s}_f \bullet \left(\frac{\mathbf{H}(\mathbf{u}_{N,P})_f}{(a_P)_f} - \frac{1}{(a_P)_f} (\beta)_{f_\Gamma} (\nabla p_d)_{f_\Gamma} + \mathbf{u}_{f,I} \right) , \tag{4.9}$$

where Eqn. (4.7) is used for the second identity, making the volumetric face fluxes conservative in the discrete form: $\sum_f F = 0$. The face fluxes F contain contributions from both the incident and the perturbed field, making them "undecomposed" as discussed in Sec. 3.2. The conservative volumetric fluxes are used to convect the perturbed and incident velocity fields in the momentum equation, signed distance LS field and other transported variables (*e.g.* for turbulence modelling equations).

4.1.3. Discretised Level Set Equation

The discretised decomposed LS equation, Eqn. (3.16) reads:

$$
\begin{aligned}
&(1-w)\left(\left\{\frac{\partial\psi_P}{\partial t}\right\}^i + \{\nabla\!\bullet\!(\mathbf{c}\psi_P)\}^i - \{\psi_P\nabla\!\bullet\!\mathbf{c}\}^i - \{b\nabla\!\bullet(\nabla\psi_P)\}^i\right) = -\left\{\frac{w}{\tau}\psi_P\right\}^i - \\
&-(1-w)\left(\left\{\frac{\partial\psi_I}{\partial t}\right\}^e + \{\nabla\!\bullet\!(\mathbf{c}\psi_I)\}^e - \{\psi_I\nabla\!\bullet\!\mathbf{c}\}^e - \{b\nabla\!\bullet(\nabla\psi_I)\}^e\right) - \\
&-(1-w)\left\{b\frac{\sqrt{2}}{\epsilon}\tanh\left(\frac{\psi}{\epsilon\sqrt{2}}\right)\right\}^e ,
\end{aligned}
\tag{4.10}
$$

where the convective LS field $\mathbf{c}$ is defined with Eqn. (3.5) and Eqn. (3.7):

$$
\mathbf{c} = \mathbf{u} + \mathbf{w}_1 + \mathbf{w}_2 = \mathbf{u} + b\frac{\sqrt{2}}{\epsilon}\tanh\left(\frac{\psi}{\epsilon\sqrt{2}}\right)\nabla\psi + b\kappa\frac{\nabla\psi}{|\nabla\psi|} . \tag{4.11}
$$

All terms on the l.h.s. of Eqn. (4.10) are discretised implicitly. The first sink term on the r.h.s. of Eqn. (4.11) arising from the implicit blending procedure is also treated implicitly, increasing the diagonal dominance of the matrix inside relaxation zones. This terms is responsible for forcing the perturbed LS field towards zero in the relaxation zone near the far–field boundaries. Other terms are explicit since the incident LS field is known at each time step.

As discussed in Sec. 2.3.4., the parameter b in Eqn. (4.11) is a purely numerical parameter in the absence of curvature–driven interface motion [36], which acts as a diffusion coefficient and a pre–factor for curvature driven terms. Sun and Beckermann [36] used a Courant–Friedrichs-Lewy (CFL) condition for the PF equation to determine the numerical value of the parameter b. A similar approach is taken in this study, with following considerations:

- b should be as small as possible to prevent excessive diffusion of the signed distance profile,
- Maximum CFL number is not limited to 1 because Eqn. (4.10) is discretised implicitly,
- b should be calculated in a manner consistent with arbitrary polyhedral 3–D FV method and its conventions.

Using the convective LS field given by Eqn. (4.11), a convective CFL number is defined as:

$$CFL_c = \frac{\mathbf{s}_f \bullet \mathbf{c}_f}{\mathbf{s}_f \bullet \mathrm{d}_f} \Delta t \,, \tag{4.12}$$

where $\mathbf{c}_f$ is the face interpolated value of convective LS field and Δt is the time step size. Similarly, the CFL number due to diffusive flux can be defined as:

$$CFL_d = b \frac{\mathbf{s}_f \bullet \nabla \psi_f}{\mathbf{s}_f \bullet \mathrm{d}_f} \Delta t \,, \tag{4.13}$$

where $\nabla \psi_f$ is the surface normal gradient of the LS field. The sum of convective and diffusive CFL numbers should not exceed the user–specified limit:

$$CFL_c + CFL_d \leq CFL_\psi \,, \tag{4.14}$$

where $CFL_\psi = 1$ is the upper bound in case of explicit solution algorithms [87]. Inequality given in Eqn. (4.14) also provides an upper bound for b.

During the solution process, the time step may be either fixed or controlled with a CFL number selected by the user based on the fluid velocity field:

$$CFL = \frac{\mathbf{s}_f \bullet \mathbf{u}}{\mathbf{s}_f \bullet \mathrm{d}_f} \Delta t \,, \tag{4.15}$$

where $\mathbf{s}_f \bullet \mathbf{u}_f = F$ is the volumetric face flux. Numerical tests show that $CFL_\psi \approx 2\, CFL$ yields good results, even though the solution is insensitive to higher values of CFL_ψ, which will be demonstrated in Sec. 6.1. Nevertheless, $b \geq 0$ is required for numerical stability since b is a diffusion coefficient.

The parameter b should be as small as possible to prevent excessive diffusion of the signed distance profile. For this reason, b is divided by a stabilisation constant $\gamma \geq \mathcal{O}(10^5)$. Finally, an expression for b can be derived expanding Eqn. (4.14):

$$b = \frac{b^0}{\gamma} \frac{CFL_\psi - CFL_c}{CFL_d} \,, \tag{4.16}$$

where b^0 denotes the parameter b from the previous iteration or time step. It will be shown in Sec. 6.3. that the exact value of the numerical parameter γ has a minor influence on the final solution.

4.1.4. Explicit Treatment of Incident Terms

Discretised governing equations: momentum equation, Eqn. (4.1); pressure equation, Eqn. (4.8) and the LS equation, Eqn. (4.10) contain terms related to incident fields that are bound to mathematical operators: time derivative, divergence and Laplacian. Ducrozet *et al.* [56] discuss two distinct approaches for their evaluation: analytical and numerical approach. In the analytical approach, additional explicit terms are evaluated analytically from the underlying wave theory (or a numerical model) used to obtain the incident wave field. In the numerical approach, the incident wave field is first mapped on the numerical grid and the operators are discretised in the underlying numerical framework. The advantage of the numerical approach is its simple implementation and low computational overhead, while its major drawback is directly related to the accuracy of evaluation of derivatives using finite order numerical approximations. Hence, if the numerical approach is used, sufficient grid resolution is necessary for incident wave propagation. In theory, such a constraint is not present if one uses the analytical approach since the incident terms do not depend on grid resolution. However, the analytical approach is more challenging to implement and would cause possibly significant computational overhead, especially for more advanced wave theories such as the HOS method. Due to its simple implementation and negligible computational overhead compared to the analytical approach, the numerical approach is used exclusively in this study.

4.1.5. Boundary and Initial Conditions

In order to obtained a unique numerical solution, boundary conditions need to be specified at the surface boundary of the CFD domain. Reader is referred to Jasak [90] for a comprehensive overview and treatment of the various boundary conditions encountered in numerical simulations, while the present text focuses on boundary treatment specific to solution decomposition presented in Sec. 3.1.

Surface boundaries are divided into three distinct categories closely related to marine hydrodynamic flows:

1. Moving or stationary walls,

2. Far–field boundaries (including the bottom) and
3. Atmospheric boundary.

The first category of boundary conditions is related to all moving and stationary walls, where following boundary conditions apply:

- Perturbed velocity field $\mathbf{u}_P$ is set to the body velocity $\mathbf{u}_b$. It is important to note that $\mathbf{u}_b$ is calculated consistently from the grid motion fluxes, obeying the Space Conservation Law (SCL) [95];
- Incident velocity field $\mathbf{u}_I$ is set to zero, so that the total velocity $\mathbf{u} = \mathbf{u}_P + \mathbf{u}_I$ yields the body velocity $\mathbf{u}_b$;
- Zero gradient in the normal direction (von Neumann boundary condition) is specified for both the perturbed and incident LS fields, ψ_P and ψ_I, respectively;
- For consistency with the Dirichlet boundary condition for velocity, zero normal gradient is prescribed for the dynamic pressure field p_d.

The second category describes all far–field boundaries, characterised by the following boundary conditions:

- Perturbed velocity field $\mathbf{u}_P$ is set to zero;
- Incident velocity field $\mathbf{u}_I$ is set to the velocity field from the underlying incident wave model $\mathbf{u}_w$. Such a combination of boundary conditions for the perturbed and incident velocity field yields the total velocity field equal to the undisturbed incident flow;
- Perturbed LS field is set to zero and;
- Incident LS field is set to the signed distance field obtained from wave elevation from the underlying incident wave model ψ_w;
- Zero gradient in the normal direction is specified for the dynamic pressure field p_d.

Table 4.1: Overview of boundary conditions for the decomposition model.

Field	Body walls	Far–field	Atmosphere
$\mathbf{u}_P$	$\mathbf{u}_P = \mathbf{u}_b$	$\mathbf{u}_P = \mathbf{0}$	$\mathbf{u}_P = \mathbf{u}_i$ and $\nabla_n \mathbf{u}_P = 0$
$\mathbf{u}_I$	$\mathbf{u}_I = \mathbf{0}$	$\mathbf{u}_I = \mathbf{u}_w$	$\mathbf{u}_I = \mathbf{0}$ and $\nabla_n \mathbf{u}_I = 0$
ψ_P	$\nabla_n \psi_P = 0$	$\psi_P = 0$	$\nabla_n \psi_P = 0$
ψ_I	$\nabla_n \psi_I = 0$	$\psi_I = \psi_w$	$\nabla_n \psi_I = 0$
p_d	$\nabla_n p_d = 0$	$\nabla_n p_d = 0$	$p_d = p_{da}$

The third category is the atmospheric boundary, with following boundary conditions:

- Perturbed velocity field $\mathbf{u}_P$ has a combined boundary condition where the zero gradient in the normal direction is applied for the outflow (positive flux through boundary faces[1]) and the prescribed velocity obtained from boundary cell–centre $\mathbf{u}_i$ is applied for the inflow (negative flux through boundary faces);

- Incident velocity field $\mathbf{u}_I$ has a similar combined boundary condition where the velocity is prescribed to zero for the inflow (instead of cell–centre value $\mathbf{u}_i$);

- Zero normal gradient is prescribed for both perturbed and incident LS fields, ψ_P and ψ_I;

- Dynamic pressure p_d at the atmosphere is set to the atmospheric dynamic pressure value p_{da} calculated as $p_{da} = p_{d0} - 0.5\rho|\mathbf{u}|^2$ for the inflow condition. For the outflow, reference value p_{d0} is used, which is usually set to zero.

Boundary conditions for the three categories and all fields of interest are presented in Table 4.1 for clarity.

---

[1] Positive flux for the outflow through boundary faces follows the convention where the boundary face normal is pointing outwards of the computational domain.

For initial conditions, the perturbed velocity and LS fields are set to zero, while the incident velocity and LS fields are initialised from the underlying potential flow model. Ducrozet *et al.* [56] presented a temporal relaxation scheme for smoother simulation start–up, which has proved unnecessary in the present model. The dynamic pressure equation is solved at the beginning of the simulation in order to initialise the dynamic pressure jump corresponding to the incident location of the free surface.

4.2. Finite Volume Discretisation of Pressure Terms

The FV discretisation of dynamic pressure terms is outlined here, as they require special attention due to the presence of jump conditions at the free surface. Note that the dynamic pressure p_d and inverse density β are present only in two places, always appearing as a product: the source term in the combined momentum equation, Eqn. (4.1) and the pressure Laplacian in the pressure equation, Eqn. (4.8).

4.2.1. Gauss Gradient Discretisation

Using the discretised Gauss' theorem, second–order accurate discretisation of the pressure gradient with the β pre–factor for a control volume P reads:

$$\begin{aligned}\beta_P \nabla p_{dP} &= \frac{\beta_P}{V_P} \sum_f \mathbf{s}_f p_{df_\Gamma} \\ &= \frac{\beta_P}{V_P} \sum_f \mathbf{s}_f \left(f_x p_{dP} + (1 - f_x) p_{dN} \right)_\Gamma \,,\end{aligned} \tag{4.17}$$

where the second identity implies linear interpolation of cell centred–values and $f_x = \overline{fN}/\overline{PN}$ is the central–differencing weight [90]. Index Γ indicates that one–sided, second–order accurate extrapolation will be used to obtain p_{dP} and p_{dN} only for cells near the free surface, using the jump conditions given by Eqn. (2.46) and Eqn. (2.47). The procedure is described in detail in Sec. 4.3. following the GFM approach presented by Huang *et al.* [15].

4.2.2. Least Squares Gradient Discretisation

Following Jasak and Weller [96], least squares discretisation of the pressure gradient reads:

$$\beta_P \nabla p_{dP} = \beta_P \sum_f w_f^2 \mathbf{G}^{-1} \bullet \mathbf{d}_f (p_{dN} - p_{dP})_\Gamma \,, \tag{4.18}$$

where index Γ denotes one–sided extrapolation for p_{dN} and p_{dP} near the free surface, $w_f = 1/|\mathbf{d}_f|$ is the least squares weight and $\mathbf{G}$ is a 3×3 symmetric tensor defined as:

$$\mathbf{G} = \sum_f w_f^2 \mathbf{d}_f \mathbf{d}_f \,. \tag{4.19}$$

The least squares evaluation of the gradient is second–order accurate irrespective of the local arrangement of neighbouring cells [96], making it a favourable choice for unstructured, skewed grids. Both gradient schemes can be easily adapted to account for pressure jump conditions using one–sided extrapolates of pressure indexed by Γ.

4.2.3. Pressure Laplacian Discretisation

Following Demirdžić [97] and Jasak [90], compact–stencil FV discretisation of the pressure Laplacian on the l.h.s. of Eqn. (4.8) reads:

$$\begin{aligned} \sum_f \mathbf{s}_f \bullet \left(\frac{1}{a_P}\right)_f (\beta)_{f\Gamma} (\nabla p_d)_{f\Gamma} = {} & \sum_f \left(\frac{1}{a_P}\right)_f (\beta)_{f\Gamma} |\mathbf{s}_f| \frac{(p_{dN} - p_{dP})_\Gamma}{|\mathbf{d}_f|} \\ & + \sum_f \mathbf{k} \bullet \left(\frac{1}{a_P}\right)_f (\beta \nabla p_d)_f^o \,. \end{aligned} \tag{4.20}$$

The first term on the r.h.s. of Eqn. (4.20) denotes the implicit contribution arising from the surface normal gradient. The second term the explicit non–orthogonal correction, defined in terms face interpolated pressure gradient $(\beta \nabla p_d)_f^o$ from the previous time step or iteration. The pressure gradient term pre–multiplied by inverse density is continuous (see Eqn. (2.47)), making it safe to interpolate from cell centres to face centres. The non–orthogonal correction vector $\mathbf{k}$ is obtained using the over–relaxed approach described by Jasak [90]. The discretised pressure equation given by Eqn. (4.20) uses a compact computational stencil: control volume P interacts only with its immediate neighbours N (see Figure 4.1).

4.3. Discretisation of the Pressure Jump Conditions

As indicated in Sec. 4.2., FV discretisation of dynamic pressure terms near the free surface requires one–sided extrapolates of β and p_d, which were hitherto left undefined. Prior to a detailed derivation and analysis, following assumptions are made in the present model:

- cell P is considered wet or dry based on the sign of the signed distance field ψ: if $\psi_P > 0$ cell is wet and consequently, if $\psi_P < 0$, cell is dry;

- if a wet cell is completely surrounded by other wet cells, usual discretisation practices are sufficient and employed (see Sec. 4.1.), since the free surface is not located in the immediate vicinity of the cell. Similarly, a dry cell completely surrounded by other dry cells does not require special attention.

Such treatment is possible because arbitrary polyhedral FV method uses a compact computational stencil: interface corrections need to be employed for faces where $\psi_P > 0$ and $\psi_N < 0$ or vice versa (wet/dry owner/neighbour pairs, making the interaction of wet/dry cells symmetric).[2] Faces which require special treatment are called "interface faces" because the sharp free surface between two phases is located somewhere between cell centres P and N. Following this definition, a mathematical criterion for identification of interface faces can be written as:

$$\psi_P \psi_N < 0\,. \tag{4.21}$$

The criterion given by Eqn. (4.21) is used to mark all interface faces after solving the LS transport equation, Eqn. (4.10). An example of interface faces is presented in Figure 4.2 for a uniform 2–D grid for clarity. Note that it is not assumed that the interface coincides with the internal faces of the grid.

---

[2] If the free surface position is captured using VOF, PF or other methods, equivalent free surface detection criterion may be derived using definitions in Figure 2.1.

4.3.1. Computational Stencil Near the Free Surface

Before deriving one–sided extrapolates of β and p_d for interface faces using dynamic pressure jump conditions based on the GFM, definition of necessary geometrical data for the computational stencil at the free surface needs to be presented. Figure 4.3 shows the computational stencil at the free surface in 2–D for clarity, without loss of generalisation for polyhedral 3–D grids. Wet cell P shares a common interface face with dry cell N and $\mathbf{d}_f$ is the vector from cell centre P to cell centre N. Note that P may be wet or dry, and consequently N may be dry or wet: yielding an interface face between the two cells. Huang *et al.* [15] define the dimensionless distance to the free surface according to the LS field as:

$$\lambda = \frac{\psi_P}{\psi_P - \psi_N}, \tag{4.22}$$

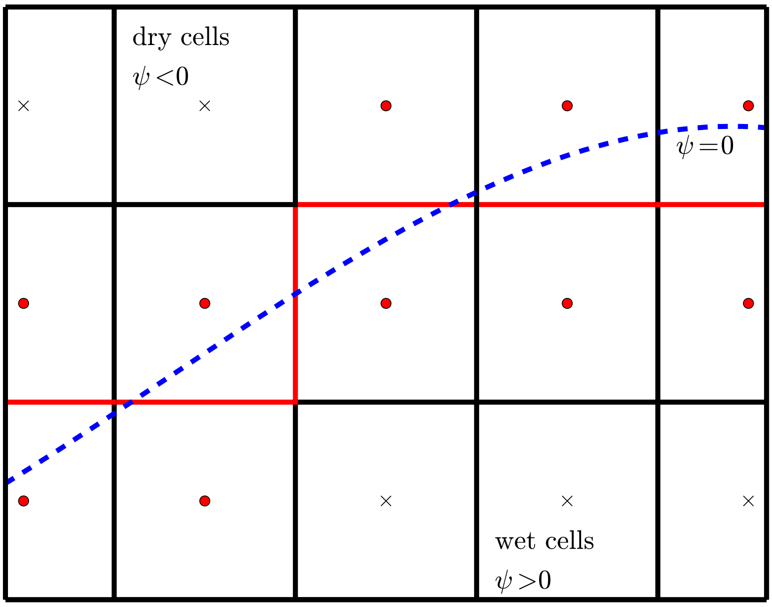

Figure 4.2: A layout of interface faces for a uniform 2–D grid. The dashed blue line denotes the free surface: $\psi = 0$. Wet cells are below the blue line: $\psi > 0$, while dry cells are above the blue line: $\psi < 0$. Interface faces are represented with red lines, where the interface face is defined as a face where the free surface is located between adjacent cell centres. Ordinary faces are denoted with black lines. Cell–centres sharing at least one interface face require interface–corrected extrapolation.

where ψ_P and ψ_N denote signed distance function to the interface at cell centres P and N, respectively. Note that λ may be easily defined in terms of the PF and VOF using Eqn. (2.37) and Eqn. (2.39). λ in Eqn. (4.22) is used to calculate the location of the free surface between wet/dry cell pairs:

$$\mathbf{x}_\Gamma = \mathbf{x}_P + \lambda \mathbf{d}_f \,. \tag{4.23}$$

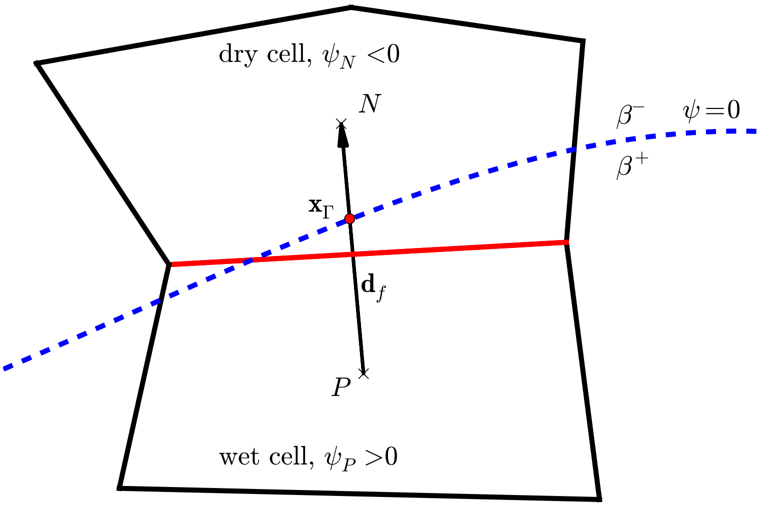

Figure 4.3: Compact polyhedral computational stencil near the free surface. Free surface is denoted with the blue dashed line. Interface face shared by cells P and N is marked with a red line, and the location of the free surface is denoted with $\mathbf{x}_\Gamma$.

Since the location of the interface given by Eqn. (4.23) is now defined, dynamic pressure jump condition, Eqn. (2.46) may be expanded as:

$$[p_d] = p_d^- - p_d^+ = (\rho^+ - \rho^-)\mathbf{g}\bullet\mathbf{x}_\Gamma = \mathcal{H} \,, \tag{4.24}$$

where p_d^- is the dynamic pressure at the infinitesimal distance towards the free surface at the lighter fluid (air) side, and p_d^+ its counterpart at the heavier fluid (water) side. ρ^+ is the density of the heavier fluid and ρ^- is the density of the lighter fluid by convention. For given free surface locations $\mathbf{x}_\Gamma$, the r.h.s. of Eqn. (4.24) can be calculated and stored as $\mathcal{H}$ for all interface faces at given time step. It is important to note that the discretisation given by Eqn. (4.24) is of the same order of accuracy as the solution of LS transport equation because the dimensionless distance λ is calculated using the signed distance field ψ in Eqn. (4.23).

4.3.2. One–Sided Pressure Extrapolation From the Wet Cell

The case where cell P is wet: $\psi_P > 0$ is considered first. In order to discretise the dynamic pressure gradient jump condition given by Eqn. (2.47), the procedure presented by Huang *et al.* [15] is used:

$$\begin{aligned}[][\beta \nabla p_d] &= \beta^- (\nabla p_d)^- - \beta^+ (\nabla p_d)^+ \\ &= \beta^- \frac{p_{dN} - p_d^-}{1-\lambda} - \beta^+ \frac{p_d^+ - p_{dP}}{\lambda} = 0\,,\end{aligned} \tag{4.25}$$

where the first term on the r.h.s. denotes a second–order accurate gradient evaluated in the air and the second term denotes a second–order accurate gradient evaluated in the water. Both gradients are evaluated at the free surface, in the normal direction from the free surface. Furthermore, p_d^- may be expressed from the discretised dynamic pressure jump condition, Eqn. (4.24) as:

$$p_d^- = p_d^+ + \mathcal{H}\,. \tag{4.26}$$

Inserting Eqn. (4.26) into Eqn. (4.25) yields the dynamic pressure at the free surface on the water side:

$$p_d^+ = \frac{\lambda\beta^-}{\overline{\beta_w}} p_{dN} + \frac{(1-\lambda)\beta^+}{\overline{\beta_w}} p_{dP} - \frac{\lambda\beta^-}{\overline{\beta_w}} \mathcal{H}\,, \tag{4.27}$$

where:

$$\overline{\beta_w} = \lambda\beta^- + (1-\lambda)\beta^+\,. \tag{4.28}$$

$\overline{\beta_w}$ represents the weighted inverse density from the water side, which depends on the distance to the free surface λ. Eqn. (4.28) follows from straightforward algebraic manipulations. Eqn. (4.27) defines the dynamic pressure at the free surface on the water side p_d^+ in terms of:

- dynamic pressure at the cell centre P, p_{dP},
- dynamic pressure at the cell centre N, p_{dN},
- density jump, $\mathcal{H}$.

Second–order accurate extrapolate of the dynamic pressure at dry cell centre N using values defined in water, can be calculated as:

$$p^+_{dN_\Gamma} = p^+_d + \frac{1-\lambda}{\lambda}\left(p^+_d - p_{dP}\right) \,, \tag{4.29}$$

where $(p^+_d - p_{dP})/\lambda$ represents normal dynamic pressure gradient at the free surface on the water side, used to extrapolate dynamic pressure from the free surface towards the dry cell centre N (hence $1-\lambda$). Substituting p^+_d given by Eqn. (4.27), Eqn. (4.29) takes the following reduced form after algebraic manipulations:

$$p^+_{dN_\Gamma} = \frac{\beta^-}{\overline{\overline{\beta_w}}} p_{dN} + \left(1 - \frac{\beta^-}{\overline{\overline{\beta_w}}}\right) p_{dP} - \frac{\beta^-}{\overline{\overline{\beta_w}}} \mathcal{H} \,. \tag{4.30}$$

Eqn. (4.30) defines a second–order accurate extrapolate of the dynamic pressure at the neighbouring cell N, obtained with the discretised jump conditions. Hence, the procedure uses jump conditions to define interface–corrected interpolation scheme for interface faces, incorporating the free surface effect in the combined governing equations: the momentum equation, Eqn. (4.1) and the pressure equation, Eqn. (4.8). Huang *et al.* [15] call this method the Ghost Fluid Method because $p^+_{dN_\Gamma}$ is defined using the one–sided extrapolation of dynamic pressure. $p^+_{dN_\Gamma}$ appears in pressure gradient discretisations: the Gauss gradient given by Eqn. (4.17) and the least squares gradient given by Eqn. (4.18); and the pressure Laplacian discretisation, Eqn. (4.20).

4.3.3. One–Sided Pressure Extrapolation From the Dry Cell

The case where cell P is dry: $\psi_P < 0$ is considered here. Dynamic pressure jump condition, Eqn. (4.24) is first used to express p^+_d as:

$$p^+_d = p^-_d - \mathcal{H} \,. \tag{4.31}$$

Discretisation of the dynamic pressure gradient jump condition, Eqn. (2.47) now yields:

$$\beta^+ \frac{p_{dN} - p^+_d}{1-\lambda} - \beta^- \frac{p^-_d - p_{dP}}{\lambda} = 0 \,. \tag{4.32}$$

Comparing Eqn. (4.32) with Eqn. (4.25), it can be observed that β^+ and β^- are interchanged, as could be expected since cell P is here considered dry. Inserting

Eqn. (4.31) into the discretised jump condition given by Eqn. (4.32) yields:

$$p_d^- = \frac{\lambda\beta^+}{\overline{\beta_d}} p_{dN} + \frac{(1-\lambda)\beta^-}{\overline{\beta_d}} p_{dP} + \frac{\lambda\beta^+}{\overline{\beta_d}}\mathcal{H}\,, \tag{4.33}$$

where:

$$\overline{\beta_d} = \lambda\beta^+ + (1-\lambda)\beta^-\,. \tag{4.34}$$

The weighted inverse densities for the dry cell, Eqn. (4.34) is not equal to the weighted inverse density for the wet cell, Eqn. (4.28): *i.e.* $\overline{\beta_d} \neq \overline{\beta_w}$. Following the same procedure as in Sec. 4.3.2., a second–order accurate extrapolate of the dynamic pressure at the wet cell centre N, using values defined in air, can be calculated as:

$$p_{dN_\Gamma}^- = p_d^- + \frac{1-\lambda}{\lambda}\left(p_d^- - p_{dP}\right)\,. \tag{4.35}$$

Substituting Eqn. (4.33) into Eqn. (4.35) yields:

$$p_{dN_\Gamma}^- = \frac{\beta^+}{\overline{\beta_d}} p_{dN} + \left(1 - \frac{\beta^+}{\overline{\beta_w}}\right) p_{dP} + \frac{\beta^+}{\overline{\beta_w}}\mathcal{H}\,. \tag{4.36}$$

Eqn. (4.36) defines a second–order accurate extrapolate of dynamic pressure if the cell P is dry and consequently, cell N is wet, where the jump conditions given by Eqn. (2.46) and Eqn. (2.47) have been used.

4.3.4. Overview of the Dynamic Pressure Extrapolation Formulae

As implied in Sec. 4.3.2. and Sec. 4.3.3., two distinct cases need to be distinguished in the dynamic pressure extrapolation using jump conditions:

- Cell P is wet and cell N is dry, yielding extrapolates $p_{dN_\Gamma}^+$ and $p_{dP_\Gamma}^-$:

$$p_{dN_\Gamma}^+ = \frac{\beta^-}{\overline{\beta_w}} p_{dN} + \left(1 - \frac{\beta^-}{\overline{\beta_w}}\right) p_{dP} - \frac{\beta^-}{\overline{\beta_w}}\mathcal{H}\,, \tag{4.37}$$

$$p_{dP_\Gamma}^- = \frac{\beta^+}{\overline{\beta_w}} p_{dP} + \left(1 - \frac{\beta^+}{\overline{\beta_w}}\right) p_{dN} + \frac{\beta^+}{\overline{\beta_w}}\mathcal{H}\,, \tag{4.38}$$

- Cell P is dry and cell N is wet, yielding extrapolates $p_{dN_\Gamma}^-$ and $p_{dP_\Gamma}^+$:

$$p_{dN_\Gamma}^- = \frac{\beta^+}{\overline{\beta_d}} p_{dN} + \left(1 - \frac{\beta^+}{\overline{\beta_d}}\right) p_{dP} + \frac{\beta^+}{\overline{\beta_d}}\mathcal{H}\,, \tag{4.39}$$

$$p_{dP_\Gamma}^+ = \frac{\beta^-}{\overline{\beta_d}} p_{dP} + \left(1 - \frac{\beta^-}{\overline{\beta_d}}\right) p_{dN} - \frac{\beta^-}{\overline{\beta_d}}\mathcal{H}\,. \tag{4.40}$$

Eqn. (4.38) and Eqn. (4.40) are derived in analogy to Eqn. (4.37) and Eqn. (4.39), where cells N and P are interchanged: *i.e.* looking from the cell N towards the cell P instead of looking from the cell P towards the cell N. Eqns. (4.37–4.40) require further comments related to code design. In OpenFOAM, cell P is denoted as owner of neighbouring cell N if the cell index P is lower than cell index N: *i.e.* $P < N$. Furthermore, cells P and N may be wet or dry, leading to expressions for:

- $p^{+}_{dN_\Gamma}$ - used when P is wet (N is dry) for discretisation regarding cell P;
- $p^{-}_{dP_\Gamma}$ - used when P is wet (N is dry) for discretisation regarding cell N;
- $p^{-}_{dN_\Gamma}$ - used when P is dry (N is wet) for discretisation regarding cell P;
- $p^{+}_{dP_\Gamma}$ - used when P is dry (N is wet) for discretisation regarding cell N.

Eqn. (4.37) and Eqn. (4.38) shall be used to prove the symmetry of the pressure Laplacian in Eqn. (4.8), which is a natural consequence due to the incompressibility condition, assumed in Ch. 2.

4.3.5. Extrapolation of Inverse Density

The discretised pressure equation Eqn. (4.8) requires face interpolated value of the inverse density, $(\beta)_{f_\Gamma}$. The inverse density is extrapolated in a straightforward way since the flow is considered incompressible:

- Extrapolation from the wet cell:

$$(\beta)_{f_\Gamma} = \beta^{+}\,, \tag{4.41}$$

- Extrapolation from the dry cell:

$$(\beta)_{f_\Gamma} = \beta^{-}\,. \tag{4.42}$$

Simple expressions for face–interpolated inverse densities are a direct consequence of the incompressibility condition, which assumes that the two fluids have constant densities.

4.4. Interface Contributions to the Discretised Pressure Terms

Sec. 4.2. presented general FV dicsretisation of dynamic pressure terms appearing in the discretised governing equations. Discretisation of the dynamic pressure gradient and Laplacian operators requires face–interpolated values for dynamic pressure and inverse density. Interface–corrected interpolation schemes based on second–order accurate discretisation of pressure jump conditions have been presented throughout Sec. 4.3. In what follows, the interface–corrected schemes with the discretised dynamic pressure gradient and Laplacian operators shall be combined, yielding interface–corrected, polyhedral discretisation of discontinuous fields.

4.4.1. Gauss Pressure Gradient Interface Contribution

In order to inspect the effect of interface–corrected schemes on the evaluation of the Gauss gradient, the case where cell P is wet is considered, while the case where cell P is dry can be easily derived following the same procedure. Eqn. (4.17) can be written in the following, split form:

$$
\begin{aligned}
\beta_P \nabla p_{dP} = & \frac{\beta_P}{V_P} \sum_{f\not\Gamma} \mathbf{s}_f \left(f_x p_{dP} + (1 - f_x) p_{dN} \right) \\
& + \frac{\beta_P}{V_P} \sum_{f\Gamma} \mathbf{s}_f \left(f_x p_{dP} + (1 - f_x) p^{+}_{dN_\Gamma} \right) \, ,
\end{aligned}
\tag{4.43}
$$

where $\sum_{f\not\Gamma}$ denotes summation over non–interface (completely in single phase, water or air) faces and $\sum_{f\Gamma}$ denotes summation over interface faces. The first sum on the r.h.s. of Eqn. (4.43) does not require special treatment: ordinary interpolation scheme is sufficient. Furthermore, if cell P is wet ($\psi_P > 0$), then $\beta_P = \beta^{+}$. For interpolation on interface faces (second sum on the r.h.s. of Eqn. (4.43)), $p^{+}_{dN_\Gamma}$ is used because cell P is wet (hence the index $+$ denoting extrapolation from water side). Interface contributions in the second sum are examined by inserting

Eqn. (4.37) into Eqn. (4.43), which yields:

$$\begin{aligned}\frac{\beta_P}{V_P}\sum_{f\Gamma}\mathbf{s}_f\left(f_x p_{dP}+(1-f_x)p^{+}_{dN_\Gamma}\right)=&\frac{1}{V_P}\sum_{f\Gamma}\mathbf{s}_f\beta^{+}p_{dP}\\&+\frac{1}{V_P}\sum_{f\Gamma}\mathbf{s}_f\frac{\beta^{+}\beta^{-}}{\overline{\beta_w}}(1-f_x)(p_{dN}-p_{dP}-\mathcal{H})\,.\end{aligned}\tag{4.44}$$

It is interesting to note that the first term on the r.h.s. of Eqn. (4.44) can be identified as first order extrapolation from cell P. Hence, the second term represents a second–order correction arising from the GFM treatment of the dynamic pressure jump conditions using second–order accurate schemes given by Eqn. (4.25) and Eqn. (4.29). Eqn. (4.44) only represents interface correction contributions for interface faces when the cell P is wet, while a similar expression can be obtained for a dry cell using $p^{-}_{dN_\Gamma}$ given by Eqn. (4.39).

4.4.2. Least Squares Gradient Interface Contribution

Following the same procedure as in Sec. 4.4.1., the least squares gradient discretisation for the wet cell P, Eqn. (4.18) is divided into two sums:

$$\begin{aligned}\beta_P\nabla p_{dP}=&\frac{\beta_P}{V_P}\sum_{f\not{\Gamma}}\mathbf{l}_f\left(p_{dN}-p_{dP}\right)\\&+\frac{\beta_P}{V_P}\sum_{f\Gamma}\mathbf{l}_f\left(p^{+}_{dN_\Gamma}-p_{dP}\right)\,,\end{aligned}\tag{4.45}$$

where $\mathbf{l}_f = w_f^2\mathbf{G}^{-1}\mathbf{\cdot}\mathbf{d}_f$ is the least squares vector. Inserting Eqn. (4.37) into the second sum on the r.h.s. of Eqn. (4.45) yields:

$$\frac{\beta_P}{V_P}\sum_{f\Gamma}\mathbf{l}_f\left(p^{+}_{dN_\Gamma}-p_{dP}\right)=\sum_{f\Gamma}\mathbf{l}_f\frac{\beta^{+}\beta^{-}}{\overline{\beta_w}}(p_{dN}-p_{dP}-\mathcal{H})\,,\tag{4.46}$$

where $\beta_P = \beta^+$ is used because cell P is wet (denoted with superscript +).

4.4.3. Interface Contribution in the Pressure Laplacian

Detailed inspection of the discretised dynamic pressure equation, Eqn. (4.8) in Sec. 4.1.2., led to the conclusion that interface–corrected interpolation schemes should preserve the symmetric property of the discretised Laplacian operator, leading to a symmetric matrix. The implicit part of the pressure equation (Laplacian operator) given by Eqn. (4.20) can be divided into two sums as in Sec. 4.4.2. and Sec. 4.4.3.:

$$\begin{aligned}\sum_f \left(\frac{1}{a_P}\right)_f (\beta)_{f_\Gamma} |\mathbf{s}_f| \frac{(p_{dN} - p_{dP})_\Gamma}{|\mathbf{d}_f|} &= \sum_{f\not\Gamma} \left(\frac{1}{a_P}\right)_f (\beta)_f |\mathbf{s}_f| \frac{p_{dN} - p_{dP}}{|\mathbf{d}_f|} \\ &+ \sum_{f\Gamma} \left(\frac{1}{a_P}\right)_f (\beta)_{f_\Gamma} |\mathbf{s}_f| \frac{p^+_{dN_\Gamma} - p_{dP}}{|\mathbf{d}_f|} \,,\end{aligned} \tag{4.47}$$

where wet owner cell P is considered. The first sum on the r.h.s. of Eqn. (4.47) denotes fully wet or fully dry faces, where interface corrections are not needed and the resulting matrix contributions are symmetric as in single–phase incompressible flows. Considering a single interface contribution for a wet owner cell P and a dry neighbour cell N pair, by inserting Eqn. (4.37) into Eqn. (4.47) yields:

$$\left(\frac{1}{a_P}\right)_f (\beta)_{f_\Gamma} |\mathbf{s}_f| \frac{p^+_{dN_\Gamma} - p_{dP}}{|\mathbf{d}_f|} = \left(\frac{1}{a_P}\right)_f \frac{|\mathbf{s}_f|}{|\mathbf{d}_f|} \frac{\beta^+\beta^-}{\overline{\beta_w}} \left(p_{dN} - p_{dP} - \mathcal{H}\right) \,, \tag{4.48}$$

where $(\beta)_{f_\Gamma} = \beta^+$ because cell P is considered wet (denoted with superscript $+$). From Eqn. (4.48), a diagonal contribution for cell P in discretisation of the pressure Laplacian at an interface face can be identified as:

$$d_P = -\left(\frac{1}{a_P}\right)_f \frac{|\mathbf{s}_f|}{|\mathbf{d}_f|} \frac{\beta^+\beta^-}{\overline{\beta_w}} \,. \tag{4.49}$$

The off–diagonal matrix coefficient in the upper triangle accounting for the influence of neighbouring cell N to cell P can be identified as:

$$a_{PN} = \left(\frac{1}{a_P}\right)_f \frac{|\mathbf{s}_f|}{|\mathbf{d}_f|} \frac{\beta^+\beta^-}{\overline{\beta_w}} \,. \tag{4.50}$$

Furthermore, an additional source term is present on the r.h.s. in the pressure Laplacian due to discretisation of jump conditions:

$$S_P = \left(\frac{1}{a_P}\right)_f \frac{|\mathbf{s}_f|}{|\mathbf{d}_f|} \frac{\beta^+\beta^-}{\overline{\beta_w}} \mathcal{H} \,. \tag{4.51}$$

Proposition 4.1. *The off–diagonal contributions arising from the interface–corrected discretisation of the Laplacian operator in the pressure equation are symmetric:*

$$a_{PN} = a_{NP} \,, \tag{4.52}$$

producing a symmetric matrix as in incompressible single–phase flows.

Proof. In order to prove the symmetry of the resulting discretised Laplacian operator obtained with the GFM treatment of jump conditions, an interface face contribution to the pressure equation for neighbouring cell N is considered:

$$\left(\frac{1}{a_P}\right)_f (\beta)_{f_\Gamma} |\mathbf{s}_f| \frac{p^-_{dP_\Gamma} - p_{dN}}{|\mathbf{d}_f|} = \left(\frac{1}{a_P}\right)_f \frac{|\mathbf{s}_f|}{|\mathbf{d}_f|} \frac{\beta^+\beta^-}{\overline{\beta_w}} \left(p_{dP} - p_{dN} + \mathcal{H}\right) , \qquad (4.53)$$

where Eqn. (4.38) is used for $p^-_{dP_\Gamma}$ and $(\beta)_{f_\Gamma} = \beta^-$ because cell N is considered dry (denoted with superscript $-$). The off–diagonal matrix coefficient in the lower triangle accounting for the influence of owner cell P to neighbouring cell N can be identified as:

$$a_{NP} = \left(\frac{1}{a_P}\right)_f \frac{|\mathbf{s}_f|}{|\mathbf{d}_f|} \frac{\beta^+\beta^-}{\overline{\beta_w}} \, . \qquad (4.54)$$

Comparison of the upper matrix coefficient given by Eqn. (4.50) and the lower matrix coefficient given by Eqn. (4.54) proves the symmetry of the matrix indicated in Eqn. (4.52), as originally postulated in Sec. 4.1.2.. ☐

Inspecting Eqn. (4.42), the diagonal matrix contribution for cell N can be identified as:

$$d_N = -\left(\frac{1}{a_P}\right)_f \frac{|\mathbf{s}_f|}{|\mathbf{d}_f|} \frac{\beta^+\beta^-}{\overline{\beta_w}} \, . \qquad (4.55)$$

By inspecting following equation pairs: Eqn. (4.54) and Eqn. (4.55); Eqn. (4.50) and Eqn. (4.49), one can observe that the matrix diagonal can be reconstructed using off–diagonal matrix coefficients as:

$$d_P = -\sum_f a_{PN} \, , \qquad (4.56)$$

as in single–phase incompressible flow, where $\sum_f$ is the summation over all neighbours of cell P: both for interface faces and non–interface faces. Eqn. (4.56) complies with the conservative nature of the FV discretisation and the symmetry property of the Laplacian operator.

Furthermore, the additional source term for the dry cell N can be identified as:

$$S_N = -\left(\frac{1}{a_P}\right)_f \frac{|\mathbf{s}_f|}{|\mathbf{d}_f|} \frac{\beta^+\beta^-}{\overline{\beta_w}} \mathcal{H} \, . \qquad (4.57)$$

It is interesting and important to note that additional source terms arising from dynamic pressure jump conditions at interface faces are antisymmetric, which can be easily seen by comparing Eqn. (4.51) and Eqn. (4.57). Hence, both source terms: S_P and S_N may be represented by an additional flux through the interface face that will be balanced by the dynamic pressure jump after solving the pressure equation.

Although the derivation presented here is valid for wet owner cell P and dry neighbour cell N pair, equivalent properties can be easily derived for dry owner cell P and wet neighbour cell N pair.

4.5. Modelling of Rigid Body Motion

Along with the presented decomposition model with GFM for two–phase incompressible and turbulent fluid flow, rigid body motion equations are introduced in Sec. 4.5.1. in order to simulate arbitrary Six Degrees–of–Freedom (6–DOF) body motion. A coupling strategy is outlined in Sec. 4.5.2., while a detailed solution algorithm will be presented in Sec. 4.6.

4.5.1. Six Degrees–of–Freedom Rigid Body Motion Equations

The fluid flow equations are solved in the global, inertial reference frame $\mathcal{O}x_g y_g z_g$. Although it is possible to solve both translational and rotational motion of a body in the global reference frame, such a procedure would result in a time–dependent moment of inertia tensor, $\mathbf{I}$ [98]. Following Carrica *et al.* [16], a moving, body–fixed reference frame $\mathcal{O}x_b y_b z_b$ is introduced, making the moment of inertia tensor constant and diagonal. Both global and body–fixed reference frames are Cartesian, right–handed coordinate systems. The origin of the body–fixed reference frame is positioned at the Centre–of–Gravity (COG) of the body, while the origin of the global reference frame is arbitrary. Orientation of the coordinate axes is arbitrary, although following definitions are usually used for the body–fixed reference frame (which at $t = 0$ often corresponds to the global reference frame):

- x axis is positive from front perpendicular (F.P.) towards aft perpendicular (A.P.) of a ship in the longitudinal direction,

- y axis is positive from portside to starboard in the transversal direction,
- z axis is positive upwards in the vertical direction.

Hence, following 6–DOF may be defined:

- Translational motions:
    1. Surge: translation along x axis,
    2. Sway: translation along y axis,
    3. Heave: translation along z axis,
- Rotational motions:
    1. Roll: rotation around x axis,
    2. Pitch: rotation around y axis,
    3. Yaw: rotation around z axis.

Detailed derivation of rigid body motion equations can be easily found in many textbooks on classical mechanics [99], hence, only a short summary is given here. The Newtonian equations governing the translational motions are formulated in the global reference frame in order to avoid inclusion of fictional forces [99]:

$$\frac{\mathrm{d}(m\mathbf{v}_g)}{\mathrm{d}t} = m\dot{\mathbf{v}}_g = m\mathbf{a}_g = \mathbf{F}_g\,, \tag{4.58}$$

where m is the mass of the rigid body, which is considered constant. $\mathbf{v}_g$ is the velocity of the rigid body where $\dot{\mathbf{v}}_g$ denotes temporal derivative, *i.e.* acceleration of the body $\mathbf{a}_g$. $\mathbf{F}_g$ is the external force acting on the rigid body in the global reference frame, which shall be defined later in the text. Given $\mathbf{F}_g$ and constant mass of the body, acceleration can be calculated directly from Eqn. (4.58). Following ordinary differential equations are used to calculate the velocity and position of the body in the global reference frame:

$$\dot{\mathbf{v}}_g = \mathbf{a}_g\,, \tag{4.59}$$

$$\dot{\mathbf{x}}_g = \mathbf{v}_g\,, \tag{4.60}$$

where $\mathbf{x}_g$ denotes the position of the body. Eqn. (4.59) and Eqn. (4.60) present 6 ordinary differential equations governing the translational motion of the body in the global reference frame.

As already indicated, the Euler equations governing the rotational motions are formulated in the body–fixed reference frame in order to avoid temporal variation of the moment of inertia tensor. Since the body–fixed reference frame presents the 3–D principal orthogonal coordinates, Euler equations can be written as:

$$\boldsymbol{\alpha}_b = \dot{\boldsymbol{\omega}}_b = \mathbf{I}_b^{-1} \bullet (\mathbf{T}_b - \boldsymbol{\omega}_b \times (\mathbf{I}_b \bullet \boldsymbol{\omega}_b)) \ , \tag{4.61}$$

where $\mathbf{I}_b$ represents constant in time, diagonal inertia tensor of the body in principal coordinate axes. $\boldsymbol{\alpha}_b$ is the rotational acceleration of the body in body–fixed reference frame and $\boldsymbol{\omega}_b$ is the corresponding rotational velocity. $\mathbf{T}_b$ represents external torque acting on the body. The first identity in Eqn. (4.61) is used to calculate the rotational velocity of the body $\boldsymbol{\omega}_b$ given the rotational acceleration.

In order to prevent the "gimbal lock" phenomena, quaternion formulation of rotations is used instead of Euler angles. The reader is referred to Coutsias and Romero [98] for a good overview of quaternion based rotations with rigid body dynamics equations in quaternion form. The governing equations for rotational angles are briefly presented here in the expanded form for clarity:

$$\begin{pmatrix} \dot{q}_0 \\ \dot{q}_1 \\ \dot{q}_2 \\ \dot{q}_3 \end{pmatrix} = \frac{1}{2} \begin{pmatrix} q_0 & -q_1 & -q_2 & -q_3 \\ q_1 & q_0 & -q_3 & -q_2 \\ q_2 & q_3 & q_0 & -q_1 \\ q_3 & -q_2 & q_1 & q_0 \end{pmatrix} \begin{pmatrix} 0 \\ \omega_{1b} \\ \omega_{2b} \\ \omega_{3b} \end{pmatrix} , \tag{4.62}$$

where q_i is the i–th component of a quaternion q and ω_{ib} is the corresponding component of a rotational velocity in the body–fixed reference frame. Quaternion q defines the transformation from global to body–fixed reference frame and vice versa [98].

External Forces and Torques

As the fluid flow equations are solved in the global reference frame, forces and torques acting on the rigid body are written in the global reference frame g:

$$\mathbf{F}_g = \mathbf{F}_{g,p} + \mathbf{F}_{g,v} + \mathbf{F}_{g,m}(\mathbf{x}, \mathbf{v}, \mathbf{q}, \boldsymbol{\omega}) + m\mathbf{g} \, , \tag{4.63}$$

$$\mathbf{T}_g = \mathbf{T}_{g,p} + \mathbf{T}_{g,v} + \mathbf{T}_{g,m}(\mathbf{x}, \mathbf{v}, \mathbf{q}, \boldsymbol{\omega}) \, , \tag{4.64}$$

where index p denotes the pressure part of the fluid force, index v denotes the viscous part and index m denotes restoring and damping forces of a mooring system. Note that the forces and torques of the mooring system may be written as a general function of rigid body displacements and velocities. Pressure and viscous fluid forces and torques are calculated using the pressure and velocity fields:

$$\mathbf{F}_{g,p} = \sum_{bf} \mathbf{s}_f p_f \, , \tag{4.65}$$

$$\mathbf{F}_{g,v} = \sum_{bf} \rho_f \nu_{e,f} \mathbf{s}_f \bullet \mathbf{S}^* \, , \tag{4.66}$$

$$\mathbf{T}_{g,p} = \sum_{bf} \mathbf{r}_f \times \mathbf{s}_f p_f \, , \tag{4.67}$$

$$\mathbf{T}_{g,v} = \sum_{bf} \mathbf{r}_f \times \left(\rho_f \nu_{e,f} \mathbf{s}_f \bullet \mathbf{S}^* \right) \, , \tag{4.68}$$

where $\sum_{bf}$ denotes summation over all body faces and $\mathbf{s}_f$ is oriented outside of the fluid domain (towards interior of the body). $\mathbf{S}^*$ represents the deviatoric part of the tensor S, which is defined as twice the symmetric part of the $\nabla \mathbf{u}$ tensor. r_f is the distance vector from a boundary face to COG of the rigid body. As indicated in Eqn. (4.59) and Eqn. (4.60), the translational motions are solved in the global reference frame, hence the external force acting on the body given by Eqn. (4.63) can be directly used without transformation to calculate the corresponding translational acceleration in Eqn. (4.58). In contrast, the rotational equations are formulated in the body–fixed reference frame, Eqn. (4.61) and Eqn. (4.62), hence the external torque acting on the body is transformed from the global frame Eqn. (4.64) into the body–fixed frame using quaternions from the previous time step or iteration, making the fluid flow–6–DOF coupling explicit.

Numerical Integration

To summarise, rigid body motion equations include 13 Ordinary Differential Equations (ODEs) that need to be solved along with the fluid flow equations given in Sec. 4.1.:

- 6 equations for rigid body translations (3 for velocity, Eqn. (4.59) and 3 for displacement, Eqn. (4.60),
- 7 equations for rigid body rotations (3 Euler equations for rotational velocity, Eqn. (4.61) and 4 for rotation angles using quaternions, Eqn. (4.62)

13 ODEs are solved with explicit adaptive step size Embedded Runge–Kutta 5th order method with Cash–Karp parameters [100]. The cost of numerical integration of additional 13 ODEs is negligible compared to the fluid flow solution.

4.5.2. Coupling Between Fluid Flow and Six Degrees–of–Freedom

The solution of rigid body motion ODEs yields body displacement and velocity. In the present model, the displacement is used to move the computational grid as a rigid body. The appealing property of such approach is the negligible CPU time overhead compared to automatic mesh deformation strategies [38, 101]. The approach also avoids possible mesh quality deterioration during automatic mesh deformation for large amplitude motions. The drawback of this approach is closely related to meshing strategies where the mesh is usually heavily graded and fine in the free surface region. Thus, large amplitude motions might cause the free surface to come into the coarse region, possibly impairing the quality of results. Due to rigid body motion, CVs in the computational grid are moving in space and time. The motion of the grid is taken into account via Reynolds transport theorem for an arbitrarily moving CV, where the grid motion flux for each face is calculated using the SCL [95]. The grid fluxes are then subtracted from the absolute convecting flux calculated in the global reference frame, as in the Arbitrary Lagrangian–Eulerian (ALE) formulation [102]. Apart from the grid motion, rigid body velocity is calculated and specified as a boundary condition for all boundary faces on the rigid body.

As the fluid flow provides external forces on the rigid body, and the rigid body motion provides grid motion and prescribed velocity boundary conditions on the body boundary, a two–way coupling strategy is necessary. In general, two distinct approaches for Fluid–Structure Interaction (FSI) exist:

1. Monolithic approach [103], where all governing equations are solved in a single system,
2. Partitioned approach [104], where fluid and solid governing equations are solved separately, while performing outer iterations to strongly couple the two solutions.

The monolithic approach would require the solution of the momentum, pressure, LS transport and rigid body motion equations within a single system, which represents a challenging task. Hence, the partitioned approach is commonly used and more suitable for marine hydrodynamics since the fluid flow equations are often solved using segregated solution algorithms. The fluid flow and rigid body motion equations are then solved separately, performing outer iterations within a time step. Simonsen *et al.* [105] report using 5 fluid flow–6–DOF iterations per time step for heave and pitch simulations of a KCS in regular head waves. A detailed flow chart of the solution algorithm is presented in the following section, Sec. 4.6.

4.6. Segregated Solution Algorithm for Nonlinear Equation Sets

Governing equations for incompressible, turbulent, free surface flow with a moving body comprise:

- Momentum equation for $\mathbf{u}_P$, Eqn. (4.2);
- Pressure equation for p_d, Eqn. (4.8);
- LS transport equation for ψ_P, Eqn. (4.10);
- 6–DOF rigid body motion equations, Eqn. (4.58), (4.60), (4.61) and (4.62).

Since the present model focuses on transient flows, a segregated Pressure Implicit with Splitting of Operator (PISO) algorithm [106] is used for pressure–velocity coupling. Pressure and velocity are also strongly coupled with the LS signed distance field that is used to define interface faces. On interface faces, interface–corrected schemes for pressure terms are employed, yielding highly nonlinear dependence of the pressure and velocity fields with the free surface location. Furthermore, the whole fluid flow solution nonlinearly depends on the rigid body motion via relative grid fluxes and velocity boundary condition on the moving body. Consequently, the external forces and torques for the 6–DOF ODEs are obtained from the fluid flow solution, integrating the pressure and viscous forces on the body. In present study, a partitioned approach is used where the pressure–velocity system is coupled with free surface and 6–DOF in an outer, Semi–Implicit Method for Pressure Linked Equations (SIMPLE) algorithm [93] loop. In OpenFOAM, the combined PISO–SIMPLE algorithm for nonlinear transient free surface flows is often called the PIMPLE algorithm.

The flow chart of the segregated solution algorithm for the nonlinear, coupled equation sets is presented in Figure 4.4. At the beginning of a time step, an outer SIMPLE loop starts by solving the 6–DOF equations and the grid is moved as a rigid body accordingly. As the grid is moved, cell–centred values of incident velocity field $\mathbf{u}_I$ and incident LS field ψ_I are evaluated analytically from the underlying potential flow wave model. After the update of incident fields, PISO loop starts by predicting the perturbed velocity field $\mathbf{u}_P$, Eqn. (4.2) with the value of pressure gradient from the previous iteration. The dynamic pressure equation, Eqn. (4.8) is formulated and solved, taking into account pressure–density coupling through interface jump conditions obtained with the GFM. New estimate of the dynamic pressure field with jumps across the free surface is then used to correct the perturbed velocity field with Eqn. (4.6) and calculate the total conservative face fluxes with Eqn. (4.9). PISO loop is repeated until a satisfactory convergence is achieved by specifying a run–time modifiable number of PISO correctors. On satisfactory convergence of the PISO loop, diffusion parameter b required for the LS transport equation is updated with Eqn. (4.16) and the perturbed LS field ψ_P is obtained by solving Eqn. (4.10). The total LS field ψ, denoting the current free surface location, is updated and used to mark interface faces using criterion defined by Eqn. (4.21). The new set of interface faces along with the necessary hydrostatic jumps $\mathcal{H}$ given by Eqn. (4.24) shall be used in next pressure–velocity corrector step to discretise dynamic pressure terms in governing equations. Furthermore, additional turbulence modelling equations are solved and the effective kinematic viscosity of the two–phase mixture is calculated using Eqn. (2.40). The convergence of the outer, SIMPLE loop is tested based on a user specified number of SIMPLE correctors, where a study on required number of outer correctors for seakeeping applications shall be presented in Ch. 7.

In present study, preconditioned Krylov subspace linear system solvers [107] are used: Connjugate Gradient (CG) method [108] for the symmetric pressure equation and stabilised Bi–Conjugate Gradient Stabilised (BiCGStab) [109] for other equations with strong hyperbolic and local characters:

- LS transport equation, Eqn. (4.10);
- Combined momentum equation, Eqn. (4.2);
- Turbulence modelling equations.

The Cholesky preconditioner is used alongside CG solver and the Incomplete Lower–Upper (ILU) preconditioner is used with the BiCGStab; both without fill–in in order to preserve the static sparseness pattern of the matrix.

4.7. Closure

The FV discretisation of nonlinear free surface flow equations has been presented. The discretisation of momentum, pressure and LS equation has been briefly outlined, followed by after notes regarding explicit treatment of explicit terms related to incident potential flow field. Solution and domain decomposition via SWENSE approach and relaxation zones, respectively, enabled general definition of boundary and initial conditions for three types of boundaries: possibly moving body, far–field and atmosphere.

The FV discretisation of pressure terms is presented in detail due to the presence of discontinuities in dynamic pressure and density across the free surface. For pressure gradient in the momentum equation, Gauss discretisation and least

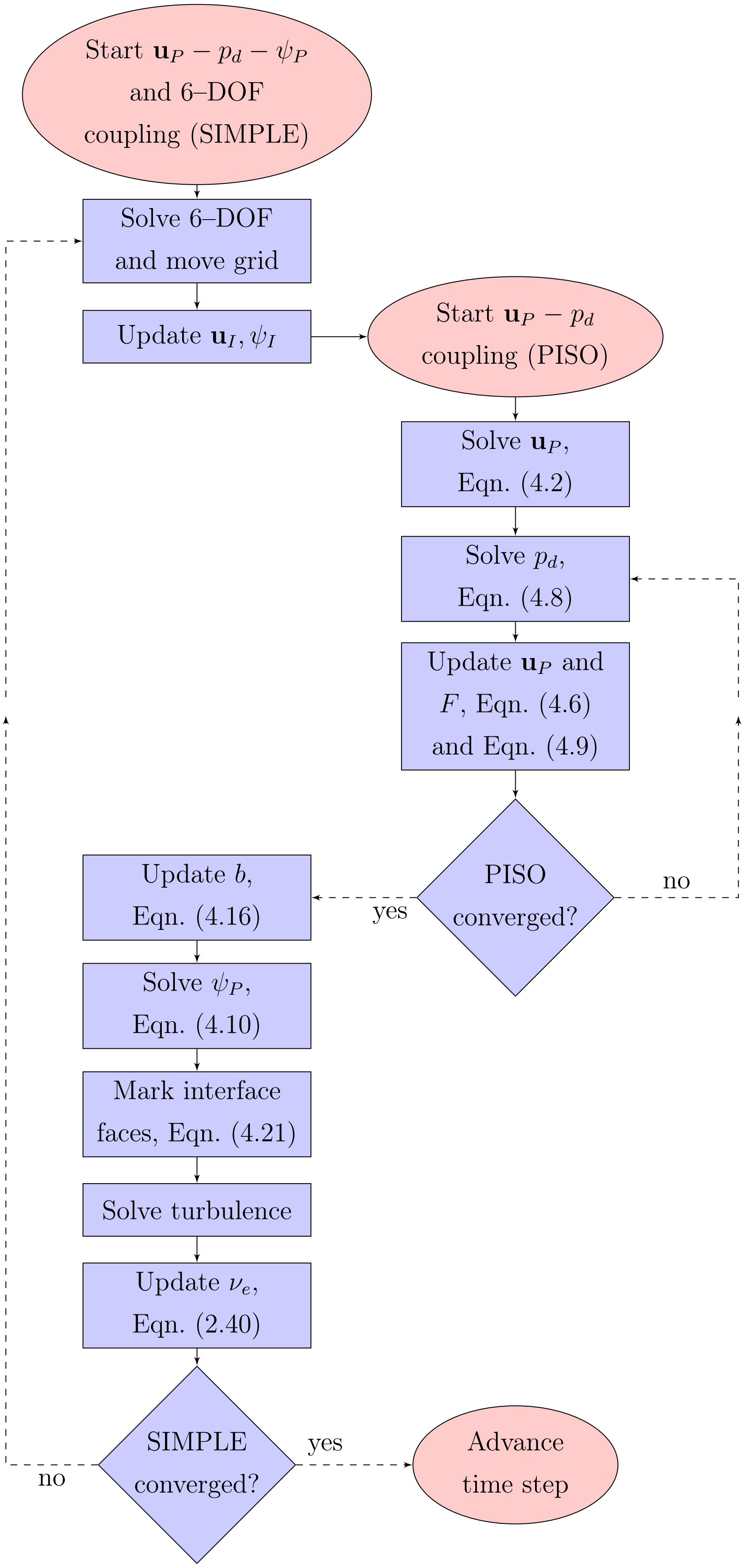

Figure 4.4: Flow chart of the segregated solution algorithm.

squares discretisation is presented, whereas for the pressure Laplacian, a compact stencil approach with explicit non–orthogonal correction is discussed.

In order to accurately represent the free surface in the present model, the FV discretisation of pressure terms requires interpolation schemes that account for dynamic pressure and density jumps across the sharp interface, which are obtained using the GFM. A procedure to calculate the free surface location using a compact computational stencil in the polyhedral FV framework is presented in detail to facilitate the derivation of one–sided pressure extrapolates using second–order accurate discretisation of jump conditions. An overview of extrapolation formulae is presented for the reader in order to simplify the implementation of the model in the existing FV based CFD code.

The one–sided extrapolates obtained via GFM are then used to incorporate the free surface via jump conditions into dynamic pressure terms. Final discretisation formulae for the Gauss and least squares gradient discretisation are presented, while the special attention has been given to the pressure Laplacian. As the elliptic pressure equation is most often the most time consuming part of an incompressible CFD algorithm, the symmetry property of the matrix needed to be addressed carefully. As the pressure equation is the Poisson equation, and the Laplacian operator is symmetric, the resulting discretisation should yield a symmetric matrix. The symmetry property of the final pressure equation using interface–corrected schemes has been proved, implying consistent discretisation of jump conditions across the free surface. The symmetry property of the matrix is also important from the numerical point of view: using specialised linear system solvers for the symmetric matrices often offers double savings in terms of CPU and memory requirements. Note that the present model is not exclusive for water and air flows, although that specific nomenclature has been used for simplicity. The model should be applicable to an arbitrary pair of immiscible fluids where surface tension effects and tangential stress balance at the free surface may be neglected.

After detailed discretisation of governing PDEs for free surface flow, rigid body motion modelling is addressed in order to successfully simulate arbitrarily moving bodies. 6–DOF equations are briefly presented, where the translational motions are formulated in the global inertial reference frame and the rotational motions are formulated in the body–fixed reference frame using quaternions in order to prevent gimbal lock phenomena. A partitioned approach for highly nonlinear 6–DOF and fluid flow coupling based on Picard iterations is discussed and the grid motion strategy is briefly presented.

Finally, a segregated (partitioned) solution algorithm based on a combination of PISO algorithm for pressure–velocity coupling and SIMPLE algorithm for coupling of the pressure–velocity system with the free surface and rigid body motion is presented. The approach iteratively resolves the nonlinear coupling between governing equation sets through multiple outer iterations in a given time step. A flow chart of the solution algorithm is presented, referencing the underlying equations throughout the text in order to simplify implementation of the model.

5. Validation and Verification Procedure

5.1. Overview

Ch. 4. presented the numerical treatment of the fully nonlinear, two–phase, incompressible and turbulent fluid flow, coupled with the 6–DOF rigid body motion equations. The basic FV discretisation is presented for all governing equations, where the special attention is given to discretisation of pressure terms. The most significant part of Ch. 4. describes the treatment of pressure jump conditions via GFM in order to obtain interface–corrected interpolation schemes, taking into account the discontinuity of dynamic pressure and density at the free surface. Finally, rigid body motion modelling is discussed and the segregated solution algorithm used to strongly resolve the tight inter–equation coupling of nonlinear equation set is presented.

This chapter presents a brief overview of the Validation and Verification (V&V) procedures used to validate and verify the developed numerical framework. The validation is simply achieved by comparing the present CFD results with analytical, other numerical and experimental data, where the absolute error is defined as:

$$E_a = S_R - S_{CFD} \, , \tag{5.1}$$

where S_R is the referent solution (analytical, other numerical or experimental results), and S_{CFD} is the solution obtained with the present CFD model. It is often more convenient to compare the results in terms of relative errors, defined as:

$$E_r = \frac{E_a}{S_R} \, . \tag{5.2}$$

Note that the relative error defined by Eqn. (5.2) is often reported in percentages.

Apart from validation, the verification needs to be carried out in order to ensure consistent behaviour of the implemented numerical algorithm and to assess corresponding uncertainties, which shall be outlined in later text.

5.2. Uncertainty Assessment

In order to estimate various numerical uncertainties associated with: temporal resolution, grid refinement, periodicity, *etc.*, guidelines presented by Roache [110] and Stern *et al.* [111] are used in this study. Based on three different CFD solutions with varying time step, grid refinement, *etc.*, discriminating ratio is calculated as:

$$R = \frac{\epsilon_{fm}}{\epsilon_{mc}} = \frac{S_f - S_m}{S_m - S_c}\,, \tag{5.3}$$

where indices f, m and c denote fine–, medium– and coarse–resolved solutions, respectively. In the grid refinement study, f stands for the fine grid solution, m for the medium grid and c for the coarse grid. Similarly for the time step resolution study, f corresponds to the smallest fine step, m to the medium and c for the largest time step. This idea may be easily generalised to other sensitivity studies where some parameters (numerical grid, time step) are varied using successive refinement/coarsening. Based on R defined by Eqn. (5.3), four different convergence types may be observed (see *e.g.* Eca and Hoekstra [112]):

- Convergence:
    1. Monotone convergence for $0 < R < 1$,
    2. Oscillatory convergence for $R < 0$ and $|R| < 1$.
- Divergence:
    3. Monotone divergence for $R > 1$,
    4. Oscillatory divergence for $R < 0$ and $|R| > 1$.

For monotone convergence, the numerically achieved order of accuracy is determined using Richardson extrapolation:

$$p = \frac{\ln(\epsilon_{fm}/\epsilon_{mc})}{\ln r}\,, \tag{5.4}$$

where r is the refinement ratio which should be kept constant between fine/medium and medium/coarse solutions. Using the achieved order of accuracy p, the grid uncertainty for monotone convergence is calculated as:

$$U = F_s \frac{|\epsilon_{fm}|}{r^p - 1}\,, \tag{5.5}$$

where $F_s = 1.5$ is the safety factor used for all test cases in this study.

In case of oscillatory convergence, the uncertainty is calculated following Stern *et al.* [111]:

$$U = F_s 0.5 |S_U - S_L| \,, \tag{5.6}$$

where S_U and S_L represent maximum (upper) and minimum (lower) result among all solutions (fine, medium and coarse).

In case of divergence, both monotone and oscillatory, the uncertainty cannot be formally assessed. However, following Simonsen *et al.* [105], the uncertainty is practically estimated using the largest deviation among multiple solutions:

$$U = F_s |S_U - S_L| \,. \tag{5.7}$$

Eqn. (5.5), (5.6) and (5.7) provide formulae for assessing numerical uncertainties for monotonically converging, oscillatory converging and diverging solutions. Within a given study (grid refinement, temporal resolution), as long as the refinement parameter may be defined, uncertainty with respect to this particular study may be assessed. Along with grid refinement and temporal resolution studies, this idea shall be exploited for some other sensitivity studies.

Throughout this study, the normalised numerical uncertainties are always reported instead of dimensioned variables:

$$\overline{U} = \frac{U}{S_f} \tag{5.8}$$

where S_f is the solution obtained with fine resolution (finest grid or smallest time step size). Furthermore, $\overline{U}$ shall be reported in percentages for convenience.

5.2.1. Grid Uncertainty Assessment

The grid uncertainty assessment is performed for majority of test cases by performing simulations with at least three computational grids. The uniform refinement ratio r is used for test cases with structured grids, while the approximately uniform refinement ratio is used for arbitrary polyhedral, unstructured grids. For 2–D grids, a refinement ratio of $r = 2$ is preferred and often used, while for 3–D grids, a smaller refinement ratio of $r < 2$ is used due to limited computational resources.

5.2.2. Temporal Discretisation Uncertainty Assessment

The uncertainty assessment corresponding to different temporal resolutions is also performed in this study. This is achieved by performing simulations with at least three successively refined time steps, where the uniform refinement ratio of $r = 2$ is used for both 2–D and 3–D test cases.

5.2.3. Periodic Uncertainty Assessment

Since the present model solves the nonlinear governing equations in time domain, temporally periodic flows need to be simulated with a fixed number of periods in order to achieve periodically steady–state solution. In order to assess the uncertainty associated with simulating a finite number of periods, all time domain signals are post processed using a moving window Fast Fourier Transform (FFT) approach. Since the base period (frequency) is always known in surface wave problems, moving window FFT approach performs an FFT for each period of the signal, yielding convergence of Fourier coefficients throughout successive periods. Before discussing detailed results for test cases used in this study, it is important to note that the convergence of Fourier coefficients is always found to be oscillatory. As an example, this is demonstrated in Figure 5.1, where the time domain signal of roll motion of the KCS model in quartering waves is presented in Figure 5.1a, and the corresponding moving window FFT plot is presented in Figure 5.1b. It can be easily seen that both the mean value and first order amplitude of the roll exhibit oscillatory convergence throughout successive encounter periods, and that a significant number of periods needs to be simulated in order to reach periodically steady–state solution. The correct number of periods depends on the problem, hence, a different approach is taken here. A sufficiently large number of encounter periods is simulated for all test cases, and the corresponding periodic uncertainty is calculated using Eqn. (5.6), where the maximum and minimum solution, S_U and S_L are obtained within last 5 periods. The low periodic uncertainty indicates that the result is close to the periodically steady–state solution, while the high periodic uncertainty indicates that an increased number of periods should be simulated in order to reach periodically steady–state solution.

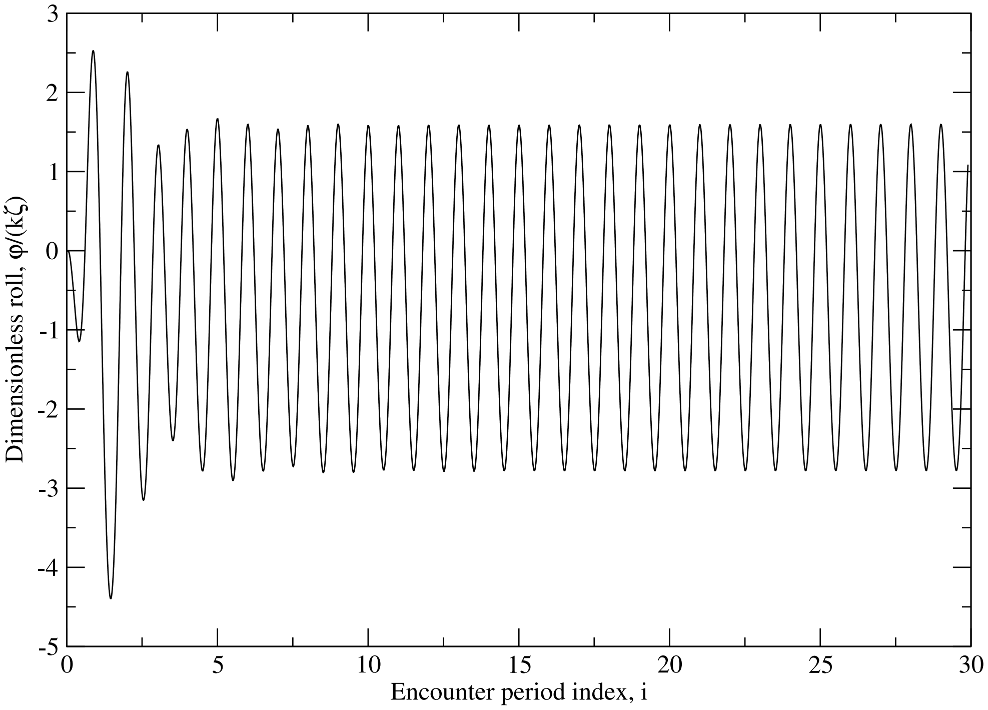

(a) Time domain signal.

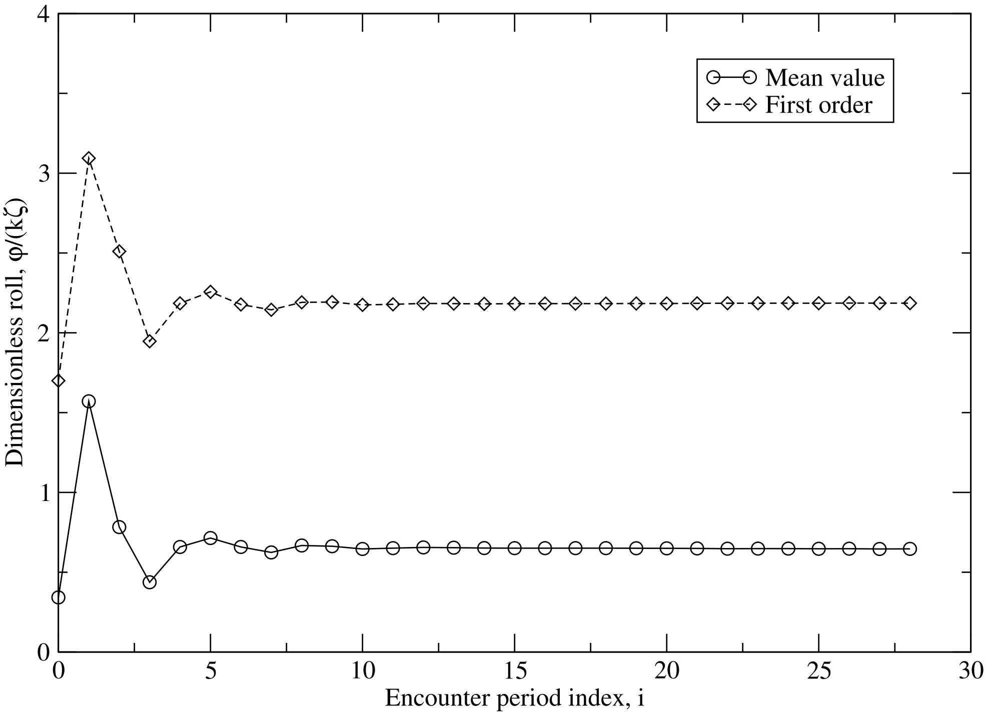

(b) Moving window FFT plot.

Figure 5.1: Periodic convergence of roll motion for the KCS case in bow waves.

5.3. Closure

A brief overview of V&V procedure has been presented in this chapter. Absolute and relative errors have been introduced in order to allow quantified validation of the present numerical model results against analytical, other numerical and experimental data.

In order to verify the present numerical model, four different convergence types have been introduced and the corresponding numerical uncertainty estimate formulae are outlined. The outlined procedures shall be used to assess and quantify grid, temporal resolution and other uncertainties corresponding to numerical settings/parameters. It is also important to note that the safety factor of $F_s = 1.5$ is introduced and shall be used in uncertainty estimates for all test cases and studies.

Finally, since most flows considered in this study are periodic in time, a periodic uncertainty estimate that relies on moving window FFT approach is explained in detail. The periodic uncertainty is closely related to the number of simulated periods, and can be directly used to estimate if the periodically steady–state solution is reached by simulating a fixed number of periods.

6. Test Cases

6.1. Overview

Ch. 5. presented an outline of V&V procedures, focusing on uncertainty assessment associated with grid refinement, temporal resolution and temporal periodicity. This chapter presents 5 sets of test cases with increasing complexity, where the relevant numerical uncertainty is assessed for each set.

As the mathematical model is exact for inviscid flow without surface tension, the first set of test cases considers an inviscid free surface flow over a 2–D ramp on structured and unstructured grids, where the simulation results are compared with the analytical solution. A simple hydrostatic test case is simulated using the same geometry, comparing the results obtained by the present approach with the results obtained using a CFD model based on conditionally averaged equations. This simple study is carried out in order to address the issue related to spurious air velocities.

The second set of test cases considers numerous simulations regarding progressive waves, including:

- LS parameters sensitivity study,
- Reflection study (varying length of relaxation zone),
- Temporal resolution refinement study (6 time steps),
- Grid refinement study (3 grids),
- Wave steepness study,
- Long simulation (100 wave periods),
- Simulation with a long domain (8 wave lengths long).

Results are compared to fully nonlinear stream function potential flow wave theory [60] for all simulations.

The third set of test cases considers higher order regular wave induced forces on a vertical, surface–piercing cylinder. Simulation results are compared to experimental data, while the grid, temporal resolution and periodic uncertainty is assessed and reported.

The fourth set of test cases considers steady resistance simulations of the KCS model at design speed, where the results are compared to available experimental data and the grid uncertainty estimate is reported.

The fifth set of test cases considers seakeeping simulations of the KCS model at design speed, for 5 head wave and 5 oblique wave cases. All results are compared with available experimental data, and each simulation is performed with 3 grids in order to assess grid uncertainty. Numerous sensitivity studies are also performed:

- Temporal resolution study (25, 50, 100, 200, 400 and 800 time steps per encounter period),
- Hydro–mechanical (fluid–flow/6–DOF) coupling study (2, 4, 6 and 8 outer PIMPLE correctors),
- Periodic uncertainty assessment for each test case.

6.2. Free Surface Flow Over a Ramp

Steady state flow over a 2–D ramp represents a standard validation test case for free surface flows [113, 114]. The geometry of the computational domain is presented in Figure 6.1. For a known inflow velocity $\mathbf{u}$ and free surface height h_1, the height of the free surface at the outlet boundary h_2 may be obtained by applying the Bernoulli and the continuity equation [114]. Density of the fluids, gravitational acceleration and inlet boundary conditions are reported in Table 6.1. The inviscid flow is easily obtained in the present model by specifying the kinematic viscosities of two fluids equal to zero. As the inviscid flow is considered, no turbulence modelling has been employed.

All time–derivative terms are discretised with the first order accurate Euler implicit scheme as the steady state solution is sought. The convection term in the momentum equation is discretised with Gauss' theorem using second–order accurate linear upwind scheme, while the convection term in the LS transport equation is discretised with second–order accurate van Leer's Total Variation Diminishing (TVD) [88] flux limiter [115] in deferred correction form [91]. The diffusion terms are discretised using central differencing with limited non–orthogonal correction in over–relaxed form [97, 90], yielding second–order accuracy. All gradient terms are discretised with Gauss' theorem using central differencing for structured grids, while the least squares discretisation [96] is employed for skewed and non–orthogonal unstructured grids. Note that all dynamic pressure terms employ interface–corrected schemes as described in detail in Sec. 4.4. Only 2 outer (Combination of SIMPLE and PISO Algorithms (PIMPLE)) correctors are used with 2 inner (PISO) correctors as the steady state solution needs to be achieved.

The uniform velocity field corresponding to the inlet value and the LS field corresponding to the calm free surface are used as the incident flow solution. Relaxation zones are not used because the reflection does not occur due to supercritical Froude number (see Table 6.1). As this test case does not have relaxation zones, the general boundary conditions as described in Sec. 4.1.5. do not apply, hence they are briefly described here. For the perturbation velocity field, following boundary conditions are used:

- Zero gradient: $\mathbf{n} \bullet \nabla \mathbf{u}_P = 0$ at the outlet,

- Fixed value: $\mathbf{u}_P = \mathbf{0}$ at the inlet,
- Slip: $\mathbf{t}\bullet(\nabla \mathbf{u}_P) = \mathbf{0}$ and $\mathbf{n}\bullet\mathbf{u}_P = 0$ at the top and bottom.

where $\mathbf{n}$ and $\mathbf{t}$ are unit normal and unit tangential vector to the face at the boundary, respectively. Boundary conditions for the perturbation LS field are set to zero gradient everywhere except at the inlet, where fixed value $\psi_P = 0$ is used. Similar boundary conditions are applied to dynamic pressure, where the zero gradient boundary condition is specified everywhere except at the top boundary, where fixed value $p_d = 0$ is used.

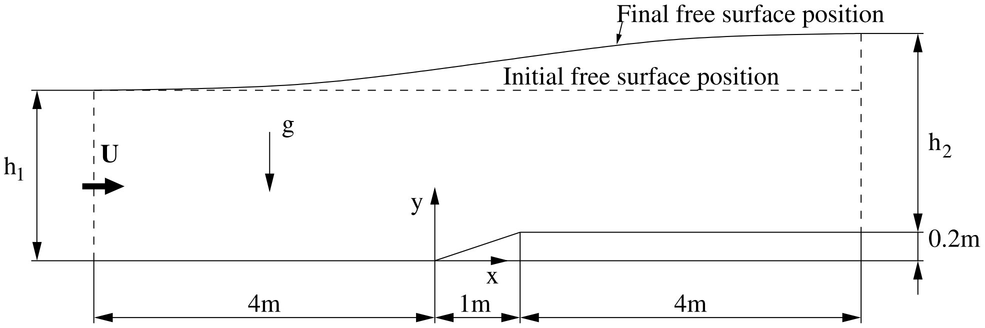

Figure 6.1: Geometry of the computational domain for the 2–D ramp test case.

Table 6.1: Simulation parameters for the 2–D ramp test case [114].

Item	Units	Value
Density of the heavier fluid	ρ_h, kg/m^3	1
Density of the lighter fluid	ρ_l, kg/m^3	0.001
Gravitational acceleration	$\mathbf{g}$, m/s^2	$[0, -9.81, 0]$
Free surface height at the inlet	h_1, m	1
Inflow velocity	$\mathbf{u}$, m/s	$[6, 0, 0]$
Froude number	$F_r = \lvert\mathbf{u}\rvert/\sqrt{\lvert\mathbf{g}\rvert h_1}$	1.92

6.2.1. Block–Structured Hexahedral Grid Refinement Study

The initial, coarse grid consists of 1 755 cells and can be seen in Figure 6.2a. Cells are graded in the longitudinal direction towards the ramp and in the vertical direction towards the undisturbed free surface. A constant grid refinement ratio [110] $r_G = 2$ is applied two times, producing two additional grids consisting of 7 020 and 28 080 cells. Steady state dynamic pressure p_d field for all grids is presented in Figure 6.2, where it can be seen that the dynamic pressure jump is resolved within a single layer of adjacent cells. The computed free surface height at the outlet boundary is compared with the analytical solution $h_{2a} = 1.08973$ m [114], where Table 6.2 presents the CFD solution for all grids and corresponding relative errors. The relative errors are lower than 1%, which is expected due to the simplicity of the test case.

The discriminating ratio calculated with three h_2 solutions corresponding to fine, medium and coarse grids is $R \approx 0.18$, hence, monotone convergence is achieved. The achieved order of spatial convergence is $p \approx 2.45$, exceeding the theoretical second order accuracy. In order to investigate peculiarly high order of spatial convergence, two Grid Convergence Indices (GCIs) are calculated based on fractional Richardson error estimators [116]:

$$GCI_{mf} = \frac{(S_m - S_f)/S_f}{r^p - 1} = 0.0003915\,, \tag{6.1}$$

$$GCI_{cm} = \frac{(S_c - S_m)/S_m}{r^p - 1} = 0.0021370\,, \tag{6.2}$$

where S_c, S_m and S_f are coarse, medium and fine grid solutions, respectively, r is the grid refinement ratio and p is the achieved order of accuracy. According to [116], whether the solutions are within asymptotic range of convergence may be verified by calculating following ratio:

$$\mathcal{A} = \frac{GCI_{cm}}{r^p GCI_{mf}} = 0.9983 \approx 1\,. \tag{6.3}$$

Since the calculated fraction in Eqn. (6.3) is close to unity, it is safe to assume that the grid solutions are within asymptotic range of convergence. Hence, the achieved order of spatial accuracy which is higher than theoretical second order accuracy may be caused by vanishing higher order derivatives for this particular problem.

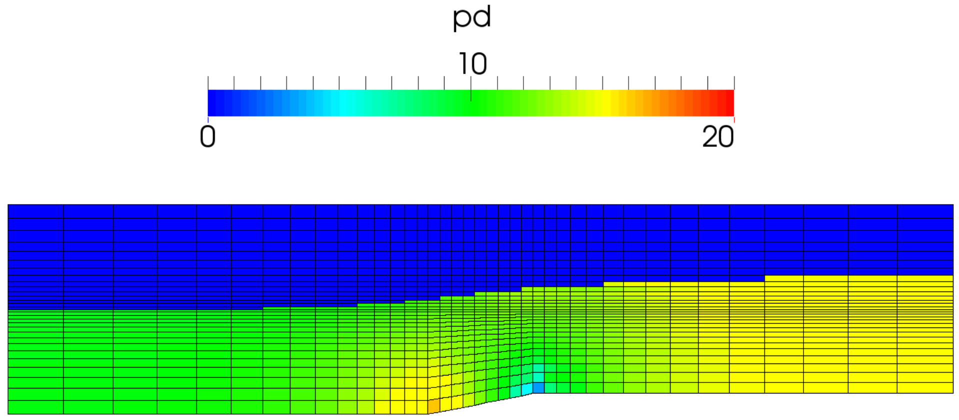

(a) 1 755 cells.

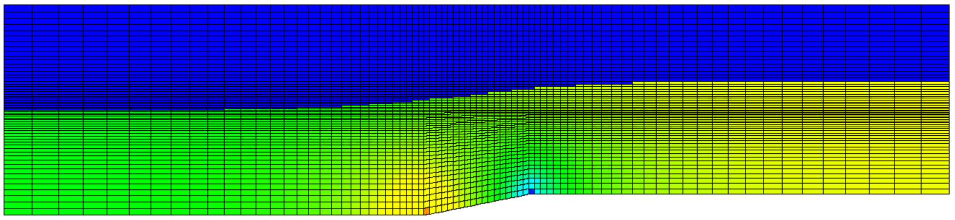

(b) 7 020 cells.

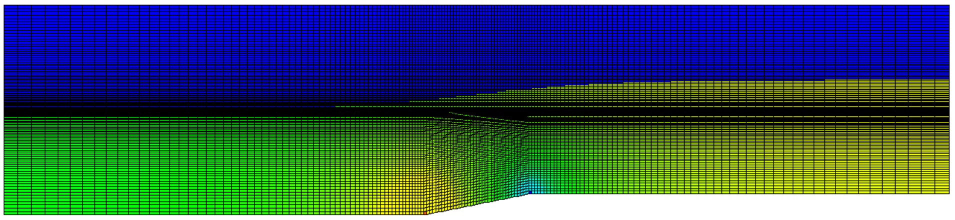

(c) 28 080 cells.

Figure 6.2: Dynamic pressure p_d at the steady state solution for three structured hexahedral grids, approximately denoting the free surface due to presence of a sharp jump.

Table 6.2: Structured grid refinement results for 2–D ramp test case.

Index	1	2	3
No. cells	1 755	7 020	28 080
h_2, m	1.09847	1.08808	1.08618
E_r, %	-0.80	0.15	0.33

Finally, grid uncertainty calculated with Eqn. (5.5) is $\overline{U} \approx 0.06\%$, which is considered small.

6.2.2. Unstructured Prismatic Grid Refinement Study

Since the present model is developed for arbitrary polyhedral, unstructured grids, three grids with prisms (triangles extruded in the third direction) are used for the unstructured grid refinement study. The coarse, medium and fine grids consist of 2 892, 13 913 and 26 112 cells, respectively. The uniform refinement ratio is not achieved as this is difficult for unstructured grid generation process, but the average grid refinement ratio is $r \approx 1.78$. The steady state dynamic pressure field is presented in Figure 6.3, where details of all grids can be seen. The calculated water height at the outlet is reported in Table 6.3, along with the relative errors, comparing the results with analytical solution. The relative errors for solutions on unstructured grids are higher compared to the relative errors obtained for block–structured grids.

The calculated discriminating ratio $R \approx -0.14$ reveals that the oscillatory convergence is achieved. Corresponding grid uncertainty is $\overline{U} = 3.6\%$, significantly larger than the grid uncertainty obtained using block–structured hexahedral grids, where $\overline{U} \approx 0.06\%$. This implies that hexahedral grids should be preferred whenever convenient for the present CFD model.

6.2.3. Hydrostatic Test Case and Spurious Air Velocities

As mathematically demonstrated in Sec. 1.2.1., the numerical model using conditionally averaged momentum equation with segregated solution algorithms is expected to cause spurious acceleration of lighter phase near the free surface. The cause of resulting spurious air velocities can be directly linked to the pressure–density coupling being resolved in the momentum equation, instead of the pressure equation. It is important to note that this numerical phenomena is unrelated to parasitic currents caused by numerical issues often encountered in atomisation calculations due to CSS model [76] for treatment of surface tension effects, which shall is demonstrated by considering the inviscid case without surface tension effects.

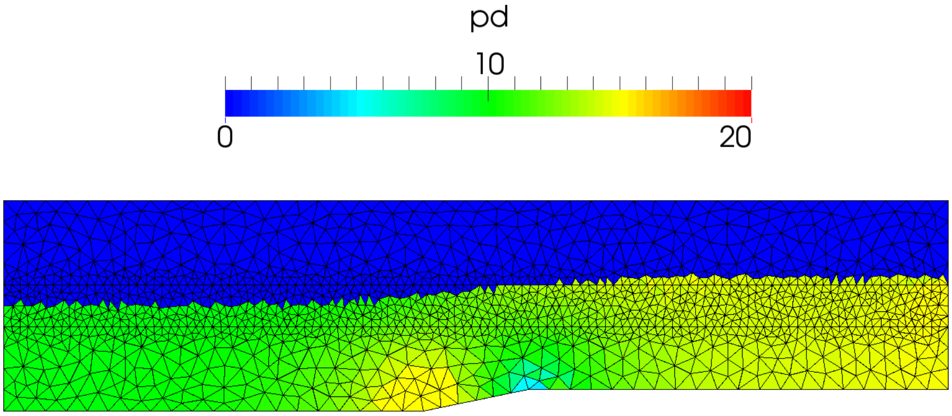

(a) 2 892 cells.

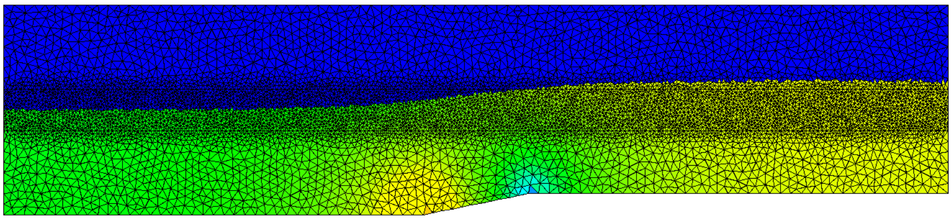

(b) 13 913 cells.

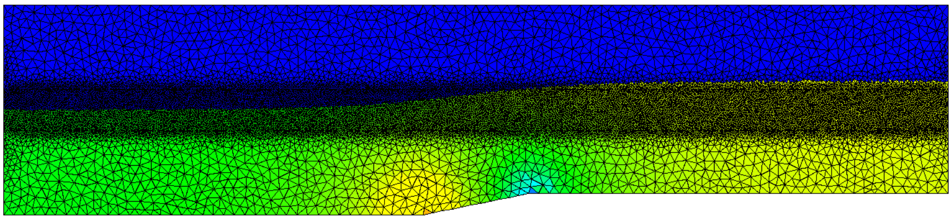

(c) 26 112 cells.

Figure 6.3: Dynamic pressure p_d at the steady state solution for three unstructured prismatic grids, approximately denoting the free surface due to presence of a sharp jump.

Table 6.3: Unstructured grid refinement results for 2–D ramp test case.

Index	1	2	3
No. cells	2 892	13 913	26 112
h_2, m	1.02772	1.07982	1.07260
E_r, %	5.69	0.91	1.57

To test the improvements using the interface–corrected interpolation schemes obtained via GFM, a hydrostatic variant of this test case is considered, where the calm free surface is frozen during the calculation and the velocity field is initialised to zero in whole domain. As the hydrostatic test case is linear, the converged solution should be obtained in a single time step. For comparison, `interFoam` two–phase flow solver (available within `foam-extend-3.2` [117]) based on conditionally averaged equations is used for comparison. Additional details regarding the `interFoam` solver can be found in numerous publications [52, 50, 51, 73, 74] as many researchers use it as a starting point for further development. In order to stress this inconsistency, the fine, structured hexahedral grid is used for hydrostatic test.

A single time step with one pressure–velocity corrector step is computed since the considered problem is linear. Velocity fields after the momentum equation (momentum predictor step) and after the pressure equation (final solution) are compared in Figure 6.4 using the two approaches. It is important to note that different velocity scales are used for each figure in order to be able to visualise the difference between the solutions. Figure 6.4a presents the velocity field after the solution of the momentum equation using the conditional averaging approach (`interFoam`), where a single layer of cells in air adjacent to the free surface has velocity magnitudes up to $\mathcal{O}(10^3)$. The extreme velocities in the intermediate step of the solution algorithm are caused by the dynamic pressure and density imbalance in the momentum equation. In the present numerical framework, the dynamic pressure–density coupling is resolved inside the pressure equation using interface–corrected scheme obtained via GFM, indicating that there should be no spurious air velocities after the momentum predictor step. This is demonstrated in Figure 6.4b, where the maximum velocity is only $\mathcal{O}(10^{-5})$ due to discretisation errors. The final velocity field (after the pressure equation) using conditional averaging approach (`interFoam`) yields velocity magnitudes of $\mathcal{O}(10^{-3})$, that is: seven orders of magnitude smaller than the velocity field obtained after the momentum predictor step. In contrast, the final velocity field using the numerical model developed within this study is the same as after the momentum predictor step. This can be easily seen by comparing Figure 6.4d and Figure 6.4b. Although the maximum velocity magnitude obtained with conditionally averaged

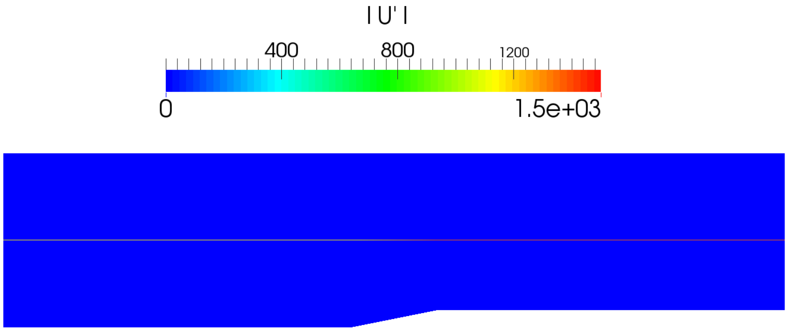

(a) Velocity field after the solution of the momentum equation, conditionally averaged equations in `interFoam`.

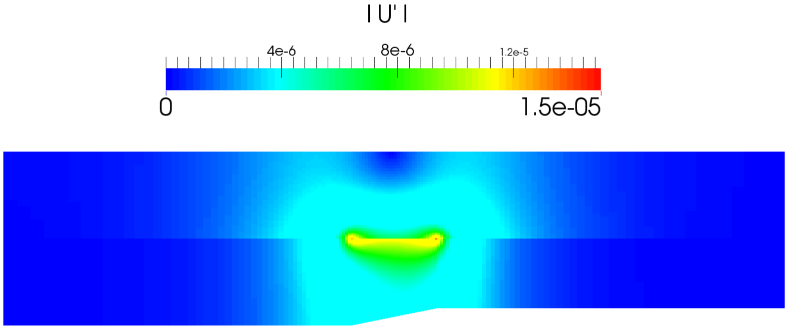

(b) Velocity field after the solution of the momentum equation, present model.

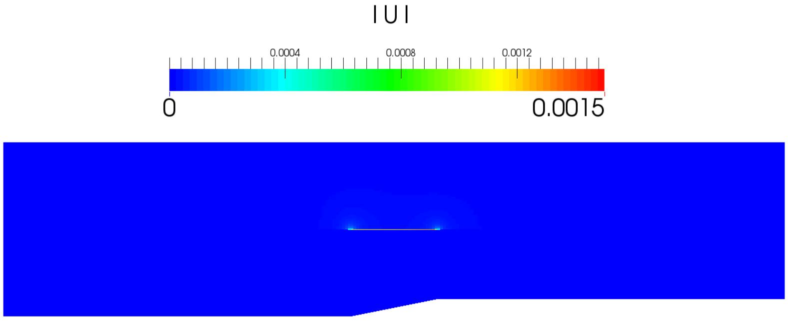

(c) Final velocity field after pressure correction step, conditionally averaged equations in `interFoam`.

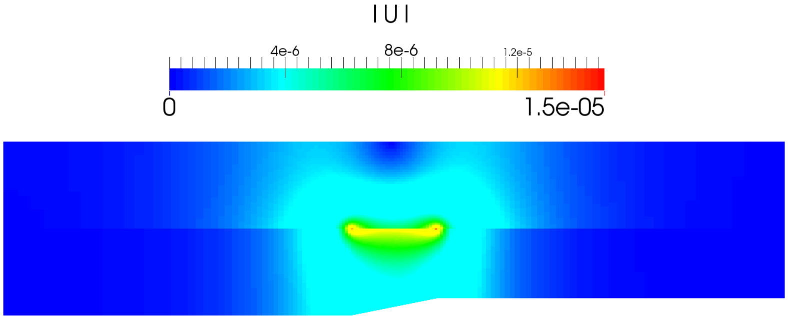

(d) Final velocity field after pressure correction step, present model.

Figure 6.4: Air velocities near the free surface for the hydrostatic test case.

approach is reduced by seven orders of magnitude after the pressure equation, the final maximum value is two orders of magnitude smaller in the present approach. It should also be noted that the velocity field of $\mathcal{O}(10^{-5})$ in the present approach can be observed both in air and water, thus indicating the level of discretisation errors, while in the conditionally averaged approach (as used in *e.g.* `interFoam`), higher velocities can be found only in air cells adjacent to the free surface. Furthermore, abrupt reduction of velocity magnitude corresponding to 7 orders of magnitude might cause numerical instabilities in conditionally averaged approach, especially when dynamic pressure and density are not properly balanced before the momentum equation, which is difficult to achieve using segregated solution algorithms. Finally, additional inconsistency may be observed in conditionally averaged approach, where the discontinuous nature of density and dynamic pressure (on continuum mechanics length scales) is not properly taken into account. Rather, density and dynamic pressure gradients (which should mathematically correspond to the Dirac delta function), are often evaluated using ordinary discretisation practices. This is avoided in the present approach by discretising dynamic pressure jump conditions with one–sided extrapolates based on the LS signed distance function and the GFM. Hence, interface–corrected schemes take into account the discontinuous nature of the density and dynamic pressure fields in free surface flows.

6.3. Progressive Wave Simulations

The second set of test cases deals with various 2–D wave propagation problems in a numerical wave tank, where the emphasis is given on sensitivity studies. First, a benchmark test case is introduced in detail, where the results are compared with fully nonlinear potential flow stream function wave theory [60]. Influence of the diffusion parameter b in the LS transport equation (see Eqn. (4.16) and Eqn. (2.41)) is assessed through LS Courant–Friedrichs-Lewy number CFL_{ψ} and stabilisation constant γ. Next, a reflection study is carried out by changing the relaxation zone length. Furthermore, temporal and grid resolution studies are performed for the benchmark test case and the corresponding numerical uncertainties are estimated. The wave steepness study is also performed by varying the wave height while keeping the wave period constant. Additionally, a long simulation is carried out by simulating 100 wave periods in order to assess the conservative properties of implicit relaxation zones and the LS method, where the periodic uncertainty is reported. Finally, a simulation with large domain (8 wave lengths long) is carried out in order to examine the effects of numerical dissipation and dispersion on wave propagation. The results of all sensitivity studies are compared with stream function wave theory [60].

The time derivative terms in all governing equations are discretised with a 50–50 blend of second–order accurate Crank–Nicolson and first–order accurate Euler implicit scheme. This formally yields a theoretical order of temporal accuracy of 1.5. Convection, diffusion and gradient terms are discretised using the same procedures as for the 2–D ramp test case (see Sec. 6.2.), where the interface–corrected interpolation schemes are employed for discontinuous dynamic pressure terms. In order to eliminate the effect of iterative uncertainty, 4 outer (PIMPLE) and 2 inner (PISO) correctors are used, lowering the residuals below 10^{-6} for all equations. Turbulence modelling has not been used as the turbulence effects may be considered negligible for regular wave propagation.

6.3.1. Benchmark Wave Propagation Case

A wave with mild steepness, $ka = 0.023$ is considered here as a benchmark wave propagation case, where the wave and simulation parameters are outlined

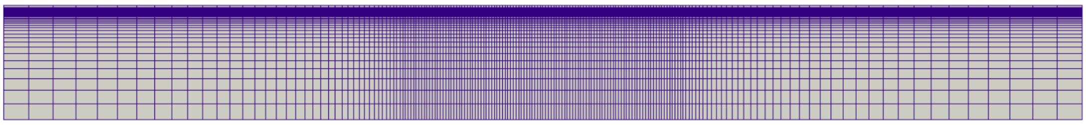

Figure 6.5: View of the whole grid.

in Table 6.4.

The 2–D computational domain extends from $x \in [0, 60]$ and $y \in [-6, 0.3]$ m. The grid consists of three longitudinal and three vertical blocks, where the cells are heavily graded towards the middle block which is 15 m ($\approx \lambda$) long (see Figure 6.5) and 0.2 m high ($\approx 2H$) (see Figure 6.6). In the middle block, there are approximately 15 cells per wave height and 100 cells per wave length, which results in maximum cell aspect ratio of $22.\dot{2}$. The resulting grid may be considered relatively coarse considering the number of cells per wave height and relatively fine considering the number of cells per wave length in the middle block. Overall, a total number of 11 700 cells is considered coarse from a computational perspective, making this grid suitable for various sensitivity studies.

In order to prevent wave reflection in wave propagation simulation, relax-

Table 6.4: Wave and simulation parameters for the benchmark case.

Wave height	H, m	0.1
Wave period	T, s	3
Wave frequency	ω, rad/s	2.0944
Wave length	λ_w, m	13.934
Wave number	k, rad/m	0.450924
Depth	d_d, m	6
Relaxation zone length	λ_r, m	22.5
Time step	Δt, s	$3.75 \cdot 10^{-3}$
LS CFL number	CFL_ψ	0.25
Stabilisation constant	γ	10^8
Width parameter	ϵ, m	0.004

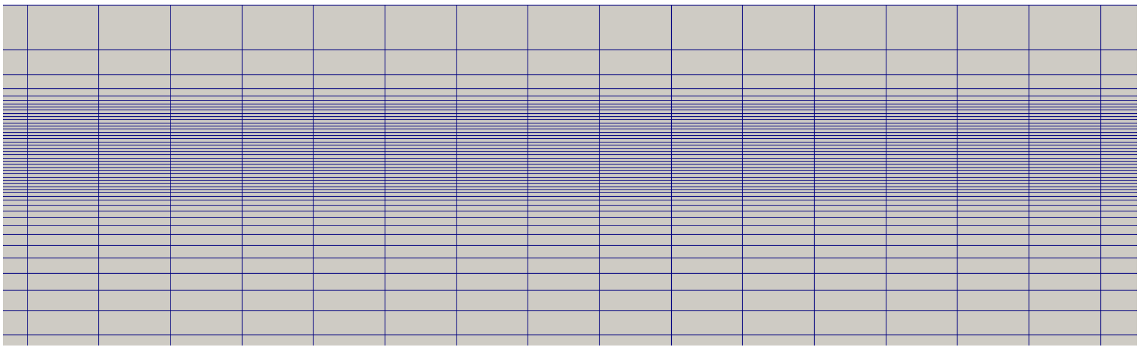

Figure 6.6: Zoomed view of the grid in the middle block near the free surface.

ation zones are positioned at far–field boundaries (left and right boundary of the grid). The length of relaxation zones is 22.5 m, where $\lambda_r \approx 1.5\lambda$. Hence, a fully nonlinear, two–phase and viscous CFD solution is obtained in the middle of the domain, spanning 15 m in the longitudinal direction and presented in the top part of Figure 6.7. Although this region represents only 25% of the domain, the exponential character of the weight field (see Eqn. (3.14) or Jacobsen *et al.* [52]) is favourable, because a part of the solution that is between 50 and 100% CFD is present in 86.5% of the domain (see middle image in Figure 6.7). For example, if $w = 0.5$, the final solution is a blend of 50% CFD solution and 50% potential flow solution. Hence, if one uses advanced potential flow wave theories, this solution is accurate as well. In this example, $96.\dot{6}\%$ of the cells are in this region, so the cell count is only slightly increased due to relaxation zones.

Wave elevation is measured in the middle part of the domain where the fully nonlinear, two–phase and viscous CFD solution is achieved. The longitudinal coordinates of wave gauges are at 25, 30 and 35 m for wave gauges 1, 2 and 3, respectively and 10 incident wave periods are simulated. Time signals of wave elevations at all three wave gauges are presented in Figure 6.8 and Figure 6.9, where only the last three (representative) periods are shown for clarity. The CFD results show good agreement with the stream function potential flow solution. The wave troughs and peaks remain within 0.1% of relative errors defined with Eqn. (5.2), while the slight phase shift may be observed in Figure 6.9b. The largest phase shift corresponds to approximately 0.6% of the wave period. This phase shift error could be related to second–order accurate convection schemes

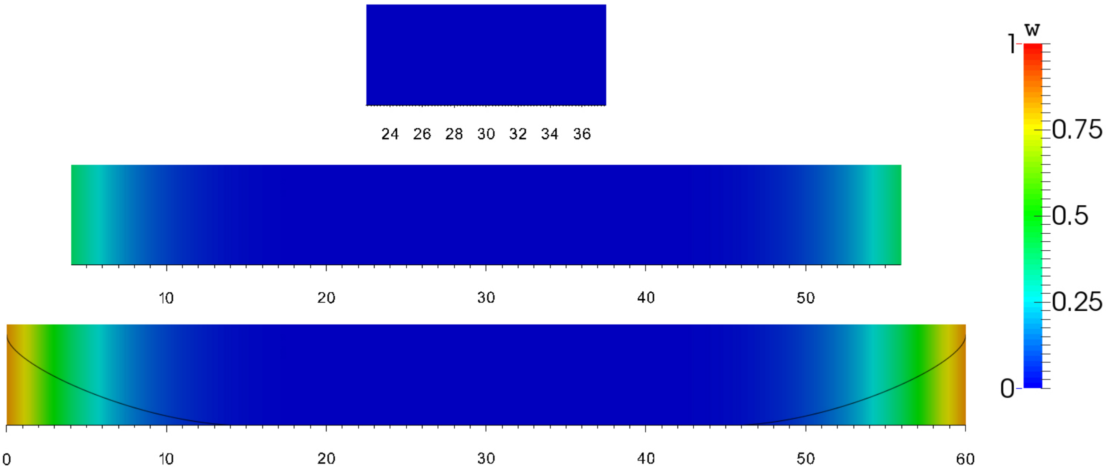

Figure 6.7: Weight field for wave propagation test case. The top image presents the area where fully nonlinear, two–phase and viscous CFD solution is obtained. The middle image presents the area where there is 50 to 100% of the CFD solution. The bottom image presents the whole domain, where the black line in the bottom image is a qualitative representation of weight function Eqn. (3.14).

used for incident wave propagation as indicated by Huang *et al.* [15]. Since it is difficult to draw concise conclusions from signals in time domain, the attention is given to frequency domain representation of the signals via moving window FFT procedure as outlined in Sec. 5.2.3.. The final frequency domain harmonic solutions are taken as the average values from last 5 periods, while the periodic uncertainty is assessed using Eqn. (5.6) with maximum and minimum values from last 5 periods.

Tables 6.5–6.7 present the first two harmonics for the CFD solution and the stream function wave theory. Only the two harmonics are presented because others can be neglected due to linearity of the considered wave [84]. Absolute value of the i^{th} harmonic is denoted with H_i, whereas the phase shift of the harmonic is denoted with γ_{H_i}. Since the second order effects are two orders of magnitude smaller for such a linear wave, the normalised relative error is introduced and calculated as:

$$E_{nr} = E_r \frac{\mathcal{O}(H_2)}{\mathcal{O}(H_1)}\,, \tag{6.4}$$

where $\mathcal{O}(H_1)$ is the order of magnitude of the first harmonic and $\mathcal{O}(H_2)$ the order of magnitude of the second harmonic. Eqn. (6.4) gives an estimate of relative error's significance in the total solution.

As indicated in Tables 6.5–6.7, the largest part of the solution is represented by the first harmonic. The second harmonic is smaller by two orders of magnitude, thus, it represents at most 1% of the total solution. The first row of Tables

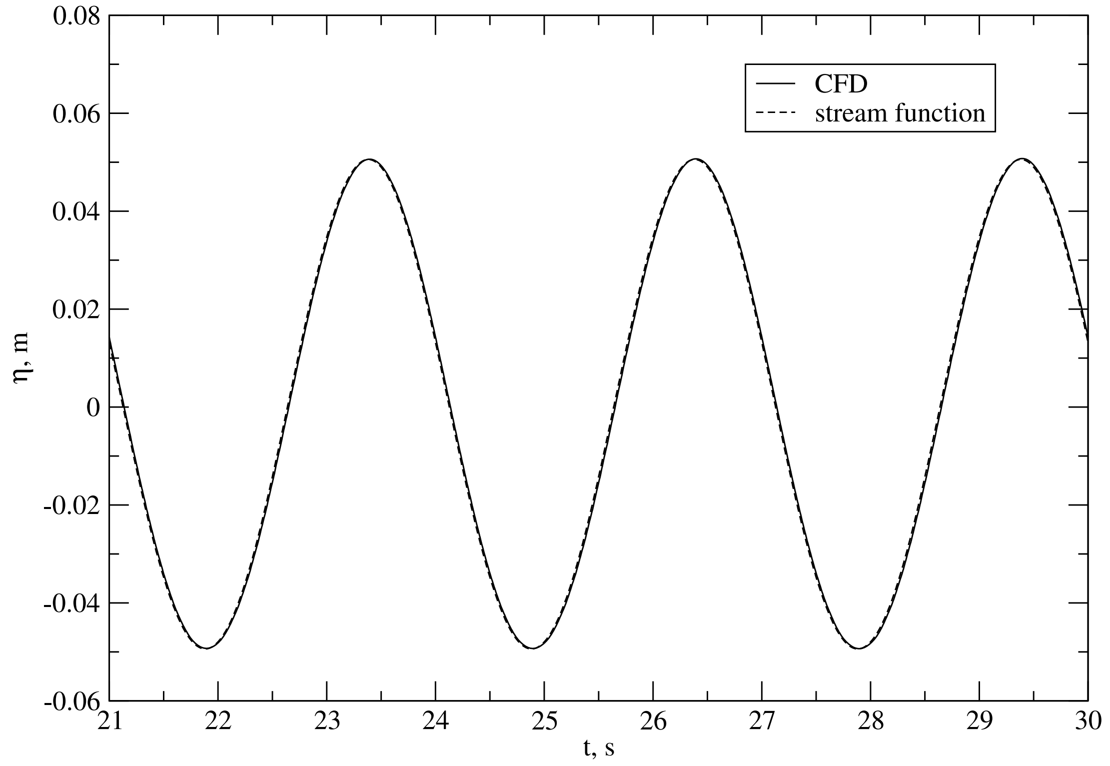

Figure 6.8: Time evolution of wave elevation during last 3 periods for wave gauge 1, $x = 25$ m.

Table 6.5: Fourier representation of wave elevation signals at wave gauge 1.

i^{th} harmonic	CFD solution	Stream function	Relative error, %	Normalised rel. error, %
H_1, m	$4.9996 \cdot 10^{-2}$	$4.9962 \cdot 10^{-2}$	-0.06	-0.06
γ_{H_1}, rad	1.2701	1.2934	1.80	1.80
H_2, m	$6.6035 \cdot 10^{-4}$	$5.8369 \cdot 10^{-4}$	-13.13	-0.13
γ_{H_2}, rad	2.5341	2.5873	2.05	0.02

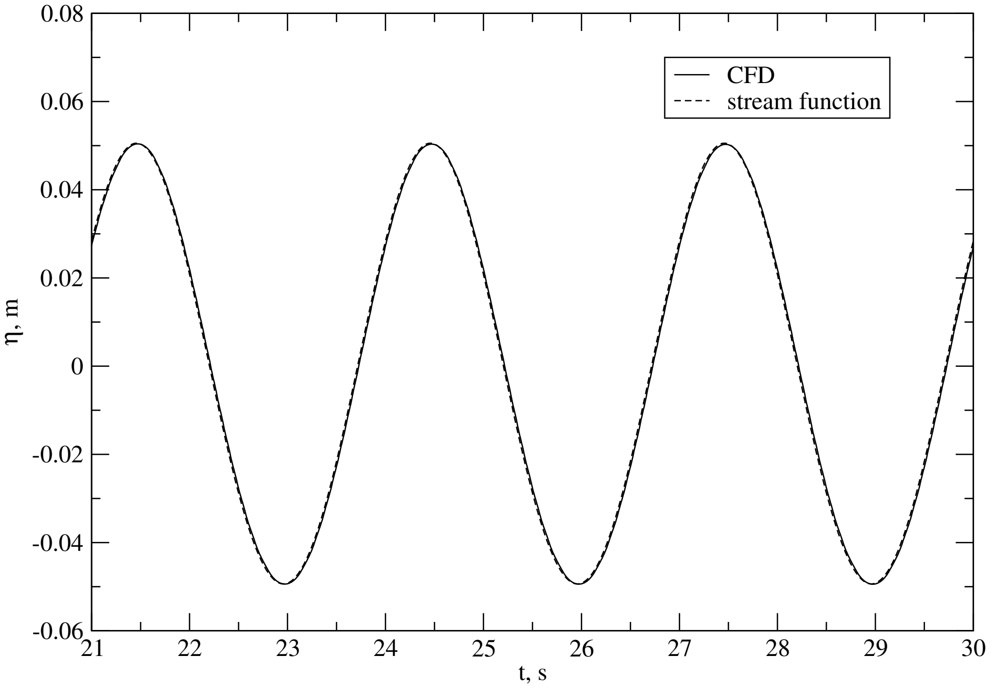

(a) Wave gauge 2, $x = 30$ m,

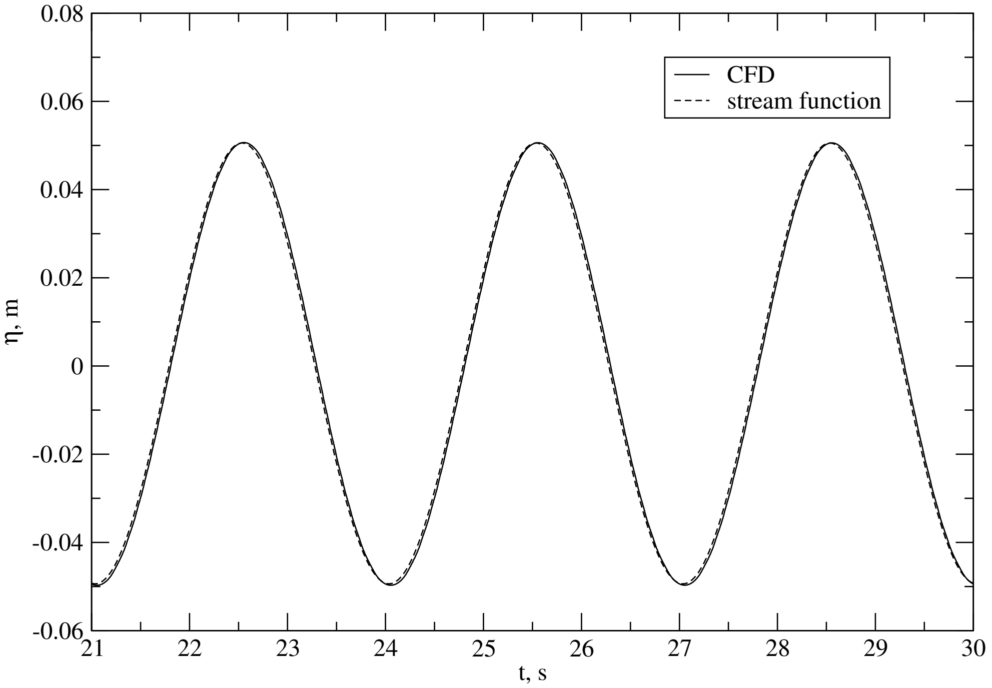

(b) Wave gauge 3, $x = 35$ m,

Figure 6.9: Time evolution of wave elevation during last 3 periods for wave gauges 2 and 3.

6.5–6.7 show that the relative error for the first order harmonic amplitude is always lower than 0.5%. Since the first harmonic represents 99% of the solution, the comparison between the CFD and the stream function solution is considered good. The normalised relative error for second order harmonic amplitude is lower than 1%. The first order harmonic phase shifts have relative errors within 3%, while the second order harmonic phase shifts have normalised relative errors lower than 1%. Generally, errors for phase shifts are higher than errors for amplitudes, which is expected in CFD wave propagation simulations. This observation agrees well with Figure 6.9, where the slight phase shift has been observed.

Table 6.6: Fourier representation of wave elevation signals at wave gauge 2.

i^{th} harmonic	CFD solution	Stream function	Relative error, %	Normalised rel. error, %
H_1, m	$4.9898 \cdot 10^{-2}$	$4.9962 \cdot 10^{-2}$	0.12	0.12
γ_{H_1}, rad	-0.9875	-0.9612	-2.74	-2.74
H_2, m	$5.4895 \cdot 10^{-4}$	$5.8369 \cdot 10^{-4}$	5.95	0.06
γ_{H_2}, rad	-1.8656	-1.9223	2.95	0.03

Table 6.7: Fourier representation of wave elevation signals at wave gauge 3.

i^{th} harmonic	CFD solution	Stream function	Relative error, %	Normalised rel. error, %
H_1, m	$5.0174 \cdot 10^{-2}$	$4.9962 \cdot 10^{-2}$	-0.42	-0.42
γ_{H_1}, rad	3.0305	3.0674	1.20	1.20
H_2, m	$5.0908 \cdot 10^{-4}$	$5.8369 \cdot 10^{-4}$	12.78	0.13
γ_{H_2}, rad	-0.2730	-0.1485	-83.84	-0.84

6.3.2. Study of Influence of the Diffusion Parameter b

The study of influence of the diffusion parameter b in the LS transport equation, (see Eqn. (4.16) and Eqn. (2.41)) is examined. As indicated in Sec. 4.1.3., b serves to maintain the signed distance profile of the LS field and to smear possible singularities during the solution process, while it depends on the specified LS CFL number, CFL_ψ and the stabilisation constant, γ (see Eqn. (4.16)). The benchmark test case is used for the study, where only the first order harmonic and phase are reported for wave gauge 2 (middle of the domain), as other signals exhibit similar behaviour.

Level Set Courant–Friedrichs-Lewy Number CFL_ψ Sensitivity

User specified LS CFL number, CFL_ψ determines the diffusion parameter as indicated by equation Eqn. (4.16). In order to assess the sensitivity of the solution with respect to the specified CFL_ψ, 8 additional simulations have been performed with following CFL_ψ numbers: 0.5, 1, 2, 4, 8, 16, 32, 64. The first order harmonic amplitudes and phases are presented in Figure 6.10, while the higher order effects are not examined in details due to linearity of the wave. Figure 6.10a presents first order harmonic amplitude for different CFL_ψ number in logarithmic scale, comparing the results with stream function wave theory. It can be seen that the results are insensitive to variations in CFL_ψ number of 2 orders of magnitude. Although piecewise monotone or oscillatory convergence is achieved for certain pairs of results, the numerical uncertainty of the first order harmonic amplitude with respect to varying CFL_ψ is quantified using Eqn. (5.7), which is considered the most conservative estimate. In Eqn. (5.7), S_U is the maximum solution and S_L is the minimum solution for 9 different CFL_ψ numbers, yielding $\overline{U} = 0.13\%$. The same procedure is applied for first order harmonic phase presented in Figure 6.10b, yielding numerical uncertainty of $\overline{U} = 0.09\%$. The numerical uncertainty is normalised with the results from the benchmark test case, where $CFL_\psi = 0.25$. Thus, it can be concluded that the wave propagation solutions are insensitive to changes in the CFL_ψ number, although it is important to note that the specified CFL_ψ must be greater than the convective CFL number, CFL_c in order to ensure positive diffusion coefficient b (see Eqn. (4.16)).

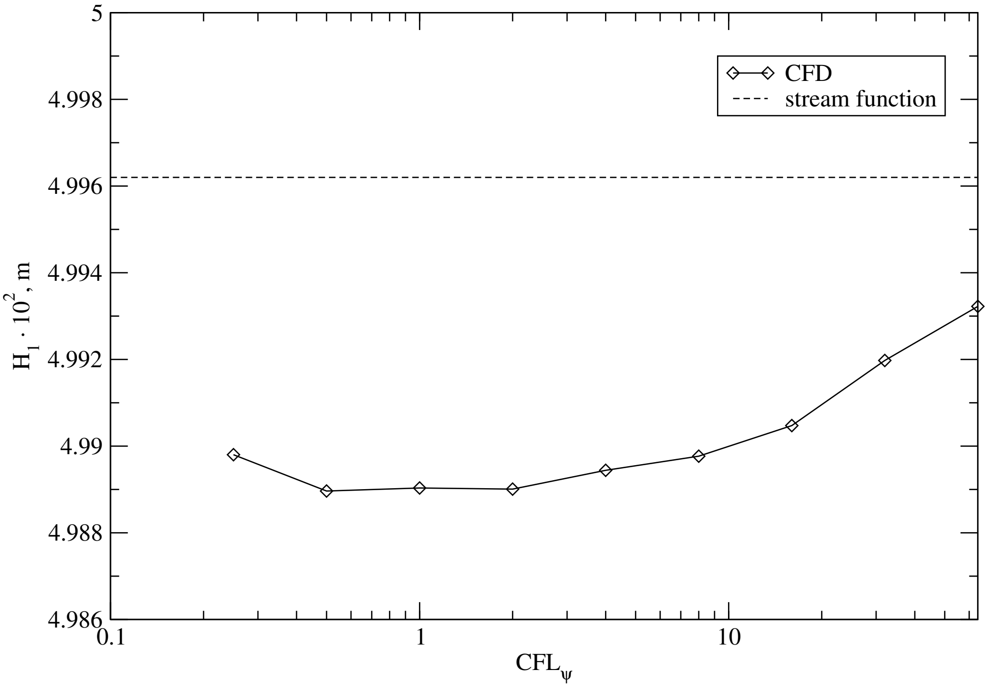

(a) First order harmonic amplitude,

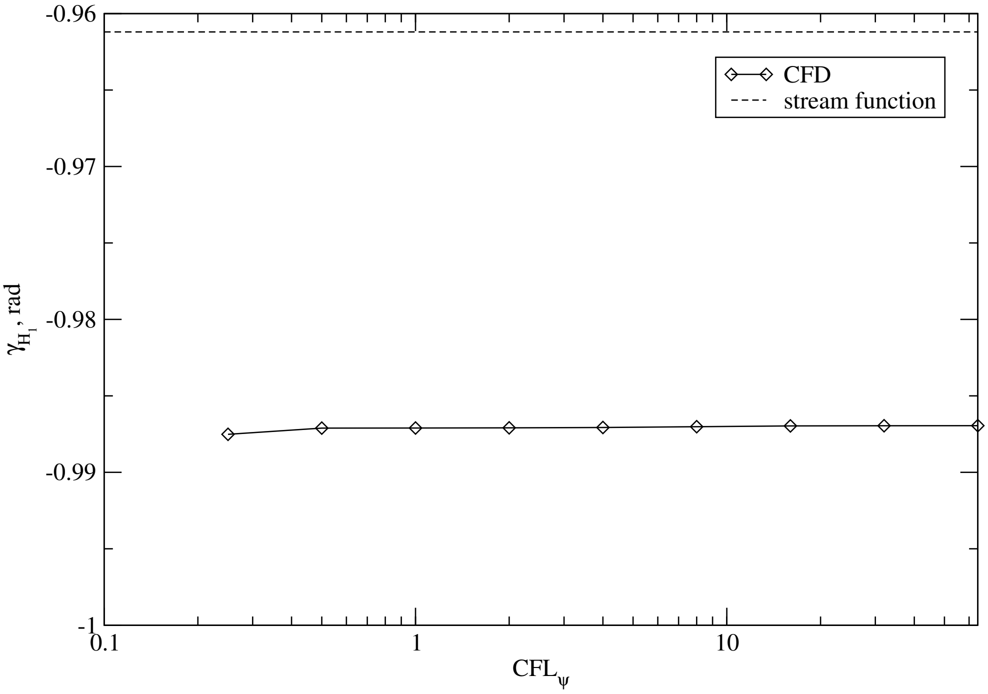

(b) First order harmonic phase,

Figure 6.10: Sensitivity of the solution with respect to CFL_ψ number.

Stabilisation Parameter γ Sensitivity

The stabilisation parameter γ in Eqn. (4.16) serves to decrease the overall diffusion parameter. The sensitivity of the solution with respect to γ is examined by simulating 6 additional cases where: $\gamma = 10^4, 10^5, 10^6, 10^7, 10^9$ and 10^{10}, covering 6 orders of magnitudes. The sensitivity of the first order harmonic with respect to stabilisation parameter γ is indicated in Figure 6.11. The first order harmonic amplitude varies approximately 0.5% for three lowest values of γ, as shown in Figure 6.11a, where it varies only slightly for $\gamma > 10^6$. The same trend can be observed for first order phase in Figure 6.11b, thus it can be concluded that a good practice would be to use $\gamma > 10^6$, which is expected since this parameter directly lowers the diffusion coefficient in the LS transform equation. Again, although piecewise monotone and oscillatory convergence is achieved for certain pairs of results, Eqn. (5.7) is used to conservatively quantify numerical uncertainty with respect to 5 largest values of γ, yielding $\overline{U} = 0.06\%$ for first order amplitude and $\overline{U} = 0.09\%$ for first order phase.

Eqn. (4.16) shows that the diffusion parameter b is inversely proportional to γ. Hence, it would be reasonable to expect that larger γ should decrease the smearing of the interface. As demonstrated in Figure 6.12, this is not true since other source terms in the LS transport equation, Eqn. (2.41) also depend on the diffusion parameter b. Figure 6.12 shows the interface resolution in terms of the VOF field (reconstructed from LS using Eqn. (2.39)) in the middle part of the domain at the end of two simulations with $\gamma = 10^4$ and $\gamma = 10^6$. The smearing of the interface is almost identical and confined across two cells as prescribed with the width parameter $\epsilon = 0.004$. It is also important to stress that the VOF field is not actually used in simulation for discretisation of dynamic pressure and density terms, only the zero LS is used: $\psi = 0$. This is demonstrated in Figure 6.13, where it can be seen that the dynamic pressure field exhibits a jump across a single interface face. The white line denotes the zero LS ($\psi = 0$ iso–countour). In order to visualise the dynamic pressure fields in both water and air, Figure 6.13 is split into two parts:

1. Figure 6.13a shows the dynamic pressure in a scale where the dynamic pressure gradient is visible in the water. The dynamic pressure varies from

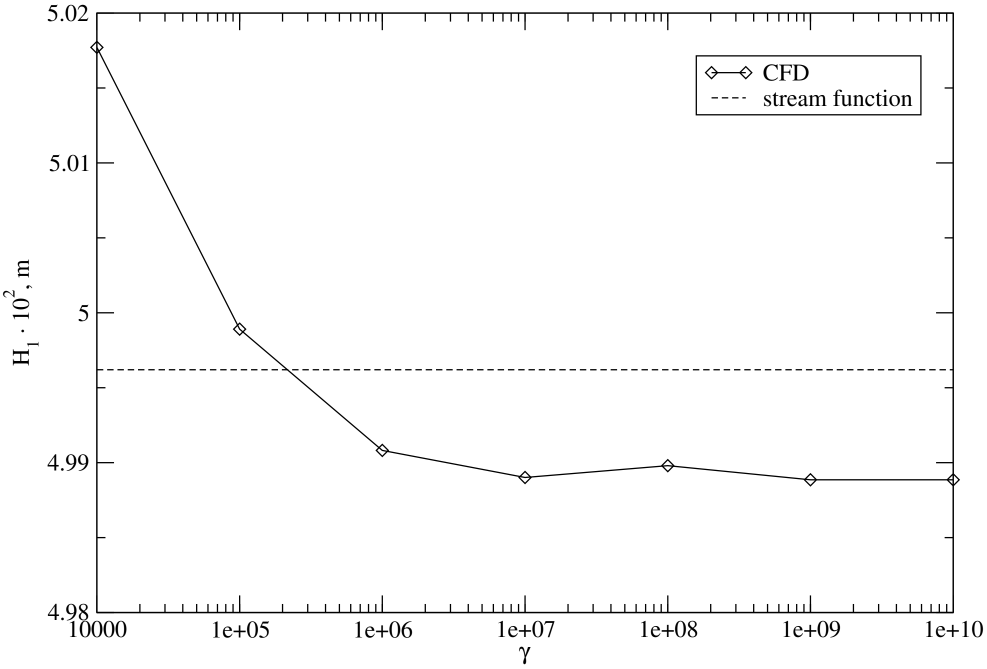

(a) First order harmonic amplitude,

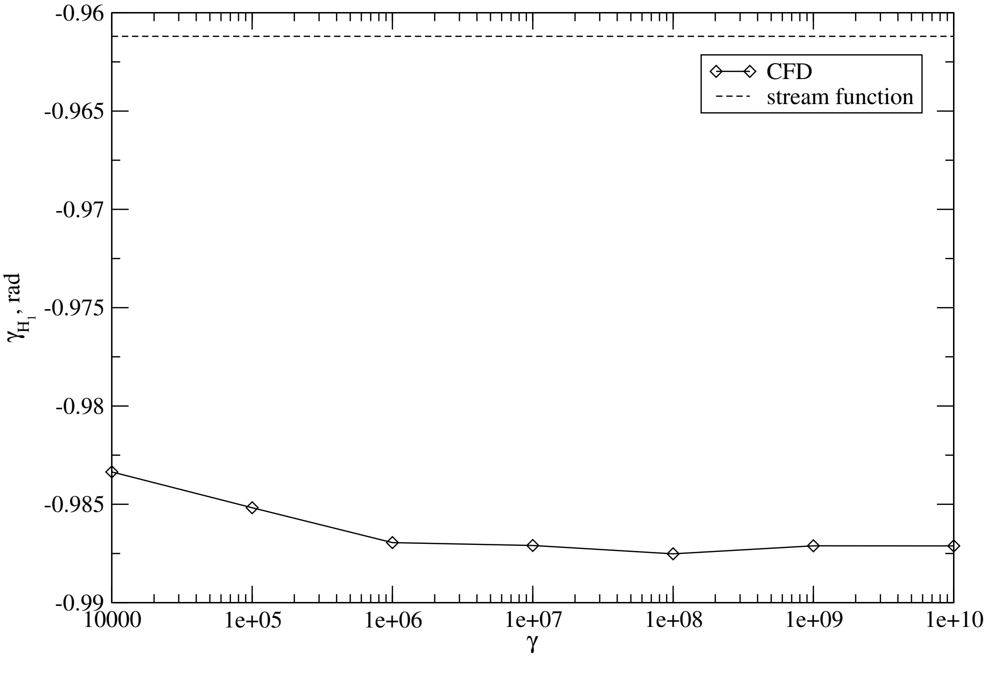

(b) First order harmonic phase,

Figure 6.11: Sensitivity of the solution with respect to γ.

approximately 50 to 400 Pa in this region ($x \in [29, 31]$ m and $y \in [-0.1, 0.1]$ m),

2. Figure 6.13b shows the dynamic pressure in a scale where the dynamic pressure gradient is visible in the air. The variation of dynamic pressure in air is from approximately -0.045 to -0.0035 Pa in the same region.

An effective difference of dynamic pressure in water and air of four orders of magnitude can be observed. This is in accordance with Eqn. (4.24) where the dynamic pressure jump across the free surface is proportional to the difference between water and air densities multiplied with the gravitational constant. Finally, Figure 6.13 indicates that the GFM successfully models the jump of dynamic pressure (and density) and that the prescribed smearing of the interface does not affect the dynamic pressure jump, as postulated in Sec. 4.3.

6.3.3. Wave Reflection Study

The reflection study is performed in order to determine the length of relaxation zones required to efficiently prevent wave reflection. The relaxation zones are positioned at far-field (inlet and outlet) boundaries as shown in Figure 6.7, where the perturbation components are gradually damped to zero, leaving a full potential flow solution. In order to determine desirable values of the relaxation zone length, λ_r is varied from $0.5\lambda_w$ to $1.5\lambda_w$ and the corresponding wave elevation signals are presented in Figure 6.14 for wave gauge 2 (middle of the domain), where only the last two periods are shown for clarity. All results show good agreement with the stream function wave theory, where the amplitude is under–predicted for smaller values of λ_r, as can be seen in Figure 6.15a, denoting the dependence of the first order harmonic amplitude with respect to λ_r. The first order phase shift is also generally larger for smaller lengths of relaxation zones as indicated in Figure 6.15b. If one neglects other numerical errors, the relative error of first order harmonic amplitude may be viewed as an estimate for the amplitude of the reflected wave. As the phase speed (celerity) of the wave is approximately 4.64 m/s, the simulation time of 30 seconds is sufficient for a reflected wave to travel trough the domain more than two times. The relative error of the first order harmonic amplitude for the smallest relaxation zone length $\lambda_r = 0.5\lambda_w$ is

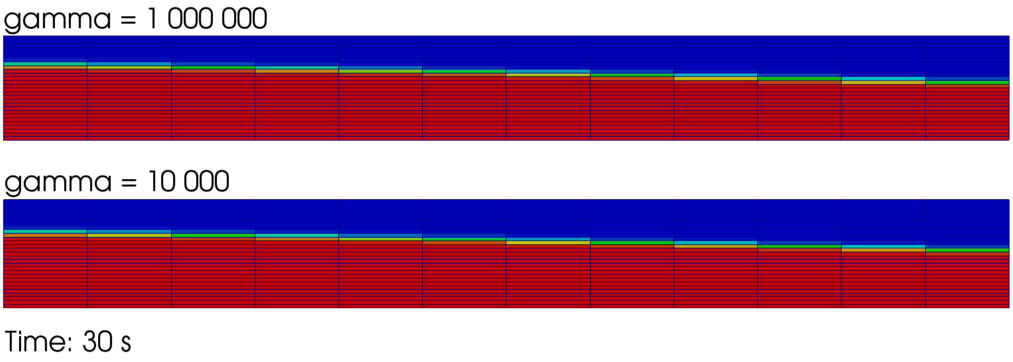

Figure 6.12: Interface resolution at the end of simulation ($t = 30$ s) for different stabilisation parameters, γ. The interface is almost identically smeared across two cells for both cases, controlled by a width parameter $\epsilon = 0.004$. Only part of the domain is shown: $x \in [29, 31]$, $y \in [-0.1, 0.1]$ for clarity.

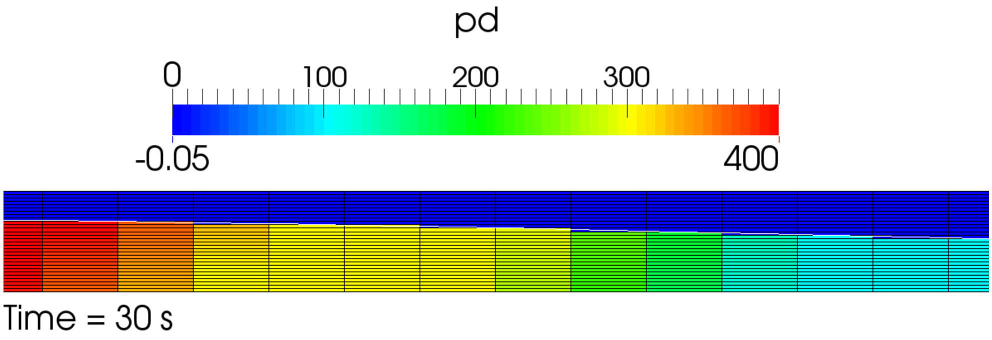

(a) Dynamic pressure scale specific to water,

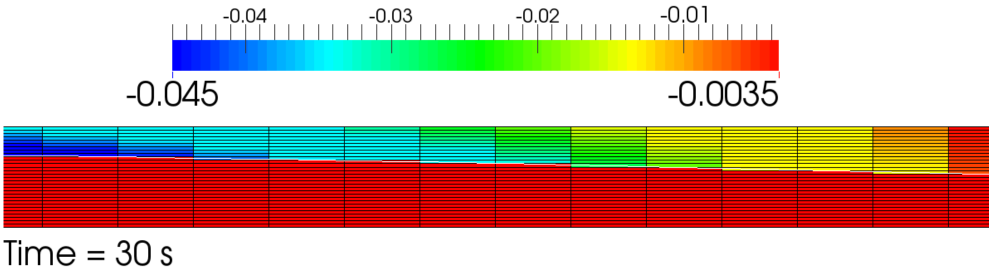

(b) Dynamic pressure scale specific to air,

Figure 6.13: Sharp dynamic pressure distribution at the end of the benchmark test case simulation. Only part of the domain is shown: $x \in [29, 31]$, $y \in [-0.1, 0.1]$ for clarity.

approximately 3%, decreasing towards 0.02% for $\lambda_r = 1.5\lambda_w$. The decrease of relative errors is monotone except for the case with $\lambda_r = 1.25\lambda_w$. The relative error of the first order harmonic phase for the smallest relaxation zone length is approximately 15%, decreasing to 3.5% for the greatest relaxation zone length. This indicates that the reflection mostly affects the phase shift, while the amplitude is less affected, which could be expected since the domain length is not a multiple of wave length. The numerical uncertainty is calculated using Eqn. (5.7) since the convergence has not been achieved for three cases where $\lambda_r \geq \lambda_w$. With the reference solution for normalisation of uncertainty corresponding to the $\lambda_r = 1.5\lambda_w$, numerical uncertainty for the first order amplitude is $\overline{U} = 1.73\%$, while for the first order phase $\overline{U} = 6.18\%$.

6.3.4. Temporal Resolution Study

The time step size is often a limiting factor in wave propagation CFD simulations, thus, a temporal resolution study is performed on the benchmark test case in order to assess the corresponding numerical uncertainty. In addition to

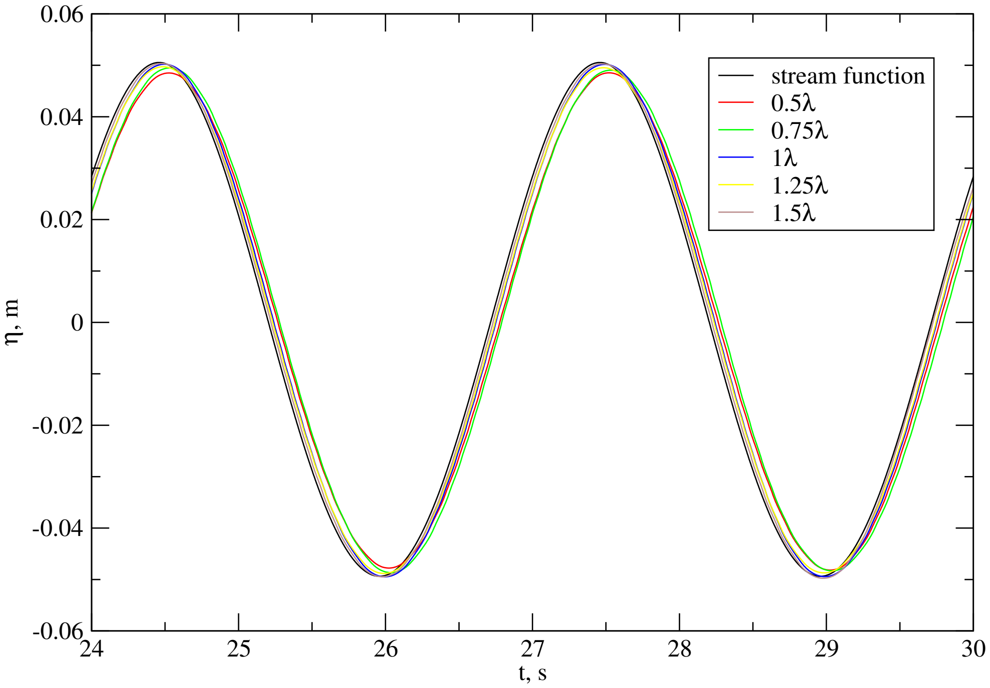

Figure 6.14: Time domain signals for last two periods, different relaxation zone lengths, λ_r.

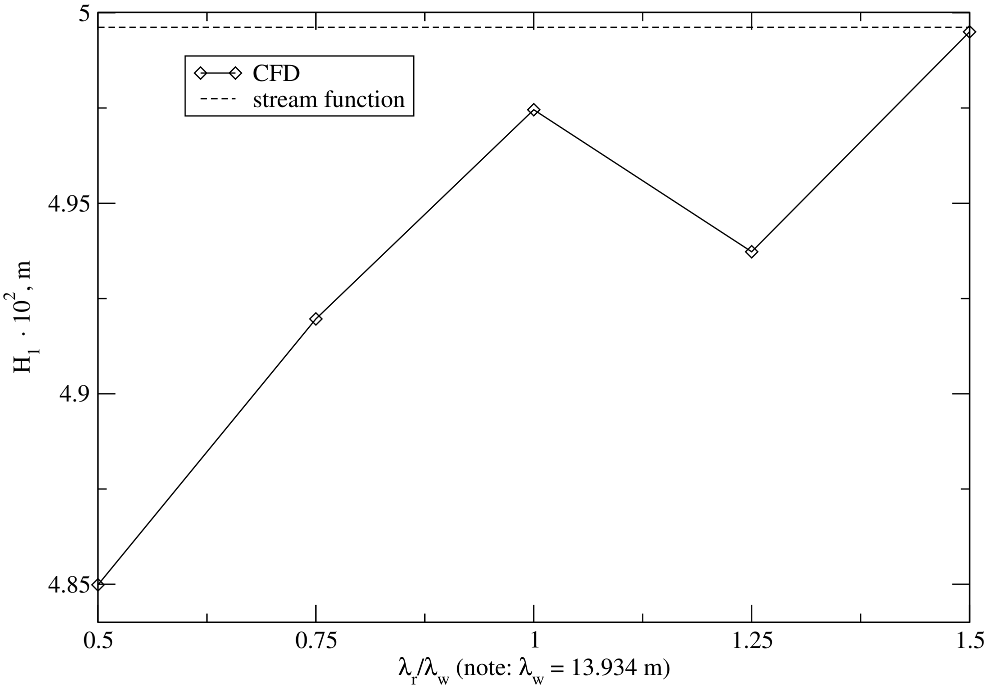

(a) First order harmonic amplitude,

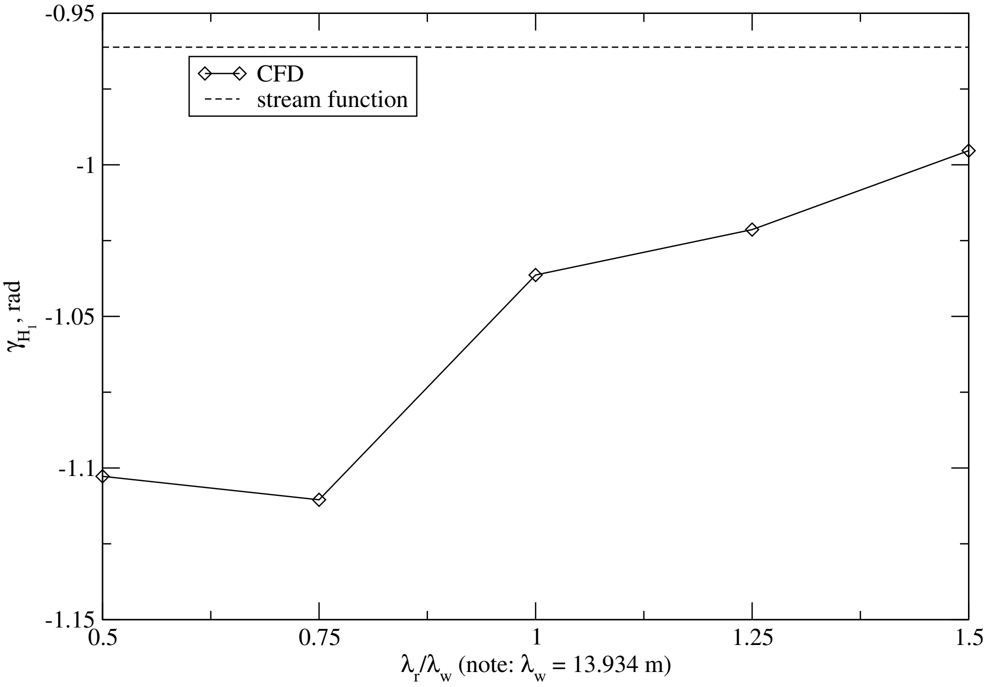

(b) First order harmonic phase,

Figure 6.15: Sensitivity of the solution with respect to relaxation zone length λ_r, frequency domain.

the benchmark test case where $n = 800$ time steps per wave period are used, 5 additional simulations are performed with $n = 25$ to $n = 400$, with a constant refinement ratio of $r = 2$. Figure 6.16 presents wave elevations at wave gauge 2 for last two periods. From the time domain signals, it can be concluded that the wave amplitude changes only slightly with extremely low temporal resolution of $n = 25$ time steps per wave period, while the phase shift is significantly more affected. This is also visible in Figure 6.17a and Figure 6.17b, where the first order harmonic amplitudes and phases are plotted for different n. Both amplitude and phase converge with increasing n, where the three solutions with $n = 200, 400$ and 800 are used to estimate achieved order of temporal convergence and numerical uncertainty. The last three solutions for the first order harmonic amplitude exhibit monotone convergence, where the achieved order of temporal accuracy is $p = 1.24$, which is smaller than theoretical order of accuracy of $p = 1.5$ (note that a blend of second–order accurate Crank–Nicolson and first–order accurate

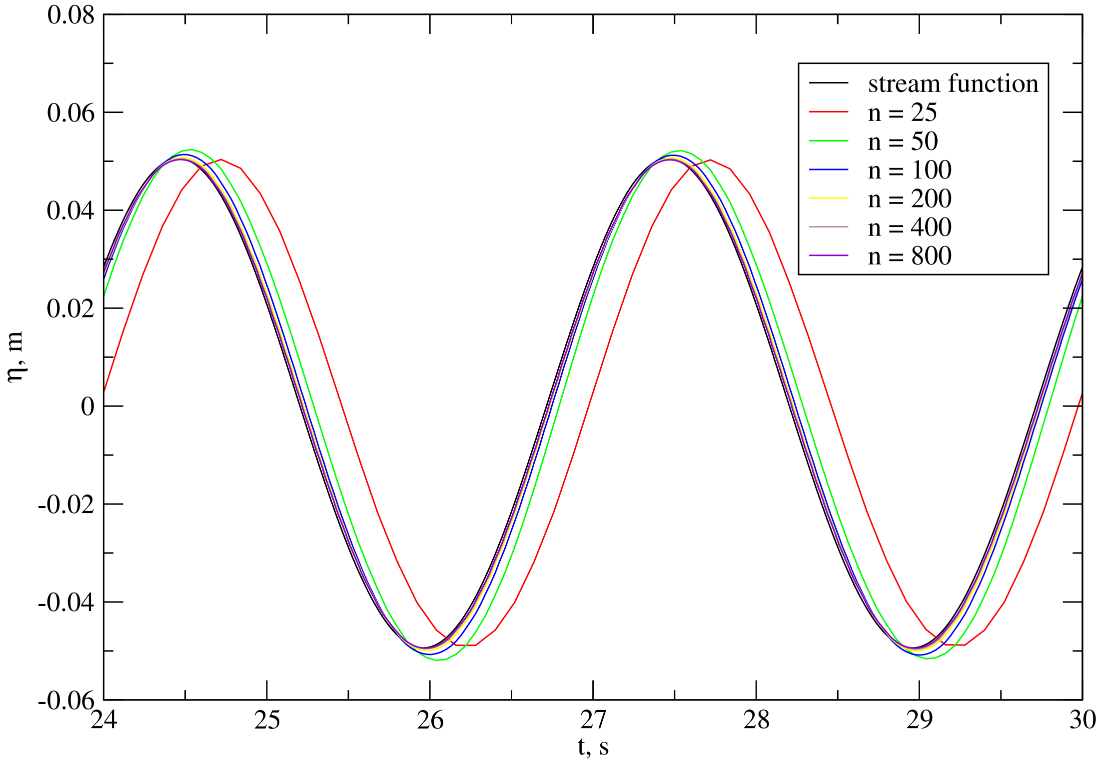

Figure 6.16: Time domain signals for last two periods, different number of time steps per encounter period, n.

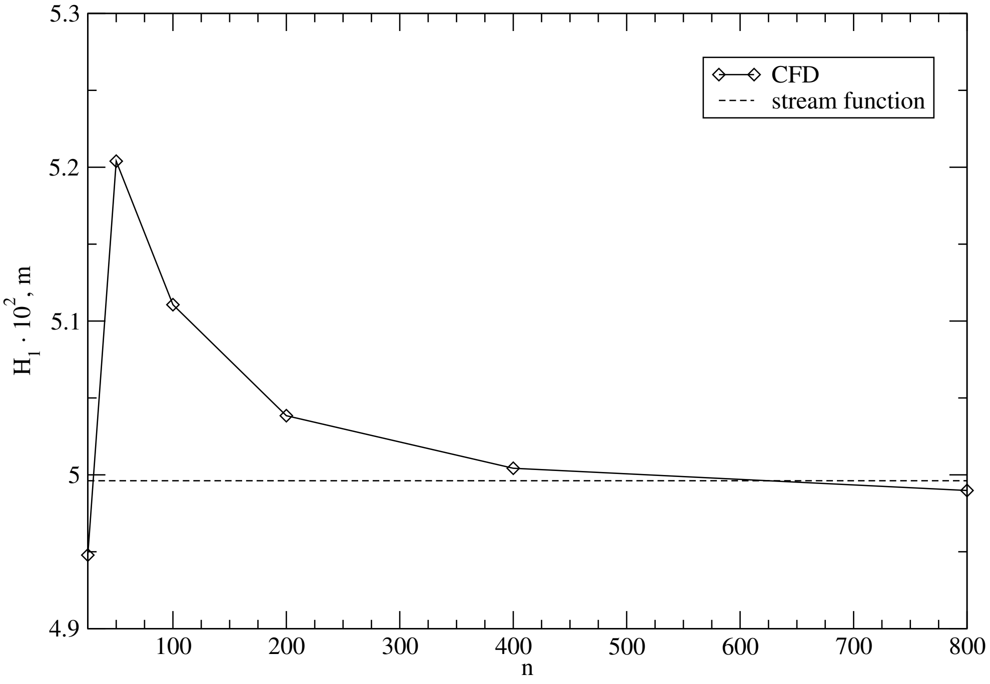

(a) First order harmonic amplitude,

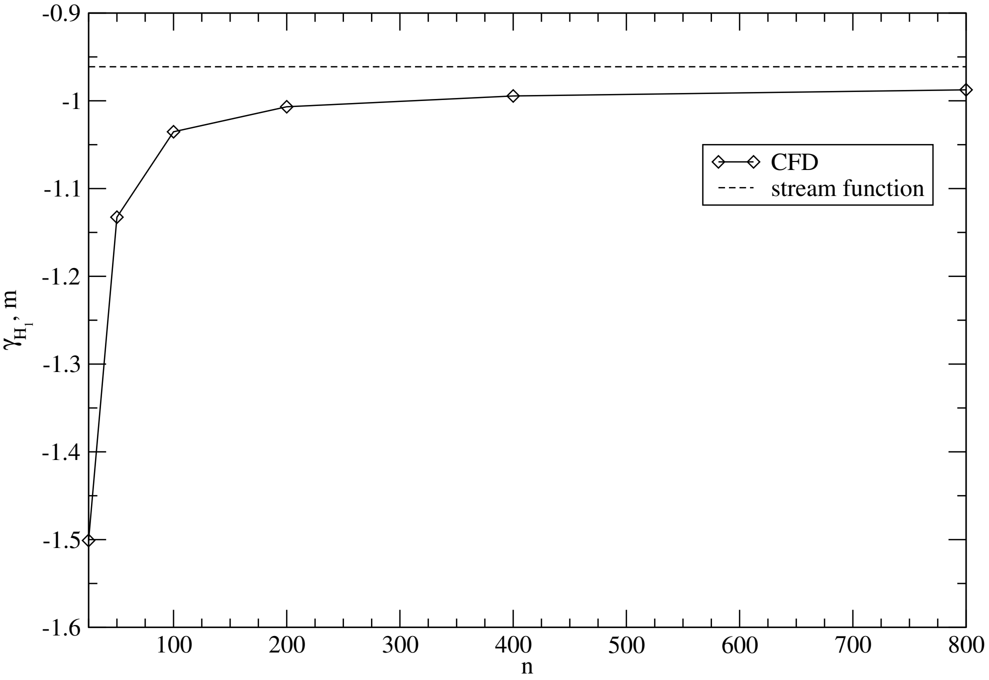

(b) First order harmonic phase,

Figure 6.17: Sensitivity of the solution with respect to the number of time steps per encounter period, n, frequency domain.

Euler implicit scheme is used). The asymptotic range ratio based on GCIs calculated with Eqn. (6.3) yields $\mathcal{A} = 0.997 \approx 1$, indicating that the solutions are within asymptotic range and the order estimate is valid. The corresponding temporal resolution uncertainty for the first order harmonic amplitude calculated with Eqn. (5.5) is $\overline{U} = 0.32\%$, which is considered low. The first order phase also exhibits monotone convergence for the last three solutions, yielding achieved order of temporal accuracy of $p = 0.81$. Although the solutions are within the asymptotic range where $\mathcal{A} = 0.993$, the low order of accuracy may be caused by small changes in the solution for large n. Even with the low achieved order of temporal accuracy, the temporal resolution uncertainty is $\overline{U} = 1.41\%$. As a reference, for $n = 100, 200$ and 400 combinations, the achieved order of temporal accuracy for the amplitude is $p = 1.08$ and for the phase $p = 1.22$.

6.3.5. Grid Refinement Study

The grid refinement study is carried out using the constant grid refinement ratio $r = 2$, producing one coarser grid with 2 970 cells and one finer grid with 46 800, along with the original grid consisting of 11 700 cells. It is important to note that the coarsest grid has approximately 7.5 cells per wave height (approximately 4 cells per wave amplitude), which may be considered coarse. The time step size is kept the same as in the benchmark test case, corresponding to 800 time steps per wave period. Figure 6.19 presents the comparison of coarse, medium and fine grid solutions with the stream function wave theory for last two periods (wave gauge 2). It is interesting to note that even the results on the coarse grid (2 970 cells) are reasonably accurate for engineering purposes. The convergence of first order harmonic amplitude with respect to grid refinement is presented in Figure 6.18a, where the monotone convergence is achieved. The achieved order of convergence is $p = 1.64$, which is lower than theoretical second–order accuracy. The asymptotic range ratio is $\mathcal{A} = 1.002$, hence the solutions for harmonic amplitudes are within the asymptotic range. The corresponding grid uncertainty is $\overline{U} = 0.16\%$, indicating extremely low sensitivity of the solution with grid refinement, which can be directly observed in Figure 6.18a where the y–axis varies within approximately 1% of the wave amplitude. The convergence

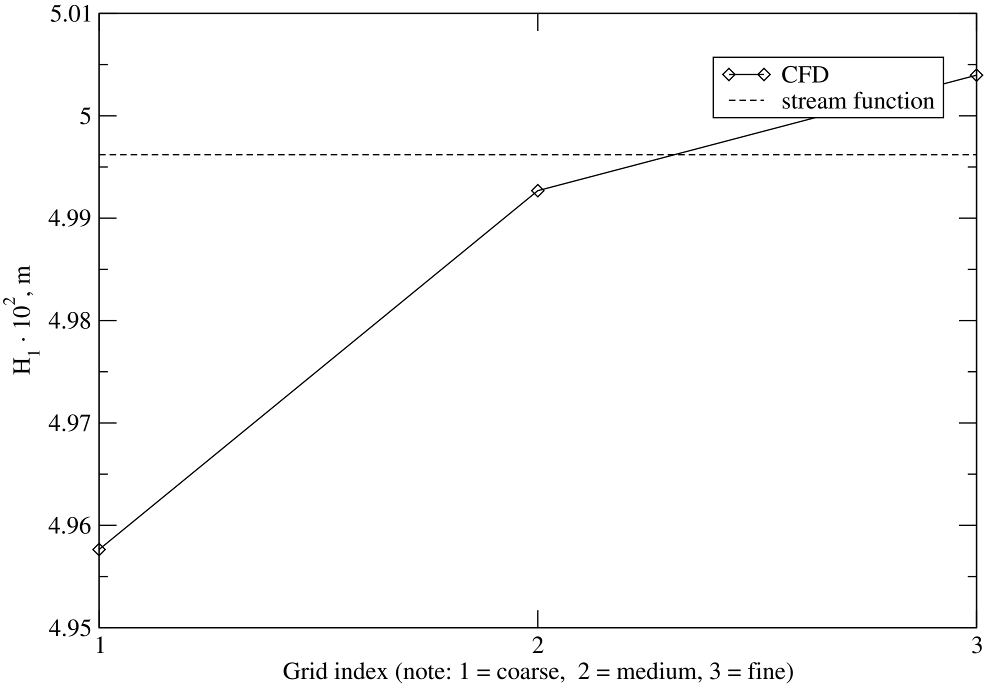

(a) First order harmonic amplitude,

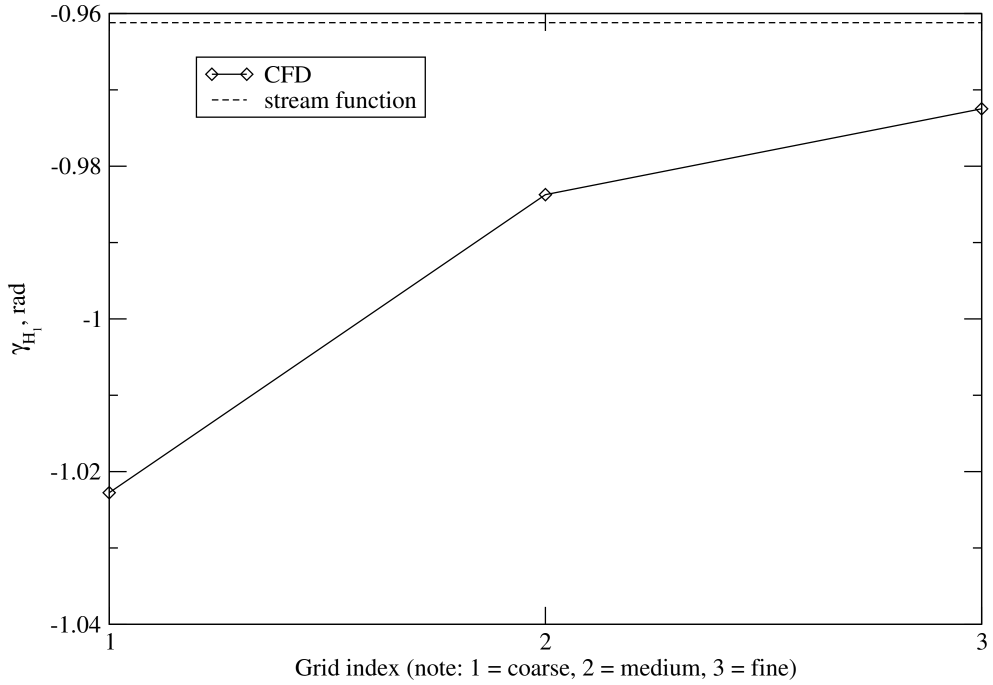

(b) First order harmonic phase,

Figure 6.18: Sensitivity of the solution with respect to grid resolution, frequency domain.

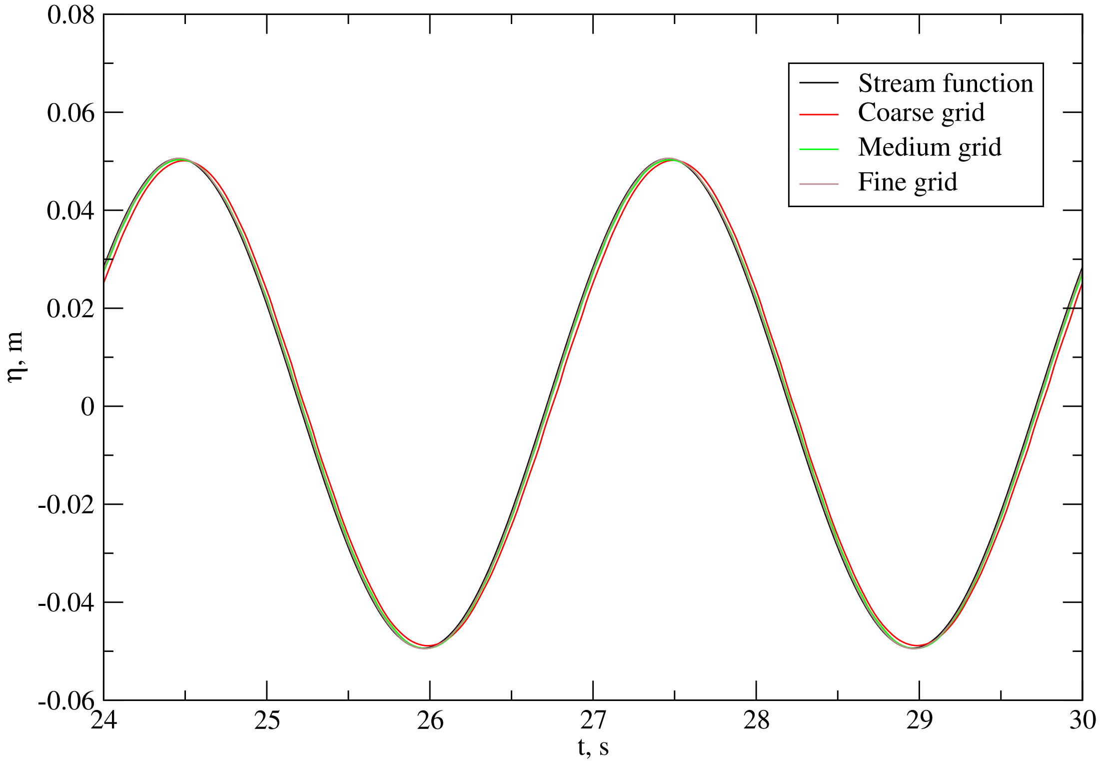

Figure 6.19: Time domain signals for last two periods, different grid resolutions.

of first order harmonic phase exhibits similar trend, as seen in Figure 6.18b. Monotone convergence is achieved and the order of convergence is $p = 1.80$. The asymptotic range is again close to unity $\mathcal{A} = 0.989$ and the corresponding grid uncertainty is low $\overline{U} = 0.70\%$ for the first order phase.

6.3.6. Steepness Study

Wave steepness is often represented by dimensionless number, ka where k is the wave number in radians per second and a is the amplitude of the wave in meters. The nonlinearity of wave increases with increasing steepness, where the theoretical deep water breaking limit corresponds to $ka \approx 0.44$ [84]. Due to nonlinearity, the wave length also changes according to the specified wave height and period, however, this change is considered small compared to the change in wave height. In this study, the wave height is gradually increased from 0.2 to 1.6 m, while the wave period, $T = 3$ seconds is kept constant, yielding a steepness range from 0.045 to 0.325 according to the nonlinear stream function

Table 6.8: Wave parameters for steepness study.

Index i	Wave amplitude a, m	Wave length λ, m	Wave number k, rad/s	Steepness ka
1	0.1	13.9546	0.4503	0.04503
2	0.2	14.0360	0.4477	0.08953
3	0.3	14.1688	0.4435	0.13304
4	0.4	14.3488	0.4379	0.17516
5	0.5	14.5714	0.4312	0.21560
6	0.6	14.8314	0.4236	0.25418
7	0.7	15.1236	0.4155	0.29082
8	0.8	15.4427	0.4069	0.32550

solution, Table 6.8. For each case, the total number of cells in the grid remained constant (11 700). However, spacing of the blocks is adjusted with wave height such that there are always 15 cells per wave height and 100 cells per wave length in the middle of the domain. This way, the grid is identical (with respect to wave parameters) to the one used in the benchmark test case.

Results for the wave steepness study are shown in Figures 6.20–6.23, where the graphs present magnitude of Fourier harmonics for waves with different steepness (see Table 6.8). Since both the stream function wave theory and present CFD model are fully nonlinear, they both capture higher order effects with increasing steepness. The first order harmonic amplitudes compare very well for $ka < 0.29$, where for the two cases with highest steepness, the CFD model under–predicts the first order harmonic amplitude. The CFD results also agree well with the stream function wave theory for higher order harmonic, where it is interesting to note that the higher order harmonics are slightly over–predicted for two highest steepnesses, Figure 6.23a and Figure 6.23b. Hence, it may be concluded that the energy is shifted from first order harmonic towards higher harmonics with increasing steepness. This may be related to vorticity and viscous effects taken into account in the present CFD model. Furthermore, Figure 6.22a to Figure 6.23b reveal that a certain amount of energy is also present between multiples of the base

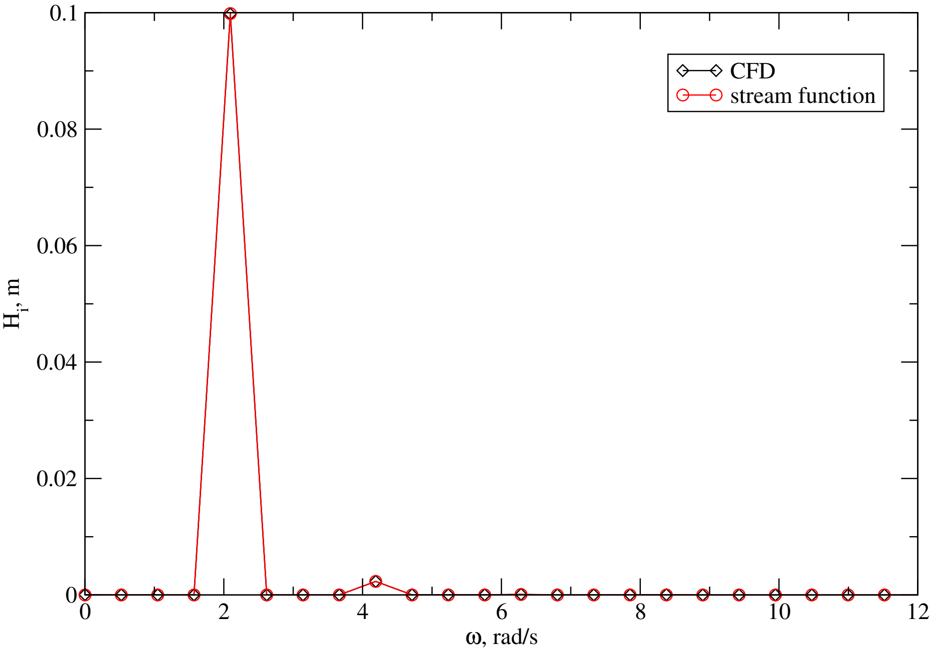

(a) Wave number 1: $ka = 0.04503$,

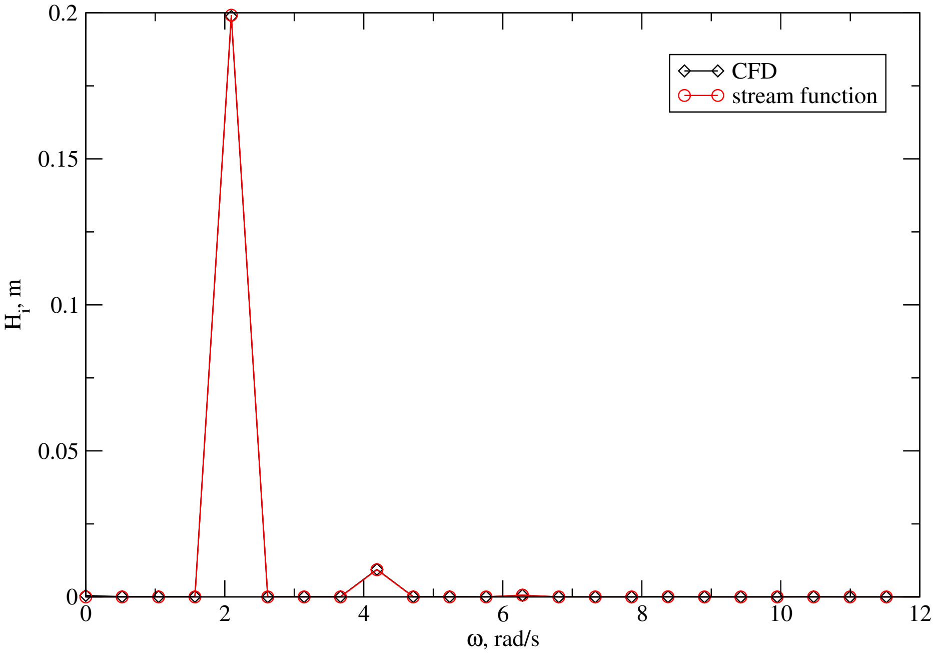

(b) Wave number 2: $ka = 0.08953$,

Figure 6.20: Fourier harmonics obtained with stream function wave theory and present CFD model for varying wave steepness, wave numbers 1 and 2.

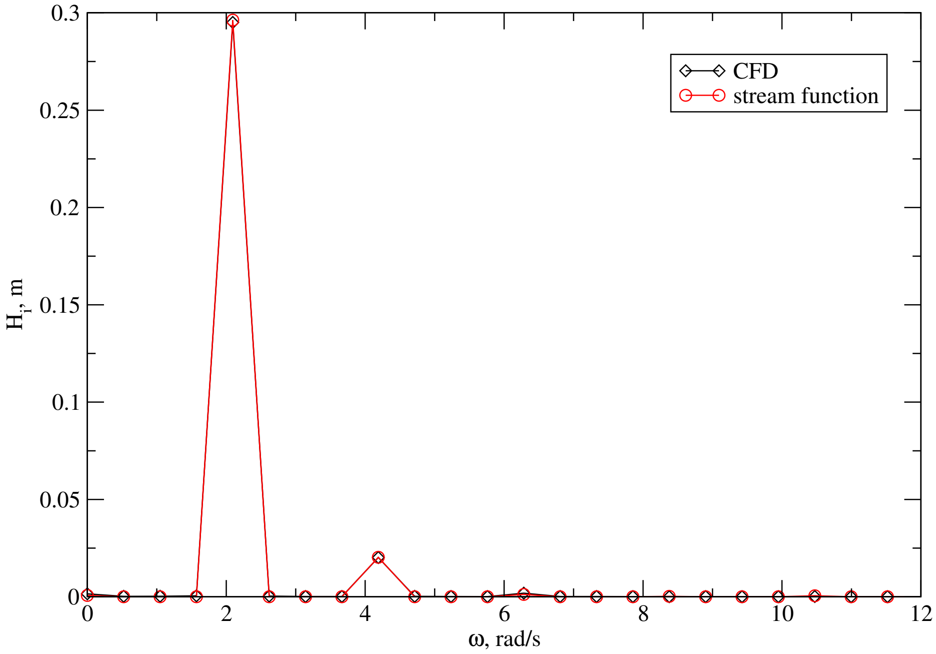

(a) Wave number 3: $ka = 0.13304$,

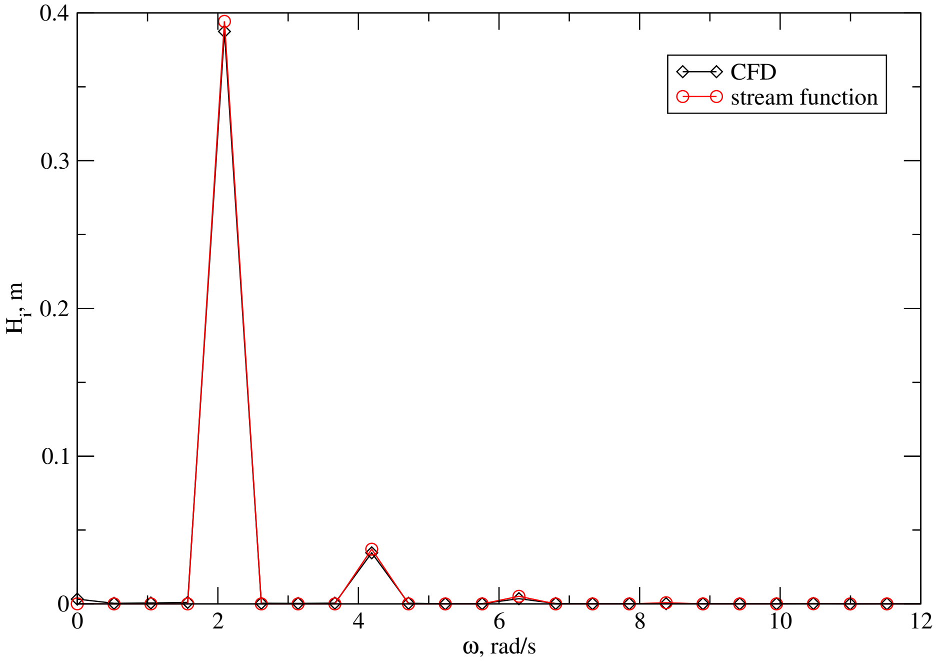

(b) Wave number 4: $ka = 0.17516$,

Figure 6.21: Fourier harmonics obtained with stream function wave theory and present CFD model for varying wave steepness, wave numbers 3 and 4.

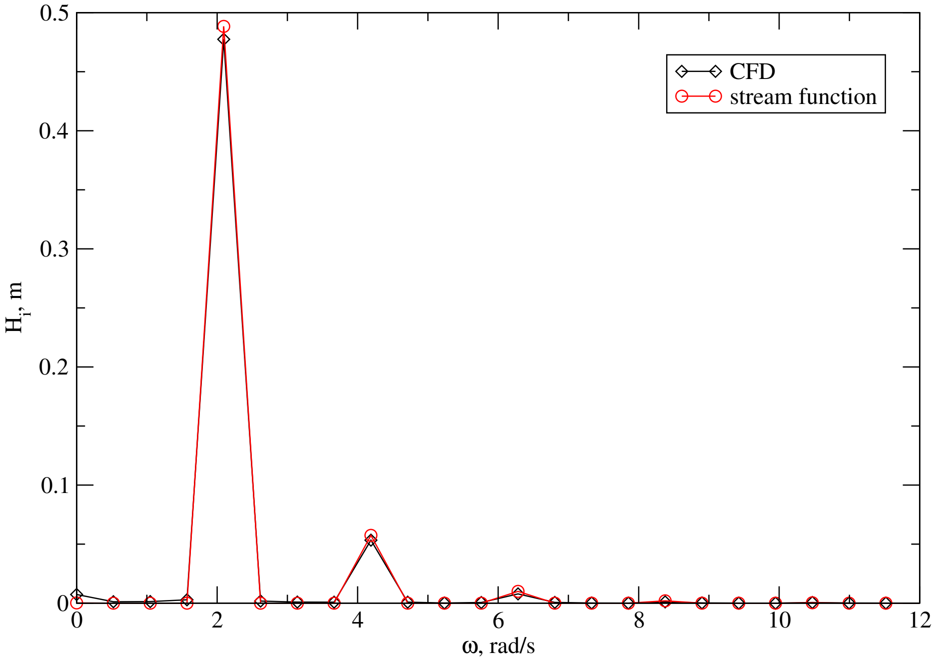

(a) Wave number 5: $ka = 0.21560$,

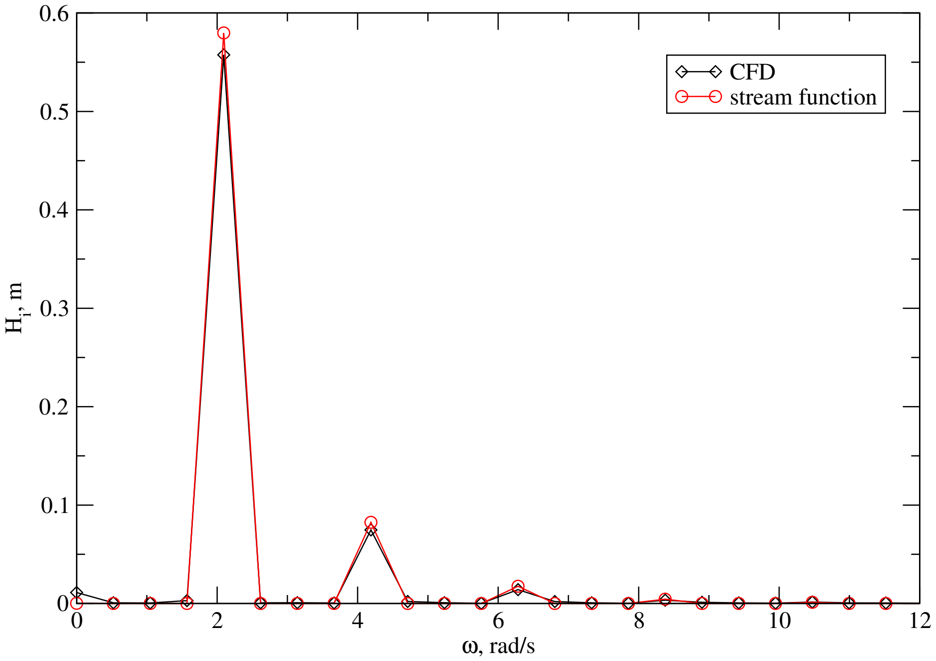

(b) Wave number 6: $ka = 0.25418$,

Figure 6.22: Fourier harmonics obtained with stream function wave theory and present CFD model for varying wave steepness, wave numbers 5 and 6.

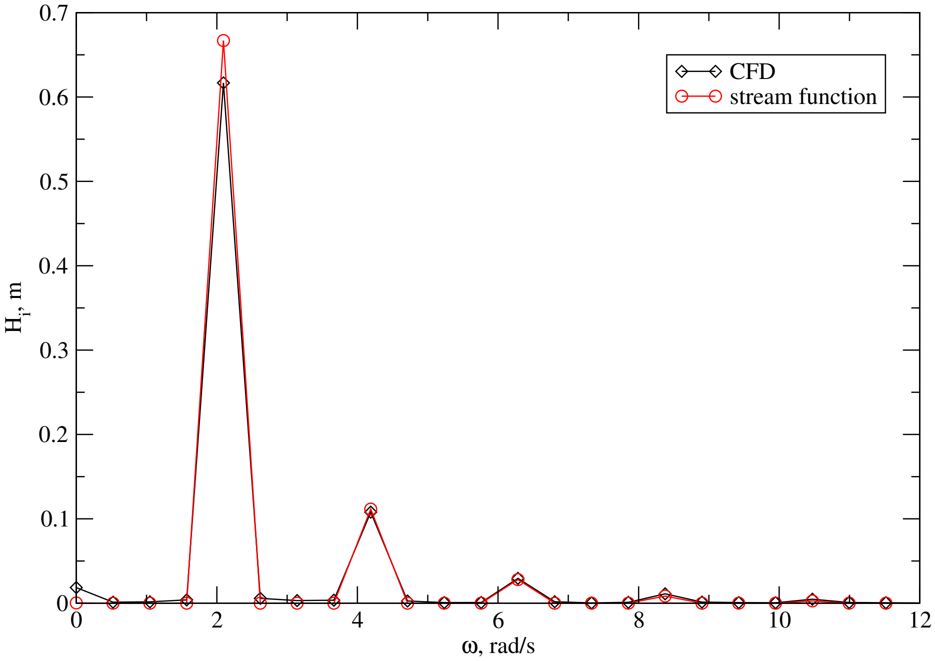

(a) Wave number 7: $ka = 0.29082$,

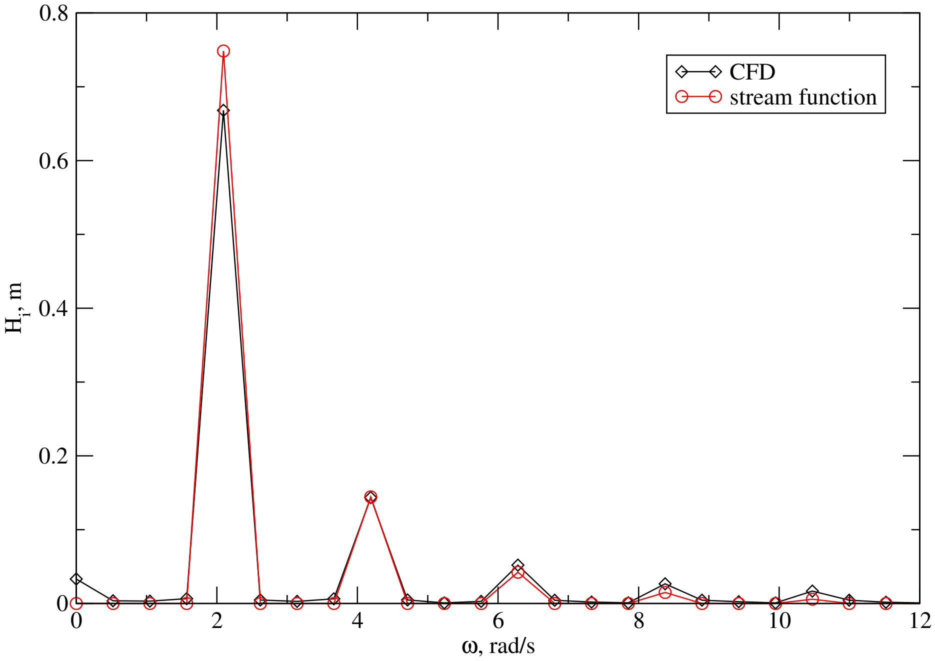

(b) Wave number 8: $ka = 0.32550$,

Figure 6.23: Fourier harmonics obtained with stream function wave theory and present CFD model for varying wave steepness, wave numbers 7 and 8.

frequency. This effect is not present in the stream function wave theory since the solution is sought in the frequency domain.

6.3.7. Long Simulation Stability Assessment

Stability of the simulation, mass conservation and periodic uncertainty are assessed with a very long simulation of the benchmark test case (see Table 6.4 in Sec. 6.3.1.) corresponding to 100 wave periods. The representative time domain signal for wave gauge 2 is presented in Figure 6.24 and Figure 6.25. Since it would be cumbersome to present the whole signal 100 periods long, the signal is split into four representative parts for clarity, each representing 10 periods throughout simulation. As indicated in Figure 6.24 and Figure 6.25, both the first order harmonic amplitude and phase remain stable during a long simulation.

In order to assess periodic uncertainty, a moving window FFT is performed through all periods and the uncertainty is calculated using Eqn. (5.6) for a set of periods: $(i-5)^{\text{th}}$ to i^{th} period, where i is the period index, starting from fifth period. For example, if $i = 50$, periods 45 to 50 are used for periodic uncertainty calculation. The behaviour of periodic uncertainty for different sets of periods is presented in Figure 6.26, where following conclusions may be drawn:

- The periodic uncertainty is lower than 0.1% for longer simulation times, while in the beginning of the simulation, the uncertainty does not exceed 0.3%. This may be considered negligibly low.
- All wave gauges exhibit highly irregular pattern of periodic uncertainty throughout periods, which the author cannot currently explain.
- Starting from $i = 11$ (periods 6 to 11), the periodic uncertainty is drastically lowered.

In the LS interface capturing method, the preservation of the signed distance function is important for both mass conservation and correct interface reconstruction required by interface–corrected schemes via GFM approach. The preservation of the signed distance profile may be seen in Figure 6.27, showing the LS field in the middle part of the domain bounded by $x \in [29, 31]$ m and $y \in [-0.4, 0.4]$ m at 50^{th} period corresponding to $t = 150$ s. The interface location is denoted by

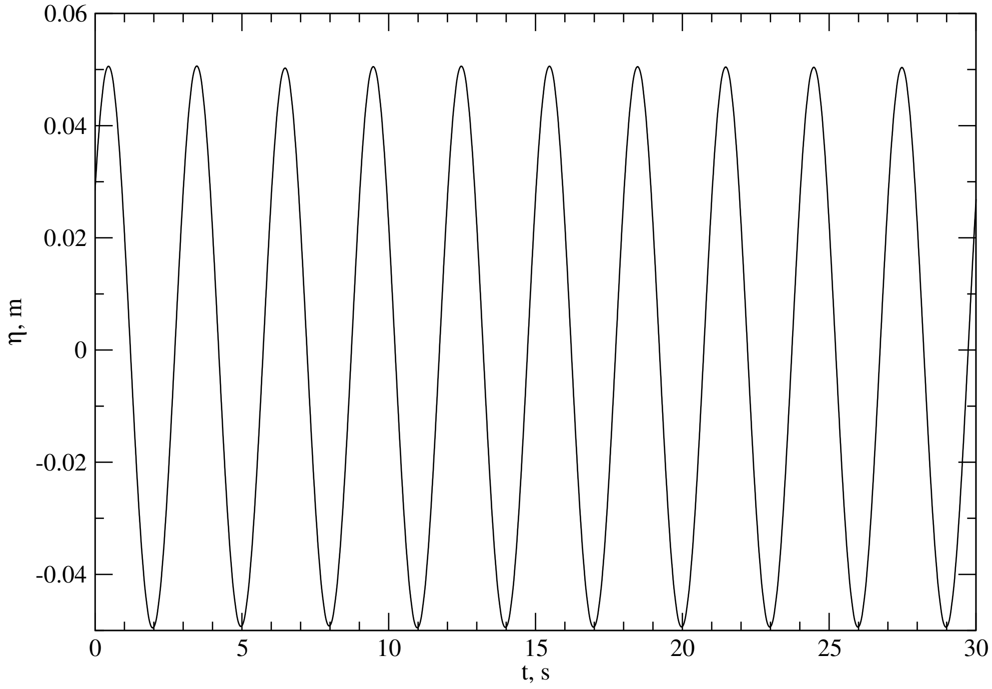

(a) Periods 1 to 10: $0 \leq t \leq 30$ s,

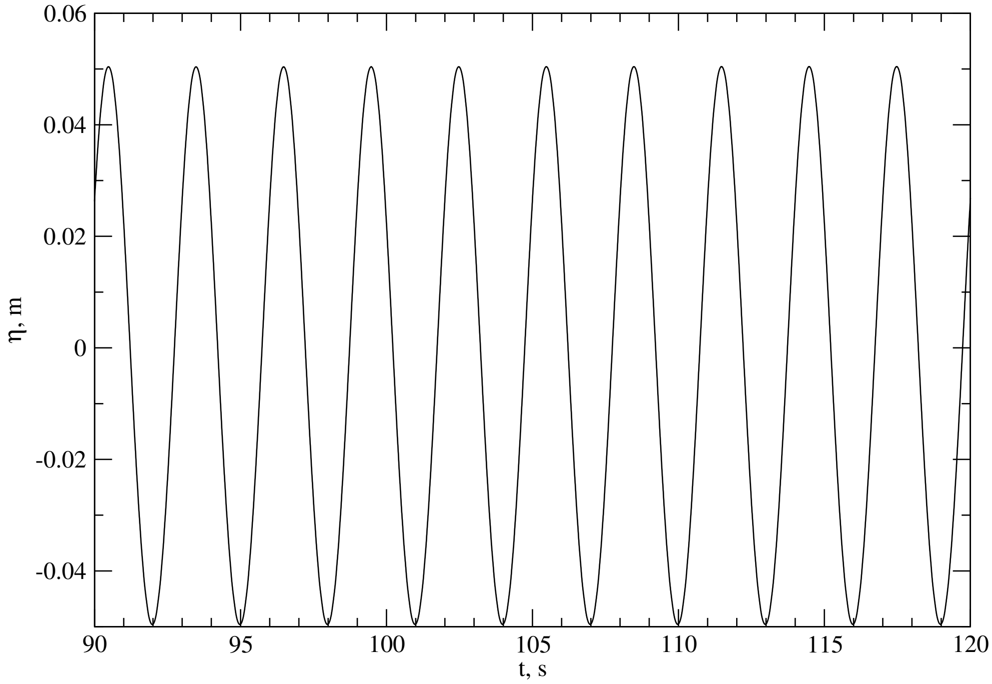

(b) Periods 30 to 40: $90 \leq t \leq 120$ s,

Figure 6.24: Time evolution of wave elevation during 100 periods for wave gauge 2, $x = 30$ m, part 1.

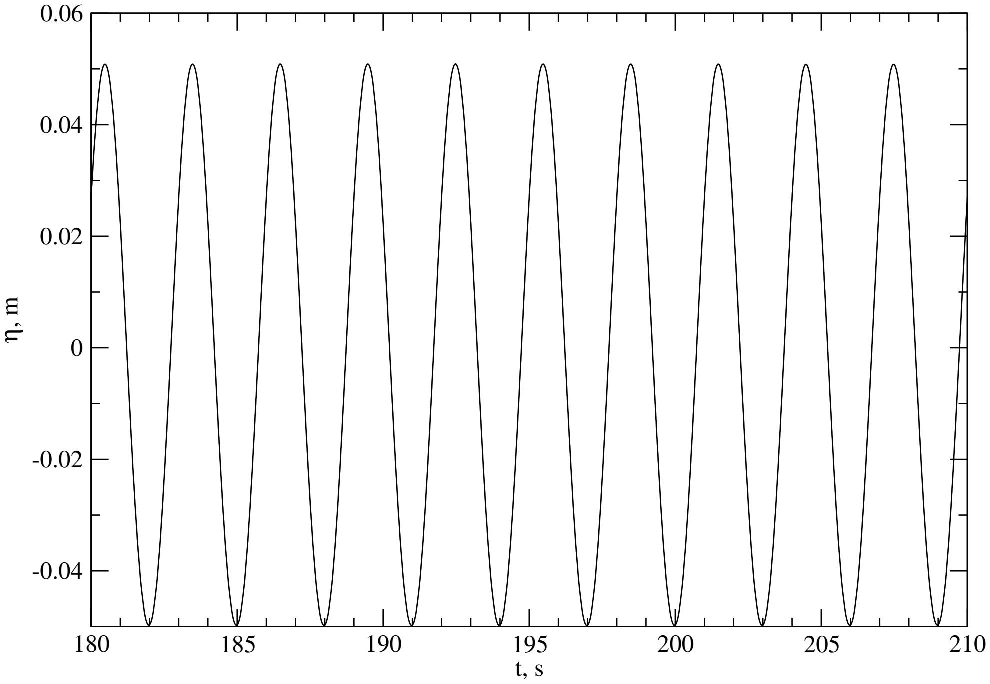

(a) Periods 60 to 70: $180 \leq t \leq 210$ s,

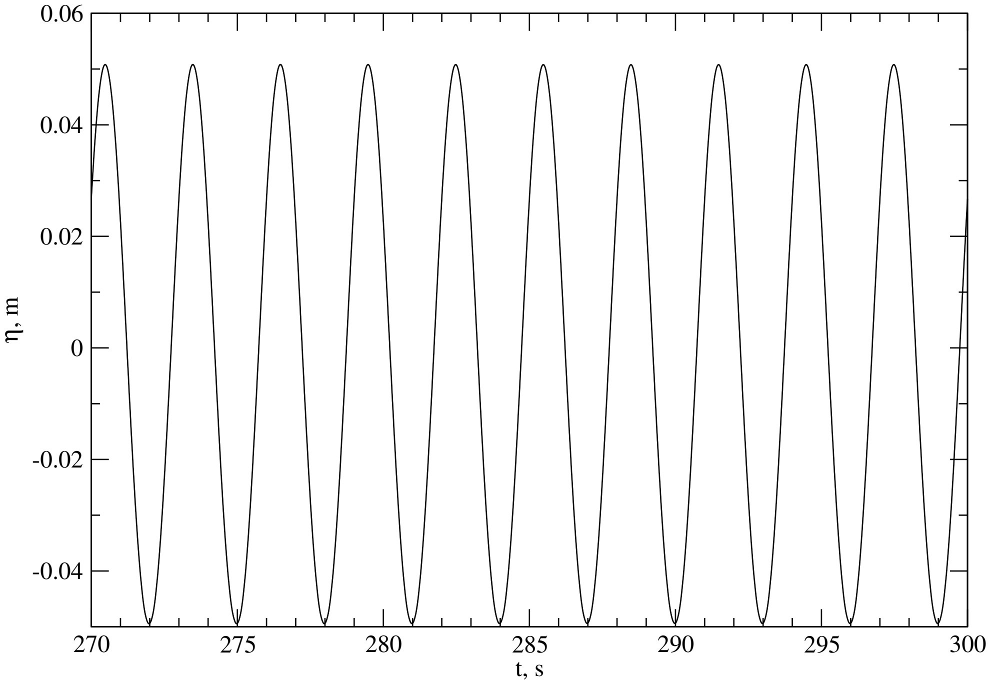

(b) Periods 90 to 100: $270 \leq t \leq 300$ s,

Figure 6.25: Time evolution of wave elevation during 100 periods for wave gauge 2, $x = 30$ m, part 2.

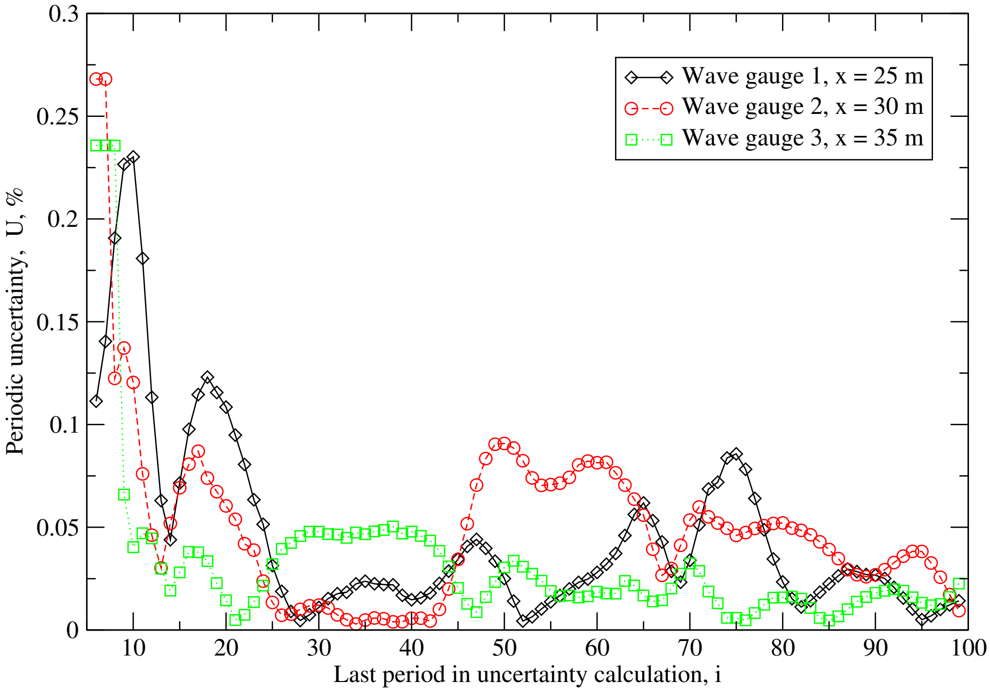

Figure 6.26: Behaviour of periodic uncertainty for all wave gauges during a long simulation.

a while line, representing zero LS ($\psi = 0$), while black lines denote iso–contours of the LS field equally spaced between -0.2 and 0.2. The signed distance profile of the LS field is well preserved.

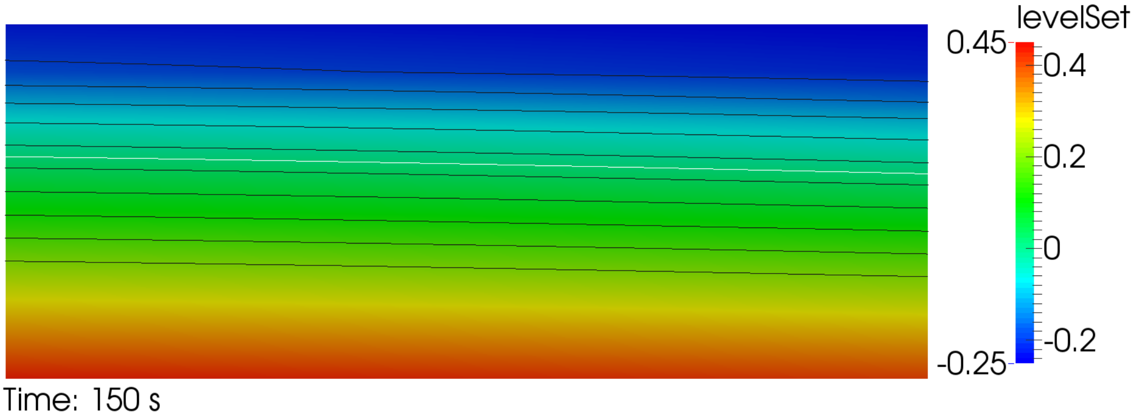

Figure 6.27: Preservation of the LS field in long simulation at $t = 150$ s.

In order to assess conservative properties of the implicitly redistanced LS method and implicit relaxation zones, the total amount of water during the simulation is closely investigated. The amount of water/air ratio changes at every time step since the domain length is not a multiple of wave length. The ratio of the volume occupied by water with respect to the total volume in the domain can be defined as:

$$G_w = \frac{\sum_P \alpha_P V_P}{\sum_P V_P}\,, \tag{6.5}$$

where α_P denotes the water fraction for cell P (calculated from the LS field with Eqn. (2.39)) and V_P is the volume of the cell. $\sum_P$ denotes summation over all cells in the grid. Figure 6.28a presents the evolution of global water ratio during last 10 periods for clarity. It is important to stress that the signal exhibits harmonic behaviour because the domain length is not directly proportional to incident wave length. Since the y–axis spans only 0.03%, good conservative properties are achieved. Nevertheless, in order to investigate the mean value of the water ratio during successive periods, a moving window FFT is performed and the results are presented in Figure 6.28b. Although the graph exhibits irregular behaviour through 100 periods, the largest deviation in the mean value is approximately $5 \cdot 10^{-4}$%, which is considered negligible for most engineering applications.

6.3.8. Long Domain Simulation

A long domain simulation is carried out in order to investigate the amount of dissipation (loss of wave amplitude) and dispersion (phase shift) related to wave propagation simulations. The same wave parameters and settings are used as in the benchmark test case (see Table 6.4, while the domain now spans from $x = 0$ to $x = 120$ m (in the longitudinal direction). The middle part of the domain where the full CFD solution is achieved contains approximately 5.5 wave lengths. As in the benchmark case, 100 cells per wave length and 15 cells per wave height are used in the full CFD region (see Figure 6.5 and Figure 6.5). Five wave gauges are used to measure wave elevation at different longitudinal coordinates: $x = 2\lambda_w, 3\lambda_w, \ldots 6\lambda_w$. The first order amplitude and phase for different x/λ_w are presented in Figure 6.29a and Figure 6.29b. The first order harmonic amplitude varies approximately 0.1% for the five wave gauges, which is significantly below cell resolution. It is interesting to note that the wave amplitude increases in direction of wave propagation (with increasing x/λ_w), hence there is no wave

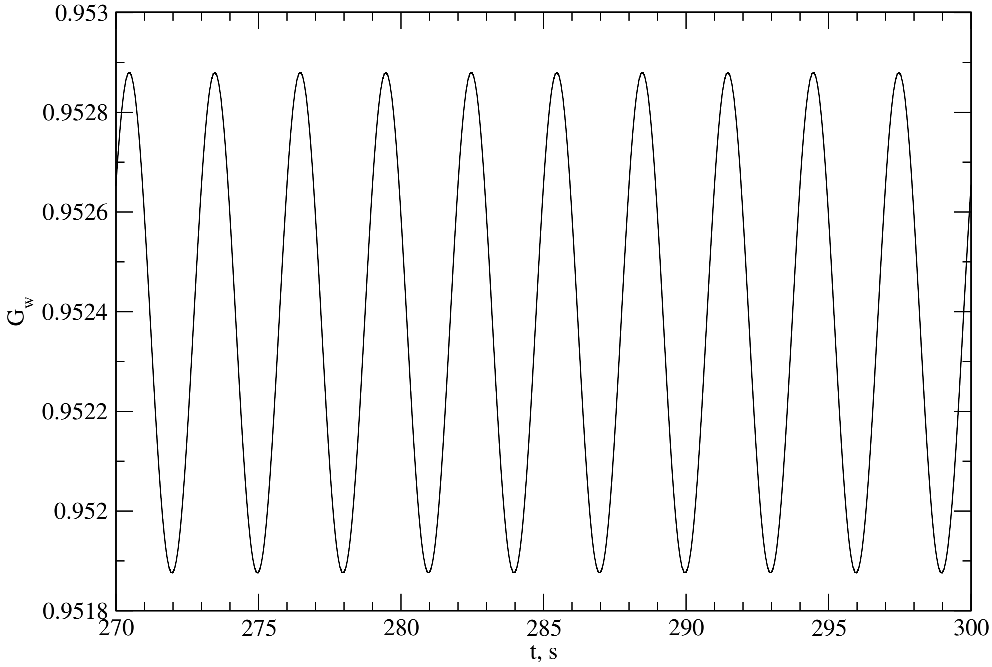

(a) Global water ratio G_r during last 10 periods for wave gauge 2, $x = 30$ m.

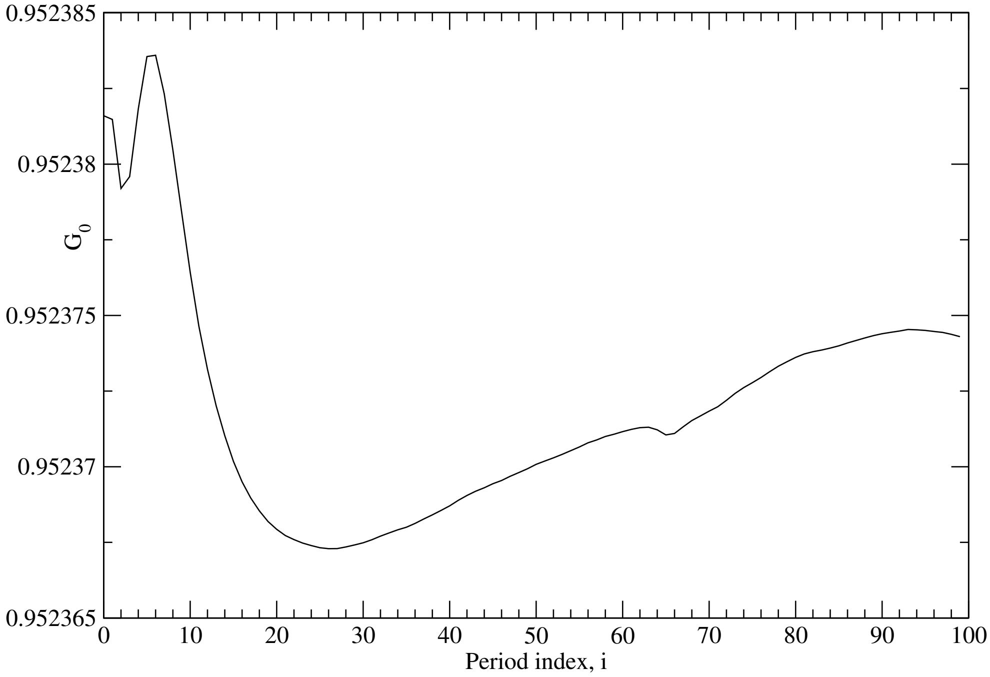

(b) Moving window FFT representation of the mean global water ratio G_0.

Figure 6.28: Global water ratio during the long simulation.

dissipation in the present simulation. The minor increase in amplitude might be explained by wave reflection off the outlet boundary, causing slightly higher wave amplitudes closer to the outlet. Figure 6.29b shows that the largest deviation of the first order harmonic phase is approximately 0.07 rad, *i.e.* 4°. It may be concluded that the dispersion error is more pronounced than the dissipation error, which might be expected when using second–order accurate schemes for wave propagation [15].

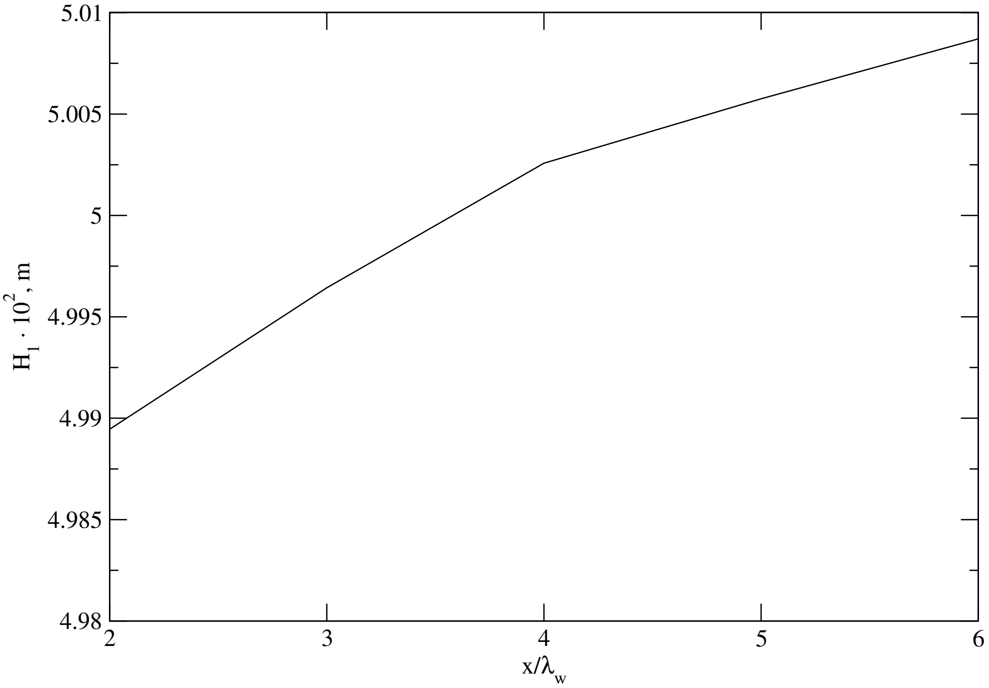

(a) First order harmonic amplitude,

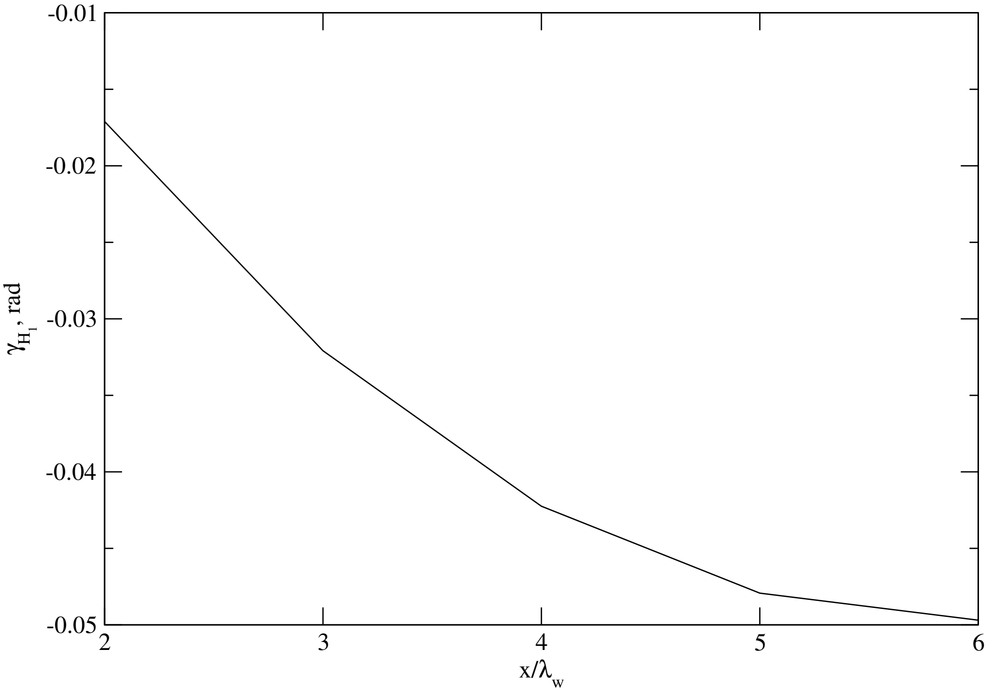

(b) First order harmonic phase,

Figure 6.29: Long domain simulation results for different wave gauges.

6.4. Higher Order Forces on a Vertical Cylinder

The third set of test cases considers regular wave diffraction of a 3–D vertical surface piercing cylinder. Since the regular wave propagation has been validated and verified in Sec. 6.3., emphasis is given here on higher order in–line forces. Although significantly smaller than the first order force, higher order forces may be important in offshore applications because of the ringing phenomena where the higher load frequency is close to the natural frequency of the structure (see [118, 119]). As the higher order forces are generally two to five orders of magnitude smaller in magnitude than the first order force, such test cases are suitable for validation of the present CFD model. Higher order forces have been thoroughly experimentally investigated by Huseby and Grue [120] for a wide range of incoming wave steepnesses. The CFD simulations are carried out for 8 wave steepnesses using the present model, where forces up to seventh order are compared to both the experimental measurements by Huseby and Grue [120] and fully nonlinear, time domain potential flow solution by Ferrant [121]. Furthermore, in order to verify the present model and calculate the achieved orders of accuracy and consequently numerical uncertainties, temporal resolution and grid refinement studies are presented for one representative test case.

The same discretisation schemes and numerical settings are employed for all test cases in this section as for the wave propagation test cases presented in the previous section, Sec. 6.3. No turbulence modelling has been employed since the turbulent effect are negligible.

6.4.1. Test Case Settings

The constant wave parameters for the considered test case are presented in Table 6.9. A single cylinder is investigated with a radius of $r = 3$ cm. Incoming wave frequency is $f = 1.425$ Hz, corresponding to the wave length of approximately $\lambda_w = 0.77$ m. The cylinder is mounted at the bottom of the wave tank (both experimental and numerical) at 0.6 m depth below the still water line. For a detailed discussion on the experimental setup, reader is referred to Huseby and Grue [120].

Additional numerical settings using the present CFD model are presented in the last 6 rows of Table 6.9. In order to successfully prevent wave reflection, relaxation zone length is set to approximately $1.5\lambda_w$, where λ_w is the incident wave length. A fixed time step of $8.772 \cdot 10^{-4}$ is used, corresponding to 800 time steps per incident wave period. This yields approximately 115 time steps per encounter period for seventh order effects, which shall be reported. The LS CFL number is set to $CFL_\psi = 1$, while the stabilisation constant is set to 10^8. It is important to note that the width parameter $\epsilon = 10^{-5}$ corresponds to sub–cell resolution. This does not cause any numerical difficulties as only the zero level set $\psi = 0$ is used to discretise the dynamic pressure and density jump conditions at the free surface via GFM.

A total of 8 test cases with varying steepness are considered in this study by changing the wave amplitude from $a \approx 0.72$ to 2.8 cm, as presented in Table 6.10. Corresponding wave steepnesses vary from $ka \approx 0.06$ to 0.24. It is also important to note that for the steepest test case (index 8 in Table 6.10), the wave amplitude $a \approx 2.9$ cm is almost equal to the cylinder radius $r = 3$ cm. All CFD simulations are carried out for 15 wave periods in order to assess periodic convergence and

Table 6.9: Wave and simulation parameters for the cylinder test case.

Cylinder radius	r, m	0.03
Wave frequency	f, Hz	1.425
Wave radian frequency	ω, rad/s	8.9535
Wave period	T, s	0.70175
Wave length	λ_w, m	0.76888
Wave number	k, rad/m	8.17185
Depth	d_d m	0.6
Relaxation zone length	λ_r, m	1.153
Time step	Δt, s	$8.772 \cdot 10^{-4}$
Number of time steps per period	n	800
LS CFL number	CFL_ψ	1
Stabilisation constant	γ	10^8
Width parameter	ϵ, m	10^{-5}

corresponding periodic uncertainties.

6.4.2. Grid Details

The bounding box of the block–structured, cylindrical grid is $x \in [-2\lambda_w, 2\lambda_w]$, $y \in [0, 2\lambda_w]$ and $z \in [-0.6, 5a]$, as presented in Figure 6.30 for the first case $i = 1$. The origin of the coordinate system is located at the centre of cylinder at still water line. The wave crest is at the origin at $t = 0$. Grids for all cases have the same extend of two wave lengths in the radial direction and the same depth of 0.6 m. The longitudinal symmetry plane is used to lower the CPU time as the flow may be considered symmetric. The cells are heavily graded towards the cylinder in the radial direction (x and y directions). In the vertical, z direction, the cells are graded towards the free surface. In the area near the cylinder, there are 120 cells per incoming wave length. Grids for all test cases consist of 552 000 orthogonal hexahedral cells, where the maximum aspect ratio for the first case is approximately 150. It is important to note that the grid consists of three layers of blocks in the vertical direction:

1. Lower block: $z \in [0, -2a]$,

Table 6.10: Wave amplitudes and steepnesses for cylinder test cases.

Index i	Wave amplitude a, m	Steepness ka
1	0.0072473	0.059224
2	0.0099250	0.081105
3	0.0126824	0.103640
4	0.0153360	0.125323
5	0.0180342	0.147374
6	0.0213882	0.174781
7	0.0246236	0.201220
8	0.0287647	0.235061

2. Middle block: $z \in [-2a, 2a]$,
3. Upper block: $z \in [2a, 5a]$.

The vertical extent of each block is defined with respect to wave amplitude, resulting in slightly different grid for each case. The number of cells per block is kept the same for all cases, always resulting in 20 cells per wave height (or 10 cells per wave amplitude).

6.4.3. Simulation Results

Simulation results are presented in the frequency domain as magnitudes and phases of the Fourier coefficients of the in–line force signal. The final result is obtained by performing a moving window FFT on the time domain signal and taking the average value of the last five periods. Following Ferrant [121] and Huseby and Grue [120], in–line force harmonics are presented in a dimensionless form:

$$F_i^{'} = \frac{F_i}{\rho_w |\mathbf{g}| r^3 \left(a/r\right)^i}\,, \tag{6.6}$$

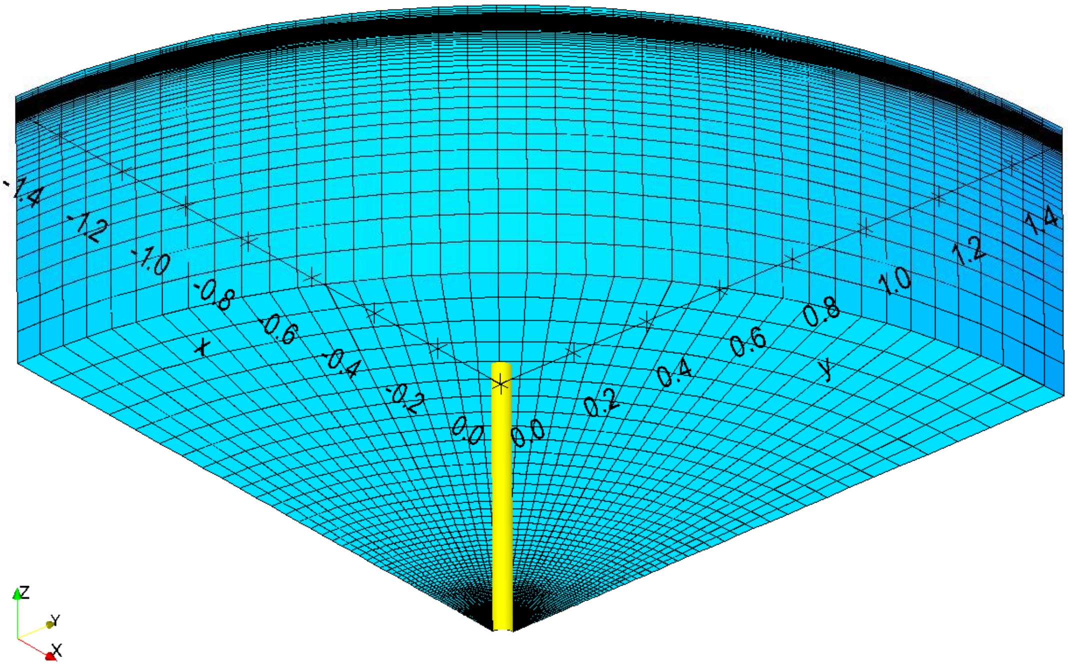

Figure 6.30: Perspective view of the cylindrical grid.

where F_i is the i–th harmonic of the force, $\rho = 1000$ kg/m^3 is the water density and $\mathbf{g} = [0, 0, -9.81]$ is the gravitational acceleration. As in experiments, the phase of force components has been measured relative to the phase of the incoming waves. It is important to note that both potential flow results [118] and experimental results [120] report only pressure part of the force:

- As Ferrant [121] used potential flow model, they do not have the ability to model viscous effects,
- While Huseby and Grue [120] have estimated the drag force due to the laminar boundary layer to be $0.1\pi\rho_w|\mathbf{g}|ar^2$, which has been excluded from the final results.

Although the present CFD model has the ability to accurately model viscous effects, only the pressure part of the force shall be presented when comparing the results with experimental and potential flow results, where a brief discussion on viscosity and vorticity effects shall be given afterwards.

Computational results for the first and higher orders of the in–line pressure force are presented in Figures 6.31–6.34 for the range of wave steepness from $ka \approx 0.06$ to 0.24. CFD results include error bars denoting the periodic uncertainty obtained using the procedure explained in Sec. 5.2.3.. Experimental results by Huseby and Grue [120] are denoted with dashed lines and squares, while the fully nonlinear, time–domain potential flow solutions by Ferrant [121] are denoted with dotted lines and plus signs.

The first order harmonic amplitudes presented in Figure 6.31a compare well with both the experimental results and potential flow results, especially up to $ka = 0.15$. For steeper waves, the CFD results under–predict the experimentally measured first order force, where the maximum relative error is approximately 5% for the wave with highest steepness $ka \approx 0.24$. Narrow error bars denote very low periodic uncertainties that are always below 0.2%.

The first order harmonic phases are presented in Figure 6.31b. CFD, experimental and potential flow first order phases vary slightly with increasing steepness. Furthermore, comparing with experimental data, both CFD results and potential flow results exhibit a phase shift. As for the harmonic amplitudes, narrow error bars denote very low periodic uncertainties.

The second order harmonic amplitudes are presented in Figure 6.31c, where a good comparison with both the experimental data and potential flow results can be observed. The trend of decreasing dimensionless second order force with increasing wave steepness is captured in CFD, even for very steep waves. Generally, computational results (both CFD and potential flow) over–predict experimentally measured values. Looking at the error bars, a slight increase in periodic uncertainties with increasing wave steepness may be observed. However, the periodic uncertainty even for the highest wave steepness is approximately 4%.

The second order harmonic phases are presented in Figure 6.31d, indicating very good agreement with potential flow results. Both CFD and potential flow phases are slightly off–set compared to experimentally measured phases, while error bars denote low periodic uncertainty, except for the case with $ka \approx 0.2$.

The third order harmonic amplitudes are presented in Figure 6.32a. CFD results agree very well with both the experimental and potential flow results over the whole range of wave steepnesses. Furthermore, narrow error bars indicate low uncertainty, again slightly increasing with increasing incoming wave steepness.

The third order harmonic phases are presented in Figure 6.32b, indicating similar behaviour as second order phases where CFD results are off–set by a constant amount compared to experimental data. The trend of phases with increasing steepness is accurately captured and most of the phases have low periodic uncertainty.

The fourth order harmonic amplitudes are presented in Figure 6.32c, where a good agreement of current CFD results with both experimental and potential flow results is shown. Periodic uncertainties are lower than 4%, which is approximately the maximum uncertainty obtained for the steepest incoming wave.

The fourth order harmonic phases are presented in Figure 6.32d, where a better agreement has been obtained compared to potential flow results than experimental measurements. It is interesting to note that the fourth order phases change only slightly with increasing wave steepness. Apart from the smallest wave steepness $ka \approx 0.06$ which has the smallest fourth order response, periodic uncertainty may be considered low as indicated by narrow error bars.

The fifth order harmonic amplitudes are presented in Figure 6.33a, where a good agreement has been obtained both with potential flow and measured results.

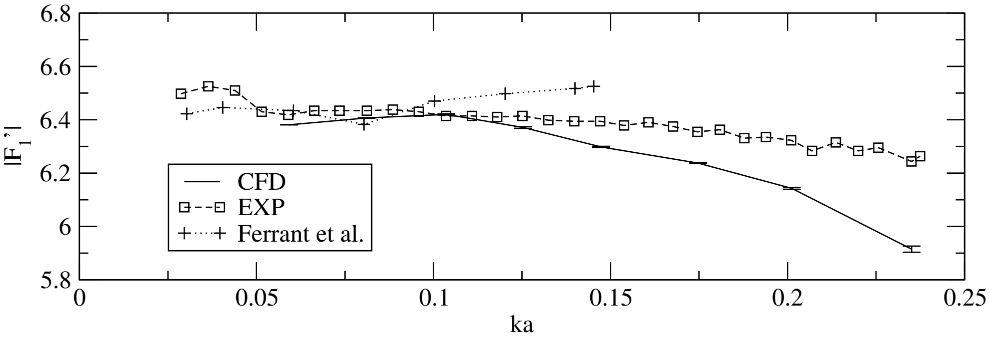

(a) First order harmonic amplitudes.

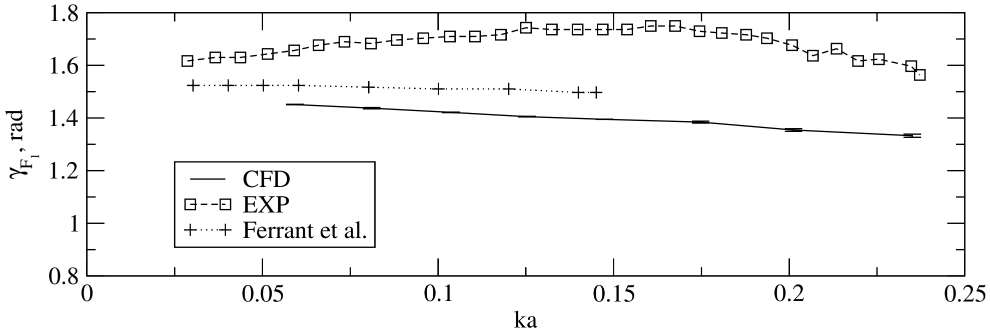

(b) First order harmonic phases.

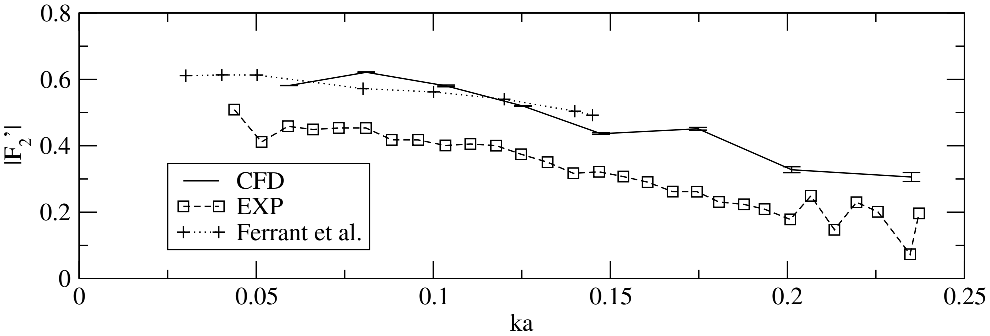

(c) Second order harmonic amplitudes.

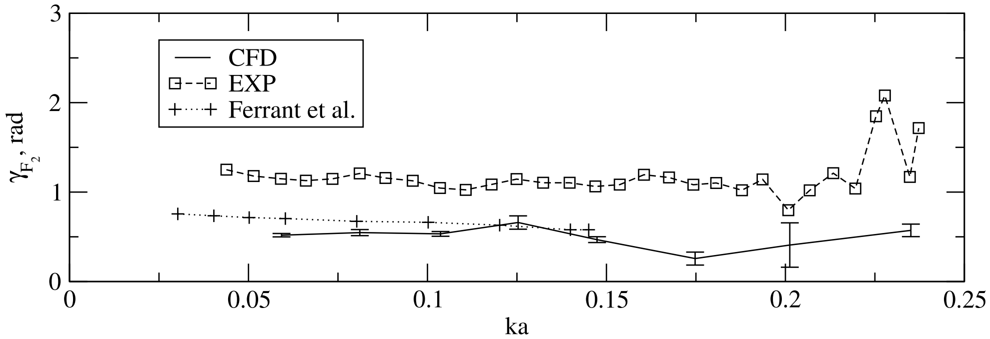

(d) Second order harmonic phases.

Figure 6.31: In–line harmonic forces on the circular cylinder, first and second order response.

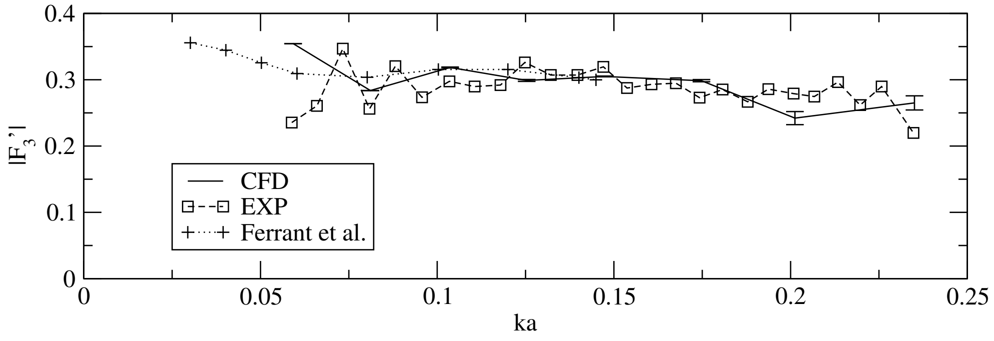

(a) Third order harmonic amplitudes.

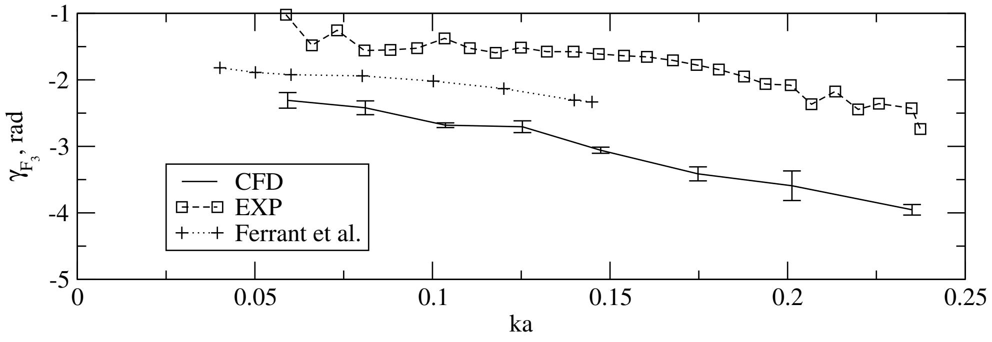

(b) Third order harmonic phases.

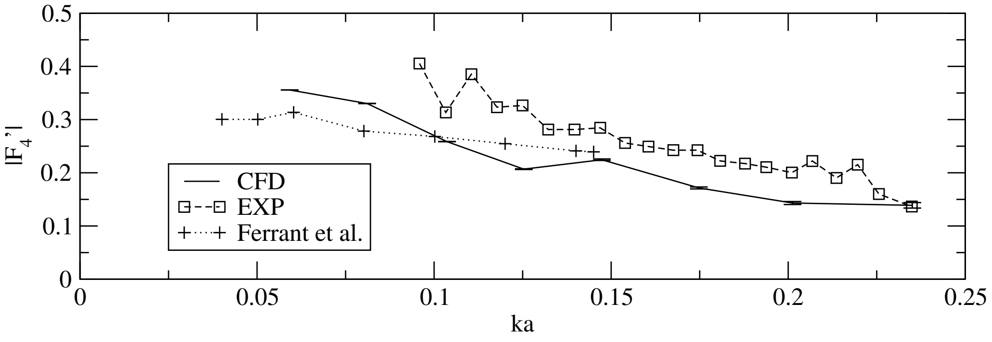

(c) Fourth order harmonic amplitudes.

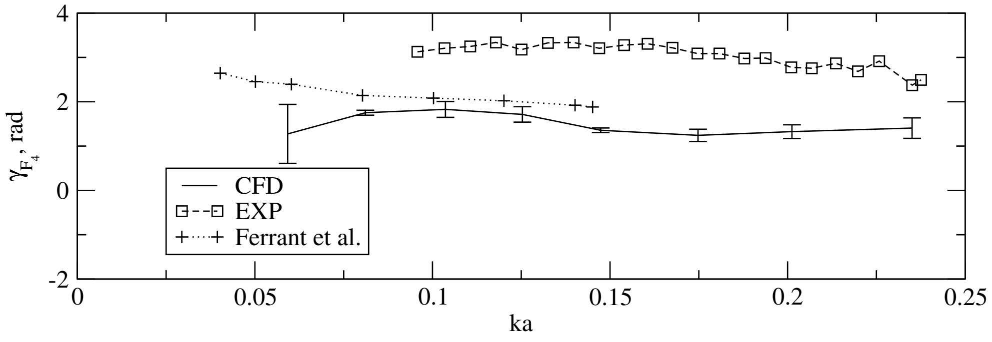

(d) Fourth order harmonic phases.

Figure 6.32: In–line harmonic forces on the circular cylinder, third and fourth order response.

It is important to note that the wave with the mildest steepness $ka \approx 0.6$ has been excluded from the figure since the fifth order response is close to the noise level in this case. The trend of the decreasing dimensionless fifth order in–line forces with increasing steepness is accurately captured and the periodic uncertainties are generally very low.

The fifth order harmonic phases are presented in Figure 6.33b. As with lower order phases, the CFD results compare well with the potential flow data, while deviating significantly from experimental data. Error bars are narrow, except for the very steep $ka \approx 0.2$ case.

The sixth order harmonic amplitudes are presented in Figure 6.33c, where the CFD results compare very well with the experimental measurements. Note that the two mildest waves have been excluded from the figure because their response is close to the noise level. Again, the error bars indicate insignificantly low periodic uncertainties.

The sixth order harmonic phases are presented in Figure 6.33d, where better agreement is obtained with potential flow results. Although offset compared to experimental measurements, sixth order harmonic phases have the same trend with increasing wave steepness compared to experimental data.

The seventh order harmonic amplitudes are presented in Figure 6.34a. It is important to stress that the seventh order response is 3 to 5 orders of magnitude smaller compare to first order response, depending on the wave steepness. Nevertheless, a very good comparison is obtained compared to both potential flow results in low wave steepness range, and experimental results in high wave steepness range. Considering very small response, the maximum periodic uncertainty of approximately 5% may be considered low.

The seventh order harmonic phases are presented in Figure 6.34b, where the CFD results are off–set compared to potential flow and experimental data. Although the periodic uncertainties for seventh order amplitudes are small, the corresponding uncertainties for phases are very high, indicating insufficient temporal resolution (note that 800 time steps per wave period have been used, yielding approximately 115 time steps per seventh order response).

Periodic convergence of seven force harmonics for the $ka \approx 0.2$ case ($i = 7$, Table 6.10) is presented in Figure 6.35, where the first order harmonic force

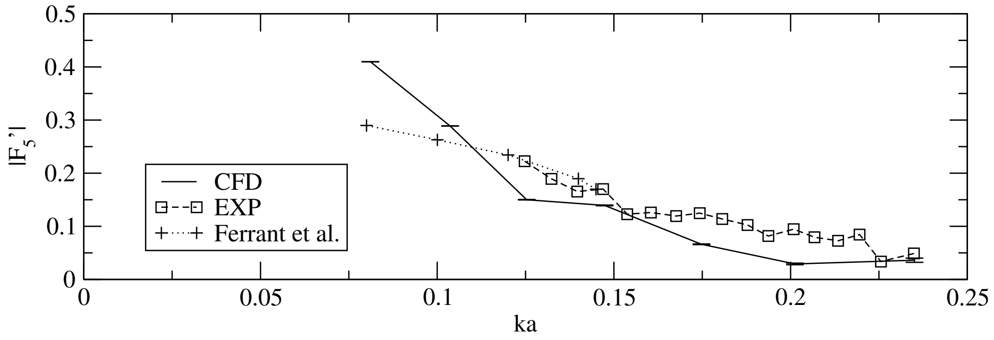

(a) Fifth order harmonic amplitudes.

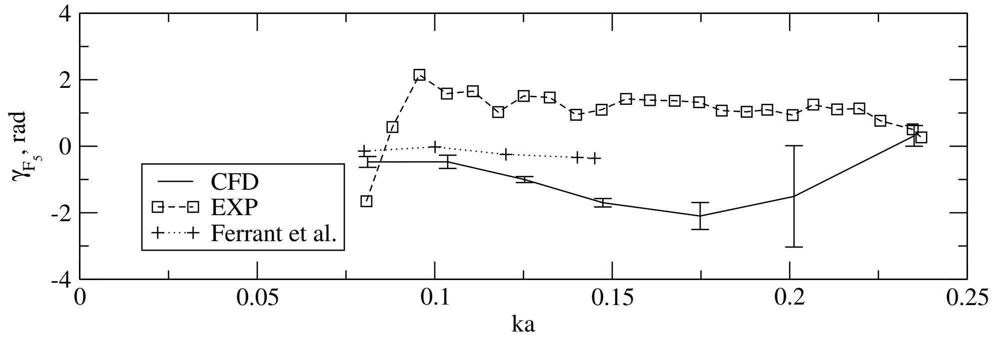

(b) Fifth order harmonic phases.

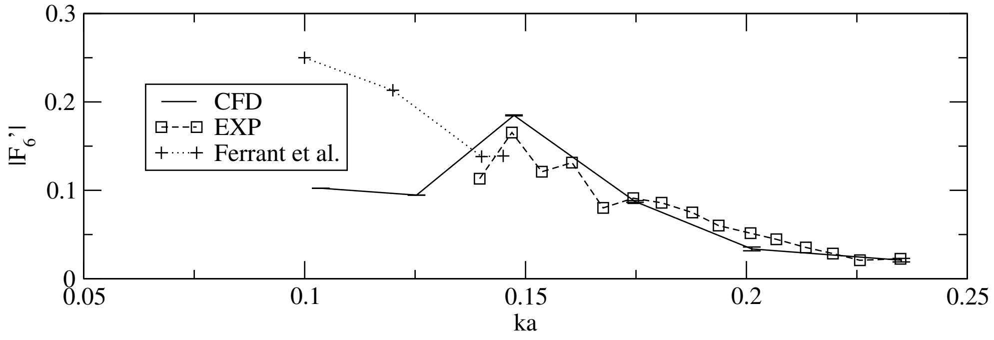

(c) Sixth order harmonic amplitudes.

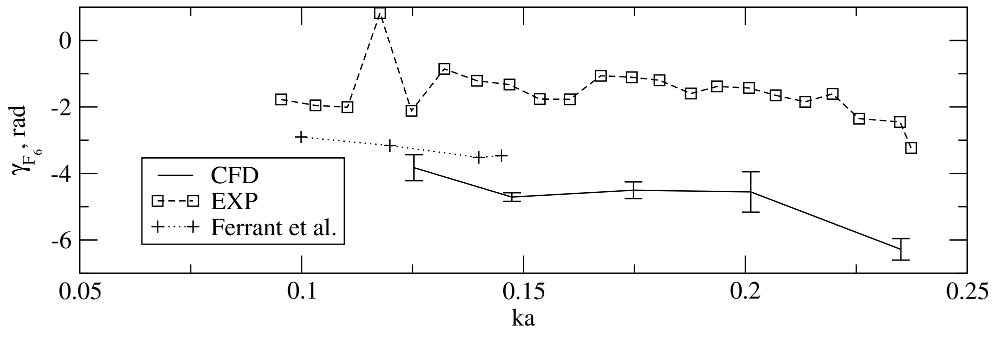

(d) Sixth order harmonic phases.

Figure 6.33: In–line harmonic forces on the circular cylinder, fifth and sixth order response.

amplitude has been divided by 10 for visualisation purposes. The amplitude of the first order harmonic force oscillates with a very narrow band through successive periods, where the value obtained within first period may be considered a good representation of the final result. All higher order force amplitudes have very large values during the first period because the CFD solution at $t = 0$ corresponds to incident flow solution. However, in successive periods all higher order forces rapidly decrease to a representative solution and exhibit oscillatory behaviour. Furthermore, it is interesting to note that the band of oscillations for second and third order harmonic amplitudes is larger compared to higher orders.

6.4.4. Temporal Resolution Study

The temporal resolution study is performed by simulating 25, 50, 100, 200, 400 and 800 time steps per wave period for the $ka \approx 0.13$ case ($i = 4$, Table 6.10), yielding a constant refinement ratio $r = 2$. It is important to note that using only 25 time steps per incident wave period yields less than 4 time steps per seventh order response.

Figure 6.36 presents time histories of the in–line force using increasing number of time steps per incident wave period. The time traces with $n \geq 100$ overlap each other, indicating that good results may be obtained even with only 100 time steps per wave period. Decreasing the number of time steps per encounter period below 100, yields significant dispersion (phase shift) error, while the dissipation (loss of amplitude) error is less pronounced.

The attention is now turned to frequency domain representation of the signals, presented in Figure 6.37. Figure 6.37a presents convergence of harmonic amplitudes with increasing number of time steps per period (from left to right). As expected, the first order harmonic amplitude is less sensitive to extremely coarse temporal resolution with $n = 25$ time steps per encounter period than higher order harmonic amplitudes. However, it is interesting to note that all higher order harmonic amplitudes are very well captured even with $n = 200$ time steps per period. Figure 6.37b presents convergence of harmonic phases, where similar trends can be observed. Extremely low temporal resolution of $n \leq 50$ time steps per period often exhibits significant dispersion errors. However, all

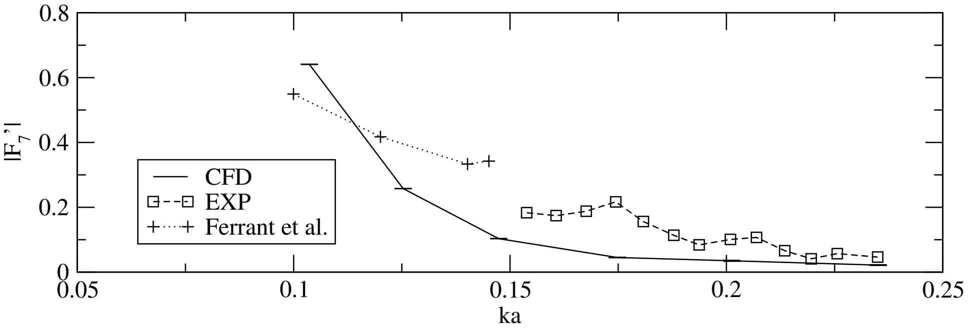

(a) Seventh order harmonic amplitudes.

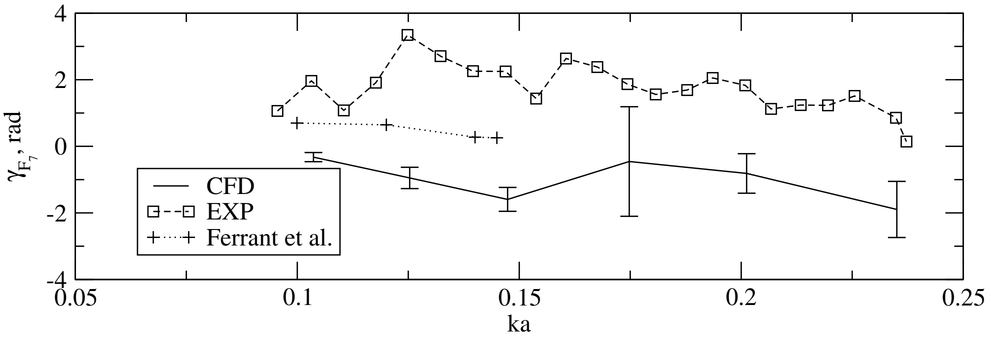

(b) Seventh order harmonic phases.

Figure 6.34: In–line harmonic forces on the circular cylinder, seventh order response.

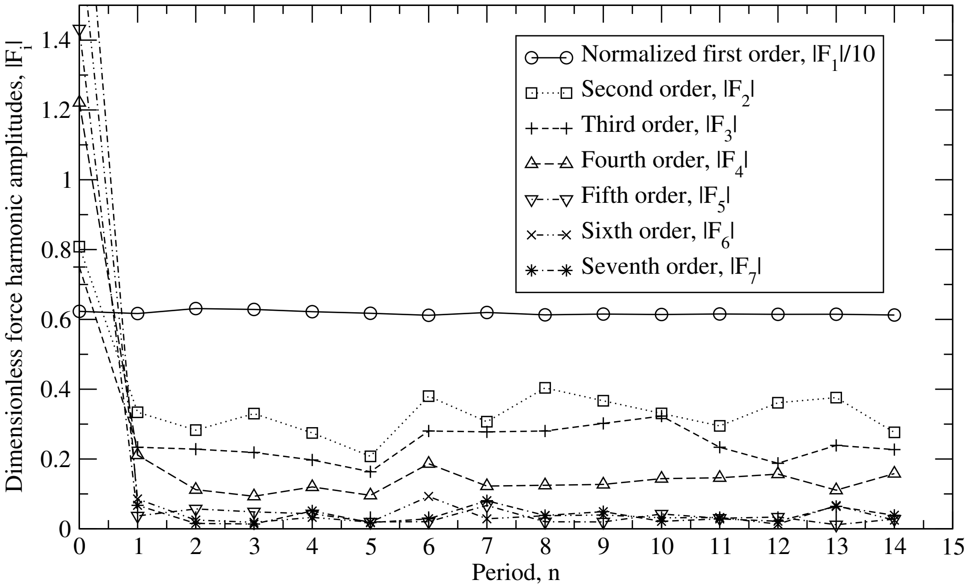

Figure 6.35: Periodic convergence of higher order forces through successive periods for $ka \approx 0.2$ case: moving window FFT plot.

harmonic phases except for the sixth order are insensitive when the number of time steps per encounter period exceeds 100. It is also interesting to note that a good result for the seventh order harmonic phase can be obtained with only 100 time steps per period, yielding approximately 14 time steps per seventh order response. This indicates that the overall solution is quite insensitive to temporal resolution and thus the required CPU resources can be significantly lowered.

Table 6.11 presents the convergence type, achieved order of convergence (where applicable) and corresponding temporal resolution uncertainties for harmonic amplitudes of the forces. Note that abbreviations MC, OC, MD and OD stand for Monotone Convergence, Oscillatory Convergence, Monotone Divergence and Oscillatory Divergence, respectively. The results presented in Table 6.11 are obtained with $n = 100, 200$ and 400 time steps per period. All harmonic amplitudes converge with increasing n, where 5 out of 7 exhibit monotone convergence, while 2 out of 7 exhibit oscillatory convergence. Since it is difficult to ensure that all orders are within the asymptotic range of convergence, the attention shall be turned to corresponding uncertainties. Generally, uncertainty increases with increasing

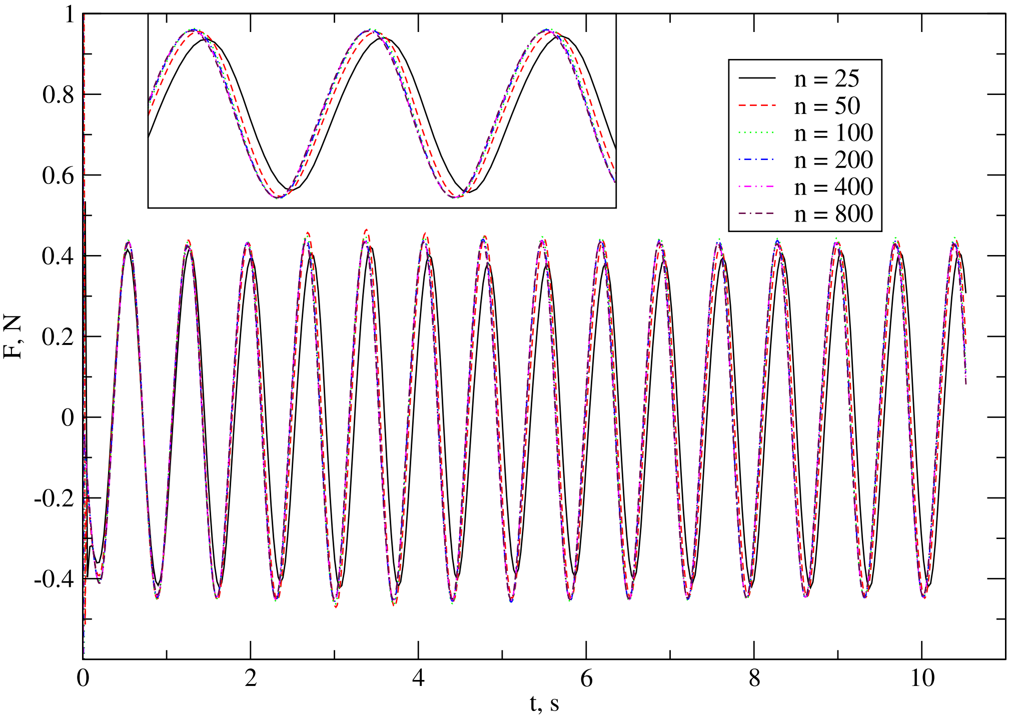

Figure 6.36: Force time signals with respect to number of time steps per period.

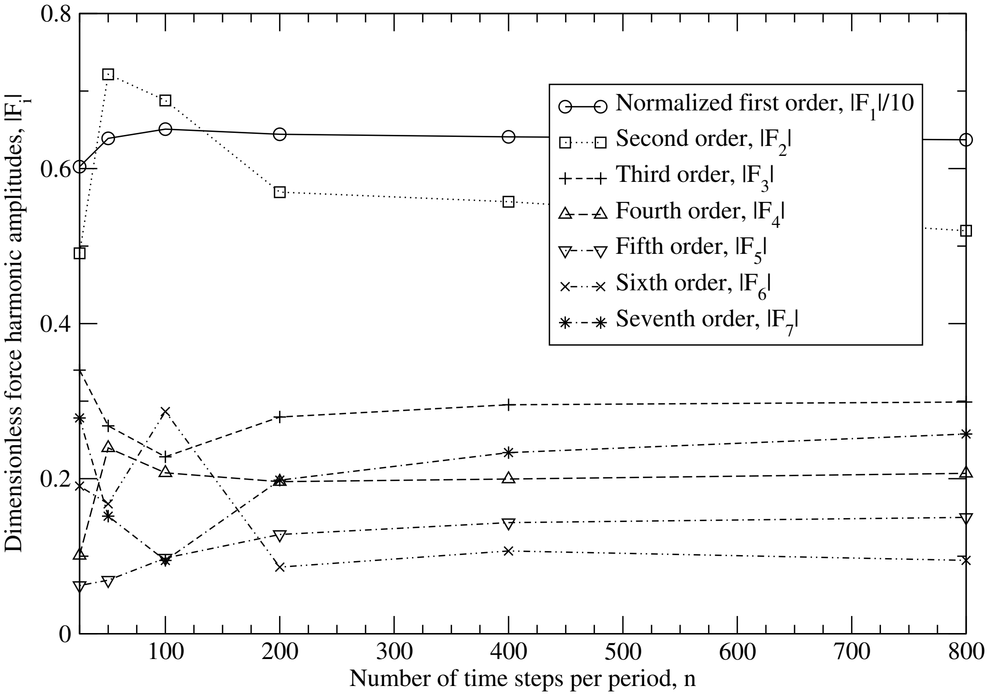

(a) Harmonic amplitudes.

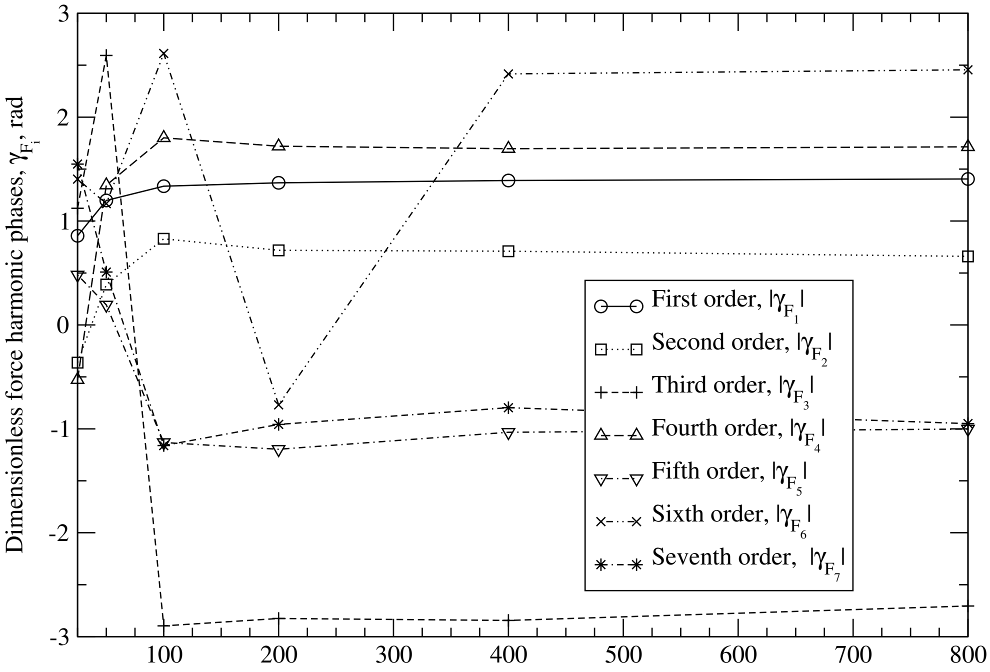

(b) Harmonic phases.

Figure 6.37: Convergence of higher order forces with increasing number of time steps per period.

order, as expected since the higher order effects are less temporally resolved. However, temporal resolution uncertainties are lesser than 1% for first and second order, while they are lesser than 5% for third and fourth order. Effects higher than fifth order have unrealistically high uncertainties due to normalisation of the uncertainty with very small measured values.

Table 6.11: Temporal resolution convergence and uncertainties for force harmonic amplitudes (obtained with $n = 100, 200$ and 400 time steps per period).

Order i	Convergence type	Order of convergence p	Uncertainty $U, \%$
1	MC	0.96	0.85
2	MC	3.25	0.39
3	MC	1.70	3.58
4	OC	N/A	4.27
5	MC	1.00	16.04
6	OC	N/A	141.03
7	MC	1.54	11.92

Table 6.12: Temporal resolution convergence and uncertainties for force harmonic phases (obtained with $n = 100, 200$ and 400 time steps per period).

Order i	Convergence type	Order of convergence p	Uncertainty $U, \%$
1	MC	0.51	5.78
2	MC	3.71	0.15
3	OC	N/A	1.87
4	MC	1.78	0.85
5	OD	N/A	23.81
6	OC	N/A	104.98
7	MC	0.34	114.19

Table 6.12 presents the same results for harmonic phases of the forces. All harmonic phases except fifth order exhibit convergence with increasing n: 3 exhibit monotone convergence and the other 3 oscillatory convergence. Uncertainties are generally lesser than 5%, except for higher order effects with non–representative high values. Reader is referred back to Figure 6.37b in order to realistically visualise the maximum deviations of the phases when using $n = 100, 200$ and 400 time steps per period.

6.4.5. Grid Refinement Study

The grid refinement study is performed on three grids, where the constant refinement (coarsening) ratio $r = 1.5$ has been applied in all three directions. Hence, the original grid with 552 000 cells is considered fine and two additional grids with 166 428 and 48 600 cells are considered medium and coarse, respectively. With respect to results obtained in the temporal resolution study, $n = 400$ time steps per period is used for grid refinement studies. Compared to the fine grid where the wave height is resolved with 20 cells, medium and coarse grids have approximately 13 and 9 cells per wave height, respectively.

Figure 6.38 presents time histories of the in–line force using the three grids, where the convergence with grid refinement of both amplitudes and phases of the in-line force can be observed. It is also interesting to note that once again, the dispersion (phase shift) error is more pronounced compared to dissipation (loss of wave amplitude) error when simulating wave phenomena on coarser grids. This is in accordance with results presented both in temporal resolution study and in wave propagation studies presented in Sec. 6.3.

As it is easier to discuss the results in the frequency domain, the convergence of harmonic amplitudes and phases of the dimensionless in–line forces with grid refinement is presented in Figure 6.39. Figure 6.39a presents the convergence of harmonic amplitudes with increasing grid resolution (from left to right). The first order amplitude is again insensitive to coarse grid resolution, while higher order effects exhibit irregular behaviour. However, it is important to note that the difference between medium and fine grid solutions is often small, *i.e.* the coarse grid results deviate the most for higher order amplitudes. Figure 6.39b presents

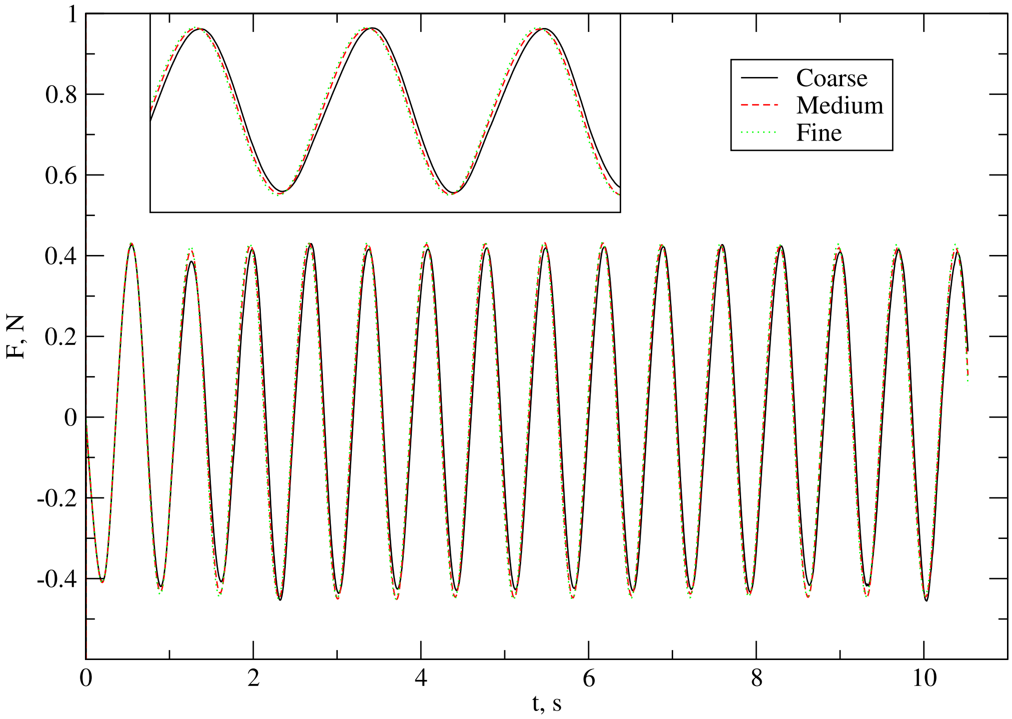

Figure 6.38: Force time signals with respect to grid resolution.

convergence of harmonic phases, where the first order harmonic phase is not significantly affected by the very coarse grid resolution. Apart from second and third order effects, higher order effects exhibit small differences between medium and fine grid solutions.

Table 6.13 presents the convergence type, achieved order of convergence (where applicable) and corresponding grid refinement uncertainties for harmonic amplitudes of the forces. All harmonic amplitudes converge with grid refinement except for the fourth order. The first, dominant order has the achieved order of accuracy of $p \approx 1.7$. The grid refinement uncertainty for the first order is lesser than 2%, while higher orders either have unrealistically low or high grid uncertainties since the solutions are not within asymptotic range. A better visualisation of the sensitivity of the results when performing simulations on medium and fine grids can be seen in Figure 6.39a. Figure 6.39b presents the convergence and uncertainties of harmonic phases, where the achieved order of accuracy is $p \approx 2.2$ for the first order harmonic phase. Three higher order phases exhibit oscillatory convergence with grid refinement with, while other three exhibit divergence, generally yielding

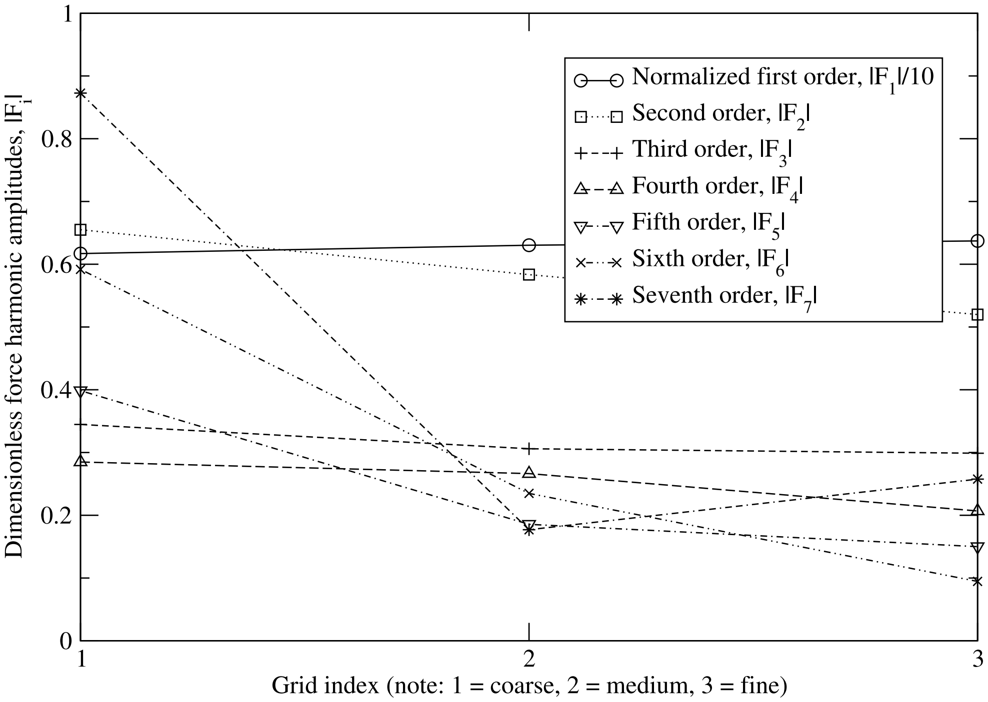

(a) Harmonic amplitudes.

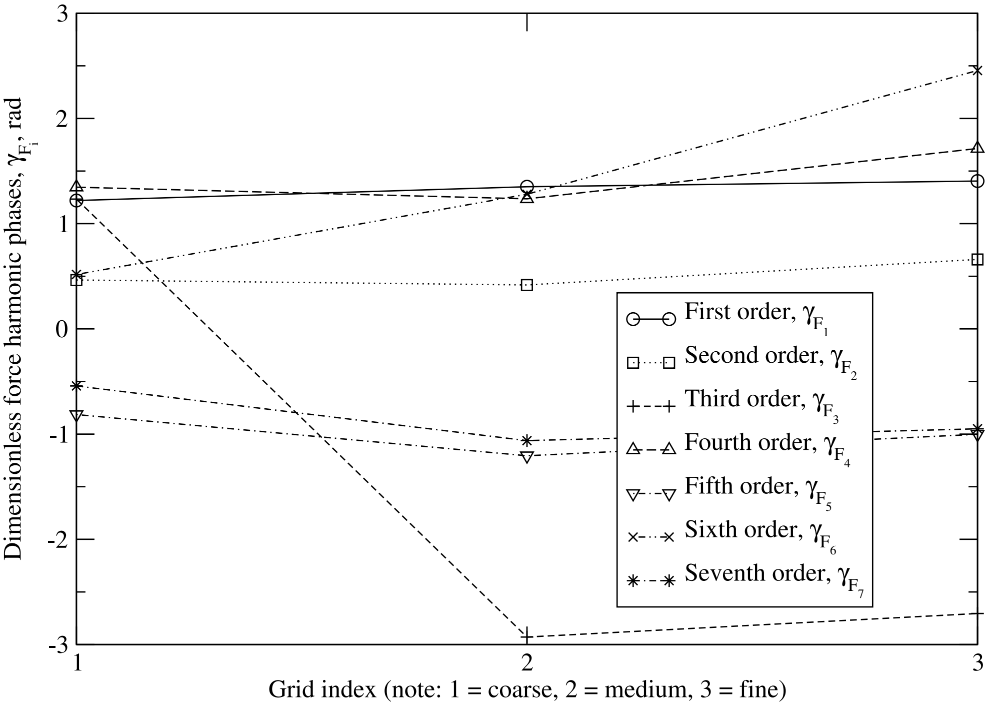

(b) Harmonic phases.

Figure 6.39: Convergence of higher order forces with grid refinement.

Table 6.13: Grid refinement convergence and uncertainties for force harmonic amplitudes.

Order i	Convergence type	Order of convergence p	Uncertainty $U, \%$
1	MC	1.68	1.62
2	MC	0.29	147.27
3	MC	4.19	0.80
4	MD	N/A	56.60
5	MC	4.31	7.13
6	MC	2.30	144.06
7	OC	N/A	202.55

Table 6.14: Grid refinement convergence and uncertainties for force harmonic phases.

Order i	Convergence type	Order of convergence p	Uncertainty $U, \%$
1	MC	2.17	4.13
2	OD	N/A	55.15
3	OC	N/A	115.42
4	OD	N/A	41.86
5	OC	N/A	29.30
6	MD	N/A	118.43
7	OC	N/A	41.07

high grid uncertainty. However, such high uncertainties are unrealistic for most items because the coarse grid solution is too far away from the converged solution (*e.g.* see Figure 6.39b where small differences between medium and fine solutions can be seen for second, third, fourth, fifth and seventh order).

6.4.6. Notes on Viscosity and Vorticity Effects

As the present CFD model has the capability of modelling vorticity and viscosity effects, some notes on vorticity effects and viscous forces are given here. Huseby and Grue [120] estimated the viscous drag force on the cylinder to be approximately $0.1\pi\rho_w|\mathbf{g}|ar^2$. Figure 6.40 presents the comparison of dimensionless viscous drag force obtained with CFD and analytical expression. The analytically calculated dimensionless drag force decreases with increasing a/r ratio, while the dimensionless drag force obtained with CFD remains almost constant. Furthermore, the analytically calculated drag force always over–predicts the corresponding CFD result. Figure 6.41 shows an example of viscous in–line force spectrum for the $ka \approx 0.13$ case, where the first order effects have largest amplitudes. The nonlinear effects up to seventh order can also be observed. Viscous force spectra for other cases are not presented here since they have similar values, *i.e.* viscous forces do not seem to be affected by the wave steepness as is the case with pressure forces. It is however important to stress that the viscous forces are significantly lower than pressure forces, *i.e.* the first order viscous force makes approximately 0.65% of the total first order force (pressure and viscous), where even lower values are obtained for higher order forces.

Vorticity effects are assessed by examining enstrophy:

$$\epsilon_n = 0.5|\nabla \times \mathbf{u}|^2\,, \tag{6.7}$$

where $\mathbf{u}$ is the total velocity field (sum of incident and perturbation components). Enstrophy is a quantity that is directly related to the rate of change of kinetic energy in the viscous fluid. This dissipation is not present in potential flow models where irrotational flow is assumed ($\nabla \times \mathbf{u} = \mathbf{0}$), while it is difficult to quantify vorticity in the experiments with free surface flows.

For $ka \approx 0.13$ case, five probes are positioned in the close proximity of the cylinder:

- *Radial direction.* 0.0001 m in the radial direction of the cylinder,
- *Vertical direction.*0.023 m below the still water line, making the probes fully submerged at all times during the simulation. As a reference, wave amplitude for this case is $a \approx 0.153$.

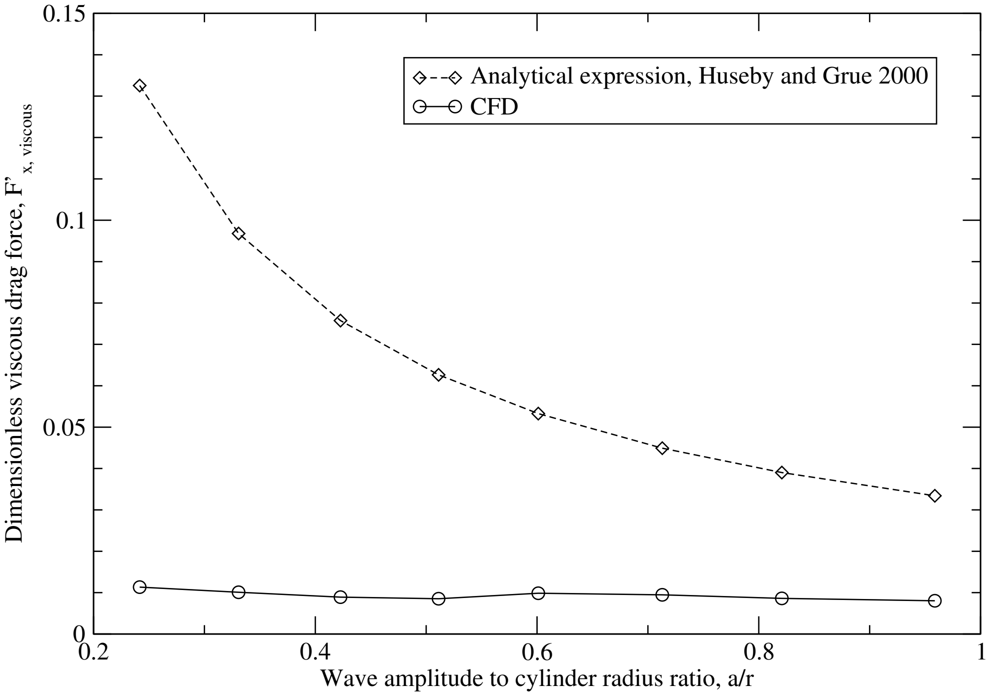

Figure 6.40: Comparison of dimensionless viscous drag forces.

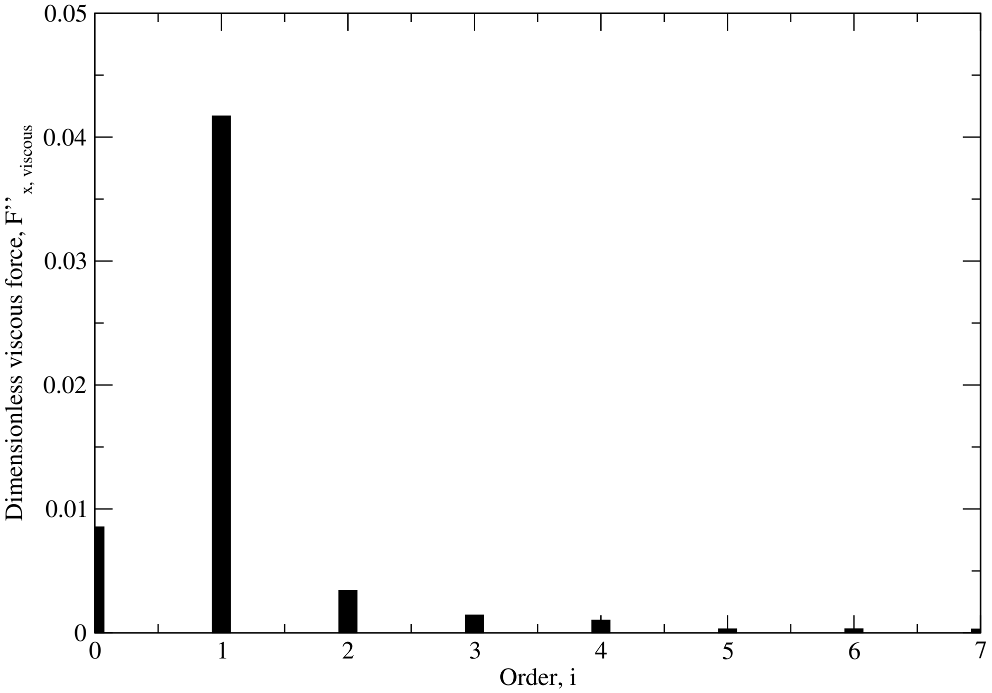

Figure 6.41: The viscous force spectrum for $ka \approx 0.13$ case.

- *Circumferential direction.* Five probes are positioned at $\Theta = 0, 45, 90, 135$ and 180° in the circumferential direction, respectively.

Figure 6.42a presents temporal variation of enstrophy at five probes, where it can be seen that the highest amplitude of enstrophy is present at the side of the cylinder ($\theta = 90°$), which may be related to the orthogonality of incident and diffracted wave fields. The enstrophy decreases, decreasing towards front and back of the cylinder, where the axis of propagation of the diffracted field is the same as the axis of propagation of the incident field. Figure 6.42b presents the spectrum of enstrophy obtained with FFT. The enstrophy at each probe exhibits significant nonlinear behaviour, where the mean value and second order effects at $f = 2.85$ Hz are dominant. It is interesting to note that these effects are approximately 3 to 4 times larger than the first order effects.

6.4.7. Flow Field Visualization

Some details regarding flow visualization are presented in this section for a steep $ka \approx 0.2$ test case.

Figure 6.43 presents the incident flow field, $\mathbf{u}_I$ in water as obtained from the stream function wave theory, whereas Figure 6.44 presents the perturbation field $\mathbf{u}_P$. The perturbation velocity magnitude is generally smaller than incident velocity magnitude, except in the close proximity of the cylinder. The perturbation velocity field rapidly decays farther from the cylinder. Since the incident wave field is extrapolated in the air, the perturbation component is significant in regions where the instantaneous free surface does not correspond to incident free surface due to wave diffraction. This indicates that a better model for evaluating incident wave field in air might be beneficial. As a reference, Figure 6.45 presents the time evolution of total velocity field obtained by summing incident and perturbation components, $\mathbf{u} = \mathbf{u}_I + \mathbf{u}_P$.

Figure 6.46 presents the incident flow field, $\mathbf{u}_I$ in air as obtained from the stream function wave theory, where the solution is simply extended in air with a limit of velocity magnitude $|\mathbf{u}_{I,max}| = 0.23$. This is done in order to pragmatically prevent nonphysical exponential growth with increasing vertical coordinate. It was interesting to observe that the perturbation velocity fields tries to counteract

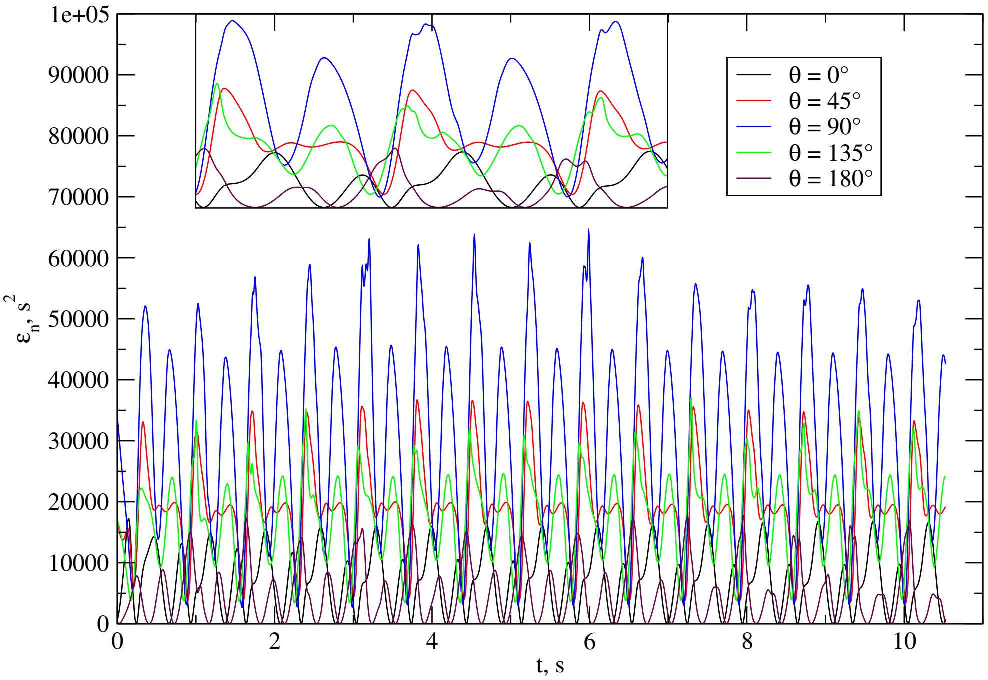

(a) Time domain.

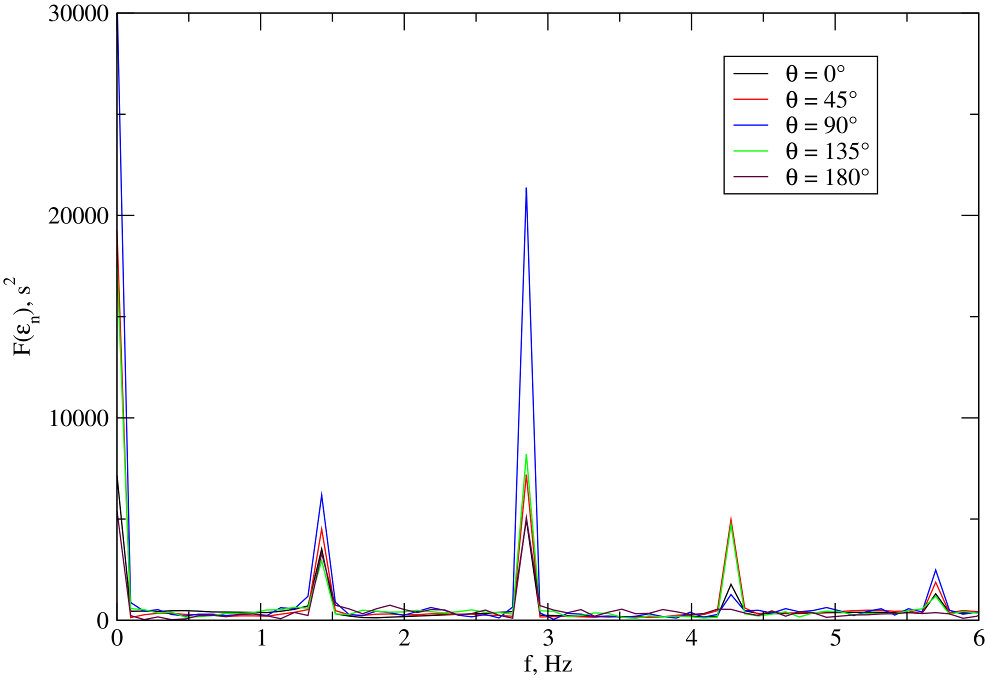

(b) Frequency domain.

Figure 6.42: Enstrophy in the vicinity of the cylinder, $ka \approx 0.13$ case.

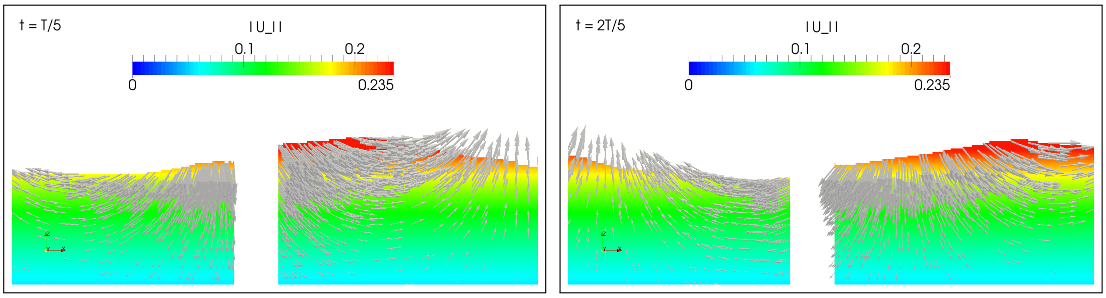

(a) $t = T/5$. (b) $t = 2T/5$.

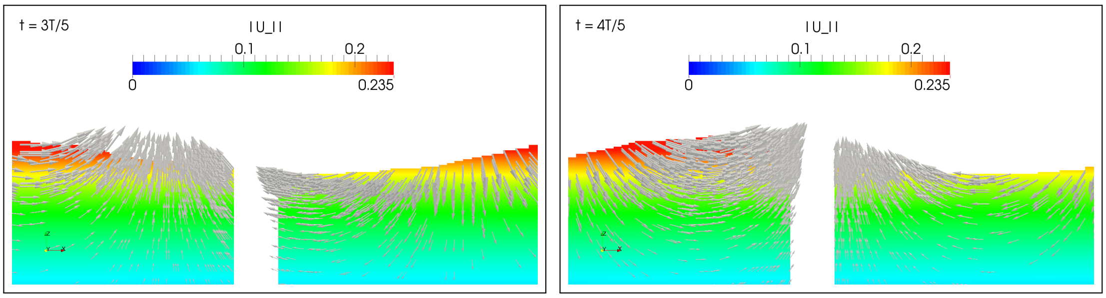

(c) $t = 3T/5$. (d) $t = 4T/5$.

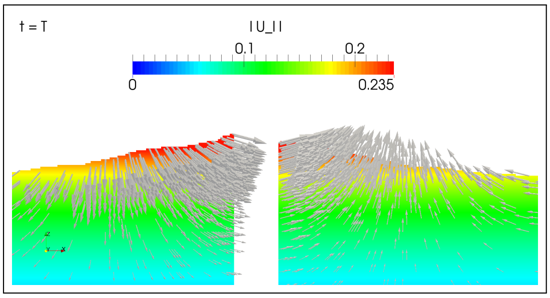

(e) $t = T$.

Figure 6.43: Incident velocity field ($\mathbf{u}_I$) near the cylinder in water during the last (15^{th} period), $ka \approx 0.2$ case.

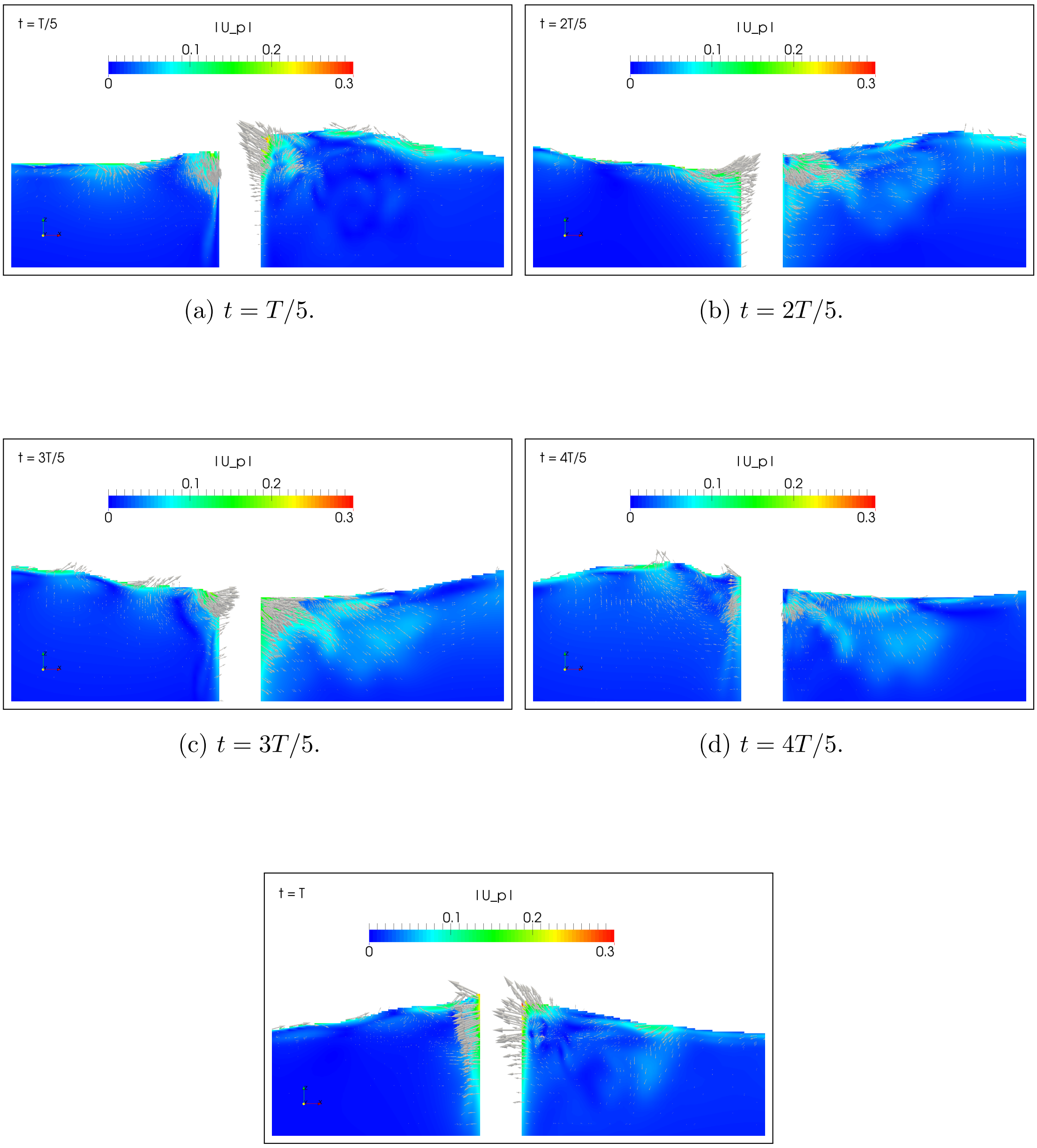

(a) $t = T/5$.

(b) $t = 2T/5$.

(c) $t = 3T/5$.

(d) $t = 4T/5$.

(e) $t = T$.

Figure 6.44: Perturbation velocity field ($\mathbf{u}_P$) near the cylinder in water during the last (15^{th} period), $ka \approx 0.2$ case.

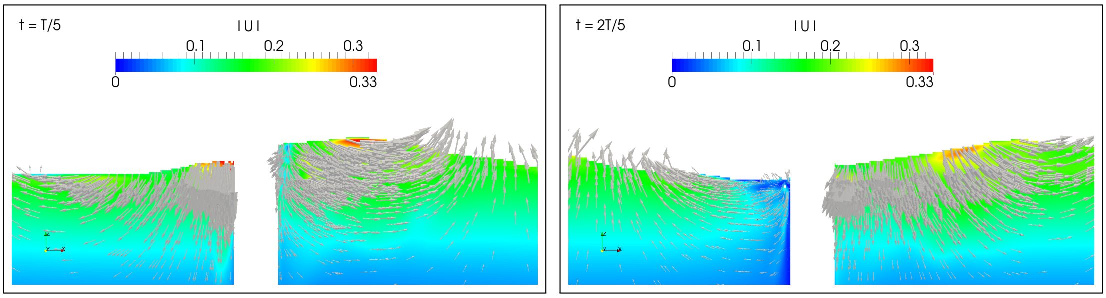

(a) $t = T/5$.　(b) $t = 2T/5$.

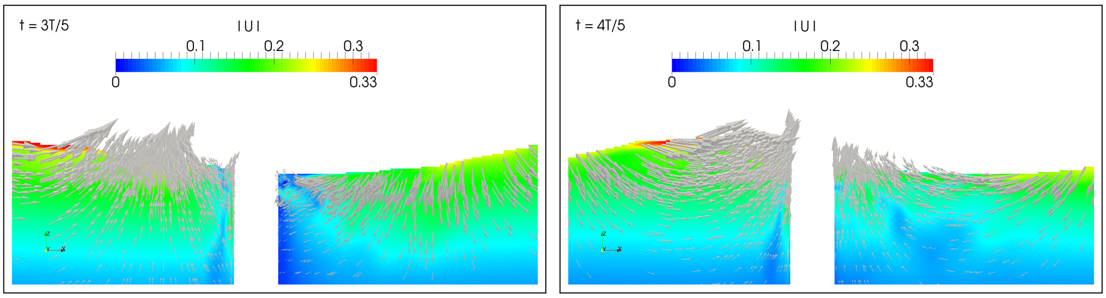

(c) $t = 3T/5$.　(d) $t = 4T/5$.

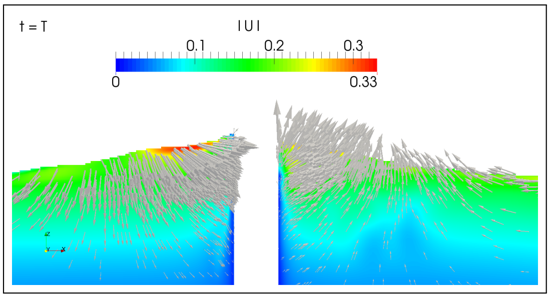

(e) $t = T$.

Figure 6.45: Total velocity field ($\mathbf{u} = \mathbf{u}_I + \mathbf{u}_P$) near the cylinder in water during the last (15^{th} period), $ka \approx 0.2$ case.

the incident velocity field in air, as indicated in Figure 6.47. The resulting total velocity field in air, presented in Figure 6.48 has smaller velocity magnitudes than the perturbation component.

Figure 6.49 presents the dynamic pressure field, p_d for the $ka \approx 0.2$ test case. No interpolation has been used for visualization of results: cell–centred values of dynamic pressure are shown on purpose in order to stress the sharp jump in dynamic pressure. In the present CFD model based on the GFM for discretisation of jump conditions at the free surface, the jump is resolved across a single face using second–order accurate discretisation. It is important to stress that the total pressure field is continuous across the free surface, as indicated in Figure 6.50, where the free surface is denoted with a white line. This is in agreement with the mathematical model presented in Ch. 7.

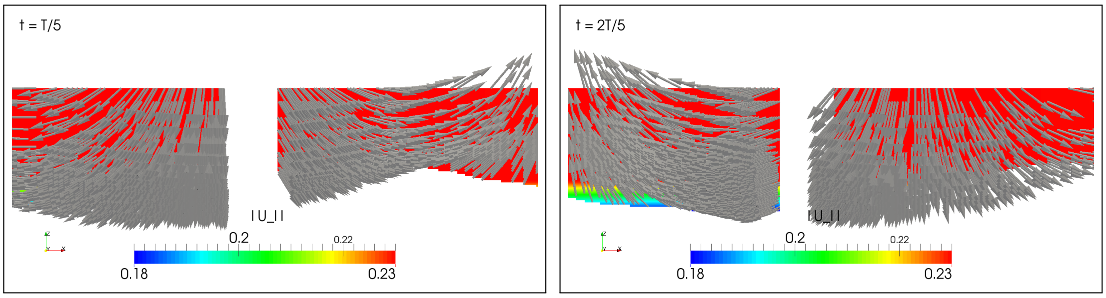

(a) $t = T/5$.　(b) $t = 2T/5$.

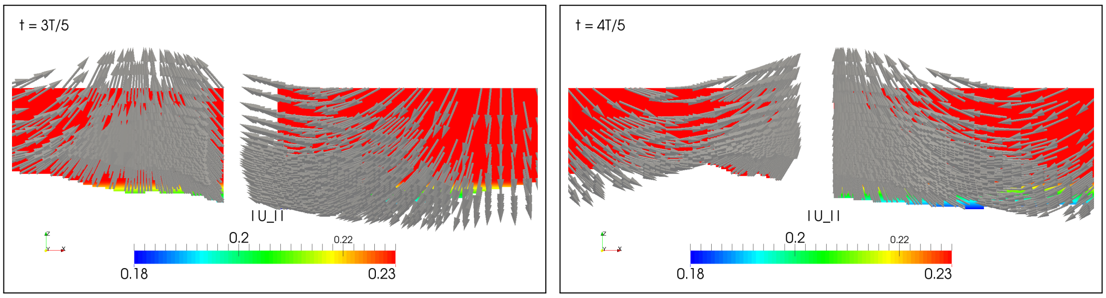

(c) $t = 3T/5$.　(d) $t = 4T/5$.

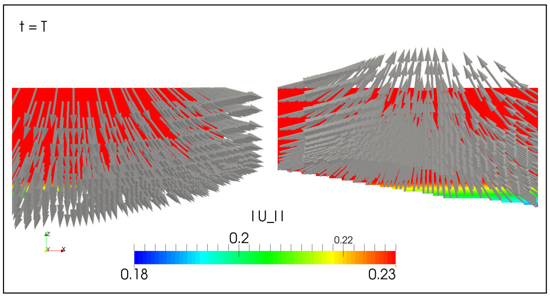

(e) $t = T$.

Figure 6.46: Incident velocity field ($\mathbf{u}_I$) near the cylinder in air during the last (15^{th} period), $ka \approx 0.2$ case.

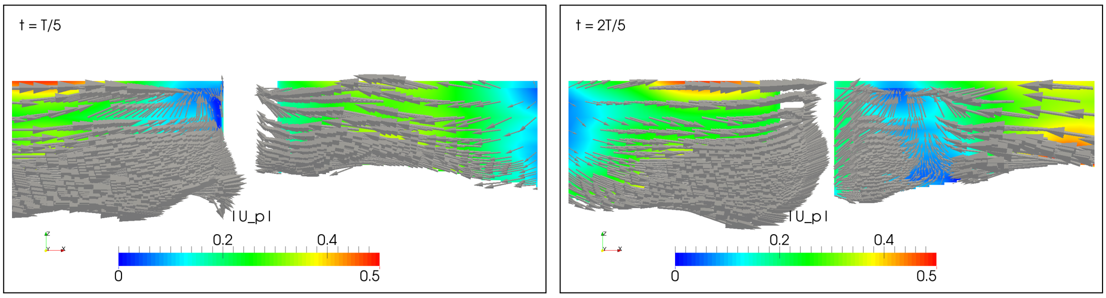

(a) $t = T/5$. (b) $t = 2T/5$.

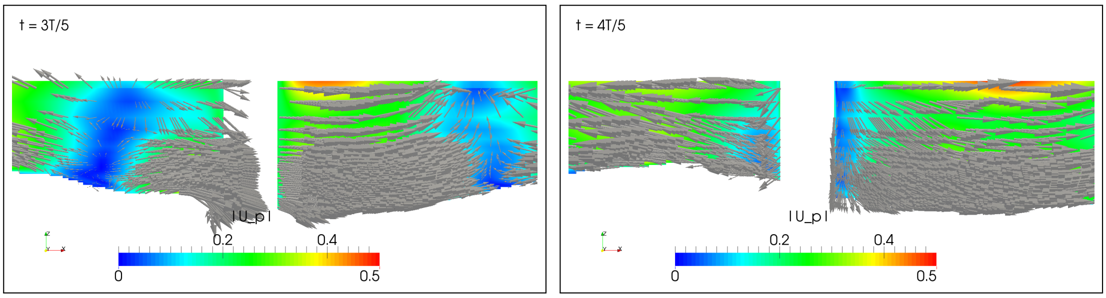

(c) $t = 3T/5$. (d) $t = 4T/5$.

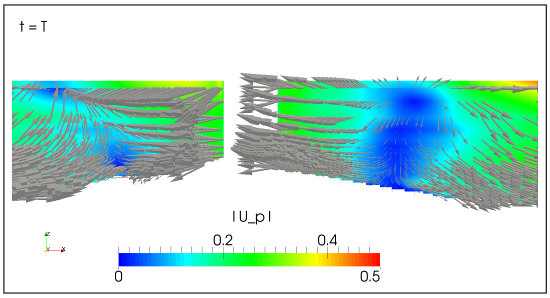

(e) $t = T$.

Figure 6.47: Perturbation velocity field ($\mathbf{u}_P$) near the cylinder in air during the last (15^{th} period), $ka \approx 0.2$ case.

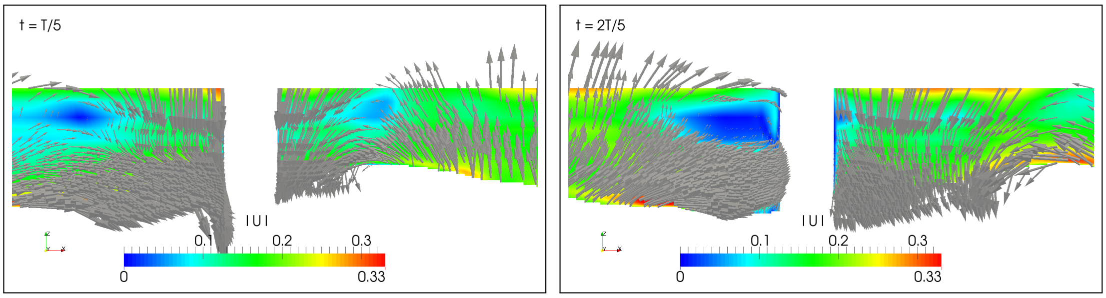

(a) $t = T/5$. (b) $t = 2T/5$.

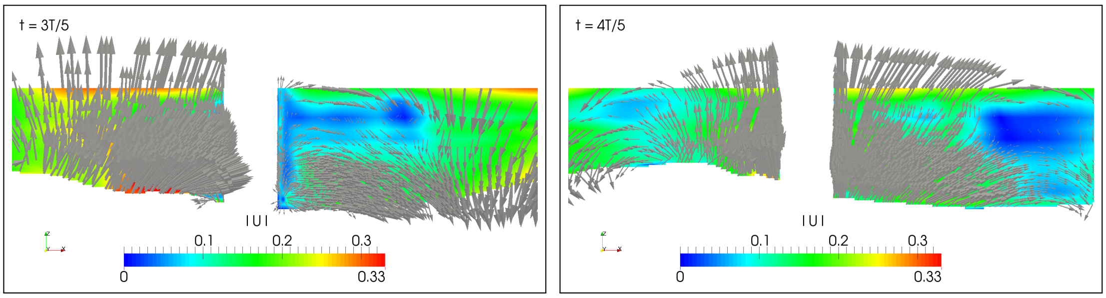

(c) $t = 3T/5$. (d) $t = 4T/5$.

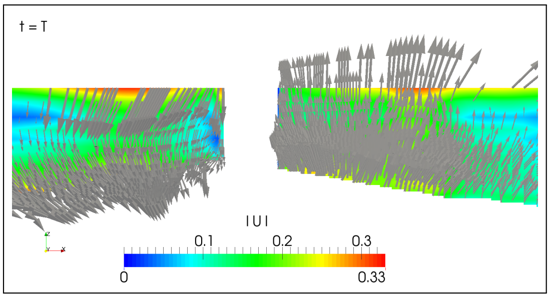

(e) $t = T$.

Figure 6.48: Total velocity field ($\mathbf{u} = \mathbf{u}_I + \mathbf{u}_P$) near the cylinder in air during the last (15^{th} period), $ka \approx 0.2$ case.

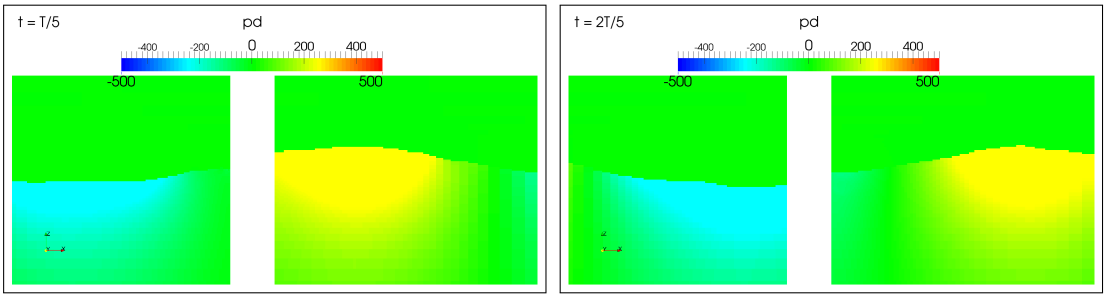

(a) $t = T/5$. (b) $t = 2T/5$.

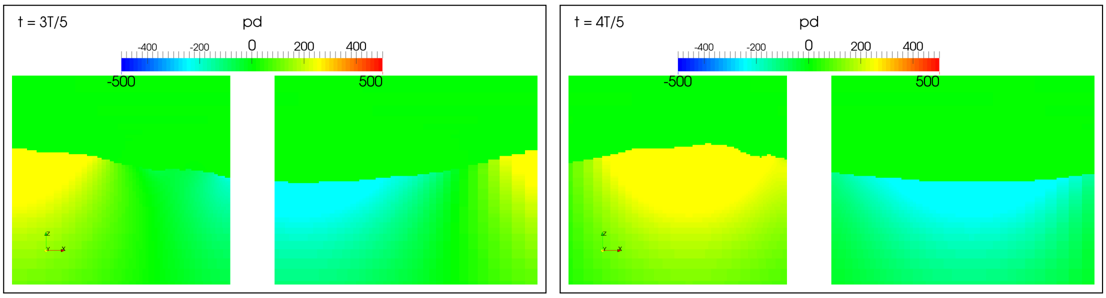

(c) $t = 3T/5$. (d) $t = 4T/5$.

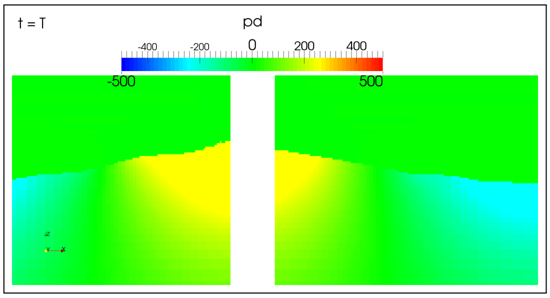

(e) $t = T$.

Figure 6.49: Dynamic pressure field near the cylinder during the last (15^{th} period), $ka \approx 0.2$ case.

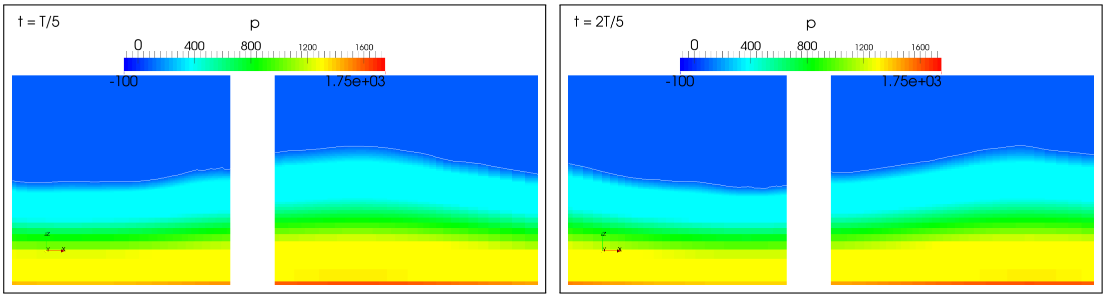

(a) $t = T/5$. (b) $t = 2T/5$.

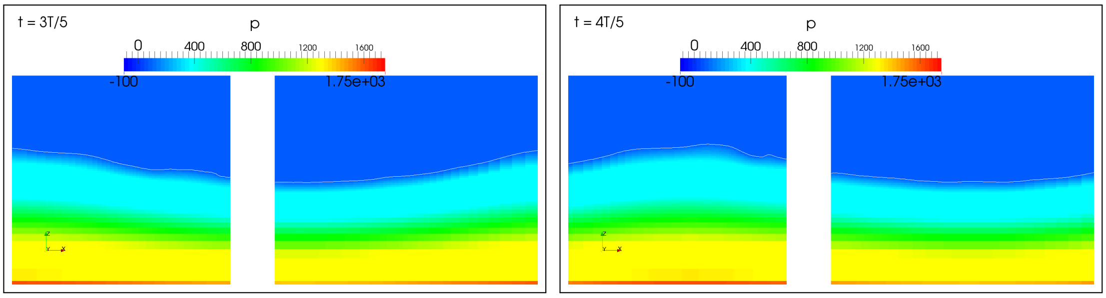

(c) $t = 3T/5$. (d) $t = 4T/5$.

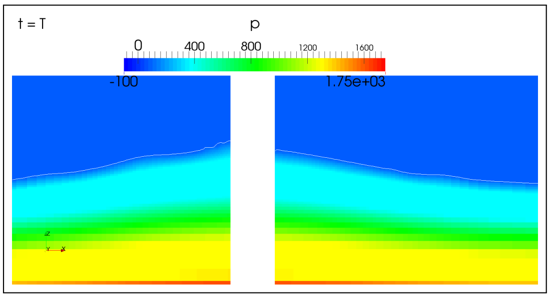

(e) $t = T$.

Figure 6.50: Total pressure field near the cylinder during the last (15^{th} period), $ka \approx 0.2$ case.

6.5. Seakeeping KCS Model Simulations at Design Speed

The final set of test cases considers seakeeping of a realistic hull form. Recently, numerous seakeeping studies have been conducted with various CFD methods. Orihara and Miyata [122] performed validation and verification for the SR–108 container ship, while Carrica *et al.* [123] performed simulations of the KCS model in head waves. The CFD seakeeping studies also included less conventional hull forms: a fast catamaran [124] and a trimaran [125]. Tezdogan *et al.* [126] performed a detailed study regarding KCS hull form in slow steaming regime in head waves, indicating that CFD simulations may be used to investigate realistic scenarios used to reduce the fuel consumption. The CFD studies regarding seakeeping rarely include sensitivity studies related to temporal discretisation and hydro–mechanical (fluid–flow/6–DOF) coupling, while the grid refinement studies are often carried out for a single case. Since almost all of CFD algorithms solve the governing equations in time domain, periodic convergence tests should be reported in order to determine number of encounter periods that need to be simulated to achieve periodically steady state solution. This has not yet been investigated in detail. This section attempts to address these sensitivities and uncertainties related to numerical settings, while validating and verifying the present methodology for most common seakeeping problems.

In general, the seakeeping of a ship or offshore structure may be viewed as marine hydrodynamics problem which depends on two sets of parameters:

1. Geometrical parameters (*i.e.* size, shape and quality of the computational grid, strongly related to particulars of the ship) and
2. Physical parameters (*i.e.* frequencies and amplitudes of the wave system (incident, diffracted and radiated waves), and ship speed).

In CFD simulations, the geometrical parameters are closely related to physical parameters to ensure proper wave propagation on a FV grid, as demonstrated in Sec. 6.3.3. (wave reflection study by varying relaxation zone length). Although the wave systems depend on many different physical quantities, the following ones may be viewed as the most influential:

- Incident wave height H,
- Fundamental wave frequency ω and the corresponding wave length, λ_w,
- Froude number $F_r = U/\sqrt{|\mathbf{g}|L_{PP}}$, where U is the forward speed of the ship,
- Encounter frequency $\omega_e = \omega(1 - \frac{U\omega}{|\mathbf{g}|}\cos\chi)$, where χ is the encounter angle,
- Brard number $\tau = U\omega_e/|\mathbf{g}|$,
- Reynolds number $R_e = UL_{PP}/\nu$.

For fixed or specified $\mathbf{g}, \nu$ and L_{PP}, the six items depend on only four parameters: wave height H, wave frequency ω, forward speed of the ship U and encounter angle χ. The possibility of simulating different wave heights, wave frequencies (consequently wave lengths) and encounter angles using the same computational domain is investigated in this study. The design ship speed is considered, while the Brard number always remains high enough so the diffracted and radiated wave fields remain behind the ship. Within linear potential flow models, wave systems are usually taken into account analytically (using a Green function), which represents the main difficulty since the Green function becomes extremely complex for general applications. Within the general CFD model based on Navier–Stokes equations, the wave systems are represented purely numerically, obstructing efficient wave propagation often causing dissipation (loss of amplitude) and dispersion (phase shift) errors (as seen in Sec. 6.3.). Hence, a simplification shall be made for seakeeping test cases as the same set of grids is going to be used for all wave parameters, thus neglecting the relation between geometrical and physical parameters. However, from a practical point of view, it is convenient to assess the accuracy of the method using the same set of grids since the grid generation process often takes a significant amount of time.

The KCS model particulars and computational grids shall be first presented for the two models used for head and oblique wave test cases. Five head wave cases are then considered, including uncertainty assessment for:

1. Periodicity (convergence of Fourier harmonics through successive encounter periods),

2. Time step resolution (uniformly coarsening the time step from 800 to 25 time steps per encounter period) for a single representative test case,
3. Hydro–mechanical (fluid–flow/6–DOF) coupling (varying number of hydro–mechanical corrector steps from 2 to 8) for a single representative test case,
4. Grid uncertainty assessment using 3 grids for each test case.

A parallel scaling test is carried out for a single representative test case. Additionally, a performance test is carried out with the coarsest grid and the lowest stable temporal resolution (25 time steps per encounter period), where the results and CPU times are discussed. Finally, five oblique wave cases are simulated, including grid and periodic uncertainty assessments. The part of the results presented here have been published in [11, 13], while the full results with all sensitivity studies are published in [127].

6.5.1. KCS Model Particulars

The KCS model is a generic container ship designed by KRISO (former MOERI) that is extensively used for validation and verification purposes in CFD. The surface grids for KCS hull, rudder and propeller, along with the corresponding geometrical parameters are available in [128]. The relevant geometrical parameters are summarised in Table 6.15 for two models used in head and oblique wave cases. The experimental measurements are performed for hull with fixed rudder, hence the wetted surface is reported for both hull and rudder. The Vertical Centre of Gravity (VCG) is located at 0.378 m from keel for Model A and at 0.168 m for Model B. The Longitudinal Centre of Bouyancy (LCB) is located at $0.0148L_{PP}$ ($1.48\%L_{PP}$) behind the midship section for both models.

6.5.2. KCS Grid and Post Processing Details

The right–handed 3–D coordinate system as defined in [128] is presented in Figure 6.51. The origin of the coordinate system is at the still water line at F.P. in the symmetry plane of the ship. x–axis is positive towards stern, y–axis is positive towards starboard and consequently, z–axis is positive upwards.

Table 6.15: Main particulars of the KCS models.

Main particulars		Model A (head waves)	Model B (oblique waves)
Length b.p.	L_{PP}, m	6.0702	2.7000
Draft	T, m	0.2850	0.1268
Beam	B, m	0.8498	0.3780
Displacement	∇, m^3	0.9571	0.0840
Wetted surface	S_w, m^2	6.6978	1.3260
Radii of inertia	K_{xx}/B	N/A	0.390
	K_{yy}/L_{PP}	0.252	0.250
	K_{zz}/L_{PP}	0.250	0.250

In order to assess grid uncertainty, three grids are used for all simulations with following dimensionless extents:

- $x_{min}/L_{PP} = -1$,
- $x_{max}/L_{PP} = 3.5$,
- $y_{min}/L_{PP} = 0$ (head waves) and -1.57 (oblique waves),
- $y_{max}/L_{PP} = 1.57$,

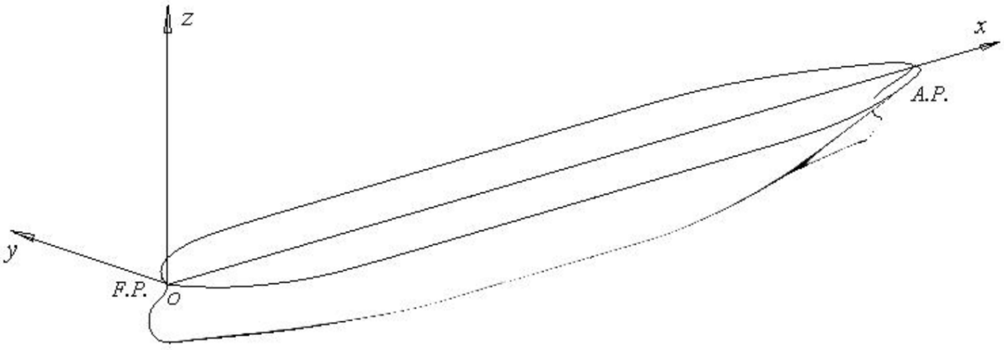

Figure 6.51: Coordinate system definition for the KCS test cases [128].

- $z_{min}/L_{PP} = -1.63$,
- $z_{max}/L_{PP} = 1.13$.

Symmetry plane is used for head wave cases in case set 2.10. [128], while for the oblique wave cases in case set 2.11., the original grids are mirrored around the symmetry plane in order to successfully simulate oblique waves. Details regarding three grids for the head wave cases with the symmetry plane are outlined in Table 6.16, while the cell count is increased by a factor of two for oblique waves, without changes in y^+ and Δz.

The coarse grid details are presented in Figure 6.52. Figure 6.52a presents a longitudinal cut corresponding to the symmetry plane of the ship, where it can be seen that the grid is refined towards the free surface in vertical direction. Figure 6.52b presents the surface grid on the hull and rudder, where additional refinement zones in bow and stern regions are visible. Transversal cut corresponding to the midship section is presented in Figure 6.52c and the vertical cut corresponding to the still water line is presented in Figure 6.52d, showing the Kelvin angle refinement. Both coarse, medium and fine grids consist of approximately 90% hexahedral cells with 10% prismatic, tetrahedral and general polyhedral cells. The maximum non–orthogonality of a face for the three grids is approximately 75 to 85 degrees, with the average non–orthogonality being approximately 8 degrees.

As requested by the Tokyo 2015 Workshop organisers [128], the time–domain signals are represented in Fourier series, where the moving window FFT approach is utilised here in addition in order to assess periodic convergence. The final CFD

Table 6.16: Grid details for the head wave cases (with symmetry plane).

Grid Index	Coarse 1	Medium 2	Fine 3
Number of cells	607 114	954 016	1 585 526
Approximate average y^+	37.6	28.5	23.2
$\Delta z/L_{PP}$ at midship	0.00173	0.00136	0.00108

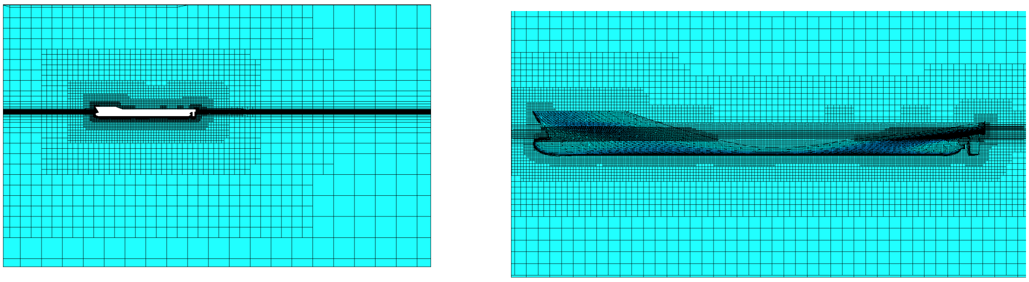

(a) Longitudinal cut (symmetry plane), (b) Surface grid on the hull,

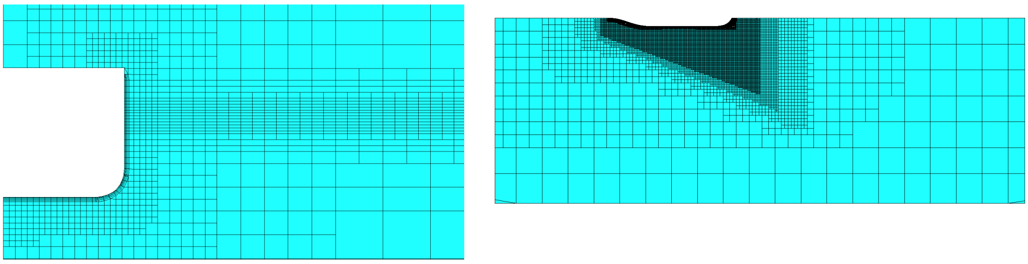

(c) Transversal cut (midship section), (d) Vertical cut (still water line),

Figure 6.52: Coarse KCS grid details.

result is reported for mean value and first order harmonic as the average value during last 5 encounter periods. It is important to note that the zeroth order harmonic (*i.e.* mean value) for all measured items is reported as twice the mean value, following the guidelines in [128].

6.5.3. Notes on Fluid Flow and Six Degrees–of–Freedom Coupling and Turbulence Modelling

The general procedure for the resolution of hydro–mechanical (fluid–flow/6–DOF) coupling is presented in Sec. 4.5.2.. This procedure is used for the oblique wave simulations, while the head wave simulations are performed with a more strongly resolved strategy, briefly outlined here. In addition to the multiple 6–DOF solutions in each outer corrector, SIMPLE loop (see Figure 4.4), the 6–DOF equations are updated after each pressure correction step. The new 6–DOF solution is then used to update the velocity field at the moving boundary (*i.e.* ship hull) for the next pressure correction step. This procedure presents a negligible computational overhead while further resolving the strong coupling between the dynamic pressure field and 6–DOF motion equations multiple times within a single time step. This procedure shall be presented in detail in future publications. The oblique wave cases have not been re–performed with this strategy due to limited amount of time for the preparation of this thesis.

$k - \omega$ SST two–equation turbulence model has been used for all test cases, where the turbulence intensity is set to 3%.

6.5.4. KCS Hull in Head Waves (Model A)

The validation and verification of the present decomposition model is first performed for regular head waves at design speed of the KCS model. Experimental results for 5 head wave cases: C1, C2, C3, C4 and C5 are publicly available in [128, 4, 23], where C1 represents the shortest wave length and the smallest wave height, see Table 6.17. The experimental measurements included total resistance coefficient, heave motion and pitch motions. Other degrees of freedom are constrained both in the experiment and in present simulations. The experimental uncertainty has not been reported, although it has been mentioned at the Workshop that the uncertainty for the total resistance may be estimated to approximately 10%.

The sensitivity studies are organised as follows:

1. The time step resolution and the hydro–mechanical coupling study is performed for the C5 test case, which has the largest wave height and wave length, and consequently the finest relative grid resolution (the highest number of cells per wave height and wave length). The studies are performed

Table 6.17: Head wave KCS test case parameters [128].

Case	C1	C2	C3	C4	C5
L_{PP}, m	6.0702				
F_r	0.261				
λ_w, m	3.949	5.164	6.979	8.321	11.840
H, m	0.062	0.078	0.123	0.149	0.196

for the coarsest grid (approximately 600 000 cells), while the periodic convergence graphs are presented and discussed for both studies.

2. The grid refinement study is carried out for all test cases, comparing the results with the available experimental data and assessing the grid uncertainty.

3. The parallel scaling test is carried out for the C5 case on coarse grid, reporting the parallel speed–up and efficiency.

4. A single performance test is carried out by simulating only four hydro–mechanical (fluid–flow/6–DOF, outer) corrector steps with only 25 time steps per encounter period in order to assess the trade–off between accuracy and performance.

Temporal Resolution Study

The temporal resolution study is performed by simulating 25, 50, 100, 200, 400 and 800 time steps per encounter period for the C5 case on the coarse grid (approximately 600 000 cells), yielding a constant refinement ratio $r = 2$. Simulations below 25 time steps per encounter period were not possible due to numerical divergence of 6–DOF motion equations. 6 outer (hydro–mechanical) correctors are used per time step, while the pressure–velocity coupling is resolved within an embedded PISO loop with 4 pressure correction steps. This yields $6 \bullet 4 = 24$ pressure updates per time step and consequently 24 updates of the 6–DOF motion equations, where the grid motion fluxes and grid position are updated 6 times (in each outer corrector step).

Figures 6.53–6.55 present convergence of heave, pitch and total resistance coefficient, respectively, with increasing number of time steps per encounter period, where it can be seen that all items converge with lower time step size as expected. It is important to note that first order harmonic amplitudes do not exhibit significant errors with substantial decrease of number of time steps per encounter period, whereas the first order harmonic phases are most affected by low temporal resolution. This is in accordance with wave propagation temporal resolution study presented in Sec. 6.3.4., where the dissipation errors are found to be signif-

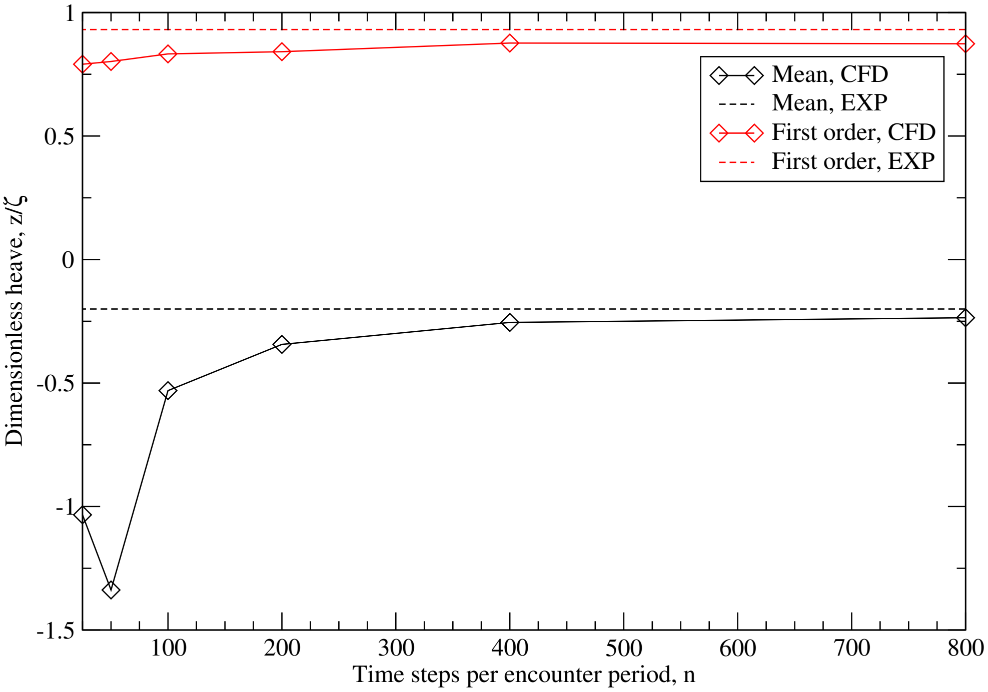

(a) Dimensionless heave amplitudes,

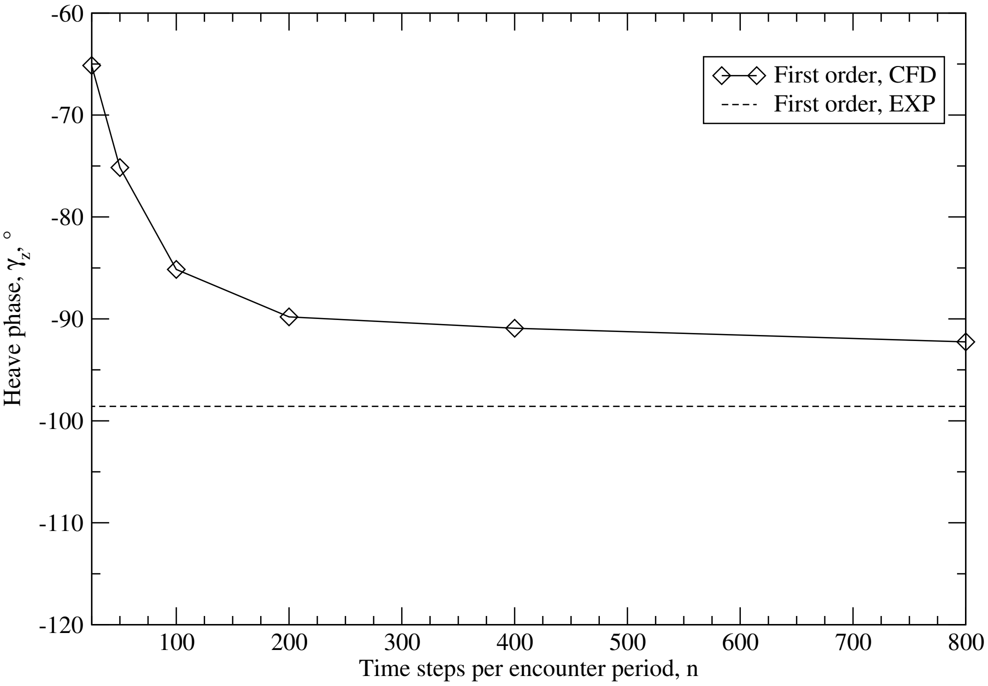

(b) Dimensionless heave phase,

Figure 6.53: Convergence of heave with increasing number of time steps per encounter period, C5 case, coarse grid (600 000 cells).

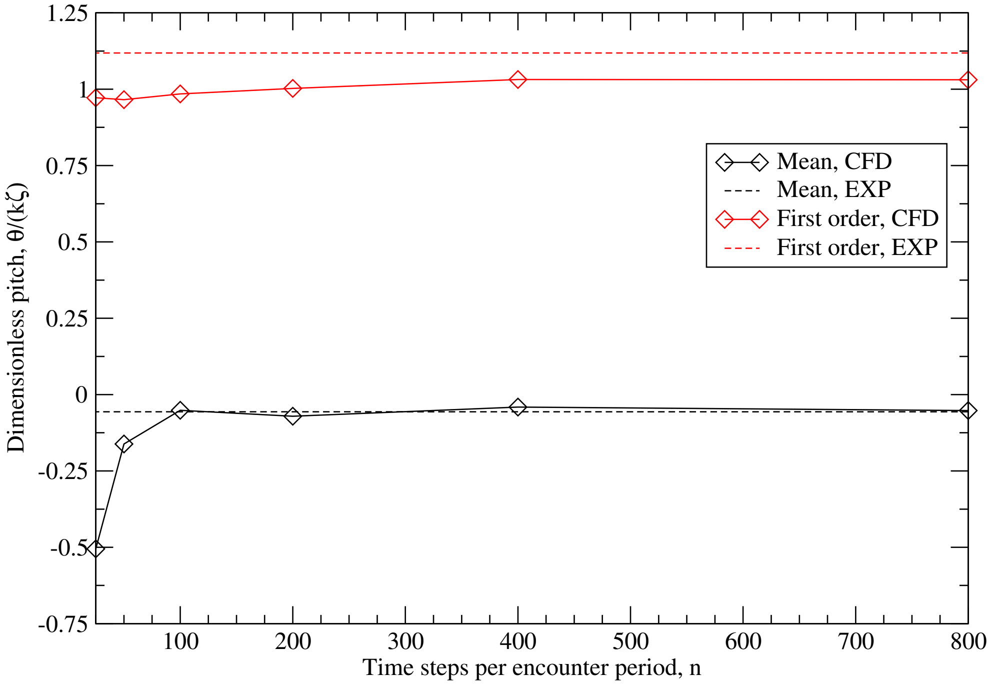

(a) Dimensionless pitch amplitudes,

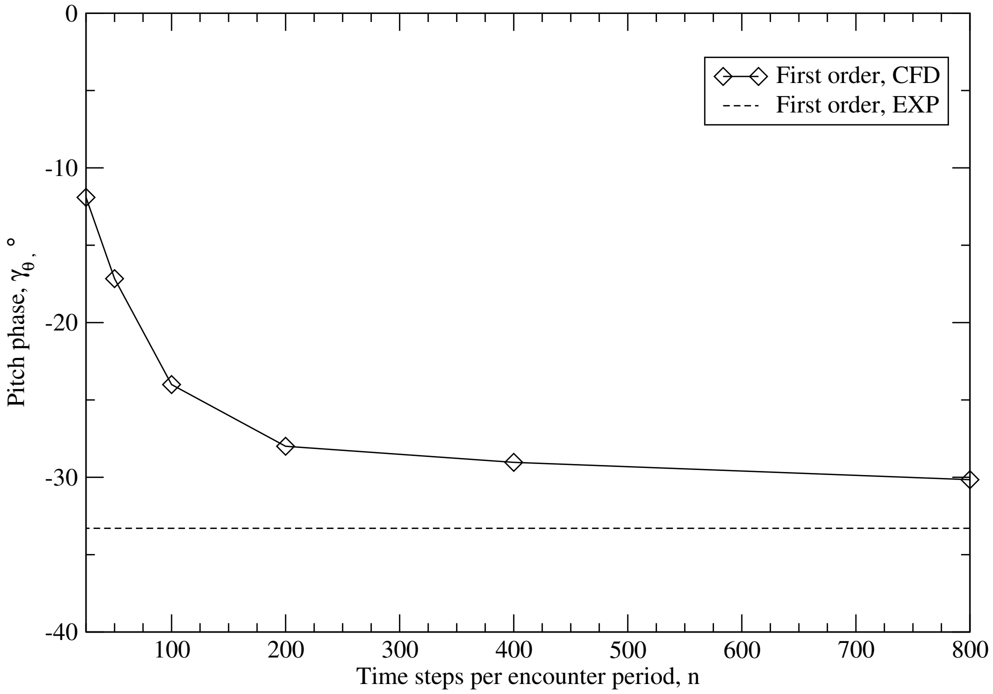

(b) Dimensionless pitch phase,

Figure 6.54: Convergence of pitch with increasing number of time steps per encounter period, C5 case, coarse grid (600 000 cells).

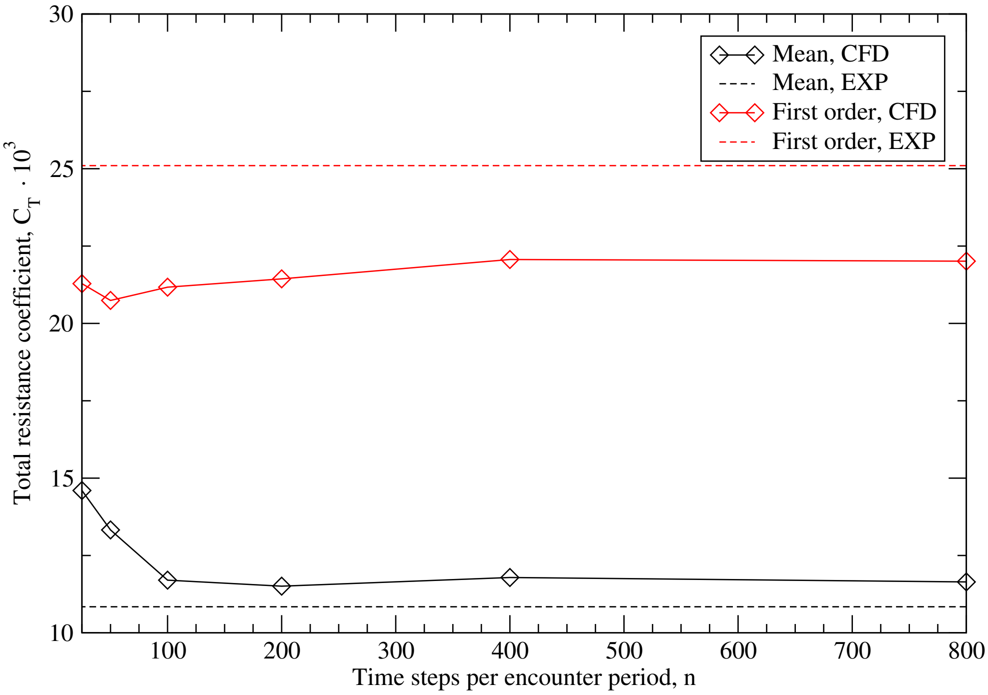

(a) Dimensionless resistance amplitudes,

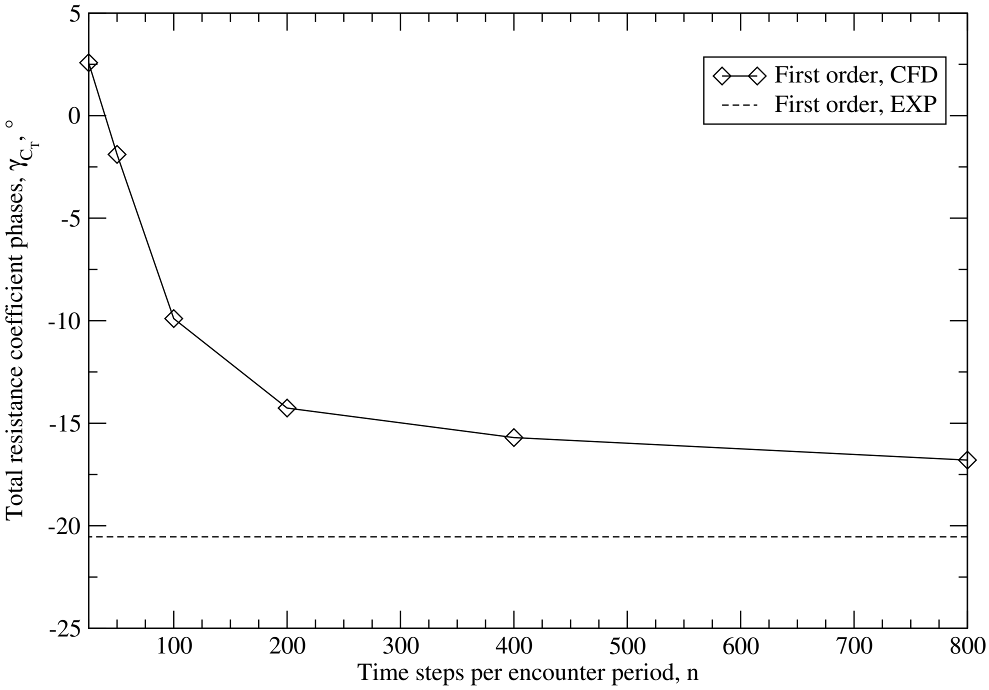

(b) Dimensionless resistance phases,

Figure 6.55: Convergence of resistance with increasing number of time steps per encounter period, C5 case, coarse grid (600 000 cells).

icantly smaller than dispersion errors. The temporal resolution of 25 time steps per encounter period yields a time step $\Delta t \approx 7.5 \cdot 10^{-2}$ s, whereas the temporal resolution of 800 time steps per encounter period corresponds to $\Delta t \approx 2.3 \cdot 10^{-3}$ s. As a reference, the encounter period for the C5 case is approximately $T \approx 1.87$ s. Hence, a difference between 800 and 25 time steps per encounter period gives a 32× speed–up with sacrifice in accuracy for first order harmonic phase shifts and mean values, while the first order harmonic amplitudes may be estimated reasonably well. This reasoning may be appealing for industrial applications since the trade–off between accuracy and computational cost is often considered.

The corresponding temporal resolution uncertainties are calculated using three solutions with the greatest number of time steps per encounter period: $n = 200, 400$ and 800. The uncertainties are reported in Table 6.18 in percentages, where items coloured with black, blue and red denote oscillatory convergence, monotone convergence and divergence (both monotone and oscillatory), respectively. All uncertainties are generally lesser than 4%, except for a few outliers which require further comments:

- The mean value of pitch has high uncertainty of 43% due to normalisation of uncertainty with the very small reference solution ($n = 800$). This can be seen in Figure 6.54a where the black line indicates that the mean value of pitch converges towards very small experimental value.

- The first order harmonic phase of the total resistance coefficient achieves monotone convergence with low order of accuracy of $p \approx 0.4$, thus resulting in high uncertainty. Here, the solutions with three time step values are not within asymptotic range (see Eqn. (6.3)), hence Eqn. (5.5) cannot be used for uncertainty estimate, and the global convergence for this item is better observed in Figure 6.55b.

Out of nine measured items, five items exhibit oscillatory convergence (black colour), two items exhibit monotone convergence (blue colour), while the remaining two items exhibit divergence (red colour) with time step refinement, as indicated in Table 6.18

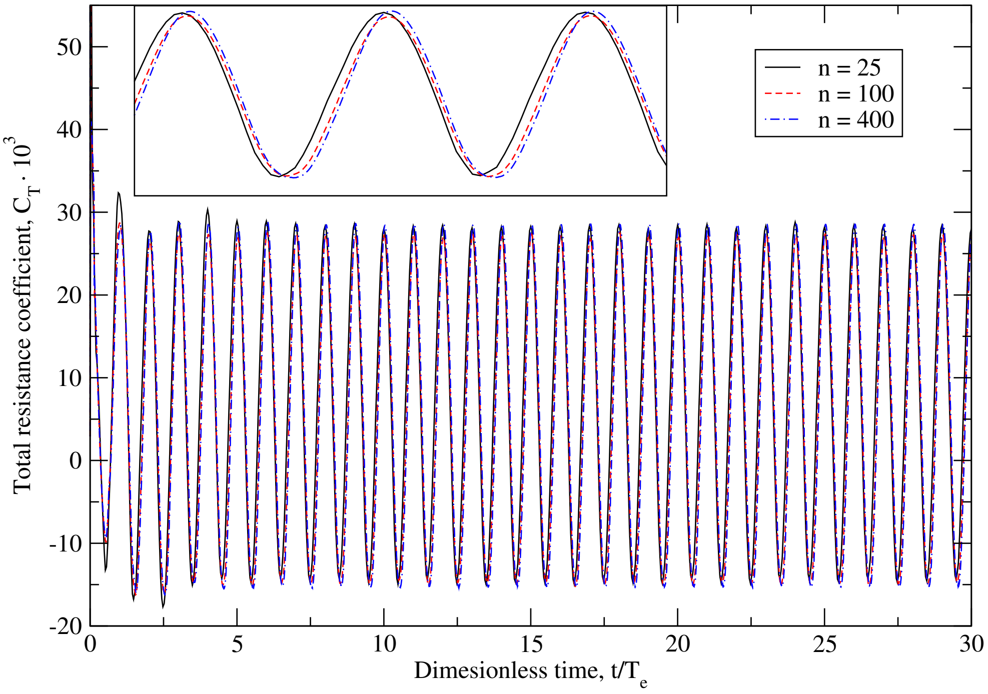

(a) Time domain signals,

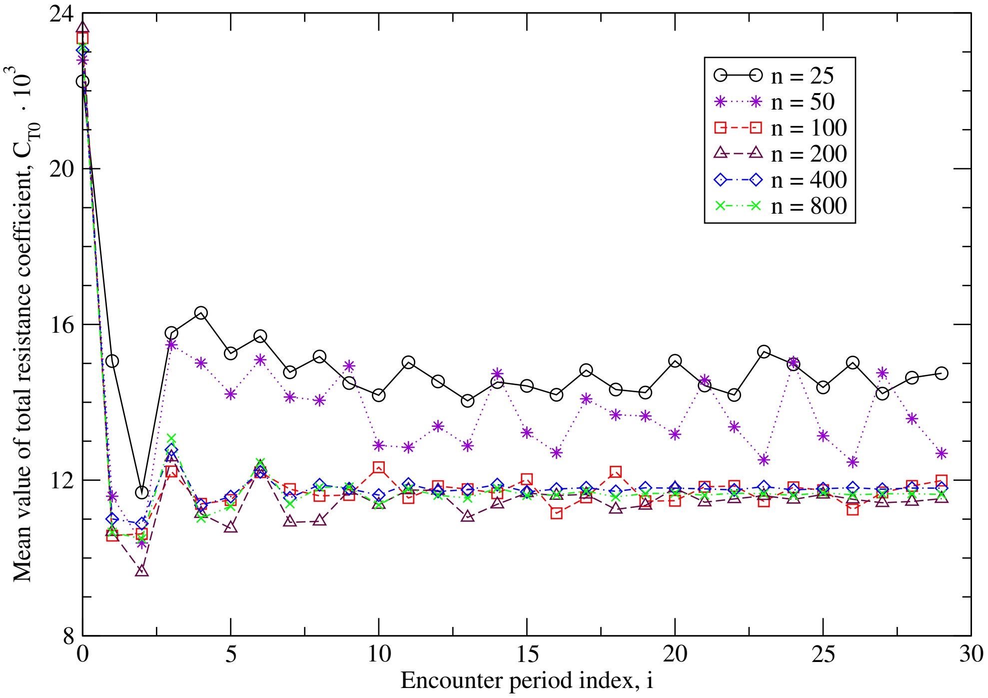

(b) Moving window FFT plot,

Figure 6.56: Convergence of the zeroth order total resistance coefficient for increasing numbers of time steps per encounter period, n.

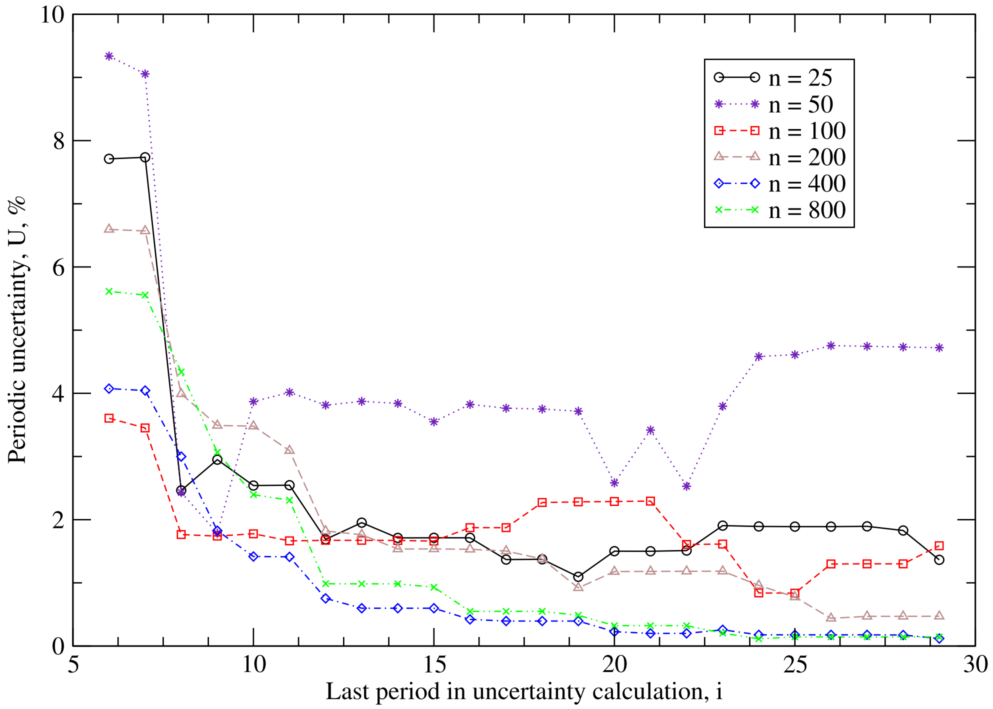

Figure 6.57: Periodic uncertainty convergence throughout periods.

Periodic uncertainty is quantified for all items via moving window FFT for different temporal resolutions. As a representative example, Figure 6.56a presents time–domain signal of the total resistance coefficient for different number of time steps per encounter period. In order to investigate the periodic convergence in detail, a corresponding moving window FFT plot is shown in Figure 6.56b, where it can be observed that the convergence throughout successive encounter periods may be classified as oscillatory. Generally, the band of oscillatory convergence reduces with increasing n, however, even with $n = 800$ time steps per encounter

Table 6.18: Temporal resolution uncertainties (obtained with $n = 200, 400$ and 800 time steps per encounter period).

Item	Heave uncertainty U_ζ, %	Pitch uncertainty U_θ, %	Resistance uncertainty U_{C_T}, %
Mean	3.29	43.00	1.81
Amplitude	3.00	2.12	2.13
Phase	3.99	10.77	31.45

period, the maximum deviation of zeroth order total resistance coefficient between encounter period 5 to 10 is approximately 9%. This indicates that a significant number of encounter periods needs to be simulated in order to reach periodically steady state solution. Furthermore, since the periodic uncertainty for all items is calculated using Eqn. (5.6) with values from 5 successive periods, the convergence of periodic uncertainty is shown in Figure 6.57. The graph demands further comments: on the x axis, the last period in uncertainty calculation i indicates that the corresponding periodic uncertainty is calculated using values from $(i-5)^{\text{th}}$ to i^{th} encounter period. Consequently, periodic uncertainty for each i is then viewed as the uncertainty which would be obtained by simulating i encounter periods. As shown in Figure 6.57, the periodic uncertainty is relatively high $(4\% < U < 8\%)$ when simulating only 6 or 7 periods, while it is reduced to $U < 2\%$ by simulating more than 10 periods. It can also be observed that the increase of number of time steps per encounter period n has a favourable influence: lowering the overall periodic uncertainty to $U \ll 1\%$ and ensuring smoother convergence.

Periodic uncertainties are presented in Table 6.19 for all simulations in the temporal resolution study, where the first column represents number of time steps per encounter period, while the second and third column represent periodic uncertainties of first order harmonic amplitudes of heave and pitch. Fourth, fifth and sixth column represent periodic uncertainties of the total resistance coefficient: zeroth order, first order amplitude and phase, respectively. Table 6.19 indicates that relatively low periodic uncertainty ($U < 5\%$) is obtained for all harmonic amplitudes even for very low temporal resolution. Periodic uncertainties of all items decrease further when the finer temporal resolution is used, where usually $U < 1\%$. For the first order harmonic phase of resistance, the periodic uncertainty is high for $n \leq 50$. It should be noted that overall low periodic uncertainties are the result of simulating at least 30 encounter periods, as can be seen in Figure 6.57.

Hydro–Mechanical Coupling Study

The hydro–mechanical coupling study is performed by using $n = 2, 4, 6$ and 8 outer correctors per time step for the C5 test case. The number of outer correctors corresponds with the number of grid motion and relative flux updates

Table 6.19: Periodic uncertainties for varying number of time steps per encounter period, n.

n	$U_{\zeta 1}, \%$	$U_{\theta 1}, \%$	$U_{C_{T0}}, \%$	$U_{C_{T1}}, \%$	$U_{C_{T\gamma 1}}, \%$
25	1.31	0.45	1.37	0.51	19.8
50	2.45	0.58	4.30	0.79	64.2
100	0.91	0.19	1.59	0.20	1.99
200	0.20	0.06	0.47	0.06	0.46
400	0.03	0.02	0.08	0.02	0.26
800	0.03	0.01	0.12	0.04	0.15

within a single time step. 4 pressure correction steps are used inside each PISO loop. Since a minor difference with 400 and 800 time steps per encounter period is observed in the temporal resolution study, 400 time steps are used for simulations in hydro–mechanical coupling study.

Figures 6.58–6.60 present convergence of heave, pitch and total resistance coefficient, respectively, with increasing number of outer correctors per time step, n. All items are extremely insensitive to varying n, indicating that accurate results may be obtained with only 2 outer correctors. This result is expected since the 6–DOF solution is strongly coupled with the pressure via velocity boundary condition at the hull, which is still updated 8 times (2 outer correctors + 4 PISO correctors = 8 pressure equations with updated hull velocity using 6–DOF motion equations). This effect shall be further investigated in a future publication. Using 2 outer correctors instead of 8 yields a speed–up of 4× with extremely minor influence on overall accuracy.

The corresponding numerical uncertainties for the hydro–mechanical coupling study are calculated using simulation results from $n = 2, 4$ and 8 outer correctors per time step, corresponding to a constant refinement ratio of $r = 2$. The uncertainties are reported in Table 6.20 in percentages, where the blue colour denotes monotone convergence and the black colour denotes oscillatory convergence. The uncertainties for all items are generally lesser than 1%, with few exceptions:

- For the same reason as discussed in the temporal resolution study, the zeroth order of pitch has unrealistically high uncertainty (see Figure 6.59a).

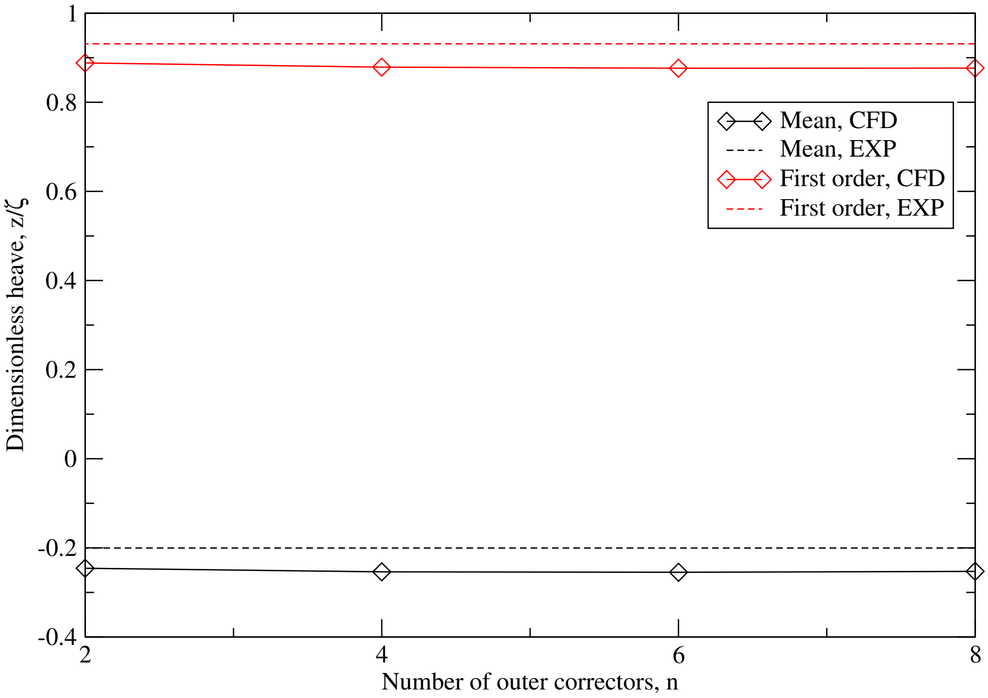

(a) Dimensionless heave amplitudes,

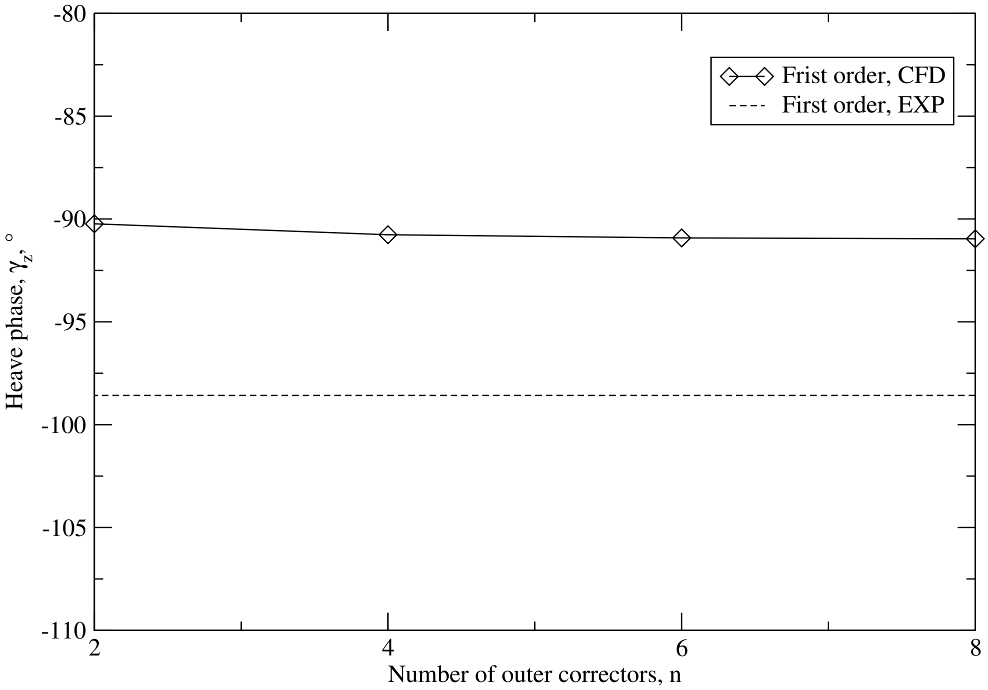

(b) Dimensionless heave phase,

Figure 6.58: Convergence of heave with increasing number of outer correctors per time step, C5 case, coarse grid (600 000 cells).

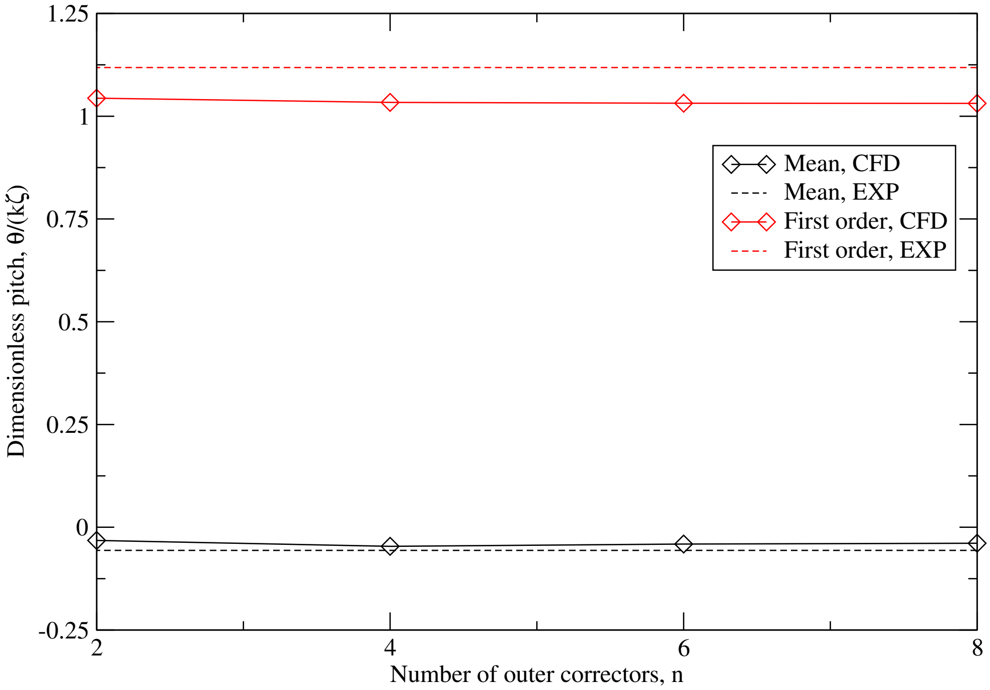

(a) Dimensionless pitch amplitudes,

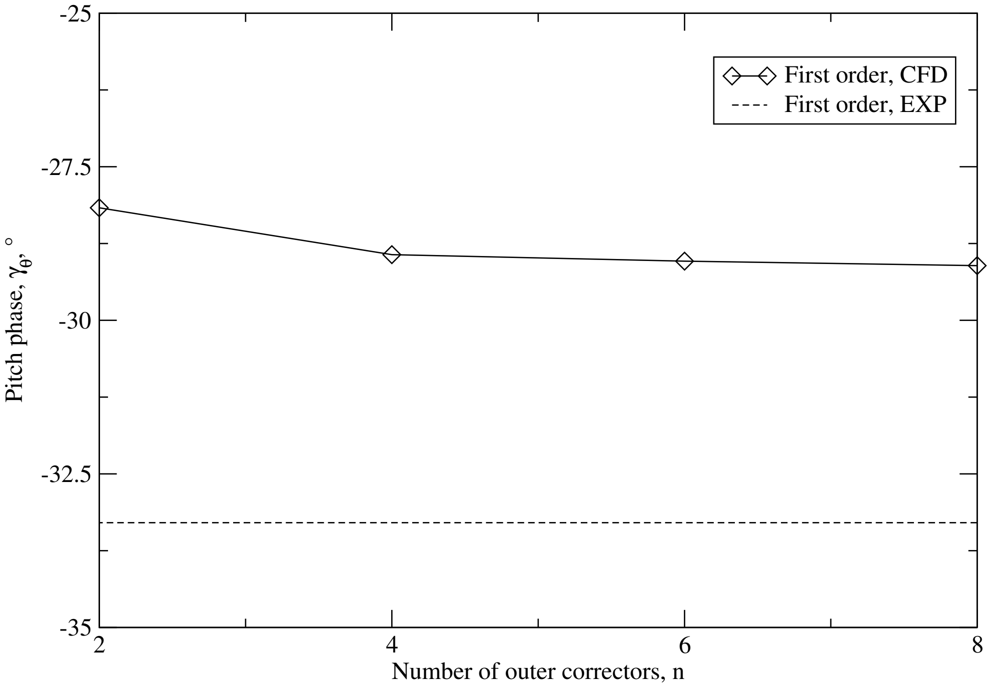

(b) Dimensionless pitch phase,

Figure 6.59: Convergence of pitch with increasing number of outer correctors per time step, C5 case, coarse grid (600 000 cells).

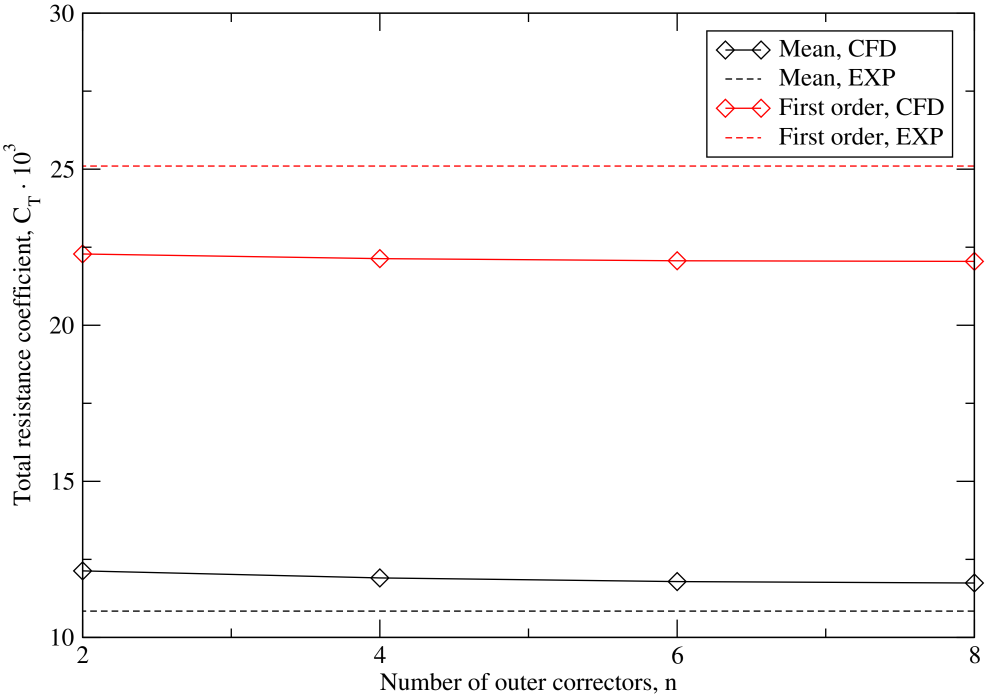

(a) Dimensionless resistance amplitudes,

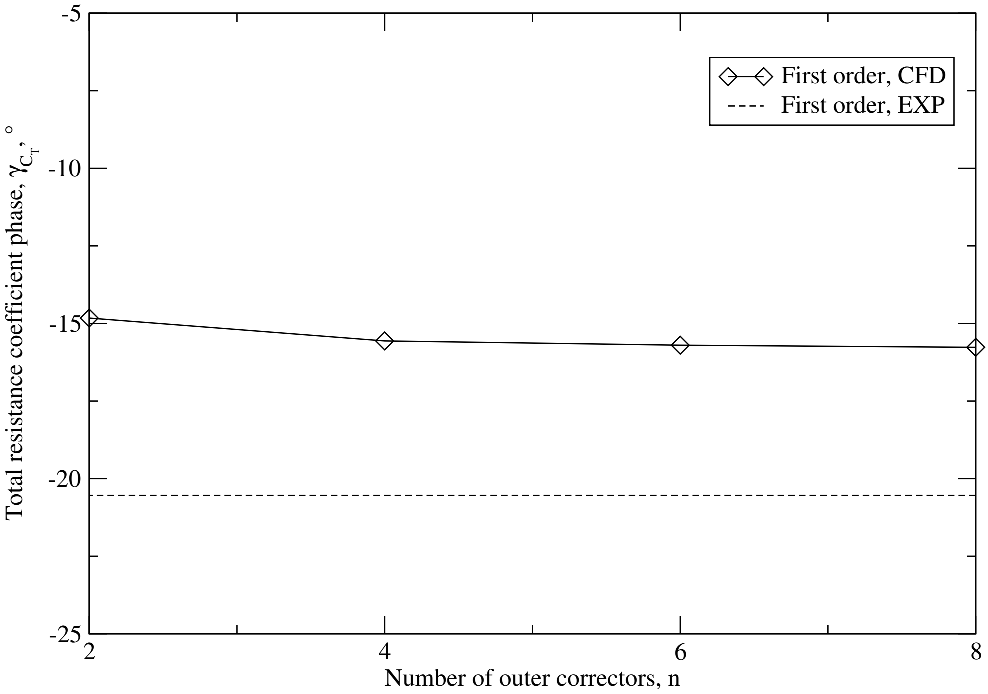

(b) Dimensionless resistance phases,

Figure 6.60: Convergence of total resistance with increasing number of outer correctors per time step, C5 case, coarse grid (600 000 cells).

- The relatively high uncertainty for the zeroth order of total resistance is due to the fact that low–order ($p \approx 0.45$) monotone convergence has been achieved for this item, indicating that the solutions are not within asymptotic range. Insensitivity of the total resistance coefficient with the increasing number of outer correctors can be seen in Figure 6.60a.

Compared to the temporal refinement study, all items exhibit convergence: 7 monotone and 2 oscillatory.

Figure 6.61a presents time domain signals of the total resistance coefficient for all simulations in the hydro–mechanical coupling study. The time–domain signals overlap, once again indicating the insensitivity of the solution to the number of outer correctors. In order to visualize periodic convergence in detail, moving window FFT plot of the zeroth order total resistance coefficient is presented in Figure 6.61b. All signals exhibit oscillatory convergence, where the band of oscillations is practically the same for all simulations. Again, in order to minimise periodic uncertainty and reach fully periodic steady state solution, more than 10 encounter periods must be simulated. Periodic uncertainties for representative items are calculated using Eqn. (5.6) with maximum and minimum values within last 5 encounter period and are reported in Table 6.21. All measured items have negligibly small periodic uncertainties, $U \ll 1\%$.

Comparing the uncertainty estimates from the hydro–mechanical coupling study with the temporal resolution study, it can be concluded that the decrease of number of outer correctors has no detrimental effect on the quality of results, whereas the decrease in number of time steps per encounter period (consequent

Table 6.20: Hydro–mechanical resolution uncertainties, obtained with $n = 2, 4$ and 8 outer correctors per time step.

Item	Heave uncertainties $U_\zeta, \%$	Pitch uncertainties $U_\theta, \%$	Resistance uncertainties $U_{C_T}, \%$
Mean	2.37	27.61	5.71
Amplitude	0.12	0.12	0.87
Phase	0.19	0.28	0.75

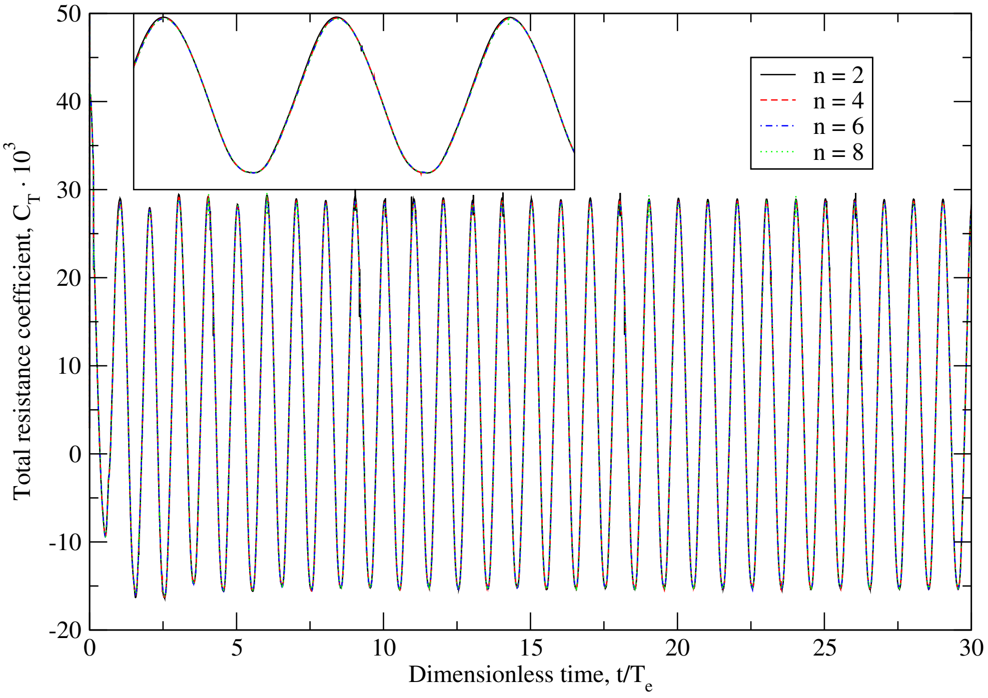

(a) Time domain signals,

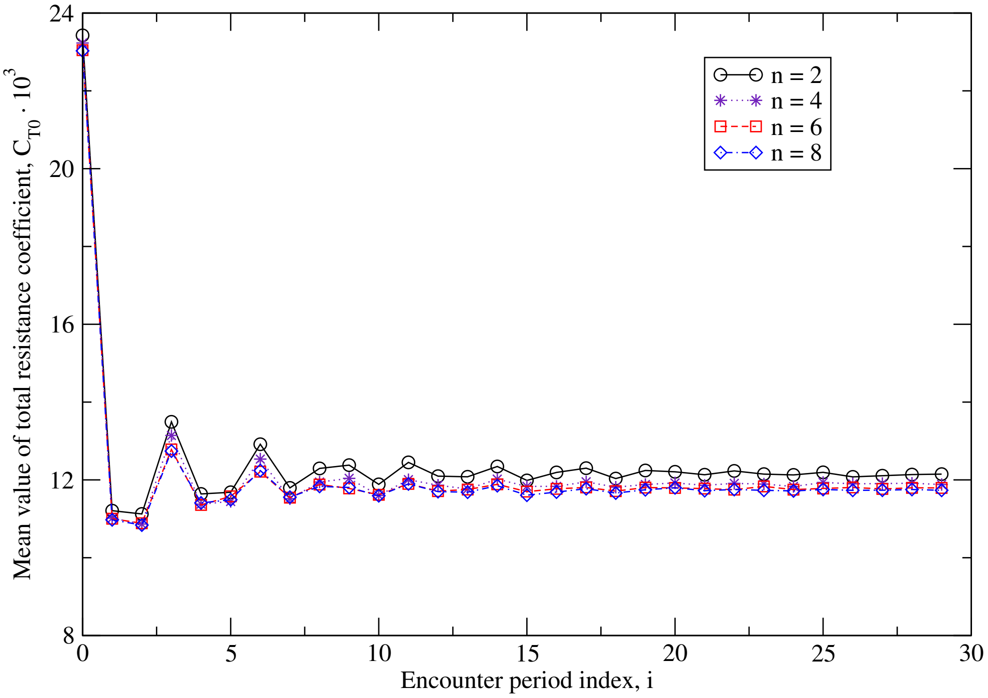

(b) Moving window FFT plot,

Figure 6.61: Convergence of the mean value of the total resistance coefficient for increasing number of outer correctors, n.

increase of the time step size) has relatively significant effect on the zeroth order and first order harmonic phases of measured items.

Grid Refinement Studies

Grid refinement studies are carried out for all test cases: C1, C2, C3, C4 and C5, using the three unstructured grids (see Table 6.16 for additional details). The grid refinement ratio is calculated as: $r = \Delta z_c/\Delta z_m \approx \Delta z_m/\Delta z_f = 1.262$, where Δz is representative height of the cell in vertical direction at the ship hull, while indices c, m and f denote coarse, medium and fine grid. Although $r = 1.262$ might be considered low for grid refinement studies, larger values of r have not been investigated due to limited time. 400 time steps per encounter period and 6 outer correctors per time step are used for all simulations in order to lower temporal and hydro–mechanical coupling uncertainties to a negligible level. Heave, pitch and total resistance coefficient are presented in Figures 6.62–6.64 in terms of transfer functions for dimensionless zeroth order, dimensionless first order harmonic amplitudes and first order harmonic phases in degrees, with respect to dimensionless wave length, λ/L_{PP}. The grid uncertainties are calculated for all items and test cases, and are presented as error bars in Figures 6.62–6.64. All results are compared with available experimental data, which did not include uncertainty estimates.

Zeroth and first order amplitude of heave are compared with experimental data in Figure 6.62a. The first order amplitude (solid red line) compares well with experimental results (dashed red line) for all wave lengths. The error bars and corresponding grid uncertainties are lesser than 2%, except for the C2 case where the grid uncertainty is approximately 5%. The zeroth order of heave (solid

Table 6.21: Periodic uncertainties for varying number of outer correctors per time step, n.

n	$U_{\zeta_1}, \%$	$U_{\theta_1}, \%$	$U_{C_{T0}}, \%$	$U_{C_{T1}}, \%$	$U_{C_{T\gamma 1}}, \%$
2	0.04	0.09	0.24	0.06	0.40
4	0.06	0.04	0.11	0.04	0.20
6	0.03	0.02	0.08	0.02	0.26
8	0.03	0.01	0.04	0.01	0.09

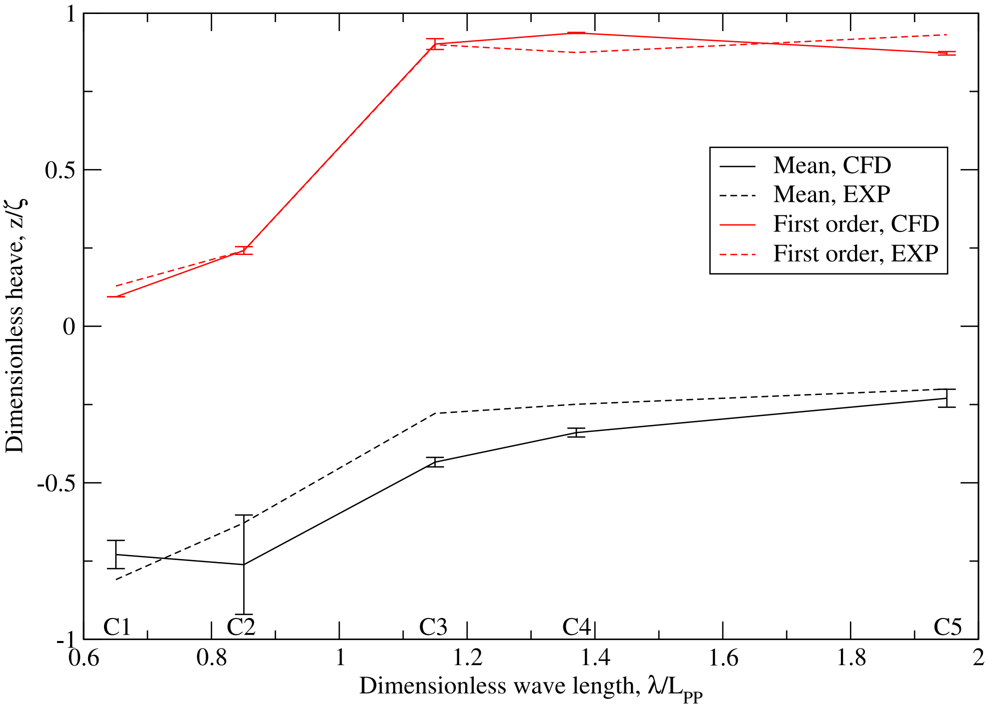

(a) Dimensionless heave transfer function,

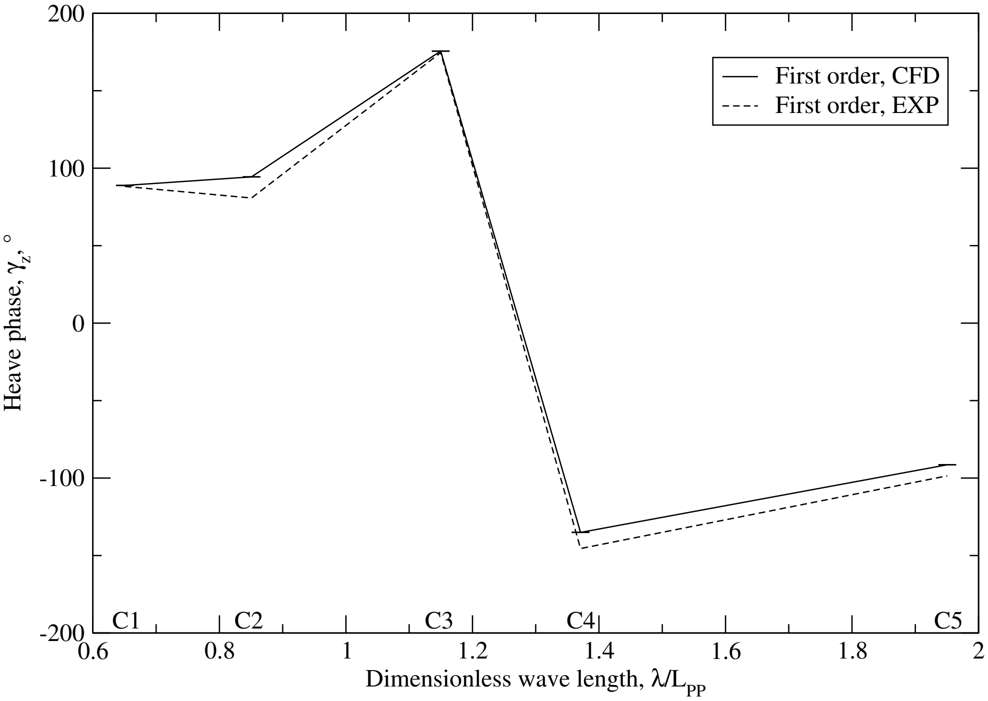

(b) Heave phase transfer function,

Figure 6.62: Transfer functions for heave for the KCS model in head waves: comparison of CFD (with error bars) with experimental measurements.

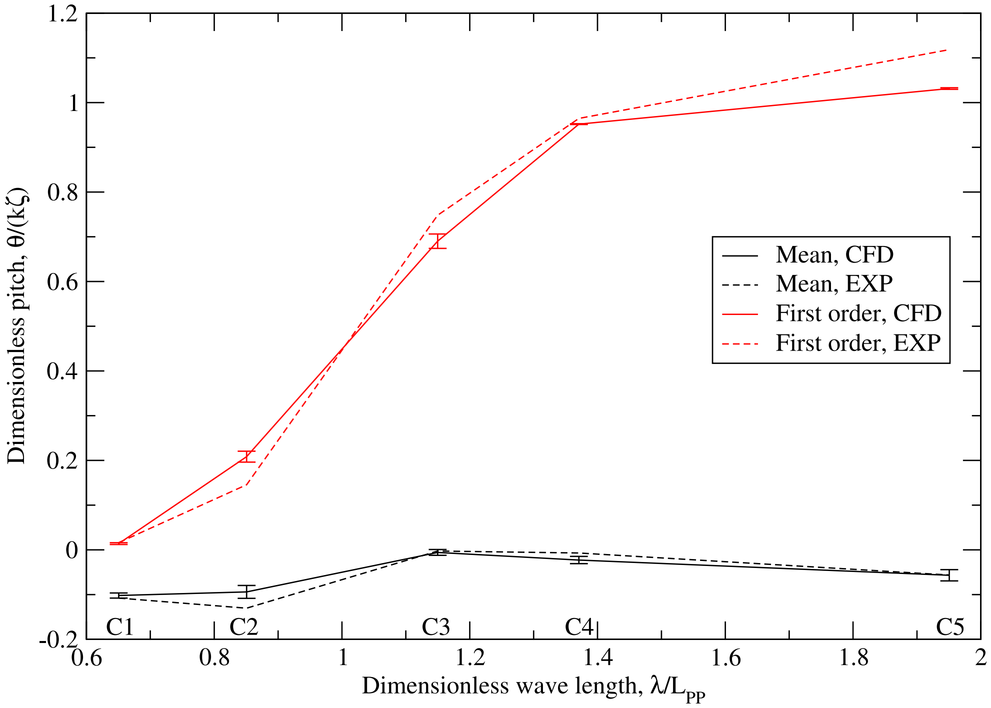

(a) Dimensionless pitch transfer function,

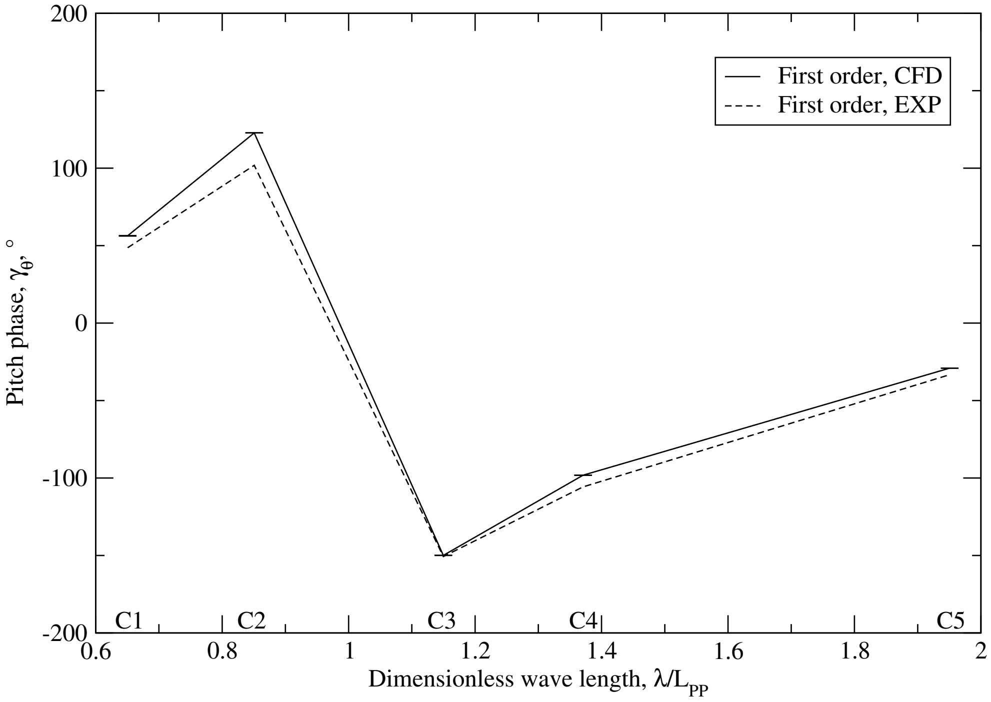

(b) Pitch phase transfer function,

Figure 6.63: Transfer functions for pitch for the KCS model in head waves: comparison of CFD (with error bars) with experimental measurements.

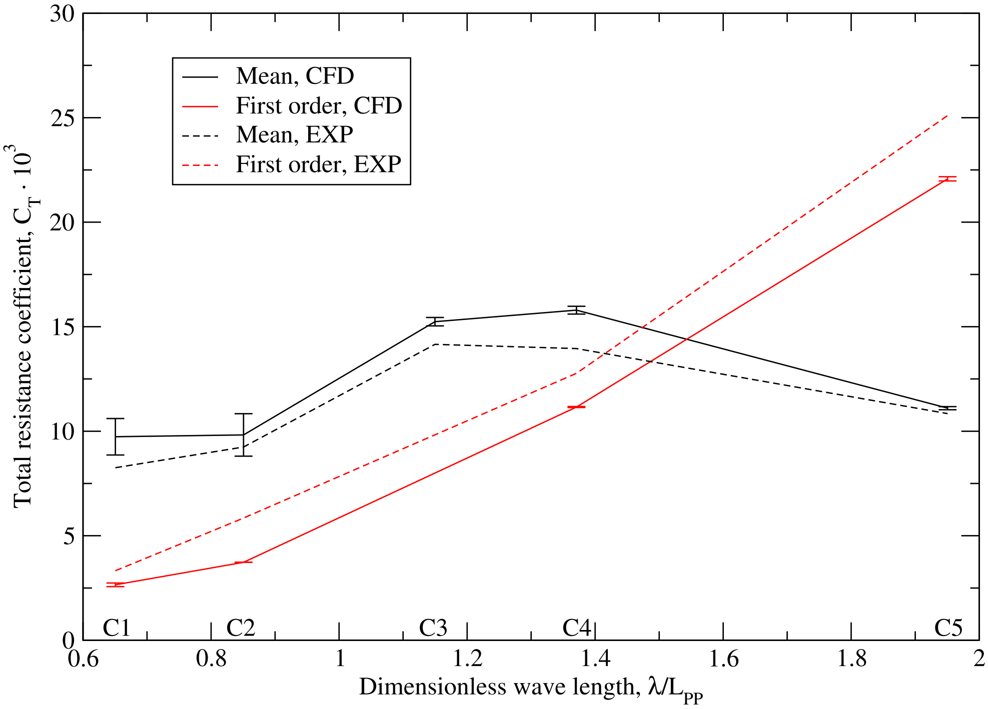

(a) Total resistance coefficient transfer function,

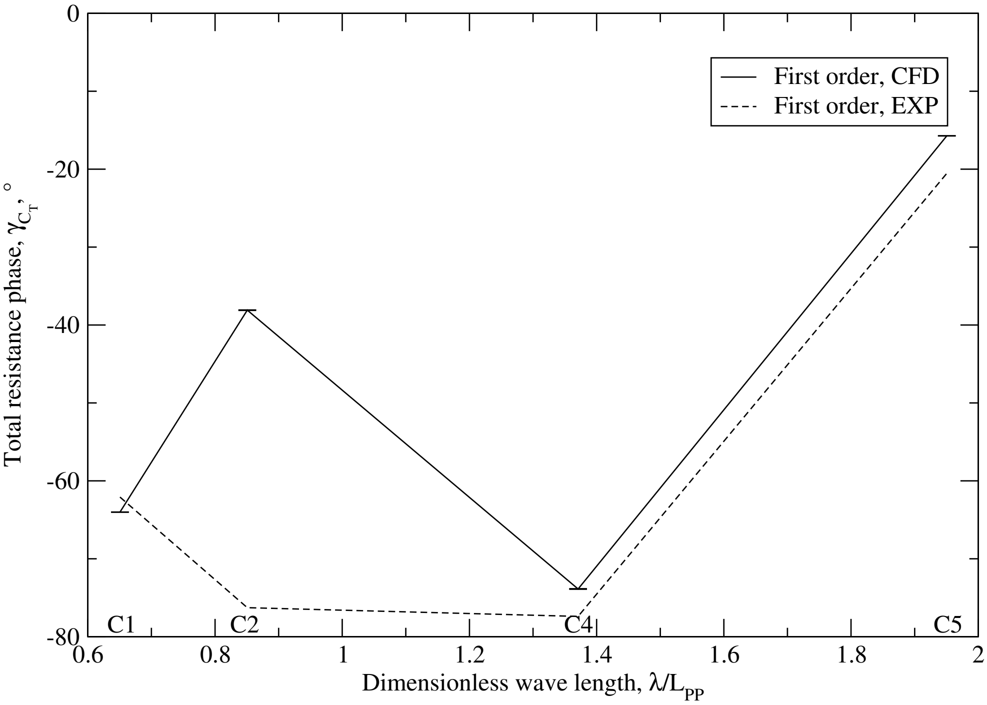

(b) Total resistance coefficient phase transfer function,

Figure 6.64: Transfer functions for resistance for the KCS model in head waves: comparison of CFD (with error bars) with experimental measurements.

black line) captures the correct trend as in experiments (dashed black line), where the CFD results over–predict the experimental values. The corresponding grid uncertainties are approximately 6% on average, except for the C2 case, where the convergence with grid refinement is not achieved, yielding high uncertainty of 20%.

The results for first order heave phases agree well with experimental measurements for all wave lengths, as shown in Figure 6.62b. Grid uncertainties are 0.9% on average, as indicated by small error bars.

Pitch motions are compared with experimental data in Figure 6.63a, where both zeroth and first order harmonic amplitude compare well with experimental data. The largest discrepancy for the first order harmonic amplitude is obtained for the C5 case, under–predicting the experimental results by approximately 8%. This might be related to large amplitude motions causing free surface to be located in coarser grid regions at motion peaks, increasing dissipation errors. Grid uncertainties are low, as can be seen from the error bars.

First order harmonic pitch phases are presented in Figure 6.63b, showing good agreement with the experimental measurements for the whole range of wave lengths. The grid uncertainties are very small, generally lesser than 2%, as indicated by narrow error bars.

Zeroth and first order amplitude of the total resistance coefficient are presented in Figure 6.64a. Zeroth order of the resistance closely follows the trend of experimental data, slightly over–predicting the experimental measurements. The grid uncertainties are approximately 10% for C1 and C2 cases. In these cases, the high uncertainties are the result of divergence with grid refinement. For C3, C4 and C5 cases, oscillatory grid convergence is achieved with small uncertainty of approximately 1%. While the mean value (zeroth order) of total resistance is slightly over–predicted compared to experimental data, the first order amplitude is slightly under–predicted. The grid uncertainties are smaller than 1% for all cases for the first order amplitude. Note that the first order amplitude of total resistance is not reported for the resonant C3 case due to difficulties in experimental settings (see [128]).

First order harmonic phases of the total resistance coefficient are presented in Figure 6.64b. For 3 out of 4 wave lengths[1], phases compare well with experimental data. The largest discrepancy of approximately 35° is obtained for the C2 case. This should be further investigated, since the corresponding grid uncertainty is only 4%. Grid uncertainties for other first order harmonic phases (C1, C4 and C5 cases) are below 3%.

Table 6.22 presents detailed grid uncertainty results for all test cases, where black, blue and red colours denote: oscillatory convergence, monotone convergence and divergence, respectively. 23 out of 45 items do not exhibit convergence with grid refinement (red items), although their grid uncertainty[2] is often below 10% of the fine grid solution. Very large and unrealistic uncertainties (*e.g.* zeroth order of pitch for the C3 case), often occur due to normalisation with extremely small values. 17 out of 22 converging items (black) exhibit oscillatory convergence with grid refinement, where the corresponding uncertainty is often below few percents. 5 items exhibit monotone convergence (blue), where the grid uncertainties are lesser than 1%, except for the first order of resistance for the C3 (resonant) case where $U \approx 11\%$. It is also interesting to note that zeroth orders have slightly higher grid uncertainties compared to first order harmonic amplitudes and phases for most items.

From Table 6.22, it can also be observed that the converging items are clustered at longer wave lengths and greater wave heights (cases C4 and C5). This is expected since these cases have finer relative grid resolution (greater number of cells per wave height and length) compared to other cases. Hence, in order to further investigate grid convergence, finer grids need to be used for other cases. For example, using fine grid (1 600 000) on the C1 case yields approximately only 9 cells per wave height (see Table 6.16). Having in mind the grid refinement study results for the wave propagation presented in Sec. 6.3.5., only 9 cells per wave height might not be sufficient for accurate wave propagation.

Periodic uncertainties are calculated for all test cases and grids, where the same behaviour as presented in Figure 6.56 for 400 time steps per encounter

---

[1] Note that the resonant C3 case is excluded from the experimental report due to difficulties in the experimental settings.

[2] Note that the grid uncertainty for diverging items is calculated as the largest deviation multiplied with a safety factor (see Eqn. (5.7)), yielding a conservative estimate.

Table 6.22: Grid refinement uncertainties.

Item		Heave uncertainties $U_{\zeta}, \%$	Pitch uncertainties $U_{\theta}, \%$	Resistance uncertainties $U_{C_T}, \%$
C1	Mean	6.18	5.61	8.97
	Amplitude	14.12	2.12	3.20
	Phase	0.18	13.39	1.37
C2	Mean	20.85	15.34	10.34
	Amplitude	5.07	5.87	0.03
	Phase	2.24	1.32	4.24
C3	Mean	3.51	112.49	1.33
	Amplitude	1.91	2.34	10.86
	Phase	0.48	0.19	7.88
C4	Mean	4.15	35.76	1.17
	Amplitude	0.19	0.10	0.21
	Phase	1.07	1.44	2.36
C5	Mean	12.47	22.15	0.68
	Amplitude	0.64	0.17	0.46
	Phase	0.72	1.54	2.63

period is observed for all measured items. To quantify, periodic uncertainties for the zeroth and first order harmonic amplitudes of heave, pitch and total resistance are always lesser than 2%, where a major portion of items has extremely low periodic uncertainty: $U \ll 1\%$. Again, it is important to stress that such a low periodic uncertainty is achieved by simulating 30 encounter periods.

6.5.5. Flow Field Visualization

Some details regarding flow visualization are presented in this section for the resonant C3 case using the coarse mesh.

Figure 6.65 presents perturbation velocity field at the symmetry plane of the ship near the bow during a representative period, while the free surface is denoted with thin white line. The perturbation velocity has highest magnitudes in the boundary layer and near the bulb and the deck, while it decays farther from the ship hull. Total velocity field in the same region is presented in Figure 6.66, where the maximum velocity magnitude is approximately 3.5 m/s at the deck when the ship pitches bow down. It can be seen that the velocity field at the symmetry plane of the ship is similar to the velocity field obtained in single–phase simulations for pitching airfoils [129]. Figure 6.67 presents perturbation velocity field at the symmetry plane near the stern of the ship. Highest perturbation velocities occur in the propeller region and behind the transom stern. This is expected since the incident velocity field does not take into account the presence of a ship. An overall effect of the perturbation velocity field to the total velocity field can be seen in Figure 6.68, where the total velocity field has smaller magnitudes in propeller region and behind the transom stern.

6.5.6. KCS Hull in Oblique Waves (Model B)

The final part of validation and verification of the present numerical framework is performed by considering KCS model in regular oblique waves at design speed. Experimental results are publicly available in [128, 4, 23] for five encounter angles:

- C1: $\chi = 0°$–head sea,
- C2: $\chi = 45°$–bow sea,
- C3: $\chi = 90°$–beam sea,
- C4: $\chi = 135°$–quartering sea,
- C5: $\chi = 180°$–following sea.

Table 6.23: Oblique wave KCS test case parameters [128].

	C1	C2	C3	C4	C5
L_{PP}, m	2.7				
F_r	0.26				
λ, m	2.7				
H, m	0.045				
χ,°	0	45	90	135	180

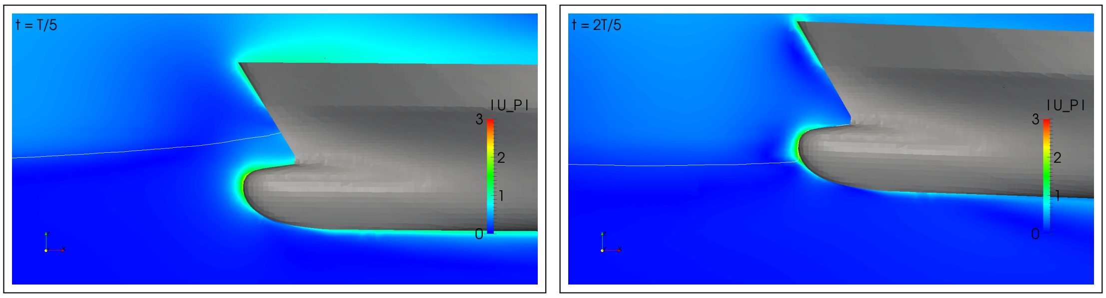

(a) $t = T/5$.

(b) $t = 2T/5$.

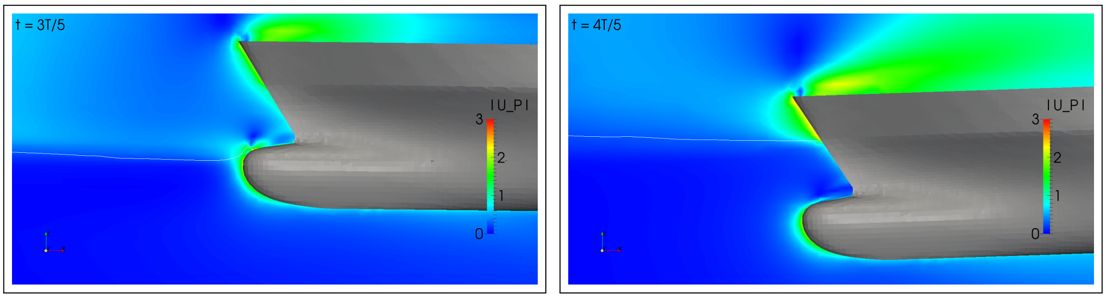

(c) $t = 3T/5$.

(d) $t = 4T/5$.

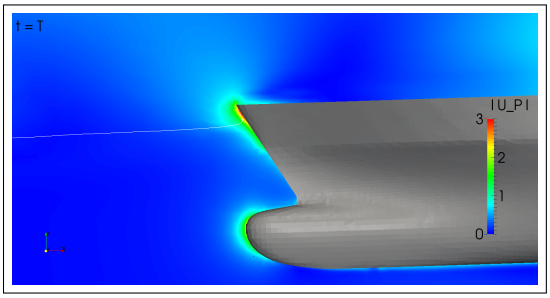

(e) $t = T$.

Figure 6.65: Perturbation velocity field ($\mathbf{u}_P$) at the symmetry plane near the bow during a representative encounter period, resonant C3 case.

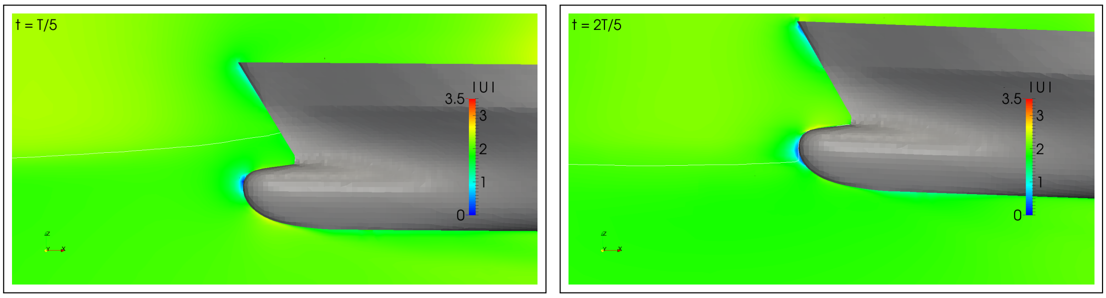

(a) $t = T/5$.

(b) $t = 2T/5$.

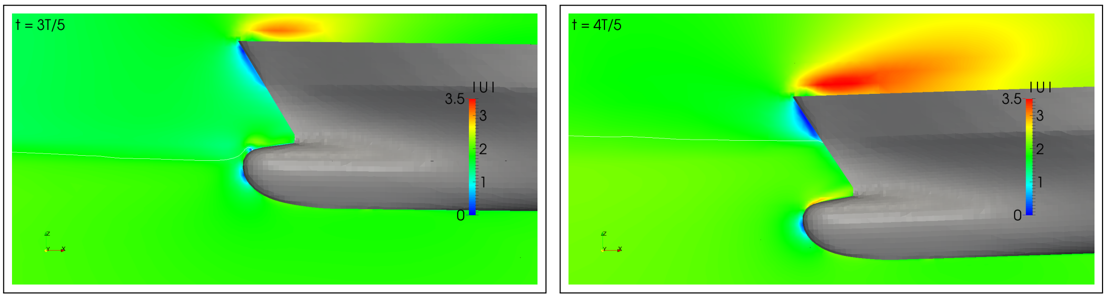

(c) $t = 3T/5$.

(d) $t = 4T/5$.

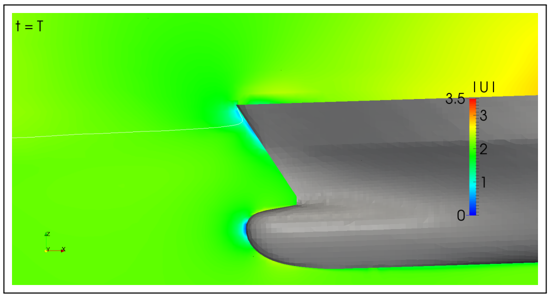

(e) $t = T$.

Figure 6.66: Total velocity field ($\mathbf{u}$) at the symmetry plane near the bow during a representative encounter period, resonant C3 case.

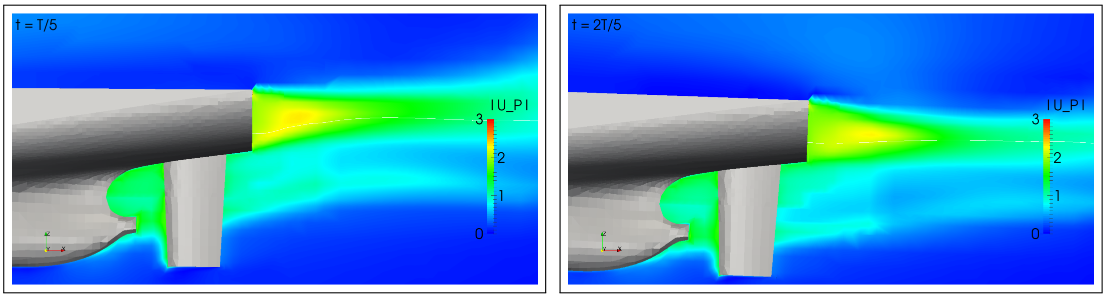

(a) $t = T/5$.

(b) $t = 2T/5$.

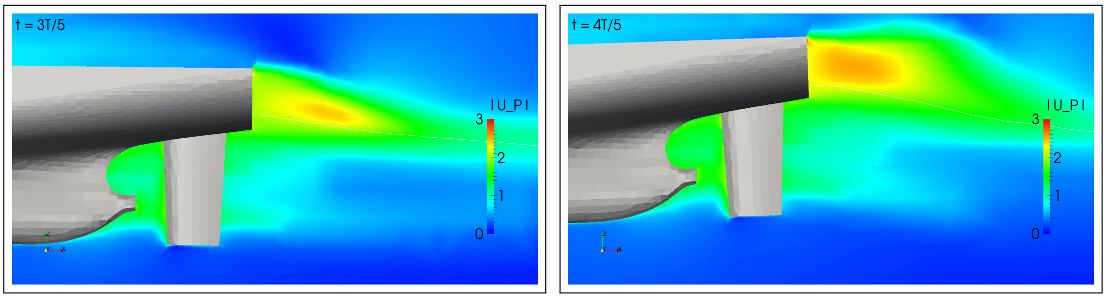

(c) $t = 3T/5$.

(d) $t = 4T/5$.

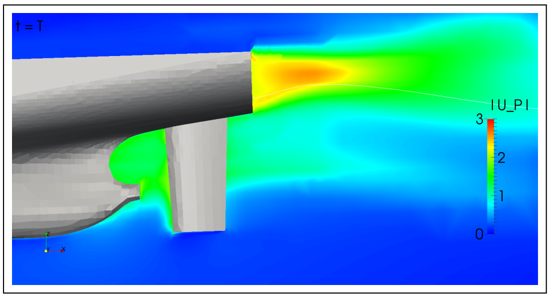

(e) $t = T$.

Figure 6.67: Perturbation velocity field ($\mathbf{u}_P$) at the symmetry plane near the stern during a representative encounter period, resonant C3 case.

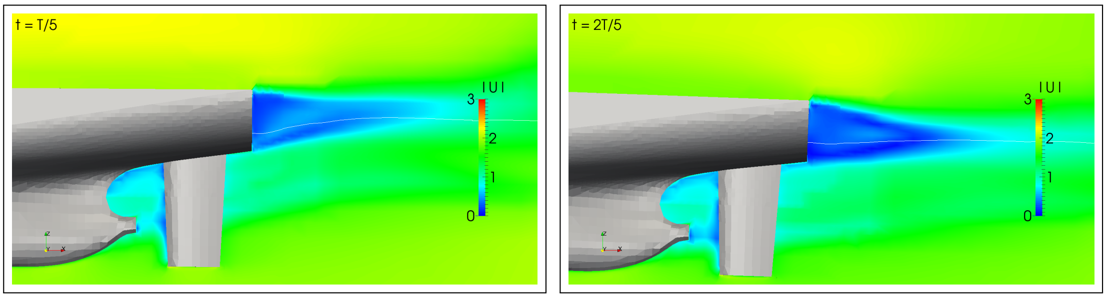

(a) $t = T/5$. (b) $t = 2T/5$.

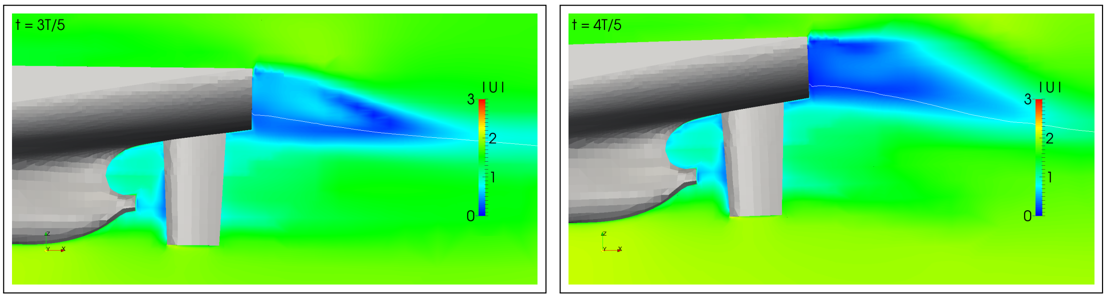

(c) $t = 3T/5$. (d) $t = 4T/5$.

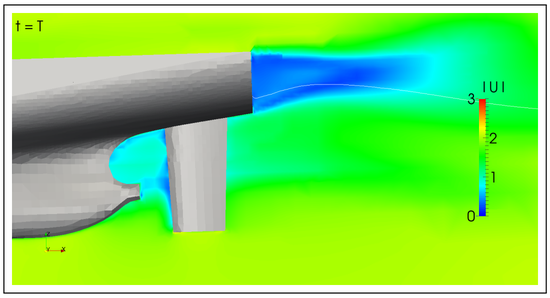

(e) $t = T$.

Figure 6.68: Total velocity field ($\mathbf{u}$) at the symmetry plane near the stern during a representative encounter period, resonant C3 case.

As shown in Table 6.23, the model is $L_{PP} = 2.7$ m long, the wave length is equal to L_{PP} and the wave height is $H = 0.045$ m. The model is towed with a spring system enabling heave, pitch and roll motions, where the total resistance is reported along with the three motions. Following recommendations published in [128], the spring system has not been modelled in present CFD simulations, where surge, sway and yaw are fully constrained, while heave, roll and pitch motions are calculated. The experimental uncertainty has not been assessed.

It should be noted that computational grids are obtained by mirroring the grids with the symmetry plane, producing three grids with approximately 1 200 000, 1 900 000 and 3 200 000 cells, as discussed in Sec. 6.5.2.

Grid Refinement Studies

The grid refinement studies are carried out for all test cases: C1, C2, C3, C4 and C5, where the grid refinement ratio remains the same: $r = 1.262$ (see Sec. 6.5.4.). 7 outer correctors and 3 PISO correctors per time step are used, where the original hydro–mechanical coupling strategy is used (see Figure 4.4). Hence, the 6–DOF is not updated after each pressure correction step in order to obtain a new estimate of the hull boundary velocity as this procedure has only been recently developed and only the head wave cases have been recalculated with this strongly–resolved coupling procedure.

Number of time steps per encounter period ($n_{\Delta t}/T_e$), number of simulated encounter periods (N_{T_e}) and the CPU time per encounter period (t_{CPU}/T_e) are presented in Table 6.24. For all simulations except for the beam waves simulation (C3) on the fine grid, a constant time step of 0.004 seconds is used. As the encounter period increases from head to following waves, the relative temporal resolution also increases from $\approx$ 200 time steps per encounter period in head waves to $\approx$ 1 000 time steps in following waves. The third column in Table 6.24 reports the total number of simulated encounter periods, which is reduced towards following waves due to limited computational resources. Nevertheless, it is important to stress that more than 20 encounter periods are always simulated in order to lower periodic uncertainty. All simulations are performed in parallel using 56 cores, where the CPU time per encounter period is reported in the last column of Table 6.24. The CPU time per encounter period for head, bow and

Table 6.24: CPU times for oblique wave simulations.

Item		$n_{\Delta t}/T_e$	N_{T_e}	t_{CPU}/T_e, h
C1	Coarse	N/A	N/A	N/A
	Medium	199	37	0.40
	Fine	199	31	0.90
C2	Coarse	225	72	0.32
	Medium	225	57	0.59
	Fine	225	60	0.67
C3	Coarse	202	60	0.35
	Medium	202	60	0.46
	Fine	329	49	1.38
C4	Coarse	610	41	0.86
	Medium	610	45	1.39
	Fine	610	29	3.03
C5	Coarse	944	45	1.28
	Medium	944	21	2.18
	Fine	944	22	4.53

beam wave simulations is generally lesser than an hour, whereas for the following waves, the CPU time per encounter period reaches up to 4 hours. This is a direct consequence of using a fixed time step as the encounter period is significantly higher with increasing encounter angles.

The results are presented in Figure 6.69 and Figure 6.70 in terms of transfer functions for heave, roll, pitch and total resistance, with respect to wave encounter angle (ship heading). As for the head wave cases, the grid uncertainties are calculated and presented as error bars for all test cases and measured items. The CFD results are compared with experimental data, which did not include uncertainty estimates. Again, it is important to note that the zeroth order is reported as twice the mean value, according to guidelines in [128].

Zeroth and first order harmonic amplitudes of heave are presented in Figure 6.69a. The first order harmonic amplitude is in good agreement with the experimental data for all wave directions, where the CFD results slightly over–

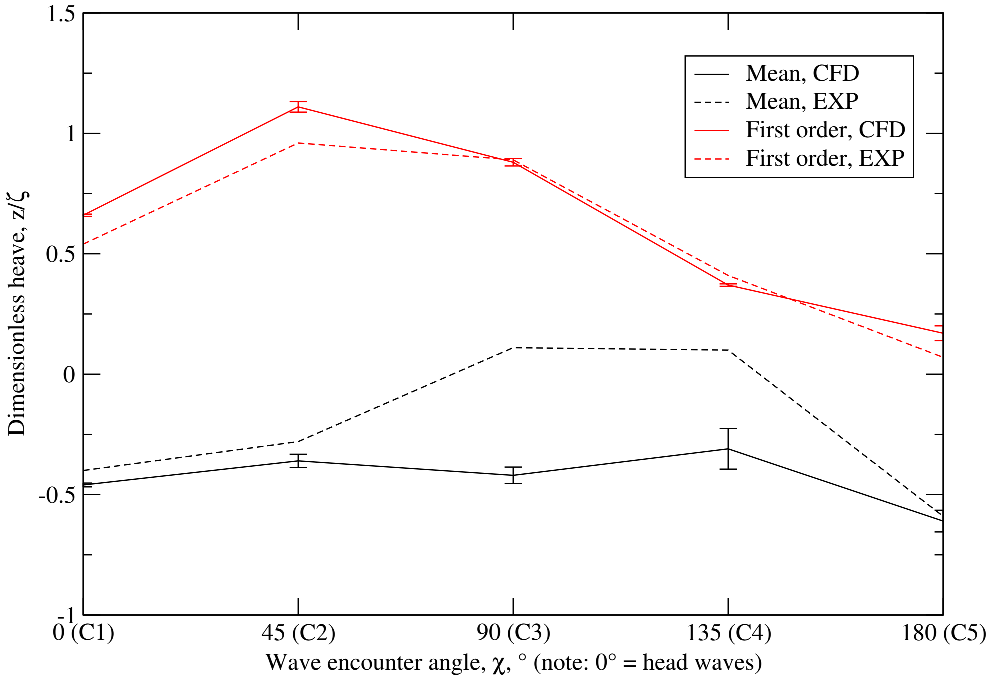

(a) Dimensionless heave transfer function,

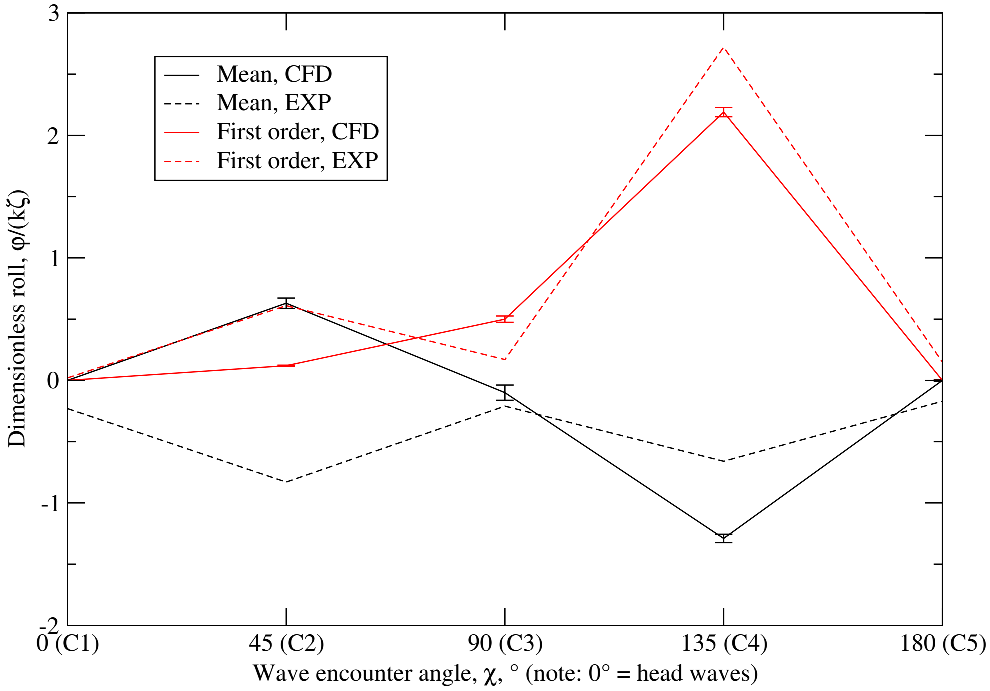

(b) Dimensionless roll transfer function,

Figure 6.69: Oblique waves KCS transfer functions for heave and roll: comparison of CFD (with error bars) with experimental measurements.

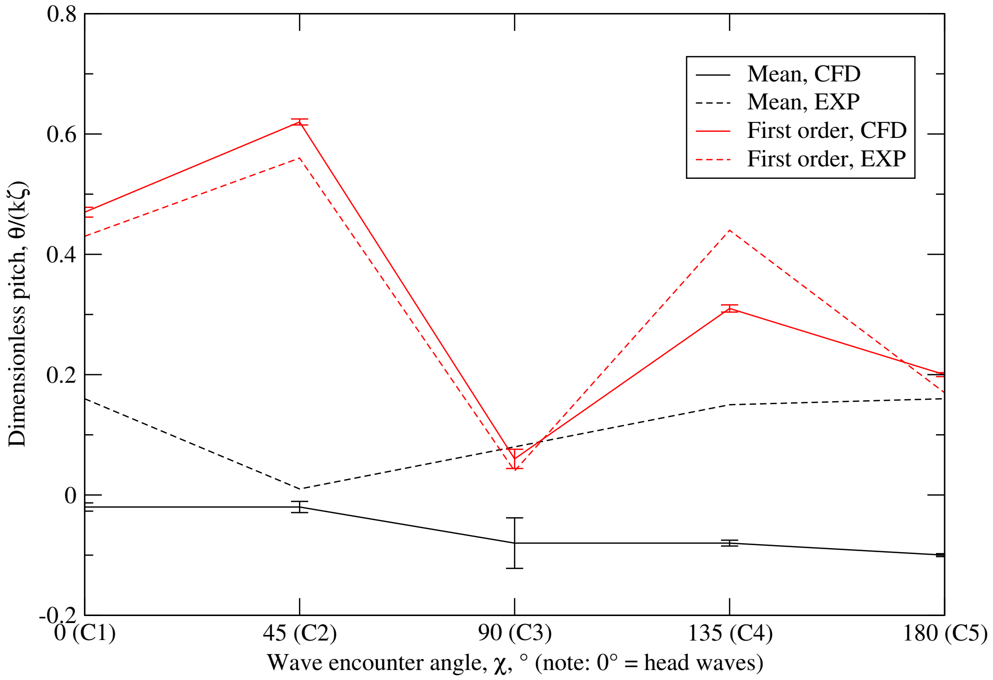

(a) Dimensionless pitch transfer function,

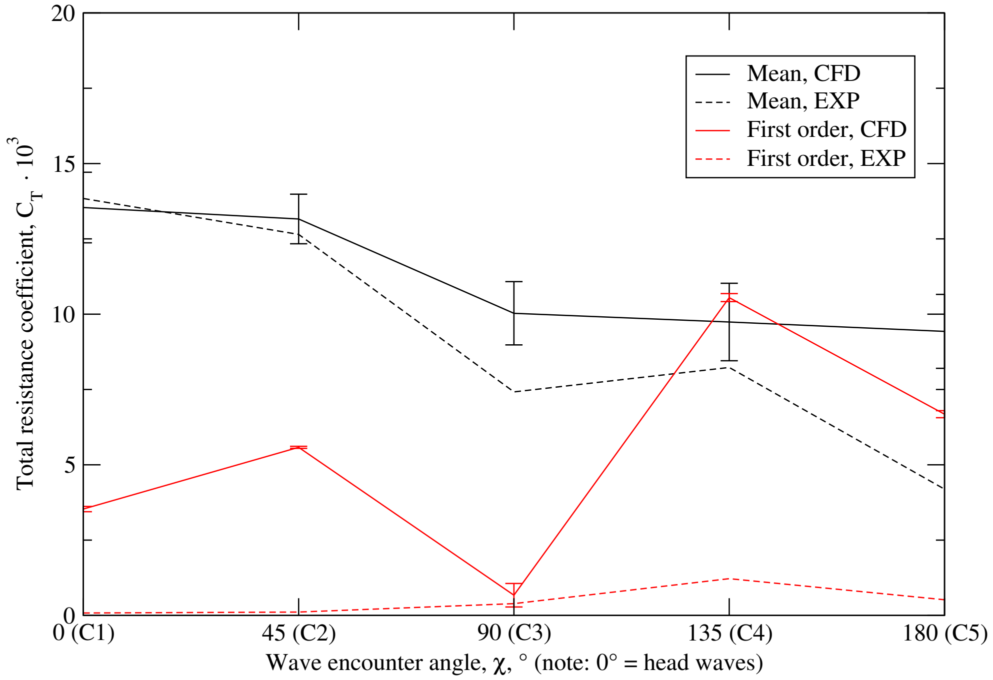

(b) Total resistance coefficient transfer function,

Figure 6.70: Oblique waves KCS transfer functions for pitch and resistance: comparison of CFD (with error bars) with experimental measurements.

predict the experimental heave amplitude for head and bow waves. The zeroth order of heave significantly deviates from the experimental measurements for the beam and quartering waves, which demands further investigation. The grid uncertainty for the zeroth order of heave is approximately 6% on average, except for the quartering wave (C4) case with grid uncertainty of 27%. The first order harmonic amplitude of heave has grid uncertainties lesser than 2% for all cases except for the following waves, where the grid uncertainty is approximately 18%. The high grid uncertainty for this case is caused by the smallest measured response (compared to heave amplitudes in other cases).

The comparison of roll motions is presented in Figure 6.69b, where it is important to note two implausible experimental roll measurements:

- The zeroth order of roll measured in head and following waves is approximately 0.6°. Author believes that this value should be closer to zero as the parametric roll does not occur for this particular setting.
- The first order harmonic amplitude of roll in beam sea is approximately the same as in following sea. Even with relatively high wave length to ship breadth ratio ($\lambda/B \approx 7.14$), it is reasonable to expect that larger roll amplitudes would be obtained compared to following waves, where the amplitude should be negligibly small.

Having this in mind, the CFD results seem more consistent since both the zeroth and first order harmonic amplitudes of roll are very close to zero for head and following waves. It should be noted that the roll motion was calculated for all simulations, including head and following waves, where a negligibly small response is obtained. The CFD results also report larger first order harmonic roll amplitude for the beam waves compared to experimental results, as expected. The first order harmonic amplitude of roll in bow and quartering waves is under–predicted compared to experimental data. The zeroth order of roll for beam waves is approximately two times smaller in CFD, while for the bow waves, the sign of the zeroth order is opposite, possibly related to a post–processing error. The zeroth order of roll in quartering waves is over–predicted by CFD compared to experimental measurements. The grid uncertainty for the zeroth order of roll in bow and quartering waves is approximately 7% and 3%, respectively, while for the beam waves the grid uncertainty is high, $U \approx 63\%$, which is caused by very small measured values. The grid uncertainty for the first order harmonic amplitude of roll in bow, beam and quartering waves is small, approximately 2.5% on average, which can be directly seen from error bars in Figure 6.69b.

The comparison of pitch motions obtained with CFD and experimental data is presented in Figure 6.70a. The zeroth order of pitch as calculated in CFD has opposite signs compared to experimental measurements, which is probably related to an error in coordinate system orientation or post processing convention. Otherwise, magnitudes of zeroth order pitch response compare reasonably well with the experimental data for all headings. The first order harmonic amplitude of pitch closely follows the trend of experimental data for all encounter angles. CFD amplitudes slightly over–predict the experimental measurements in all wave headings except in quartering waves, where the experimental value is under–predicted. Narrow error bars denote small deviations with grid refinement for zeroth order, with beam wave case being an outlier with $U \approx 50\%$. The grid uncertainty for the first order harmonic amplitude of pitch is lesser than 2% for all cases, except for the beam waves case with $U \approx 29\%$, which is expected due to normalisation of uncertainty with extremely small values.

Zeroth and first order harmonic amplitudes of the total resistance coefficient are presented in Figure 6.70b. As for the roll motion, certain implausible experimental data have been observed:

- The experimentally measured mean value of the total resistance coefficient in beam sea (case C3) case is reported to be $3.71 \cdot 10^{-3}$, while the measured steady resistance coefficient with the same KCS model and the same Froude number (case C0, see [128]) is $4.66 \cdot 10^{-3}$. Hence, experimental measurements report approximately 20% lower mean value of total esistance in beam waves compared to calm water simulation, which is considered implausible,

- The first order harmonic amplitudes of the total resistance coefficient are very small for all encounter angles, probably due to the spring system used in the experimental setting. This inconsistency is demonstrated by comparing the first order harmonic amplitude of the total resistance coefficient

> with respect to wave height divided by ship length (H/L_{PP}). In Figure 6.71, circles represent the results from head wave cases (see Sec. 6.5.4.), and the X denotes the head waves case from the oblique wave cases (case C1). The measured first order harmonic amplitude of total resistance coefficient for the C1 case in oblique wave cases is approximately 0.1, while for the same H/L_{PP} ratio, the interpolated total resistance coefficient should be approximately 5, yielding a discrepancy of order of magnitude. Note that the same Froude number of 0.26 is used for both head and oblique wave cases [128].

The zeroth order of the calculated total resistance coefficient follows the trend of the experimental data, except for the already mentioned beam wave case where the highest discrepancy may be observed. The zeroth order in head and bow waves is well predicted and the CFD trend of decreasing resistance coefficient from beam to following waves is expected. The first order harmonic amplitude of the total resistance coefficient does not compare well with experimental data, as expected following the previous comments. The CFD results for first order harmonic amplitudes seem plausible since the smallest amplitude is obtained for the beam waves case, which is not the case in experimental measurements. The grid uncertainty for the zeroth order of approximately 10% on average is higher than the corresponding grid uncertainty for the head wave cases. The first order harmonic amplitudes of the total resistance coefficient have low grid uncertainty lesser than 3%, with the exception of beam waves case with $U \approx 58\%$. High grid uncertainty for the beam waves case is expected since an order of magnitude lower response is measured compared to other cases (specifically bow and quartering waves).

Periodic uncertainties are very low: lesser than 1% for almost all zeroth and first order harmonic amplitudes of heave, roll, pitch and total resistance coefficient. Low periodic uncertainties are achieved because a large number of encounter periods is simulated for each test case, as shown in Table 6.24. This is demonstrated in detail in Figure 6.72 and Figure 6.73, where Figure 6.72a presents time evolution of roll motion for the bow waves case on the fine grid, while Figure 6.72b presents the convergence of zeroth and first order harmonic amplitudes of roll throughout successive encounter periods. Only the roll is presented and discussed in detail since it usually represents the most challenging

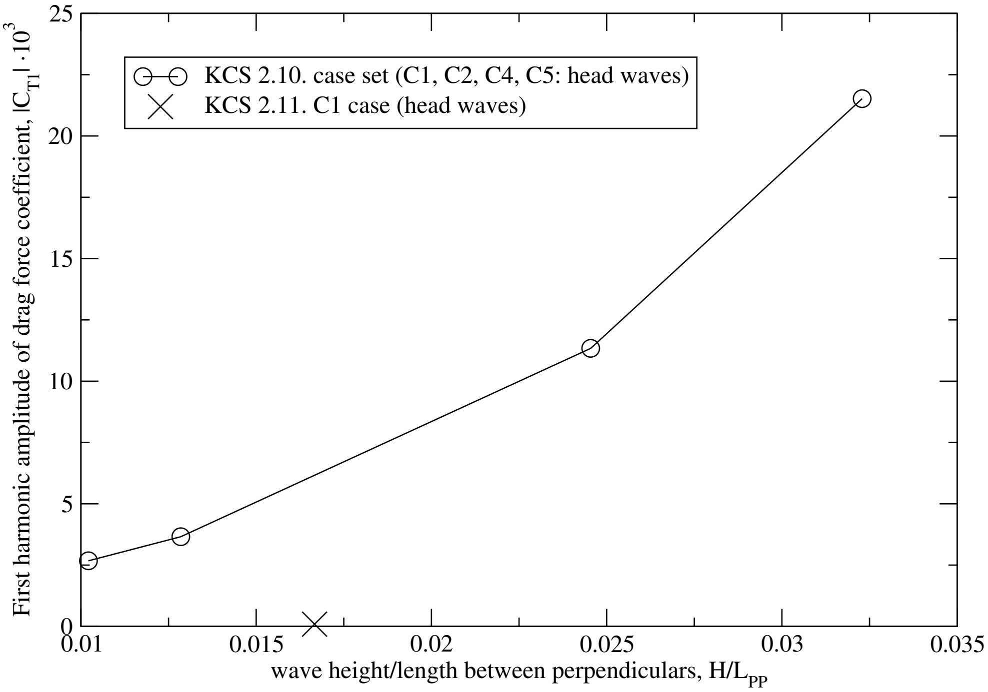

Figure 6.71: Discrepancy of the experimental resistance coefficient in head waves.

item for bow and quartering waves. From both the time domain and the moving window FFT plot in Figure 6.72, one can observe that at least 25 encounter periods need to be simulated in order to reach fully developed periodic solution. Also, Figure 6.72b reveals a small drift in the mean value of roll of approximately $9 \cdot 10^{-4}$ degrees per encounter period, which needs to be further investigated.

As the most significant roll response is obtained for the quartering waves, the periodic convergence is examined in detail and shown in Figure 6.73. Compared to the bow waves case in Figure 6.72, the periodically steady state solution is obtained within fewer number of encounter periods. This is expected for following reasons:

- Note that the same time step is used for both bow and quartering waves, yielding 225 time steps per encounter period for bow waves and 610 time steps per encounter period for quartering waves (see Table 6.24). As observed in Figure 6.56b from the temporal resolution study, the periodic convergence is improved when larger number of time steps per encounter period (*i.e.* smaller time step) is used,

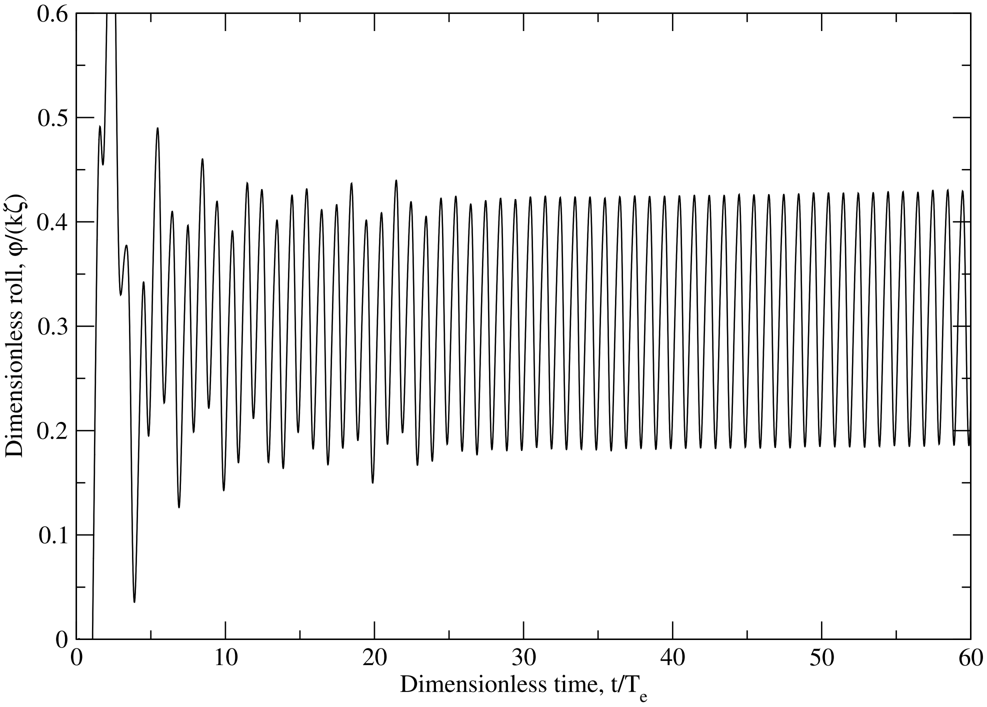

(a) Time domain signal: bow waves,

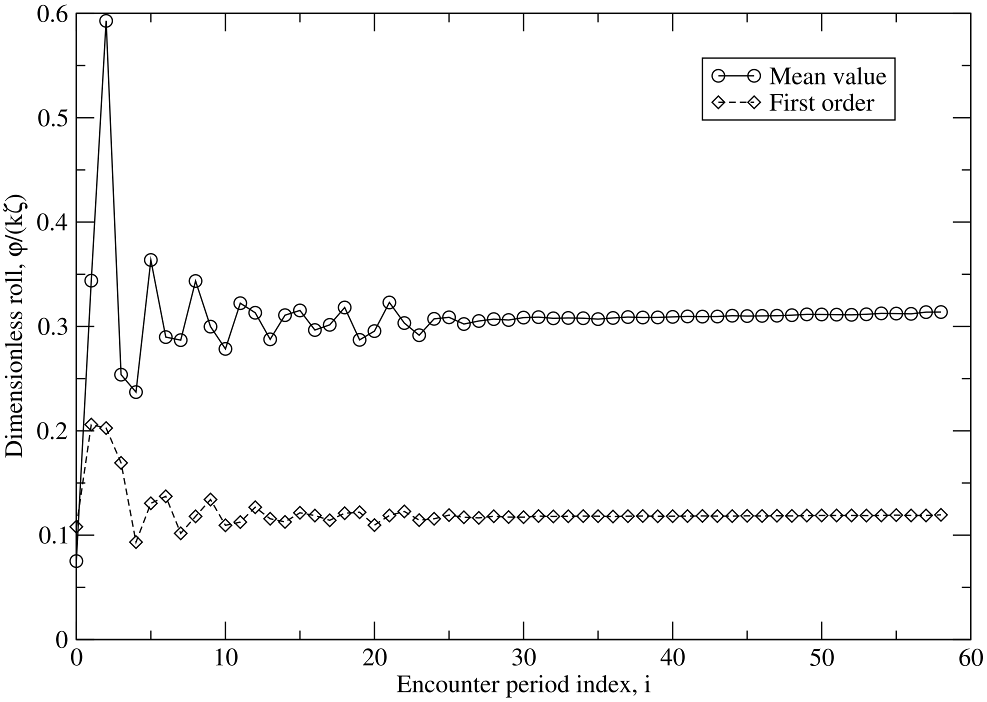

(b) Moving window FFT plot: bow waves,

Figure 6.72: Periodic convergence of roll motion for the bow waves case on the fine grid.

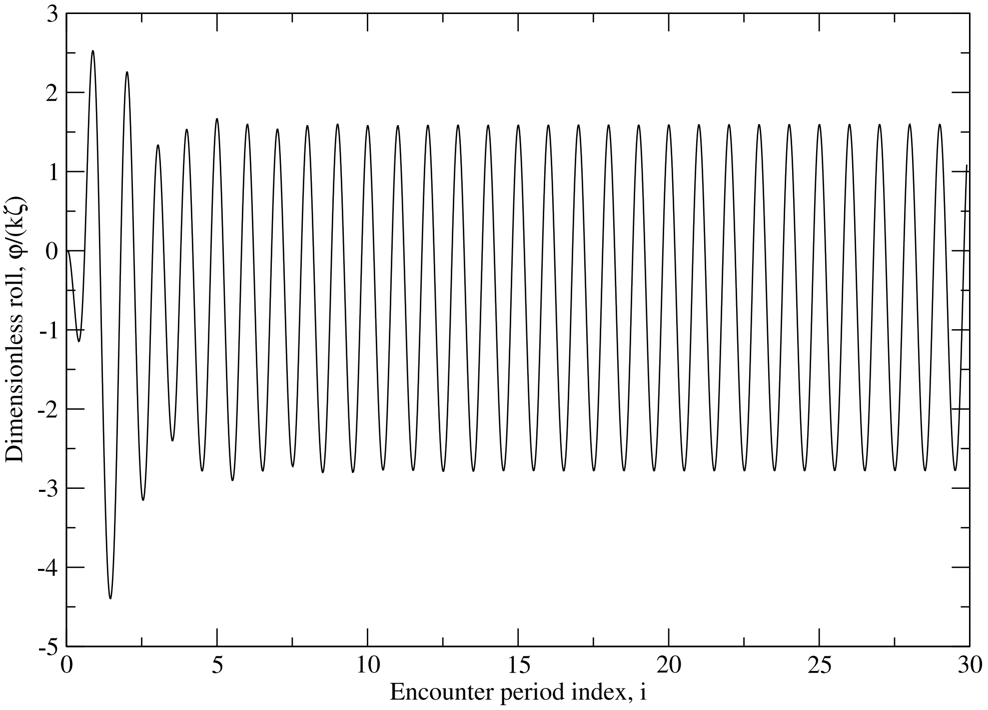

(a) Time domain signal: quartering waves,

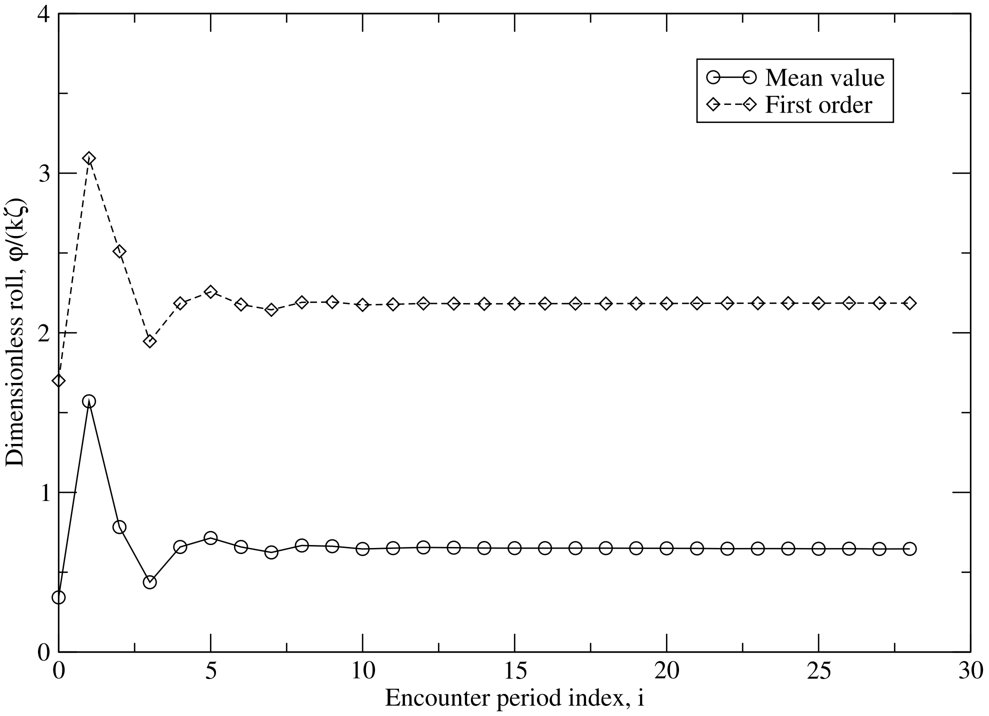

(b) Moving window FFT plot: quartering waves,

Figure 6.73: Periodic convergence of roll motion for the quartering waves case on the fine grid.

- The first order harmonic roll amplitude is order of magnitude higher compared to the bow waves case, making it easier to resolve.

6.6. Case Specific Conclusions and Closure

Detailed V&V has been presented for increasingly complex sets of test cases:

1. Free surface flow over a ramp,
2. Progressive wave simulations,
3. Higher order forces on a vertical cylinder,
4. Seakeeping of KCS models at design speed in head and oblique waves.

Validation has been performed by comparing the CFD results with analytical, other numerical and experimental data, depending on the test case. For all test cases, extensive verification has been carried out by performing numerous sensitivity studies, including: grid refinement study, temporal resolution study and periodic uncertainty assessment. The attention is now turned to each test case separately, where the global conclusions shall be outlined in Ch. 7..

Free Surface Flow Over a Ramp

Free surface flow over a ramp has been the first test case used to validate and verify the present decomposition model. The results confirmed that the dynamic pressure jump across the free surface is resolved across a single face as indicated in Ch. 4. where a detailed derivation of the interface–corrected schemes via GFM has been presented. Furthermore, a simple hydrostatic case has been considered on the same geometry and the results have been compared to the numerical model based on conditionally averaged equations (`interFoam` from `foam-extend-3.2` [117]), where the present model does not spuriously accelerate the lighter phase because the pressure–density coupling has been transferred to the pressure equation instead of the momentum equation.

Two grid refinement studies have been presented, using hexahedral and prismatic grids. The hexahedral grid refinement study yields monotone convergence with the achieved order of accuracy of $p \approx 2.45$, while the prismatic grid refinement study yields oscillatory convergence. Corresponding numerical uncertainties were approximately 0.06% for hexahedral and 3.6% for prismatic grids. Although the grid refinement uncertainties are small for both grid refinement studies, it is interesting to note that the uncertainty is significantly higher when one uses unstructured grids. However, this was expected since the uniform refinement is extremely difficult to achieve using unstructured grids. All results show good agreement compared to the analytical solution regarding height of the water at the outlet.

Progressive Wave Simulations

Numerous sensitivity studies have been performed for the progressive wave simulations using relatively coarse grid with approximately 11 700 cells. All results have been compared to fully nonlinear potential flow stream function wave theory [60]. During wave propagation, the dynamic pressure jump across the free surface is well captured, accurately resolving the dynamic pressure distribution in both water and air.

The first sensitivity study considering the influence of the diffusion parameter b in the LS transport equation (see Eqn. (4.16) and Eqn. (2.41)) revealed that the solution is extremely insensitive to specified LS CFL number, CFL_ψ and stabilisation parameter, γ.

The wave reflection study has been performed by varying relaxation zone length from 50% to 150% of the incident wave length, where it has been observed that the relaxation zone should be as large as possible to prevent wave reflection. However, for practical purposes, very good results can be obtained with relaxation zone length equal to the incident wave length, with reflection estimate lesser than 0.5%.

Temporal resolution study revealed that the dispersion (phase shift) error is significantly larger than the dissipation error (loss of amplitude) when using extremely low temporal resolution corresponding to 25 time steps per incident wave period. To quantify, the phase shift difference compared to highly resolved solution with 800 time steps per period is approximately 30°, while the amplitude is lowered by only 1%. The achieved orders of temporal accuracy range from $p = 1$ to $p = 1.25$, which is smaller than theoretical order of accuracy $p = 1.5$ (recall that a blend of Crank–Nicolson and Euler implicit has been used). The corresponding temporal resolution uncertainties are lesser than 1.5%.

Grid refinement study has been performed by considering one coarser and one finer grid compared to the original, medium grid. In spite of the coarse grid having only 7.5 cells per wave height and approximately 3 000 cells, good wave propagation results have been obtained. The achieved order of spatial accuracy $p = 1.64$ and $p = 1.80$ has been obtained for amplitudes and phases, respectively. The corresponding grid refinement uncertainties are lesser than 1%.

A steepness study has been carried out by considering eight waves with increasing steepness up to $ka \approx 0.33$, where good comparison with the stream function wave theory has been obtained. It is interesting to note that with increasing steepness, CFD tends to under predict the first order amplitude, while over predicting higher order effects.

A long simulation lasting 100 incident wave periods has been performed to address the conservative properties of the LS method and implicit relaxation zones, and to estimate the periodic uncertainty via moving window FFT. During the long simulation, the mean value of the global water/air ratio changes by $5 \cdot 10^{-4}\%$, which indicated very good conservative properties and is considered negligibly low. The periodic uncertainty through 100 periods has generally been smaller than 0.05%, while the signed distance property of the LS has been well preserved.

As a last sensitivity study, a long domain simulation has been performed where the maximum deviation in wave amplitude with respect to position of wave gauges is 0.4%, while the maximum deviation in phase shift is approximately 4°. This again indicates that the dispersion (phase shift) error is higher.

Higher Order Forces on a Vertical Cylinder

Higher order forces on a vertical, circular cylinder due to regular waves with increasing steepness (up to $ka \approx 0.24$) have been assessed. In–line forces have been compared to experimental measurements by Huseby and Grue [120] and fully nonlinear potential flow solution by Ferrant *et al.* [118], where a good comparison has been obtained up to seventh order. The agreement of harmonic amplitudes is very good compared to both sets of results, while the phase shifts agree slightly better with potential flow results [118] than with experimental measurements. It is also interesting to stress that the seventh order response is three to five orders of magnitude smaller than the first order response, depending on the wave steepness. Periodic uncertainty has been assessed for all measured items and test cases, where it is negligibly low for harmonic amplitudes, while sometimes significant for harmonic phases of orders higher than fourth in very steep waves.

The temporal resolution study has been carried out by simulating from 25 to 800 time steps per incident wave period. As expected, higher order effects have not been accurately captured with extremely low temporal resolution, although a very good estimate of all higher order effects can be obtained by using approximately 200 time steps per incident wave period. As in the wave propagation test cases, dispersion error is more significant than the dissipation error when using coarse temporal resolution.

The grid refinement study has been carried out by coarsening the original, fine grid with 552 000 cells twice with refinement ratio of $r = 1.5$. Although the first order effects are well resolved on the coarse grid, which has approximately 9 cells per wave height, higher order effects deviate significantly compared to finer grid solutions. However, both harmonic amplitudes and phases, from first to seventh order vary only slightly from medium to fine grid.

Seakeeping KCS Simulations at Design Speed

The most extensive set of sensitivity studies has been carried out for seakeeping KCS simulations at design speed and high Brard numbers. Validation of the model is performed for 5 head wave cases and 5 oblique wave cases publicly available at the Tokyo 2015 Workshop [128]. For all head wave cases, mean values and first order harmonic amplitudes and phases of heave, pitch and total resistance coefficients compare well with the experimental data. For the oblique wave test cases, the discrepancy between CFD and experimental results is larger, where it is believed that several inconsistencies indicate some issues in the experimental setting. Unfortunately, repeatability studies for experiments have not been reported and consequently the experimental uncertainty has not been determined.

Various sensitivity studies included 48 simulations in total:

- 6 simulations for the temporal resolution study,
- 4 simulations for the hydro–mechanical coupling study,

- 7 short simulations for the parallel scaling test,
- 1 performance test,
- 15 simulations for all head wave cases,
- 15 simulations for all oblique wave cases,

assessing four types of uncertainties related to: temporal resolution, grid refinement, number of outer correctors for hydro–mechanical coupling and periodic uncertainty.

The temporal resolution study revealed that the simulation with only 25 time steps per encounter period is stable, as was the case in wave propagation and cylinder diffraction studies. Compared to highly resolved temporal resolution using 800 time steps per encounter period, first order harmonic amplitudes of motions and the total resistance may be predicted reasonably well with significantly lower temporal resolution. The largest detrimental effect when using low temporal resolution is observed for the first order harmonic phases and mean values. The periodic convergence is also smoother and the corresponding periodic uncertainty is lower when using increased number of time steps per encounter period.

The hydro–mechanical coupling study has shown that the final solution is extremely insensitive to the number of outer correctors when one uses the strong coupling strategy where the 6–DOF equations are solved after each pressure correction step, thus providing updated velocity boundary condition at the hull. Hence, a realistic speed–up of 4× is easily obtained by simulating only 2 outer correctors instead of 8.

The strong parallel scaling test performed up to 56 cores has shown that the significant speed–up may be gained even when the domain decomposition yields approximately 10 000 cells per core. However, the achieved parallel efficiency on 56 cores is approximately 60%, which is believed to be related to inefficient memory bus. This still needs to be further investigated and optimised for High Performance Computing (HPC) applications.

A single performance test has been carried out by simulating the C5 head waves case on a coarse grid using 56 cores, with 25 time steps per encounter period and 4 outer correctors. The simulation finished in half an hour for 30 encounter periods, yielding approximately 30 seconds of CPU time for 1 second of physical time. Such trade–off between accuracy and CPU time may be important for industrial applications regarding optimisation of hull shape with respect to added resistance in waves, where extremely high number of cases would need to be considered.

Regarding periodic, temporal resolution, hydro–mechanical coupling and grid uncertainties, following observations can be summarised:

- Periodic uncertainties for all simulations are generally an order of magnitude lower that temporal resolution and grid refinement uncertainties. It is important to note that such low periodic uncertainties are ensured only when one performs a significant number of encounter periods (at least more than 10),

- Uncertainties related to hydro–mechanical coupling are also negligibly small compared to temporal resolution and grid refinement uncertainties,

- Grid refinement and temporal resolution uncertainties are of the same order of magnitude. The corresponding uncertainties are very small for first order amplitudes and phases, often below few percent, while the grid uncertainties, seem to be higher for the mean values, on average,

- Grid uncertainties for the oblique wave cases are higher compared to the head wave cases, which has been expected since the complexity of the cases is higher because of the roll motion. Large roll amplitudes cause the free surface to be located outside the grid refinement region around the still water line, possibly introducing additional numerical errors.

Periodic convergence of roll in bow and quartering waves has been presented and investigated in detail, where it has been shown that at least 20 encounter periods need to be simulated in order to lower the periodic uncertainty down to a negligibly small level.

Finally, following conclusions may be drawn for seakeeping simulations in head and oblique waves at design speed and high Brard numbers:

- Accurate results regarding motions and total resistance may be obtained by using relatively coarse computational grids (ranging from 600 000 to 3 200 000 cells). This is expected since the large portion of ship's heave and pitch motion is related to restoring forces and moments,

- In order to achieve a periodically steady–state solution, a significant number of encounter periods needs to be simulated. The number of periods is dependent on time step size and heading of the ship, where the convergence of certain items can be observed by performing moving window FFT as a post processing step,

- For the present numerical model, accurate results may be expected with 200 time steps per encounter periods and only 2 outer correctors (coupling the flow field with rigid body motion), which is directly related to the recently developed highly resolved strategy for fluid–flow and 6–DOF equations coupling,

- For head wave cases, accurate results may be obtained by neglecting the relationship between investigated wave systems and geometrical parameters of the grid, thus indicating that relatively coarse grids with reduced number of cells per wave height and length may be used.

7. Conclusions and Future Work

7.1. Decomposition Model Based on Ghost Fluid Method

Most of today's CFD algorithms for marine hydrodynamics rely on conditionally averaged equations. This approach has been considered in the early stages of this study, but has proven to be numerically inadequate when used with segregated solution algorithms since the pressure–density coupling is resolved within the momentum equations, often causing spurious acceleration of the lighter phase. Furthermore, that model relies on calculating the gradient of the density, being a step function, using ordinary discretisation schemes. For these reasons, the starting point of this study is the Ghost Fluid Method [15, 45, 49, 47, 48] which starts from the assumption that the jump conditions at the free surface have to be taken into account by using one–sided extrapolates from corresponding fluid. This approach, applied to arbitrary polyhedral FV discretisation procedures, yields second–order accurate interface–corrected interpolation schemes for dynamic pressure and density, both of which have a discontinuity at the free surface. Hence, the Heaviside function for dynamic pressure and density is taken into account in the discretisation, yielding accurate resolution of their jumps at the free surface, across a single internal face. It is important to stress that the present model does not make the assumption that the free surface is aligned with internal faces of the grid, rather, the second–order accurate location of the interface is calculated using the signed distance function in the LS interface capturing method.

The LS method [35, 28, 82, 83, 46, 130] has been widely used as an accurate interface capturing method for two–phase flow modelling. One of the main advantages of the method is the unboundedness of the signed distance field, making it easier to advect. However, the LS method based on signed distance field has two practical limitations:

1. It is not conservative since the signed distance field does not represent any conserved physical property (as is the case in the VOF method where the volume fraction is the transported variable),

2. The signed distance property of the LS field is not preserved after the usual advection step and some form of additional, explicit redistancing is often required.

In this thesis, both problems are addressed by considering the PF method. The PF method [36, 37] advects the tangent hyperbolic profile across the free surface. However, the PF transport equation has additional terms which advect the free surface while maintaining the tangent hyperbolic profile. Sun and Beckermann [36] have then derived the LS transport equation from the PF equation, which now implicitly preserves the signed distance profile during the transport. The present study implements the implicitly redistanced LS transport equation into arbitrary polyhedral FV discretisation with reformulation of explicit source terms into implicit convection terms, favourable for strongly conservative FV discretisation. The use of the LS signed distance field has a strong advantage when combined with the solution decomposition by SWENSE approach.

The SWENSE solution decomposition, originally developed by Ferrant *et al.* [20] splits the unknown variables in the mathematical model into incident, potential flow wave field and perturbation components. Hence, considering the LS method based on signed distance field, only the perturbation around the potential flow solution is calculated in CFD. This facilitates wave transport as the additional terms in governing equations are explicit and ordinary second–order accurate interpolation schemes may be used. The SWENSE method hence efficiently introduces waves in the computation, however, their unwanted reflection off far–field boundaries needs to be addressed as well.

While several approaches for preventing wave reflection exist in the literature, the domain decomposition approach by Jacobsen *et al.* [52] is followed in this thesis. The approach relies on relaxation zones, where the CFD solution is blended with the target, usually potential flow solution. In this thesis, the implicit treatment of relaxation zones, recently published by Jasak *et al.* [53] is used. Inside relaxation zones, all perturbation fields are forced to zero, leaving non–reflecting potential flow solution.

Following a brief summary of the implemented numerical model presented above, the contribution of this study in the field of large–scale, two–phase flow modelling in CFD may be divided into following parts:

- Derivation and implementation of the GFM method for treatment of interface jump conditions within arbitrary polyhedral FV method using compact computational stencil, yielding second–order accurate interface–corrected schemes for discontinuous fields,
- Reformulation and implementation of the implicitly redistanced LS method in strongly conservative FV framework, where the additional terms are mathematically recast into convective terms,
- Implementation of the solution decomposition strategy based on SWENSE approach, where the original method is modified in accordance with the strongly conservative FV method,
- Formulation of the domain decomposition strategy based on relaxation zones has been modified in order to account for SWENSE solution decomposition.

Finally, the combination of the above mentioned methods for treatment of discontinuities at the free surface, interface capturing method and solution and domain decomposition has not been implemented in any numerical framework prior to this study.

7.2. Validation and Verification

The resulting numerical model is systematically tested by performing numerous sensitivity studies on test cases of industrial importance. As the present methodology is especially suitable for wave modelling, most of the test cases consider progressive ocean waves: wave propagation studies, assessment of higher order forces on a circular cylinder and seakeeping of a ship. The model is successfully validated by comparing the computational results with analytical, other numerical and experimental data. As today's CFD algorithms are complex and generally have a significant number of input parameters, it is often possible to find the certain set of input parameters (time step size, grid resolution) in order to obtain the correct solution to a given problem. In this thesis, a significant amount of attention is given to various sensitivity studies in order to address different kinds of numerical uncertainties: temporal discretisation uncertainty, grid refinement uncertainty, periodic uncertainty and others.

Following general conclusions can be drawn from temporal resolution and grid refinement studies performed for all test cases:

- Although the present numerical model is developed with arbitrary polyhedral grid assumption, better convergence properties are obtained by using successively refined block–structured hexahedral grids,
- The numerical model is stable with relatively coarse grids and large time steps, while still providing a reasonably good estimate of the solution even when only 25 time steps per period are used or there are only several cells across wave height. This trade–off between accuracy and performance might be beneficial and exploited for optimisation purposes, where the accurate solutions are not sought in the early design stage,
- The dispersion (phase shift) errors are always higher than the dissipation errors (loss of amplitude), yielding higher numerical uncertainties for harmonic phases compared to amplitudes,
- The model accurately captures higher order nonlinear effects, even when the CFD domain is relatively small.

The periodic uncertainty is also assessed for each case set by performing moving window FFT on the time domain signal. This yields convergence of harmonic amplitudes and phases through successive periods, where the corresponding periodic uncertainty may then be estimated. The periodic uncertainty is an indicator regarding whether the truly periodic stead–state is achieved. For wave propagation cases and higher order forces, reasonable periodic convergence is generally ensured within few periods. This is not the case in seakeeping simulations, where it is shown that sometimes more than 20 encounter periods need to be simulated in order to reach periodically steady–state solution. The author believes that this is strongly related to nonlinear coupling between the flow field and the 6–DOF motion equations, where a significant amount of time is required for the mean values of motions to converge.

Furthermore, the numerical model is efficient as, CPU times reported for the seakeeping calculations in Sec. 6.5. indicate. As an example, 33 head wave simulations have been carried out in two weeks using 56 cores. The outcome of these simulations is a good estimate of the transfer function of the ship, including four kinds of numerical uncertainties. Hence, if the uncertainty estimate is not required (*e.g.* in the early design stage of the ship), it is possible to obtain an accurate estimate of the added resistance transfer function at design speed in a few days.

Interested reader is referred to group's YouTube channel [129] for animations regarding some simulations carried out for this.

7.3. Proposals for Future Work

The present numerical model is developed within `foam-extend`, which is a community driven fork of the Open Field Operation And Manipulation software. Since Open Field Operation And Manipulation and `foam-extend` heavily rely on object–oriented programming paradigm in C++, the framework is easy to extend and maintain.

One of the topics for future work would be the analytical evaluation of explicit incident terms arising from SWENSE decomposition. Analytical evaluation of explicit terms directly related to wave propagation, should further facilitate wave transport as the discretisation error would then vanish. This approach has been implemented by Ducrozet *et al.* [56] in differential FD framework and needs further investigation for its implementation in integral FV framework.

The two–way coupling with more advanced numerical models should also be investigated in future work. As an example, it might be beneficial to couple the CFD solution with diffraction/radiation BEM potential flow solution, where the computational cost of the BEM is significantly smaller than the CFD. This could allow accurate propagation of radiated and diffracted fields towards the far–field boundaries and consequently, the CFD computational domain could be further reduced.

Furthermore, if accurate simulations of slamming and sloshing events were to be performed, it might be important to consider compressibility effects for the air. The whole mathematical model would then need to be reformulated in order to include varying density in governing equations. Nevertheless, this thesis could then serve as a guideline to derive interface–corrected interpolation schemes via GFM approach for treatment of discontinuities at the free surface.

Regarding V&V, seakeeping at low Froude and Brard numbers needs to be investigated in detail. The author doubts that ordinary two–equation turbulence models will provide suitable results for seakeeping of a ship at low Froude numbers because the orbital velocity in the wave may be greater than the forward speed of the ship. This would result in adverse pressure gradients along the hull, making two–equation models inappropriate. On the other hand, simulations of freely floating ships without the forward speed should not impose any difficulties as no turbulence modelling needs to be employed.

Appendices

A Derivation of the Level Set Transport Equation From the Phase Field Equation

Following Sun and Beckermann [36], the PF equation in the absence of curvature–driven interface motion reads:

$$\frac{\partial \phi}{\partial t} + \mathbf{u}{\bullet}\nabla\phi = b\left(\nabla{\bullet}\left(\nabla\phi\right) + \frac{\phi\left(1-\phi^2\right)}{\epsilon^2} - \kappa|\nabla\phi|\right) . \tag{A1}$$

The PF can be explicitly defined in terms of the LS field:

$$\phi(\psi) = \tanh\left(\frac{\psi}{\epsilon\sqrt{2}}\right) . \tag{A2}$$

Noting the identity given by Eqn. (A2), each term in Eqn. (A1) may be written in terms of the signed distance field ψ using the chain rule:

- Time derivative term (first term on the l.h.s., Eqn. (A1)):

$$\frac{\partial \phi}{\partial t} = \frac{\partial \phi}{\partial \psi}\frac{\partial \psi}{\partial t} , \tag{A3}$$

- Convection term (second term on the l.h.s., Eqn. (A1)):

$$\mathbf{u}{\bullet}\nabla\phi = \mathbf{u}\frac{\partial \phi}{\partial \psi}{\bullet}\nabla\psi , \tag{A4}$$

- Diffusion term (first term on the r.h.s., Eqn. (A1)):

$$b\nabla{\bullet}\left(\nabla\phi\right) = b\frac{\partial^2 \phi}{\partial \psi^2}|\nabla\psi|^2 + b\frac{\partial \phi}{\partial \psi}\nabla{\bullet}\left(\nabla\psi\right) , \tag{A5}$$

  where Faà di Bruno's generalisation of the chain rule for the higher order derivatives (Laplacian second order term) has been used,

- Curvature driven term (second term on the r.h.s., Eqn. (A1)):

$$\begin{aligned} b\frac{\phi\left(1-\phi^2\right)}{\epsilon^2} &= \frac{b}{\epsilon^2}\tanh\left(\frac{\psi}{\epsilon\sqrt{2}}\right)\left(1-\tanh^2\left(\frac{\psi}{\epsilon\sqrt{2}}\right)\right) \\ &= \frac{b}{\epsilon^2}\tanh\left(\frac{\psi}{\epsilon\sqrt{2}}\right)\operatorname{sech}^2\left(\frac{\psi}{\epsilon\sqrt{2}}\right) , \end{aligned} \tag{A6}$$

  where $\operatorname{sech}^2 x = 1 - \tanh^2 x$ trigonometric identity has been used,

- Counter curvature driven term (third term on the r.h.s., Eqn. (A1)):

$$- b\kappa|\nabla\phi| = -b\kappa\frac{\partial\phi}{\partial\psi}|\nabla\psi| \,, \tag{A7}$$

Furthermore, following identities may be easily obtained by differentiating Eqn. (A2) with respect to signed distance field ψ:

$$\frac{\partial\phi}{\partial\psi} = \frac{1}{\epsilon\sqrt{2}}\,\mathrm{sech}^2\left(\frac{\psi}{\epsilon\sqrt{2}}\right) , \tag{A8}$$

$$\frac{\partial^2\phi}{\partial\psi^2} = -\frac{1}{\epsilon^2}\tanh\left(\frac{\psi}{\epsilon\sqrt{2}}\right)\mathrm{sech}^2\left(\frac{\psi}{\epsilon\sqrt{2}}\right) . \tag{A9}$$

Inserting the identities given by Eqn. (A3) to Eqn. (A9) into the PF transport equation, Eqn. (A1), yields implicitly redistanced LS equation:

$$\begin{aligned}
&\frac{1}{\epsilon\sqrt{2}}\,\mathrm{sech}^2\left(\frac{\psi}{\epsilon\sqrt{2}}\right)\frac{\partial\psi}{\partial t} + \frac{1}{\epsilon\sqrt{2}}\,\mathrm{sech}^2\left(\frac{\psi}{\epsilon\sqrt{2}}\right)\mathbf{u}\mathbf{\cdot}\nabla\psi = \\
&-b\frac{1}{\epsilon^2}\tanh\left(\frac{\psi}{\epsilon\sqrt{2}}\right)\mathrm{sech}^2\left(\frac{\psi}{\epsilon\sqrt{2}}\right)|\nabla\psi|^2 + b\frac{1}{\epsilon\sqrt{2}}\,\mathrm{sech}^2\left(\frac{\psi}{\epsilon\sqrt{2}}\right)\nabla\mathbf{\cdot}\left(\nabla\psi\right) + \\
&+b\frac{1}{\epsilon^2}\tanh\left(\frac{\psi}{\epsilon\sqrt{2}}\right)\mathrm{sech}^2\left(\frac{\psi}{\epsilon\sqrt{2}}\right) - b\kappa\frac{1}{\epsilon\sqrt{2}}\,\mathrm{sech}^2\left(\frac{\psi}{\epsilon\sqrt{2}}\right)|\nabla\psi| \,.
\end{aligned} \tag{A10}$$

Multiplying Eqn. (A10) with $\epsilon\sqrt{2}/\,\mathrm{sech}^2\left(\psi/(\epsilon\sqrt{2})\right) \neq 0$ yields the final form of implicitly redistanced LS transport equation:

$$\frac{\partial\psi}{\partial t} + \mathbf{u}\mathbf{\cdot}\nabla\psi = b\left(\nabla\mathbf{\cdot}\left(\nabla\psi\right) + \frac{\sqrt{2}}{\epsilon}\left(1 - |\nabla\psi|^2\right)\tanh\left(\frac{\psi}{\epsilon\sqrt{2}}\right) - \kappa|\nabla\psi|\right) , \tag{A11}$$

which is equivalent to Eqn. (2.41) using $\kappa = \nabla\mathbf{\cdot}\left(\nabla\psi/|\nabla\psi|\right)$.

B Picard Linearisation of the Hyperbolic Tangent Source Term

The Picard linearisation procedure is carried out for the hyperbolic tangent source term in the LS transport equation, Eqn. (3.10). The source term can be written in the following form:

$$S(\psi) = b\frac{\sqrt{2}}{\epsilon}\tanh\left(\frac{\psi}{\epsilon\sqrt{2}}\right) = a_1 \tanh\left(a_2\psi\right)\ , \tag{B1}$$

where a_1 and a_2 are non–negative constants, since $b \geq 0$ and $\epsilon \geq 0$. Expanding the r.h.s. of Eqn. (B1) in the Taylor series around the value from the previous time step or iteration ψ^o yields:

$$S(\psi^n) = S(\psi^o) + \left(\frac{\partial S}{\partial \psi}\right)^o \left(\psi^n - \psi^o\right)\ , \tag{B2}$$

with:

$$\left(\frac{\partial S}{\partial \psi}\right)^o = a_1 a_2 \,\mathrm{sech}^2(a_2\psi^o)\,. \tag{B3}$$

Substituting Eqn. (B3) into Eqn. (B2) yields a linearised version of the source term:

$$\begin{aligned} S(\psi^n) &= a_1\tanh(a_2\psi^o) + a_1 a_2\,\mathrm{sech}^2(a_2\psi^o)\left(\psi^n - \psi^o\right) \\ &= S_1 + S_u\psi^n - S_u\psi^o\,. \end{aligned} \tag{B4}$$

This procedure divides the original source term into two parts: terms S_1 and $S_u\psi^o$ are explicit since they are bound to the value of ψ_o from the previous time step or iteration, while the $S_u\psi^n$ term can be made implicit. However, S_u appearing on the r.h.s. of the LS transport equation, Eqn. (3.10) is always non–negative. For its implicit treatment, this term would have to be transferred to the l.h.s. of the equation, making S_u non–positive. Hence, an additional diagonal contribution of $-S_u$ would decrease the diagonal dominance of the resulting matrix. This procedure is therefore omitted, and the original source term given by Eqn. (B1) is treated explicitly in the LS transport equation, Eqn. (3.10). The explicit treatment of the source term renders its solution decomposition unnecessary.

Bibliography

[1] F. Stern, J. Yang, Z. Wang, H. Sadat-Hosseini, M. Mousaviraad, B. S., T. Xing, Computational Ship Hydrodynamics: Nowadays and Way Forward, in: Proceedings of the 29^{th} ONR Symposium on Naval Hydrodynamics, 2012, pp. 1–73.

[2] L. Larsson, F. Stern, M. Visonneau, Numerical Ship Hydrodynamics: An assessment of the Gothenburg 2010 workshop, Springer, 2013. `doi:10.1007/978-94-007-7189-5`.

[3] O. El Moctar, U. Lantermann, P. Mucha, J. Höpken, T. Schellin, RANS–Based Simulated Ship Maneuvering Accounting for Hull–Propulsor–Engine Interaction, Ship Technol. Res.: Schiffstechnik 61 (2015) 142–161. `doi:10.1179/str.2014.61.3.003`.

[4] L. Larsson, F. Stern, M. Visonneau, N. Hirata, T. Hino, J. Kim (Eds.), Tokyo 2015: A Workshop on CFD in Ship Hydrodynamics, Vol. 2, NMRI (National Maritime Research Institute), Tokyo, Japan, 2015.

[5] J. Otzen, C. D. Simonsen, F. Stern, RANS Simulation and Validation of Added Resistance and Motions of the KCS in Regular Head Waves, in: Proceedings of the Tokyo 2015: A Workshop on CFD in Ship Hydrodynamics, Vol. 3, 2015, pp. 273–278.

[6] J. Kim, K.-S. Kim, Y.-C. Kim, Y. Kim, T. Lim, S.-H. Van, Numerical Simulation of the Flow Around Ships in Calm Sea and in Regular Head Waves by Using WAVIS Code, in: Proceedings of the Tokyo 2015: A Workshop on CFD in Ship Hydrodynamics, Vol. 3, 2015, pp. 321–326.

[7] H. Kobayashi, K. Ohashi, N. Hirata, Flow Simulations Using Overset Grid Assembler UP_GRID and Navier–Stokes Solver NAGISA, in: Proceedings of the Tokyo 2015: A Workshop on CFD in Ship Hydrodynamics, Vol. 3, 2015, pp. 353–358.

[8] B. d'Aure, B. Mallol, C. Hirsch, Resistance and Seakeeping CFD Simulations for the Korean Container Ship, in: Proceedings of the Tokyo 2015: A Workshop on CFD in Ship Hydrodynamics, Vol. 3, 2015, pp. 359–364.

[9] M. Tenzer, S. Sigmund, U. Lantermann, B. el Moctar, Prediction of Ship Resistance and Ship Motions in Calm Water and Regular Waves Using RANSE, in: Proceedings of the Tokyo 2015: A Workshop on CFD in Ship Hydrodynamics, Vol. 3, 2015, pp. 413–418.

[10] G. Filip, K. Maki, Seakeeping Analysis of the KCS Vessel in Regular Waves, in: Proceedings of the Tokyo 2015: A Workshop on CFD in Ship Hydrodynamics, Vol. 3, 2015, pp. 419–424.

[11] V. Vukčević, H. Jasak, Seakeeping Validation and Verification Using Decomposition Model Based on Embedded Free Surface Method, in: Proceedings of the Tokyo 2015: A Workshop on CFD in Ship Hydrodynamics, Vol. 3, 2015, pp. 437–442.

[12] H. Sadat-Hosseini, Y. Sanada, M. Stocker, F. Stern, S. Toxopeus, T. Castiglione, C. Simonsen, J. F. Otzen, KCS Added Resistance for Variable Heading, in: Proceedings of the Tokyo 2015: A Workshop on CFD in Ship Hydrodynamics, Vol. 3, 2015, pp. 309–314.

[13] V. Vukčević, H. Jasak, Validation and Verification of Decomposition Model Based on Embedded Free Surface Method for Oblique Wave Seakeeping Simulations, in: Proceedings of the Tokyo 2015: A Workshop on CFD in Ship Hydrodynamics, Vol. 3, 2015.

[14] P. Queutey, M. Visonneau, An interface capturing method for free–surface hydrodynamic flows, Comput. Fluids 36 (2007) 1481–1510. doi:10.1002/j.compfluid.2006.11.007.

[15] J. Huang, P. M. Carrica, F. Stern, Coupled ghost fluid/two–phase level set method for curvilinear body–fitted grids, Int. J. Numer. Meth. Fluids 44 (2007) 867–897. doi:10.1002/fld.1499.

[16] P. M. Carrica, R. V. Wilson, R. W. Noack, F. Stern, Ship motions using single–phase level set with dynamic overset grids, Comput. Fluids 36 (2007) 1415–1433. `doi:10.1016/j.compfluid.2007.01.007`.

[17] P. M. Carrica, R. V. Wilson, F. Stern, An unsteady single–phase level set method for viscous free surface flows, Int. J. Numer. Meth. Fluids 53 (2007) 229–256. `doi:10.1002/fld.1279`.

[18] C. Klaij, C. Vuik, SIMPLE–type preconditioners for cell–centered, colocated finite volume discretization of incompressible Reynolds–averaged Navier–Stokes equations, Int. J. Numer. Meth. Fluids 71 (2013) 830–849. `doi:10.1002/fld.3686`.

[19] C. Klaij, On the stabilization of finite volume methods with co–located variables for incompressible flow, J. Comput. Phys. 297 (2015) 84–89. `doi:10.1016/j.jcp.2015.05.012`.

[20] P. Ferrant, L. Gentaz, D. Le Touzé, A new RANSE/Potential Approach for Water Wave Diffraction, in: Proceedings of the Numerical Towing Tank Symposium, NuTTS, 2002.

[21] H. G. Weller, G. Tabor, H. Jasak, C. Fureby, A tensorial approach to computational continuum mechanics using object oriented techniques, Comput. Phys. 12 (1998) 620–631.

[22] H. Jasak, A. Jemcov, Z. Tuković, Openfoam: A c++ library for complex physics simulations, International Workshop on Coupled Methods in Numerical Dynamics, IUC, Dubrovnik, Croatia.

[23] L. Larsson, F. Stern, M. Visonneau, N. Hirata, T. Hino, J. Kim (Eds.), Tokyo 2015: A Workshop on CFD in Ship Hydrodynamics, Vol. 3, NMRI (National Maritime Research Institute), Tokyo, Japan, 2015.

[24] F. R. Batchelor, An Introduction to Fluid Dynamics, Cambridge University Press, 1967.

[25] G. Tryggvason, R. Scardovelli, S. Zaleski, Direct Numerical Simulations of Gas-Liquid Multiphase Flows, Cambridge University Press, 2011.

[26] C. Hirt, B. Nicholls, Volume of fluid method for dynamics of free boundaries, J. Comput. Phys. 39 (1981) 201–221.

[27] O. Ubbink, R. I. Issa, A method for capturing sharp fluid interfaces on arbitrary meshes, J. Comput. Phys. 153 (1999) 26–50.

[28] M. Sussman, P. Smereka, S. Osher, A level set approach for computing solutions to incompressible two-phase flow, J. Comput. Phys. 114 (1994) 146–159.

[29] R. Folch, J. Casademunt, A. Hernández-Machado, Phase–field model for Hele–Shaw flows with arbitrary viscosity contrast. I. Theoretical approach, Phys. Rev. E 60 (1999) 1724.

[30] O. Ubbink, Numerical prediction of two fluid systems with sharp interfaces, Ph.D. thesis, Imperial College of Science, Technology & Medicine, London (1997).

[31] S. Muzaferija, M. Perić, P. Sames, T. Schelin, A two–fluid Navier–Stokes solver to simulate water entry, in: Proceedings of the 22nd Symposium on Naval Hydrodynamics, 1998, pp. 638–651.

[32] H. Rusche, Computational fluid dynamics of dispersed two - phase flows at high phase fractions, Ph.D. thesis, Imperial College of Science, Technology & Medicine, London (2002).

[33] J. A. Sethian, Level Set Methods: Evolving Interfaces in Geometry, Fluid Mechanics, Computer Vision and Materials Science, Cambridge University Press, 1996.

[34] S. Osher, R. Fedkiw, Level Set Methods and Dynamic Implicit Surfaces, Springer, 2003.

[35] M. Sussman, E. Fatemi, An efficient, interface-preserving level set redistancing algorithm and its application to interfacial incompressible fluid flow, SIAM J. Sci. Comput. 20 (4) (1999) 1165–1191.

[36] Y. Sun, C. Beckermann, Sharp interface tracking using the phase–field equation, J. Comput. Phys. 220 (2007) 626–653. doi:10.1016/j.jcp.2007.05.025.

[37] Y. Sun, C. Beckermann, A two–phase diffusive–interface model for Hele–Shaw flows with large property contrasts, Physica D 237 (2008) 3089–3098. doi:10.1016/j.physd.2008.06.010.

[38] Z. Tuković, H. Jasak, A moving mesh finite volume interface tracking method for surface tension dominated interfacial fluid flow, Comput. Fluids 55 (2012) 70–84.

[39] K. Kissling, J. Springer, H. Jasak, S. Schütz, K. Urban, M. Piesche, A Coupled Pressure Based Solution Algorithm Based on the Volume–of–Fluid Approach for Two or more Immiscible Fluids, in: V European Conference on Computational Fluid Dynamics, ECCOMAS CFD, 2010.

[40] S. Wang, J. Glimm, R. Samulyak, X. Jiao, C. Diao, An Embedded Boundary Method for Two Phase Incompressible Flow, ArXiv e-prints.arXiv:1304.5514.

[41] H. Johansen, P. Colella, A Cartesian Grid Embedding Boundary Method for Poisson's Equation on Irregular Domains, J. Comput. Phys. 147 (1998) 60–85. doi:10.1006/jcph.1998.5965.

[42] R. K. Crockett, P. Colella, D. T. Graves, A Cartesian Grid Embedded Boundary Method for Solving the Poisson and Heat Equations with Discontinuous Coefficients in Three Dimensions, J. Comput. Phys. 230 (2010) 613–628. doi:10.1016/j.jcp.2010.12.017.

[43] R. P. Fedkiw, T. Aslam, S. Xu, The ghost fluid method for deflagration and detonation discontinuities, J. Comput. Phys. 154 (2) (1999) 393–427.

[44] M. Kang, R. P. Fedkiw, X.-D. Liu, A boundary condition capturing method for multiphase incompressible flow, J. Sci. Comput. 15 (3) (2000) 323–360.

[45] O. Desjardins, V. Moureau, H. Pitsch, An accurate conservative level set/ghost fluid method for simulating turbulent atomization, J. Comput. Phys. 227 (18) (2008) 8395–8416.

[46] E. Olsson, G. Kreiss, A conservative level set method for two phase flow, J. Comput. Phys. 210 (1) (2005) 225–246.

[47] M. Kaneda, T. Haruna, K. Suga, Ghost-fluid-based boundary treatment in lattice boltzmann method and its extension to advancing boundary, Appl. Therm. Eng. 72 (1) (2014) 126–134.

[48] B. Lalanne, L. R. Villegas, S. Tanguy, F. Risso, On the computation of viscous terms for incompressible two-phase flows with level set/ghost fluid method, J. Comput. Phys. 301 (2015) 289–307.

[49] W. Bo, J. W. Grove, A volume of fluid method based ghost fluid method for compressible multi-fluid flows, Comput. Fluids 90 (2014) 113–122.

[50] P. Higuera, J. Lara, I. J. Losada, Realistic wave generation and active wave absorption for Navier-Stokes models: Application to OpenFoam®, Coast. Eng. 71 (2013) 102–118. doi:10.1016/j.coastaleng.2012.07.002.

[51] P. Higuera, J. Lara, I. J. Losada, Simulating coastal engineering processes with OpenFoam ®, Coast. Eng. 71 (2013) 119–134. doi:10.1016/j.coastaleng.2012.06.002.

[52] N. G. Jacobsen, D. R. Fuhrman, J. Fredsøe, A wave generation toolbox for the open-source CFD library: OpenFoam®, Int. J. Numer. Meth. Fluids 70 (9) (2012) 1073–1088. doi:10.1002/fld.2726.

[53] H. Jasak, V. Vukčević, I. Gatin, Numerical Simulation of Wave Loads on Static Offshore Structures, in: CFD for Wind and Tidal Offshore Turbines, Springer Tracts in Mechanical Engineering, 2015, pp. 95–105.

[54] R. Luppes, B. Düz, H. van der Heiden, P. van der Plas, A. Veldman, Numerical simulations of two–phase flow with COMFLOW: past and recent developments, in: Proceedings of the ECCOMAS 2012 Conference, 2012, pp. 1–16.

[55] P. Higuera, I. Losada, J. L. Lara, Three-dimensional numerical wave generation with moving boundaries, Coast. Eng. 101 (2015) 35–47.

[56] G. Ducrozet, A. P. Engsig-Karup, H. B. Bingham, P. Ferrant, A non-linear wave decomposition model for efficient wave–structure interaction. Part A: Formulation, validations and analysis, J. Comput. Phys. 257 (2014) 863–883.

[57] G. Reliquet, A. Drouet, P.-E. Guillerm, E. Jacquin, L. Gentaz, P. Ferrant, Simulation of wave-body interaction using a single-phase level set function in the swense method, in: ASME 2013 32nd International Conference on Ocean, Offshore and Arctic Engineering, American Society of Mechanical Engineers, 2013.

[58] C. Monroy, G. Ducrozet, A. Bonnefoy, A. Babarit, P. Ferrant, RANS simulations of a CALM buoy in regular and irregular seas using the SWENSE method, in: Proceedings of the Twentieth International Off–shore and Polar Engineering Conference, 2010, pp. 678–685.

[59] R. Marcer, C. Audiffren, C. Dassibat, de Jouette C., P. E. Guillerm, Seakeeping modelling in calm water and in waves using the CFD code Eole, in: 11ème Journées de l'Hydrodynamique, 2007, pp. 1–12.

[60] M. M. Rienecker, J. D. Fenton, A Fourier approximation method for steady water waves, J. Fluid Mech. 104 (1981) 119–137.

[61] B. J. West, K. A. Brueckner, R. S. Janda, A New Numerical Method for Surface Hydrodynamics, J. Geophys. Res. 92 (C11) (1987) 11803–11824.

[62] D. G. Dommermuth, D. K. P. Yue, A high-order spectral method for the study of nonlinear gravity waves, J. Fluid Mech. 184 (1987) 267–288.

[63] G. Ducrozet, F. Bonnefoy, D. Le Touzé, P. Ferrant, 3-D HOS simulations of extreme waves in open seas, Nat. Hazards Earth Syst. Sci. 7 (2007) 109–122.

[64] D. C. Wilcox, Turbulence Modeling for CFD, DCW Industries, 1993.

[65] F. R. Menter, Two-equation eddy-viscosity turbulence models for engineering applications, AIAA J. 32 (8) (1994) 1598–1605.

[66] F. R. Menter, M. Kuntz, R. Langtry, Ten years of industrial experience with the SST turbulence model, Turb. Heat Mass Tran. 4 (2003) 625–632.

[67] F. S. Pereira, G. Vaz, L. Eca, On the Numerical Requirements of RANS and Hybrid Turbulence Models, in: Proceedings of the MARINE 2015 Conference, 2015, pp. 886–902.

[68] D. Li, J. Hallander, T. Johansson, R. Karlsson, Cavitation Dynamics and Underwater Radiated Noise Signature of a Ship with a Cavitating Propeller, in: Proceedings of the MARINE 2015 Conference, 2015, pp. 401–412.

[69] S. C. on CFD in Marine Hydrodynamics, Final report and Recommendations to the 27^{th} ITTC, [Available online; accessed 20 August 2015] (August–September 2014).

[70] Gothenburg Workshop, Gothenburg 2010: A Workshop on CFD in Ship Hydrodynamics, `http://www.insean.cnr.it/sites/default/files/gothenburg2010/index.html`, [Online; accessed 20 August 2015] (2010).

[71] D. Christ, The Naval Hydro Pack and its Application in the Simulation of Ship Hydrodynamics, in: 8^{th} OpenFOAM Workshop, 2013.

[72] H. Schlichting, K. Gersten, Boundary Layer Theory, 8th Edition, Springer, 1967.

[73] B. T. Paulsen, H. Bredmose, H. B. Bingham, An efficient domain decomposition strategy for wave loads on surface piercing circular cylinders, Coast. Eng. 86 (2014) 57–76. `doi:10.1016/j.coastaleng.2014.01.006`.

[74] B. T. Paulsen, H. Bredmose, H. B. Bingham, N. G. Jacobsen, Forcing of a bottom-mounted circular cylinder by steep regular water waves at finite depth, J. Fluid Mech. 755 (2014) 1–3. `doi:10.1017/jfm.2014.386`.

[75] C. Dopazo, On conditional averages for intermittent turbulent flows, J. Fluid Mech. 81 (1977) 433–438.

[76] N. Ashgriz, Handbook of atomization and sprays: theory and applications, Springer Science & Business Media, 2011.

[77] Z. Tan, D. V. Le, K. M. Lim, B. C. Khoo, An Immersed Interface Method for the Incompressible Navier–Stokes Equations with Discontinuous Viscosity Across the Interface, SIAM J. Sci. Comput. 31 (2009) 1798–1819. `doi:10.1137/080712970`.

[78] K. Ito, Z. Li, Interface Conditions for Stokes Equations with a Discontinuous Viscosity and Surface Sources, Appl. Math. Lett. 19 (2006) 229–234. `doi:10.1016/j.aml.2005.02.041`.

[79] K. P. Chen, W. Saric, H. A. Stone, On the deviatoric normal stress on a slip surface, Phys. Fluids A 12 (2000) 3280–1.

[80] G. Tryggvason, B. Bunner, A. Esmaeeli, D. Juric, N. Al-Rawahi, W. Tauber, J. Han, S. Nas, Y.-J. Jan, A Front-Tracking Method for Computations of Multiphase Flow, J. Comput. Phys. 169 (2001) 708–759. `doi:10.1006/jcph.2001.6726`.

[81] T. Kleefsman, Water impact loading on offshore structures, Ph.D. thesis, Rijks universiteit Groningen (2005).

[82] P. Gómez, J. Hernández, J. López, On the reinitialization procedure in a narrow-band locally refined level set method for interfacial flows, Int. J. Numer. Methods Eng. 63 (2005) 1478–1512.

[83] D. Hartmann, M. Meinke, W. Schröder, Differential equation based constrained reinitialization for level set methods, J. Comput. Phys. 227 (2008) 6821–6845.

[84] L. H. Holthuijsen, Waves in Oceanic and Costal Waters, Delft University of Techonlogy and UNESCO-IHE, 2007.

[85] R. G. Dean, R. A. Dalrymple, Water Wave Mechanics for Engineers and Scientists, Vol. 2: Advanced Series on Ocean Engineering, World Scientific, 2010.

[86] J. M. J. Journeé, W. Massie, Offshore Hydromechanics, Delft University of Technology, Cambridge University Press, 2001.

[87] C. Hirsch, Numerical Computation of Internal and External Flows, Vol. 1: Fundamentals of Numerical Discretization, John Wiley & Sons, 1988.

[88] C. Hirsch, Numerical Computation of Internal and External Flows, Vol. 2: Computational Methods for Inviscid and Viscous Flows, John Wiley & Sons, 1984.

[89] S. V. Patankar, Numerical Heat Transfer and Fluid Flow, Taylor and Francis, 1980.

[90] H. Jasak, Error analysis and estimation for the finite volume method with applications to fluid flows, Ph.D. thesis, Imperial College of Science, Technology & Medicine, London (1996).

[91] J. H. Ferziger, M. Peric, Computational Methods for Fluid Dynamics, Springer, 1996.

[92] H. K. Versteeg, W. Malalasekera, An Introduction to Computational Fluid Dynamics: The Finite Volume Method, Pearson Education Limited, 1995.

[93] S. V. Patankar, D. B. Spalding, A calculation procedure for heat, mass and momentum transfer in three-dimensional parabolic flows, Int. J. Heat Mass Transf. 15 (1972) 1787–1806.

[94] C. M. Rhie, W. L. Chow, A numerical study of the turbulent flow past an isolated airfoil with trailing edge separation, AIAA J. 21 (1983) 1525–1532.

[95] I. Demiridžić, M. Perić, Space conservation law in finite volume calculations of fluid flow, Int. J. Numer. Meth. Fluids 8 (1988) 1037–1050. `doi:{10.1002/fld.1650080906}`.

[96] H. Jasak, H. G. Weller, Application of the finite volume method and unstructured meshes to linear elasticity, Int. J. Numer. Methods Eng. 48 (2000) 267–287.

[97] I. Demirdžić, On the Discretization of the Diffusion Term in Finite–Volume Continuum Mechanics, Numer. Heat Transfer, Part B 68 (2015) 1–10. `doi:10.1080/10407790.2014.985992`.

[98] E. A. Coutsias, L. Romero, The quaternions with an application to rigid body dynamics, Department of Mathematics and Statistics.

[99] H. Goldstein, C. Poole, J. Safko, Classical Mechanics, Addison Wesley, 2000.

[100] W. H. Press, S. A. Teukolsky, W. T. Vetterling, B. P. Flannery, Numerical Recipes in C++: The Art of Scientific Computing, Cambridge University Press, 2002.

[101] H. Jasak, v. Tuković, Autmatic mesh motion for the unstructured Finite Volume Method, Trans. FAMENA 30 (2) (2006) 1–18.

[102] J. Donea, A. Huerta, Finite Element Methods for Flow Problems, Wiley, 2003.

[103] J. Hron, S. Turek, A monolithic FEM/multigrid solver for an ALE formulation of fluid-structure interaction with applications in biomechanics, Springer, 2006.

[104] H. G. Matthies, J. Steindorf, Partitioned strong coupling algorithms for fluid–structure interaction, Comput. Struct. 81 (8) (2003) 805–812.

[105] C. D. Simonsen, J. F. Otzen, S. Joncquey, F. Stern, EFD and CFD for KCS heaving and pitching in regular head waves, J. Mar. Sci. Technol. 18 (2013) 435–459. `doi:10.1007/s00773-013-0219-0`.

[106] R. I. Issa, Solution of the implicitly discretised fluid flow equations by operator-splitting, J. Comput. Phys. 62 (1986) 40–65.

[107] Y. Saad, Iterative Methods for Sparse Linear Systems (2nd Edition), Society for Industrial and Applied Mathematics Philadelphia, SIAM, 2003.

[108] M. Hestens, E. Steifel, Method of conjugate gradients for solving linear systems, J. Res. 29 (1952) 409–436.

[109] H. van der Vorst, Bi-cgstab: a fast and smoothly converging variant of bi-cg for the solution of nonsymmetric linear systems, SIAM J. Sci. Comput. 13 (1992) 631–644.

[110] P. Roache, Quantification of uncertainty in computational fluid dynamics, Ann. Rev. Fluid. Mech. 29 (1997) 123–160.

[111] F. Stern, R. V. Wilson, H. W. Coleman, E. G. Paterson, Comprehensive Approach to Verification and Validation of CFD Simulations–Part 1: Methodology and Procedures, J. Fluids. Eng 123(4) (2001) 793–802. `doi:10.1115/1.1412235`.

[112] L. Eca, M. Hoekstra, A procedure for the estimation of the numerical uncertainty of cfd calculations based on grid refinement studies, J. Comput. Phys. 262 (2014) 104–130. `doi:10.1016/j.jcp.2014.01.006`.

[113] S. Muzaferija, M. Perić, Computation of free–surface flows using the finite–volume method and moving grids, Numer. Heat Transfer, Part B 32 (1997) 369–384.

[114] Z. Tuković, Finite volume method on domains of varying shape (in Croatian), Ph.D. thesis, Faculty of Mechanical Engineering and Naval Architecture, Zagreb (2005).

[115] B. van Leer, Towards the ultimate conservative difference scheme. IV. A new approach to numerical convection, J. Comput. Phys. 23 (1977) 276–299.

[116] NPARC Alliance CFD Verification and Validation Web Site, Examining Spatial (Grid) Convergence, `http://www.grc.nasa.gov/WWW/wind/valid/tutorial/spatconv.html`, [Online; accessed 1 April 2016] (2016).

[117] `foam-extend`, The OpenFOAM Extend Project, `http://www.extend-project.de/`, [Online; accessed 27 April 2016] (2016).

[118] P. Ferrant, v. Malenica, B. Molin, Nonlinear wave loads and runup on a vertical cylinder, in: Advances in Fluid Mechanics, Nonlinear Water Wave Interaction, WIT Press, 1999.

[119] S. Malenica, B. Molin, Third harmonic wave diffraction by a vertical cylinder, J. Fluid Mech. 302 (1995) 203–229.

[120] M. Huseby, J. Grue, An experimental investigation of higher–harmonic wave forces on a vertical cylinder, J. Fluid. Mech. 414 (2000) 75–103.

[121] P. Ferrant, Fully non linear interaction of long–crested wave packets with a three dimensional body, in: Proceedings of the 22^{nd} ONR Symposium on Naval Hydrodynamics, 1998, pp. 59–72.

[122] H. Orihara, H. Miyata, Evaluation of added resistance in regular incident waves by computational fluid dynamics motion simulation using an overlapping grid system, J. Mar. Sci. Technol. 8 (2003) 47–60.

[123] P. M. Carrica, H. Fu, F. Stern, Computations of self-propulsion free to sink and trim and of motions in head waves of the KRISO Container Ship (KCS) model, Appl. Ocean Res. 33 (2011) 309–320.

[124] T. Castiglione, F. Stern, S. Bova, M. Kandasamy, Numerical investigation of the seakeeping behavior of a catamaran advancing in regular head waves, Ocean Eng. 38 (2011) 1806–1822. `doi:10.1016/j.oceaneng.2011.09.003`.

[125] C.-S. Wu, D.-C. Zhou, L. Gao, Q.-M. Miao, CFD computation of ship motions and added resistance for a high speed trimaran in regular head waves, Int. J. Nav. Arch. Ocean Eng. 3 (2011) 105–110.

[126] T. Tezdogan, Y. K. Demirel, P. Kellett, M. Khorasanchi, A. Incecik, O. Turan, Full-scale unsteady RANS CFD simulations of ship behaviour and performance in head seas due to slow steaming, Ocean Eng. 97 (2015) 186–206.

[127] V. Vukčević, H. Jasak, I. Gatin, S. Malenica, Seakeeping Sensitivity Studies Using the Decomposition CFD Model Based on the Ghost Fluid Method, in: Proceedings of the 31st Symposium on Naval Hydrodynamics, 2016.

[128] Tokyo Workshop, Tokyo 2015: A Workshop on CFD in Ship Hydrodynamics, `http://www.t2015.nmri.go.jp/`, [Online; accessed 20 August 2015] (2015).

[129] H. Jasak, V. Vukčević, V. Škurić, T. Uroić, G. Cvijetić, I. Gatin, R. Keser, Group's YouTube Channel: 8th Floor CFD@FSB, `https://www.youtube.`

com/channel/UCsK6xZg4PxyJiO2GWR1lm1w, [Online; accessed 21 April 2016] (2016).

[130] E. Olsson, G. Kreiss, S. Zahedi, A conservative level set method for two phase flow ii, J. Comput. Phys. 225 (1) (2007) 785–807.

Abbreviations

2–D two–dimensional. v, x, 1, 12, 52, 53, 76, 77, 80, 82, 83, 85, 87, 91, 92

3–D three–dimensional. 1, 45, 53, 65, 76, 77, 124, 158

6–DOF Six Degrees–of–Freedom. ii, iv, 63, 64, 66–69, 71–74, 81, 156, 158, 161–163, 171, 189, 204, 206, 211

A.P. aft perpendicular. 63

ALE Arbitrary Lagrangian–Eulerian. 67

BEM Boundary Element Method. 1, 2, 29, 211

BiCGStab Bi–Conjugate Gradient Stabilised. 70

CFD Computational Fluid Dynamics. vi, viii, ix, 1–3, 6–9, 14, 29–32, 34–36, 38, 39, 47, 72, 74, 75, 80, 84, 86, 93–95, 97, 104, 111–115, 120, 124, 125, 128, 129, 132, 134, 143, 150, 156–158, 160, 178–181, 189–195, 200, 202, 203, 207–211

CFL Courant–Friedrichs-Lewy. 45, 46, 91, 92, 98, 125, 201

CG Connjugate Gradient. 70

COG Centre–of–Gravity. 63, 66

CPU Central Processing Unit. xi, 1, 12, 67, 72, 126, 136, 158, 189, 190, 205, 211

CSS Continuous Surface Stress. 14, 86

CV Control Volume. 39, 67

DES Detached Eddy Simulation. 8

DNS Direct Numerical Simulation. 8

F.P. front perpendicular. 63, 158

FD Finite Difference. 6, 9, 10, 31, 211

FE Finite Element. 9, 31

FFT Fast Fourier Transform. vii, 77–79, 94, 116, 120, 121, 127, 135, 145, 160, 169, 175, 196–198, 202, 206, 210

FSI Fluid–Structure Interaction. 68

FV Finite Volume. ii, 6, 9–11, 30–32, 37–43, 45, 47, 49–52, 59, 62, 70, 72, 74, 156, 207–209, 211

GCI Grid Convergence Index. 84, 108

GFM Ghost Fluid Method. iv, 5, 6, 10, 17, 28, 29, 40, 43, 44, 50, 53, 56, 60, 62, 63, 69, 72, 74, 88, 90, 102, 116, 125, 150, 200, 207, 209, 212

HOS Higher Order Spectral. 8, 31, 47

HPC High Performance Computing. 204

ILU Incomplete Lower–Upper. 70

ITTC International Towing Tank Conference. 8

KCS KRISO (MOERI) Container Ship. iii–v, viii–xi, 2, 11, 68, 77, 78, 81, 156–159, 161–163, 165, 167, 169, 171, 173, 175, 177–181, 183–185, 187, 189, 191–195, 197, 199, 200, 203

LCB Longitudinal Centre of Bouyancy. 158

LES Large Eddy Simulation. 8

LS Level Set. i, ii, iv, vii, 4–7, 9, 11, 23–27, 29, 32, 34, 37, 38, 44–50, 52–54, 68–70, 80, 82, 83, 90–92, 98, 100, 116, 119, 120, 125, 201, 202, 207–209, 215–217

MC Monotone Convergence. 136, 138, 142

MD Monotone Divergence. 136, 142

OC Oscillatory Convergence. 136, 138, 142

OD Oscillatory Divergence. 136, 138, 142

ODE Ordinary Differential Equation. 66, 67, 69

OpenFOAM Open Field Operation And Manipulation. 3, 10, 58, 69, 211

PDE Partial Differential Equation. 27, 39, 72

PF Phase Field. i, iv, 4, 5, 9, 23–26, 32, 45, 52, 54, 208, 215, 216

PIMPLE Combination of SIMPLE and PISO Algorithms. 69, 81, 82, 91

PISO Pressure Implicit with Splitting of Operator. 69, 73, 82, 91, 163, 171, 189

RANS Reynolds Averaged Navier–Stokes. 1, 2, 8

SCL Space Conservation Law. 48, 67

SGS Sub–Grid Scale. 8

SIMPLE Semi–Implicit Method for Pressure Linked Equations. 69, 70, 73, 161

SST Shear Stress Transport. 8, 162

SWENSE Spectral Wave Explicit Navier–Stokes Equations. i, 7, 9, 11, 25, 30, 31, 33, 34, 38, 43, 70, 208, 209, 211

TVD Total Variation Diminishing. 82

URANS Unsteady Reynolds Averaged Navier–Stokes. 8

V&V Validation and Verification. iii, iv, 10, 12, 74, 76, 78–80, 200, 209, 212

VCG Vertical Centre of Gravity. 158

VOF Volume–of–Fluid. i, 4, 6, 23–25, 28, 32, 52, 54, 100, 208

Curriculum Vitae

Vuko Vukčević, born in Dubrovnik on 12/June/1989 has finished mathematical and natural sciences high school in Dubrovnik. During his undergraduate and graduate studies in naval architecture at Faculty of Mechanical Engineering and Naval Architecture, University of Zagreb, he won numerous awards and acknowledgements as the best student in naval architecture. After finishing his undergraduate and graduate studies with highest honours, he started working as a research assistant at the Faculty of Mechanical Engineering and Naval Architecture. His primary research interests are related to the area of Computational Fluid Dynamics (CFD) in OpenFOAM, precisely: modelling of fully nonlinear, turbulent free surface flows in marine hydrodynamics, general polyhedral Finite Volume discretisation, and coupling of potential flow and CFD for wave modelling. He is actively involved in the `foam-extend` project, where he contributed to the development of block–coupling functionalities and solvers and he implemented the ILU preconditioner with arbitrary level of fill–in for both ordinary lower–diagonal–upper matrices and corresponding block matrices. He also has advanced programming skills in C++, adhering to the object oriented and generic programming paradigms.

Declaration

Parts of the work presented in this thesis have been published in some articles presented below.

Journal Articles

[1] V. Vukčević, H. Jasak, S. Malenica, Decomposition model for naval hydrodynamic applications, Part I: Computational method, Ocean Engineering 121 (2016) 37–46. doi:10.1016/j.oceaneng.2016.05.022.

[2] V. Vukčević, H. Jasak, S. Malenica, Decomposition model for naval hydrodynamic applications, Part II: Verification and validation, Ocean Engineering 121 (2016) 76–88. doi:10.1016/j.oceaneng.2016.05.021.

[3] V. Vukčević, A. Werner, N. Degiuli, Application of smoothed particle hydrodynamics method for simulating incompressible laminar flow, Transactions of FAMENA 36 (4) (2013) 1–12.

Conference Articles

[1] v. B. G. I. Vukčević, V., H. Jasak, Validation and Verification of Seakeeping in OpenFOAM, in: Proceedings of the XXII. Symposium Sorta, 2016, pp. 135–142.

[2] I. Gatin, V. Vukčević, H. Jasak, Coupling of Higher Order Spectral Method and Computational Fluid Dynamics, in: Proceedings of the XXII. Symposium Sorta, 2016, pp. 127–134.

[3] V. Vukčević, H. Jasak, I. Gatin, S. Malenica, Seakeeping Sensitivity Studies Using the Decomposition CFD Model Based on the Ghost Fluid Method, in: Proceedings of the 31st Symposium on Naval Hydrodynamics, 2016.

[4] G. Cvijetić, H. Jasak, V. Vukčević, Finite Volume Implementation of Non–Linear Harmonic Balance Method for Periodic Flows, in: Proceedings of the 54th AIAA Aerospace Sciences Meeting, 2016.

[5] V. Vukčević, H. Jasak, Validation and Verification of Decomposition Model Based on Embedded Free Surface Method for Oblique Wave Seakeeping Simulations, in: Proceedings of the Tokyo 2015: A Workshop on CFD in Ship Hydrodynamics, Vol. 3, 2015.

[6] V. Vukčević, H. Jasak, Seakeeping Validation and Verification Using Decomposition Model Based on Embedded Free Surface Method, in: Proceedings of the Tokyo 2015: A Workshop on CFD in Ship Hydrodynamics, Vol. 3, 2015, pp. 437–442.

[7] I. Gatin, H. Jasak, V. Vukčević, Validation and Verification of Steady Resistance KCS Simulations With Sinkage and Trim Using Embedded Free Surface Method, in: Proceedings of the Tokyo 2015: A Workshop on CFD in Ship Hydrodynamics, Vol. 3, 2015, pp. 431–436.

[8] I. Gatin, V. Vukčević, H. Jasak, CFD Validation of a Container Ship in Calm Water and Head Seas, in: Proceedings of the 18th Numerical Towing Tank Symposium, NUTTS, 2015.

[9] V. Vukčević, H. Jasak, S. Malenica, Assessment of Higher–Order Forces on a Vertical Cylinder with Decompostion Model Based on SWENSE Method, in: Proceedings of the 18th Numerical Towing Tank Symposium, NUTTS, 2015.

[10] G. Contento, G. Lupieri, V. Vukčević, H. Jasak, Numerical Study of Unsteady Breaking Waves Induced by a Submerged Hydrofoil at Steady Forward Speed, in: Proceedings of the 18th International Conference on Ships and Shipping Research, 2015, pp. 104–114.

[11] V. Vukčević, H. Jasak, S. Malenica, Solution and Domain Decomposition Model for Naval Hydrodynamics: RANS and Potential Flow Coupling, in: Proceedings of the VI International Conference on Computational Methods in Marine Engineering (MARINE 2015), 2015, pp. 903–918.

[12] V. Vukčević, A. Östman, H. Jasak, Rapid Simulations of Pure Sway Motion Using FVM in OpenFOAM, in: SIMMAN 2014: Workshop on Verification and Validation of Ship Manoeuvring Simulation Methods, 2014.

[13] H. Jasak, V. Vukčević, D. Christ, Rapid Free Surface Simulation for Steady-State Hull Resistance with FVM using OpenFOAM, in: Proceedings of the 30th Symposium on Naval Hydrodynamics, 2014, pp. 548–554.

[14] V. Vukčević, H. Jasak, OpenFOAM in Marine Hydrodynamics, in: Proceedings of the XXI. Symposium Sorta, 2014.

[15] I. Gatin, V. Vukčević, H. Jasak, Simulation of Wave Impact Loads in OpenFOAM, in: Proceedings of the XXI. Symposium Sorta, 2014.

[16] V. Vukčević, H. Jasak, A Conservative Level Set Method for Interface Capturing in Two-Phase flows, in: Proceedings of the 11th World Congress on Computational Mechanics (WCCM XI), 2014, pp. 1082–1095.

[17] H. Jasak, I. Gatin, V. Vukčević, Numerical Simulation of Wave Loading on Static Offshore Structures, in: Proceedings of the 11th World Congress on Computational Mechanics (WCCM XI), 2014, pp. 5151–5159.

[18] V. Vukčević, H. Jasak, Primjena naval hydro paketa za dvofazna strujanja, in: Šesti susret Hrvatskoga društva za mehaniku, 2014.

[19] I. Gatin, V. Vukčević, H. Jasak, Primjena naval hydro paketa za proračun valnih opterećenja, in: Šesti susret Hrvatskoga društva za mehaniku, 2014.

Miscellaneous

[1] V. Vukčević, Numerical modelling of coupled potential and viscous flow for marine applications - in preparation, Ph.D. thesis, Faculty of Mechanical Engineering and Naval Architecture, University of Zagreb, PhD Thesis (2016).

[2] V. Vukčević, Application of computational fluid dynamics in the motion analysis of ships and offshore platforms (in croatian), Master's thesis, Faculty of Mechanical Engineering and Naval Architecture, University of Zagreb, Croatia (2013).

[3] V. Vukčević, Computational Fluid Dynamics Based on Particle Approach (in Croatian, Batchelor's Thesis), Faculty of Mechanical Engineering and Naval Architecture, University of Zagreb, Croatia, 2013.

[4] V. Vukčević, H. Jasak, Decomposition Model for Naval Hydrodynamics: Recent Advances, in: 10th OpenFOAM® Workshop, 2015.

[5] I. Gatin, V. Vukčević, H. Jasak, Implementation of Higher Order Spectrum Method for nonlinear wave propagation in OpenFOAM, in: 10th OpenFOAM® Workshop, 2015.

[6] V. Vukčević, H. Jasak, Finite Volume Implementation of SWENSE Method, in: 9th OpenFOAM® Workshop, 2014.

[7] K. Jareteg, V. Vukčević, H. Jasak, `pUCoupledFoam` - an open source coupled incompressible pressure-velocity solver based on foam-extend, in: 9th OpenFOAM® Workshop, 2014.

[8] I. Gatin, V. Vukčević, H. Jasak, Simluation of Wave Loads on Offshore Static Structures, in: 9th OpenFOAM® Workshop, 2014.

[9] H. Jasak, I. Gatin, V. Vukčević, Numerical Simulation of wave Loads on Static Offshore Structures, in: Water Wave Theories and the Marine Industries Workshop, Cambridge, 2014.

[10] V. Vukčević, H. Jasak, I. Gatin, Freak Wave and Green Sea Simulations using OpenFOAM, in: ERCOFTAC meeting in UDINE, 2014.

[11] H. Jasak, V. Vukčević, V. Škurić, T. Uroić, G. Cvijetić, I. Gatin, R. Keser, Group's YouTube Channel: 8th Floor CFD@FSB, `https://www.youtube.com/channel/UCsK6xZg4PxyJiO2GWR1lm1w`, [Online; accessed 21 April 2016] (2016).